25 June 2010 | $10

Science

AAAS

CONTENTS continued >>

page 1624

page 1640

COVER

Three-dimensional representation of the emission of electrons from a neon atom upon absorption of a photon from an attosecond extreme ultraviolet pulse. The orange surface plot represents the resulting electron energy distribution, which, when probed by an ultrashort light wave (yellow line), reveals an unexpected time delay between the emission of electrons from different atomic orbitals. See page 1658.

Image: Christian Hackenberger/Ludwig-Maximilians-Universität, Munich, Germany

DEPARTMENTS

Published by AAAS

BREVIA

RESEARCH ARTICLES

REPORTS

CONTENTS continued >>

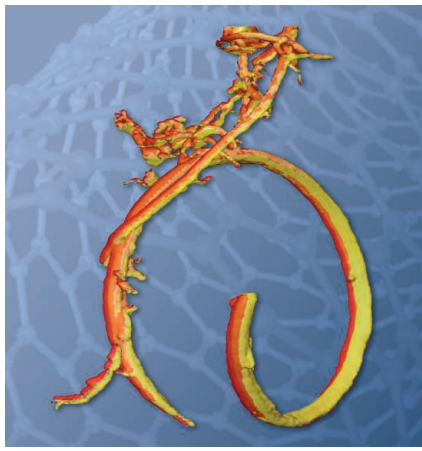

page 1668

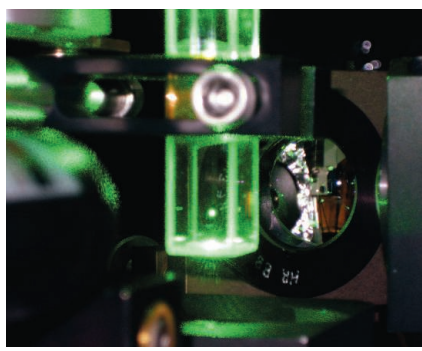

page 1673

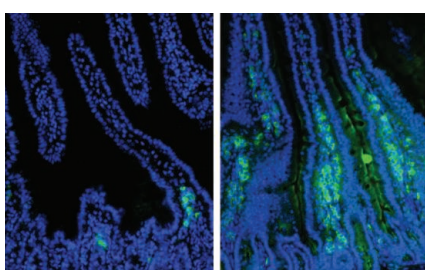

pages 1646 & 1705

SCIENCEONLINE

SCIENCEXPRESS
www.sciencexpress.org

Tissue-Engineered Lungs for in Vivo Implantation
T. H. Petersen et al.
Decellularized rat lungs rebuilt with new cells in vitro can function at a rudimentary level when implanted back into a rat.
10.1126/science.1189345
>> Science *Podcast*

Genetic Reactivation of Cone Photoreceptors Restores Visual Responses in Retinitis Pigmentosa
V. Busskamp et al.
A bacterial ion pump rescues visual function in damaged cone-photoreceptor cells in mouse models of retinitis pigmentosa.
10.1126/science.1190897

The Structure of cbb_3 Cytochrome Oxidase Provides Insights into Proton Pumping
S. Buschmann et al.
The third class of heme-copper oxidases reveals new structural solutions to achieve redox-driven proton translocation.
10.1126/science.1187303

Asymmetric Density Dependence Shapes Species Abundances in a Tropical Tree Community
L. S. Comita et al.
Seedling survival in a tropical forest shows that species abundance is related to a species' sensitivity to conspecific neighbors.
10.1126/science.1190772

Switched Magnetospheric Regulation of Pulsar Spin-Down
A. Lyne et al.
Irregularities in pulsar rotation rates can be explained by quasi-periodic, abrupt changes in the pulsar magnetosphere.
10.1126/science.1186683

Simulated Rapid Warming of Abyssal North Pacific Waters
S. Masuda et al.
Computer simulations suggest a possible reason for the warming of North Pacific bottom water during the past four decades.
10.1126/science.1188703

TECHNICALCOMMENTS

Comment on "30,000-Year-Old Wild Flax Fibers"
C. Bergfjord et al.
Full text at www.sciencemag.org/cgi/content/full/328/5986/1634-b

Response to Comment on "30,000-Year-Old Wild Flax Fibers"
E. Kvavadze et al.
Full text at www.sciencemag.org/cgi/content/full/328/5986/1634-c

SCIENCENOW
www.sciencenow.org
Highlights From Our Daily News Coverage

Genes for Height Hiding in Plain Sight
Team argues that genes have been invisible because of their tiny effects.

Romanian Cave May Boast Central Europe's Oldest Cave Art
Bison, bear, and other drawings extend early artists' reach to Central Europe up to 35,000 years ago.

Chimpanzees Kill for Land
Like humans, chimp males kill their neighbors to grab territory.

SCIENCESIGNALING
www.sciencesignaling.org
The Signal Transduction Knowledge Environment

EVOLUTION OF SIGNALING SYSTEMS

EDITORIAL GUIDE: (R)evolution of Complex Regulatory Systems
R. Linding
Understanding the implications of the changes in signaling systems requires analysis in both cellular and evolutionary time scales.

PERSPECTIVE: Wnt Signaling in Axial Patterning and Regeneration—Lessons from Planaria
E. M. De Robertis
Positional information generated by Wnt signaling determines whether heads or tails will form in wounded flatworms.

PERSPECTIVE: Infrared Snake Eyes—TRPA1 and the Thermal Sensitivity of the Snake Pit Organ
V. C. Panzano et al.
Many vertebrates and invertebrates rely on the ion channel TRPA1 to detect both warmth and chemicals.

RESEARCH ARTICLE : Nodal Signaling Recruits the Histone Demethylase Jmjd3 to Counteract Polycomb-Mediated Repression at Target Genes
Ø. Dahle et al.
Developmental signaling integrates with epigenetic processes to control the expression of Nodal target genes.

SCIENCECAREERS
www.sciencecareers.org/career_magazine
Free Career Resources for Scientists

SCIENTISTS WORKING WITH VOLUNTEERS

Trusting the Public
S. Gaidos
Scientists are figuring out how to tap the experiences and observations of nonscientists.

Collaborating With Citizen Scientists
L. Laursen
Scientists who rely on volunteers for data collection need to learn about management and marketing.

Science Careers Blog
Science *Careers Staff*
Get frequent updates, including advice, opinion, news, and funding opportunities.

SCIENCETRANSLATIONAL MEDICINE
www.sciencetranslationalmedicine.org
Integrating Medicine and Science

COMMENTARY: Patient-Centered Outcomes Research Institute—The Intersection of Science and Health Care
C. Clancy and F. S. Collins
Robust scientific evidence can assist the nation in making informed decisions about health care.

COMMENTARY: Multidimensional Results Reporting to Participants in Genomic Studies—Getting It Right
I. S. Kohane and P. L. Taylor
Understanding participants better can help guide the reporting of individual research results.

RESEARCH ARTICLE: Nuclear Role of WASp in the Pathogenesis of Dysregulated T_H1 Immunity in Human Wiskott-Aldrich Syndrome
M. D. Taylor et al.

PERSPECTIVE: Alternative Control—What's WASp Doing in the Nucleus?
M. A. Teitell
Aberrant histone modification is implicated in the pathogenesis of a rare genetic disorder.

RESEARCH ARTICLE: Safety and Antithrombotic Efficacy of Moderate Platelet Count Reduction by Thrombopoietin Inhibition in Primates
E. I. Tucker et al.
Inhibition of platelet production minimizes clot formation without increasing bleeding in baboons.

SCIENCEPODCAST
www.sciencemag.org/multimedia/podcast
Free Weekly Show
Download the 25 June *Science* Podcast to hear about tissue-engineered lungs, the uncertainty in extracting natural gas from shale, your letters to *Science*, and more.

SCIENCEINSIDER
news.sciencemag.org/scienceinsider
Science Policy News and Analysis

SCIENCE (ISSN 0036-8075) is published weekly on Friday, except the last week in December, by the American Association for the Advancement of Science, 1200 New York Avenue, NW, Washington, DC 20005. Periodicals Mail postage (publication No. 484460) paid at Washington, DC, and additional mailing offices. Domestic individual membership and subscription (51 issues): $146 ($74 allocated to subscription). Domestic institutional subscription (51 issues): $910; Foreign postage extra: Mexico, Caribbean (surface mail) $55; other countries (air assist delivery) $85. First class, airmail, student, and emeritus rates on request. Canadian rates with GST available upon request, GST #1254 88122. Publications Mail Agreement Number 1069624. **Printed in the U.S.A.**

Change of address: Allow 4 weeks, giving old and new addresses and 8-digit account number. **Postmaster:** Send change of address to AAAS, P.O. Box 96178, Washington, DC 20090–6178. **Single-copy sales:** $10.00 current issue, $15.00 back issue prepaid includes surface postage; bulk rates on request. The identification code for *Science* is 0036-8075. *Science* is indexed in the *Reader's Guide to Periodical Literature* and in several specialized indexes.

AAAS
ADVANCING SCIENCE, SERVING SOCIETY

Martin Rees is Master of Trinity College, Cambridge, UK, and president of the Royal Society.

The Royal Society's Wider Role

THE ROYAL SOCIETY IS CURRENTLY CELEBRATING ITS 350TH ANNIVERSARY. IN ITS EARLIER YEARS, Christopher Wren, Robert Hooke, Robert Boyle, Samuel Pepys, and other "ingenious and curious gentlemen" met regularly in London. Their motto was to "accept nothing on authority." They did experiments, peered through newly invented telescopes and microscopes, and dissected weird animals. But, as well as indulging their curiosity, they were immersed in the practical agenda of their era: improving navigation, exploring the New World, and rebuilding London after the Great Fire of 1666. Today, our horizons have hugely expanded. Earth no longer offers an open frontier but seems constricted and crowded—a "pale blue dot" in the immense cosmos. But the Royal Society's core values have enduring relevance. Today's scientists, like their forbears, probe nature and nature's laws by observation and experiment, but they should also engage broadly with the needs of society and with public affairs.

Such engagement is needed more than ever before, and on a global scale. Science transforms our lives, sometimes with staggering speed. Spin-offs from molecular genomics could soon change our lives as much as those from the microchip have already done. We must confront widely held anxieties that genetics, brain science, and artificial intelligence may "run away" too fast. And rapid advances raise profound questions: Is the world getting warmer, and why? Who should access the "readout" of our personal genetic code? How will lengthening life span affect society? Should nuclear power stations or wind farms keep the lights on? Should we use more insecticides or plant genetically modified crops? How much should computers be allowed to invade our privacy? Such critical questions transcend party politics, but because they are long-term, they tend to be trumped by more urgent items. Many require action on an international scale, as all parts of the world are more closely networked today than ever before.

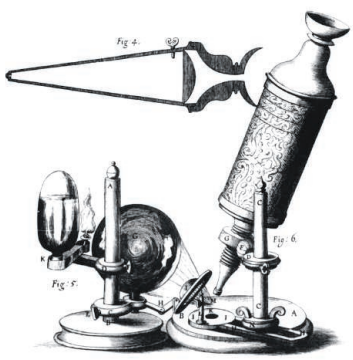

Most people live lives that are safer and healthier than those of their ancestors. We have tamed some of the risks from nature. But gross inequalities still leave two billion deprived of some basic needs. World population is destined to rise to around nine billion by mid-century; were the rise to continue beyond that point, it would create even more pressure on resources and the environment. We've now entered a unique century, the first in the 45 million centuries of Earth's history, in which one species—ours—could determine, for good or ill, the entire planet's future.

I conclude as I began, with a flashback; this time to the atomic scientists of the Manhattan Project during World War II. Fate had assigned them a pivotal role in history. Many returned with relief to peacetime academic pursuits. But the ivory tower wasn't, for them, a sanctuary. Hans Bethe, Rudolf Peierls, Jo Rotblat, and others worked throughout their lives to control the power they had helped unleash. These men were an elite group—the alchemists of their time, possessors of secret knowledge. Today's dominant issues, in contrast, span all the sciences, are far more open, and are often global. There is less demarcation between experts and laypersons. Campaigners and bloggers enrich the debate. But professionals have special obligations; the atomic scientists were fine exemplars of this. Scientists shouldn't be indifferent to the fruits of their ideas. They should try to foster benign spin-offs, and they should prevent, so far as they can, dubious or threatening applications.

Unprecedented pressures confront the world, but there are unprecedented prospects too. The benefits of globalization must be fairly shared. There's a widening gap between what science allows us to do and what is prudent or ethical. Everyone should debate these choices, but the agenda must be guided by science academies and by individual scientific citizens, engaging, from all political perspectives, with the media and with a public attuned to the scope and limits of science. There is a greater role than ever for the Royal Society and its sister academies around the world.

– Martin Rees

10.1126/science.1193400

Published by AAAS

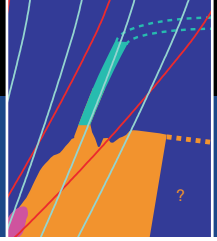

Sighting of a mantle plume
1622

The promise and perils of shale gas
1624

GULF OIL DISASTER

Looking Beyond the Spill, Obama Highlights Long-Term Restoration

As disastrous as the oil spill has been, the *Deepwater Horizon* tragedy is just the latest affliction for wetlands in the Gulf of Mexico. For decades this productive coastline has been sliced apart by navigation channels and chewed through by invasive rodents. Worse, engineering of the Mississippi River has starved the delta of the sediment needed to keep it above sea level. All told, nearly 6000 square kilometers of wetlands have disappeared underwater in the past 100 years. Even though about $1.2 billion has been committed over the past 2 decades by the state of Louisiana and the federal government, efforts to restore the ecosystem are dwarfed by the scope of the problem.

But now advocates have hopes for new momentum. In a primetime speech about the oil spill, President Barack Obama last week called for long-term restoration and put the secretary of the Navy, Ray Mabus, who was governor of Mississippi from 1988 to 1992, in charge of developing a plan. "It is the first time that any president has clearly articulated a national interest in restoring this remarkable but collapsing deltaic ecosystem," says Jim Tripp of the Environmental Defense Fund, an advocacy group in Washington, D.C. The speech "indicates a real sense of national priority and urgency."

Scientists say the plan should focus on diverting large amounts of sediment-laden water from the Mississippi River to build land. Because sediment supply is limited and sea level is rising, it's crucial to site the diversions strategically for maximum land-building. "The big hurdles are going to be the social, political, and economic problems involved in making a big diversion," says Harry Roberts, a coastal geologist at Louisiana State University (LSU), Baton Rouge.

To date, most restoration efforts have been relatively small, such as rebuilding specific wetlands with dredged sediment. In 2000, the state of Louisiana released a plan that laid out ambitious, but relatively vague, goals—and a price tag of $14 billion. What eventually crystallized, after the Bush Administration scaled the plan back, was the $1.9 billion Louisiana Coastal Area study (*Science*, 25 November 2005, p. 1264). The Army Corps of Engineers has been authorized to build 15 restoration projects, including three sediment diversions, but none of the major projects has yet received funding to start construction.

Two prototype diversions are already in operation. These concrete gateways, which channel river water so that it deposits sediment into wetlands, haven't built much land. That's mostly because they are operated at low levels; they divert only about 1% to 2% of the river's flow. Last year, Wonsuck Kim, now at the University of Texas, Austin, and others calculated that larger diversions would create a significant amount of land. By placing the structures midway between New Orleans and the mouth of the river, and diverting 45% of the spring flood stage, the sediment would build some 2740 square kilometers of land over 100 years, they reported 20 October in *Eos*. Such gains would "represent dramatic improvements over the "do nothing" situation," they concluded.

Even large diversions won't be enough to rebuild all the lost land, however, according to a recent study by Roberts of LSU and Michael Blum, now at ExxonMobil. Given that sea level is rising three times faster than it was 1000 years ago, and that at little as half as much sediment now reaches the Gulf of Mexico—the rest is trapped by dams in the Mississippi River watershed—there will be a large net loss of land by 2100, they reported in the June 2009 issue of *Nature Geoscience*. Although not all experts think the future is that grim, the study suggests that sediment diversions will be more about retrenching than recouping land. "We need to be very smart about where we put the sediment and diversions," Roberts says.

Roberts and other scientists recommend locating diversions as close to land as possible, where there is less erosion and the delta isn't subsiding as quickly as it is farther offshore; in these places, more land can be built with less sediment. But residents of Plaquemines Parish, along the southernmost extent of the river, would like to see diversions farther seaward (see map), where they would protect towns and other infrastructure. Louisiana's 2007 comprehensive master plan for coastal restoration did not decide locations for diversions but presented two "conceptual scenarios."

One reason the master plan isn't resolved yet is that even the concept of diversions can alarm some stakeholders. By introducing more fresh water

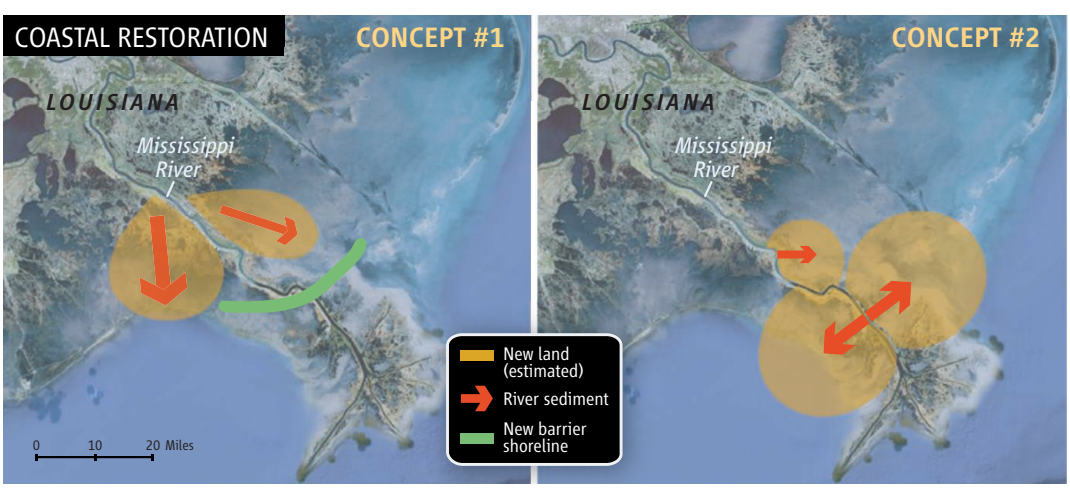

Tough choices. Louisiana's coastal plan includes a proposal (*left*), recommended by scientists, to divert river water and maximize new land. Another concept (*right*) would disrupt fisheries less and better protect downstream infrastructure.

SOURCE CREDITS (LEFT TO RIGHT): USGS; CPRA

Published by AAAS

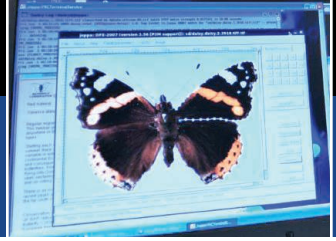

Insect ID by computer
1628

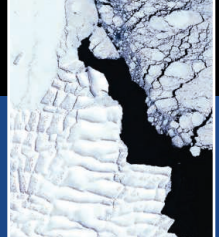

East Antarctic ice vulnerability
1630

into wetlands, for example, diversions can harm oyster beds that have sprung up as salt water intruded into the sinking wetlands. The shipping industry worries that the structures could accidentally create shoals where ships need to anchor. Clinton Willson, a coastal and water resources engineer at LSU Baton Rouge, and other experts are optimistic that the negative impacts of diversions on shipping could be minimized.

In March, the White House Council on Environmental Quality (CEQ) released a road map to help federal agencies and the state draft a more specific vision for coastal restoration, due by this fall. This road map will inform Mabus's plan, as will input from residents, officials, scientists, and conservationists, says CEQ spokesperson Christine Glunz.

Funding remains a major issue. The price tag for restoring as much of the coast as possible to long-term health will likely run in the tens of billions of dollars, says Denise Reed of the University of New Orleans. It's possible that payments made by BP for damages caused by the spill could cover some of the restoration, but ultimately, a new funding mechanism will be needed, says Tripp, perhaps a surcharge on oil from the gulf. Certainly, the current trend of federal appropriations to the corps won't suffice; Tripp predicts it would take 200 years to get the job done. And inaction is not an option: "The status quo is ongoing collapse." **–ERIK STOKSTAD**

PALEOANTHROPOLOGY

Lucy's 'Big Brother' Reveals New Facets of Her Species

First came Lucy. Then came Lucy's baby, an infant of her species. Now comes Lucy's "big brother": the partial skeleton of a large male of *Australopithecus afarensis*, unveiled this week in the *Proceedings of the National Academy of Sciences*. The roughly 40% complete skeleton has been nicknamed Kadanuumuu, which means "big man" in the Afar language of the Afar Depression of Ethiopia, where it was found. "It was huge—a big man, with long legs," says lead author Yohannes Haile-Selassie, a paleoanthropologist at the Cleveland Museum of Natural History in Ohio.

Dated to 3.6 million years ago, the new skeleton is almost half a million years older than Lucy and the second oldest skeleton found of a possible human ancestor. It had long legs and a torso and a pelvis more like those of a modern human than an African ape, showing that fully upright walking was in place at this early date, Haile-Selassie says. Although headless, the skeleton also preserves parts not found before in Lucy's species. "It is important because it provides the ribs and scapula," or shoulder blade, says paleoanthropologist Carol Ward of the University of Missouri, Columbia.

In 2005, a sharp-eyed member of Haile-Selassie's team, Alemayehu Asfaw, spotted a fragment of lower arm bone on the ground at Woranso-Mille, about 48 kilometers north of Lucy's grave at Hadar (*Science*, 11 March 2005, p. 1545). Over the next 4 years, the team unearthed the shoulder blade, collarbone, ribs, and neck vertebra, the first time those bones were found together in an *A. afarensis* adult. The team also found a pelvis, an arm, and leg bones. Although they never found the skull or teeth, which are typically used to assign species, the skeleton's age and similarity to Lucy suggest that it belongs to her species, says co-author Owen Lovejoy of Kent State University in Ohio.

The robust male stood between 1.5 and 1.7 meters tall, about 30% larger than Lucy. Isolated bones of other individuals suggest that some males were even larger, so the new skeleton doesn't settle a long-standing debate over just how much sexual dimorphism there was in *A. afarensis*, Lovejoy says. The shoulder blade looks more like that of a gorilla and a modern human than that of a chimpanzee. The curvature of the second rib suggests a wide rib cage at the top and a barrel shape overall, similar to that of modern humans and distinct from the more funnel-shaped rib cage of a chimpanzee, the authors say.

This skeleton also gives a leg up to researchers who had proposed that Lucy's legs were proportionately longer compared with her arms than a chimpanzee's, says paleoanthropologist Terry Harrison of New York University in New York City. He agrees with the authors that the new skeleton is "not apelike in limb proportions."

Lovejoy argues that these nonchimpanzee-like features support a hypothesis he has championed that the last common ancestor shared between hominins and other great apes didn't look much like chimpanzees, as many had once thought (*Science*, 2 October 2009, p. 36). Ward agrees that the shoulder "provides further evidence that in the ways that *A. afarensis* is not like a human, it is not always like a chimpanzee."

But paleoanthropologist William Jungers of Stony Brook University in New York state is skeptical. He points out that the ribs are damaged and that the limb proportions depend primarily on just one complete leg bone; thus, the skeleton can't say much new about leg length. Expect more data—and more debate—from this newest member of Lucy's family. **–ANN GIBBONS**

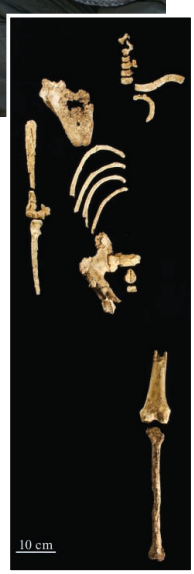

Big man. Yohannes Haile-Selassie excavates the oldest skeleton (*right*) known for Lucy's species.

CREDITS: WORMIL PROJECT; (INSET) Y. HAILE-SELASSIE *ET AL., PROC NATL ACAD SCI* (2010) © REPRINTED WITH PERMISSION FROM *PNAS*, AND WORANSO-MILLE PROJECT, ETHIOPIA

Published by AAAS

NEWSMAKER INTERVIEW

Amid War, Appraising the Mineral Wealth of Afghanistan

When U.S. geologists visited the Afghanistan Geological Survey in Kabul in 2004 to launch an assessment of the country's mineral resources, they walked into a shell of an office building that had been bombed during the conflict of the previous decade. Since then, U.S. and Afghan geologists have been conducting field surveys and analyses, building on Russian maps and reports prepared during the Soviet occupation of the 1980s. The U.S. Geological Survey (USGS) issued a preliminary assessment in 2007, but the findings made headlines only last week when *The New York Times* reported that officials had "discovered" that Afghanistan harbored mineral wealth estimated at more than $1 trillion. That includes vast deposits of copper and iron ore, cobalt, molybdenum, and gold, which Pentagon officials say could transform Afghanistan's economy.

Ground truth. Geologists Jack Medlin (*left*) and Said Mirzad (*right*) studied the resources hidden beneath the stark Afghan landscape.

Two geologists who have helped manage the survey are **Jack Medlin**, a regional specialist in USGS international programs, and **Said Mirzad**, who directed the Afghanistan Geological Survey until 1979 and currently serves as Afghanistan Program coordinator at USGS. Last week, they spoke to *Science* about the past, present, and future of mineral exploration in the war-torn country. Their remarks have been edited for length and clarity. **–YUDHIJIT BHATTACHARJEE**

Q: How did USGS get involved in Afghanistan?

J.M.: Our involvement goes back to 1952, when we began work with the Afghans on water resources. In the early '60s, we were responsible for the installation of a seismic station in Kabul. But all that ended in 1973.

In October 2001 [after the U.S.-led invasion], we came up with a plan to help in the reconstruction of the country. It called for an oil and gas assessment, a water-resource assessment, a mineral assessment, and an earthquake-hazard assessment.

Q: Surely there was previous work done on estimating the country's mineral wealth?

S.M.: Absolutely. In my time [1960s and 1970s], we had 22 groups of geologists roaming around Afghanistan doing geological surveys. We established the geological map of the country.

J.M.: The Russians did a tremendous amount of exploration work in the 1980s. They produced a number of mineral-exploration reports. Copies were produced in English and Dari; there was also a Russian copy that went back to Russia that most people think was different from the one that was left behind with the Afghans.

Q: How did you go about conducting the mineral-resource assessment?

J.M.: In 2004, we went to visit with our Afghan counterparts in the Afghan Geological Survey. The building had been destroyed by the mujahedeen—the plumbing had been stripped out, the electrical wiring was gone.

We asked to see the library and discovered all these reports that were stacked in these rooms. The Afghan geologists said they had taken the reports home to preserve them and store them; now they were bringing them back, which we were delighted to see.

Q: Said, some of these geologists must have been your former colleagues, right?

S.M.: Yes. There were nearly 100 Afghan geologists there. I asked them, "What are you doing here?" They said, "We arrive here at 10:30 every morning, stay till 2; then we sell cigarettes and fruit at street corners." The director was driving a taxi after 4. They were reporting to work because the Taliban had told them that they couldn't go anywhere. They told me that they had given up hope that they would do geology ever again.

Q: What did you do after finding the old reports? Did you do any fieldwork?

J.M.: We started by organizing and compiling the data, working with 30 Afghan geologists and engineers. We selected certain areas for field study, and the Afghan geologists went to those sites to collect rocks; at some sites, they dug trenches several hundred feet long to get fresh work. There were landmines in some areas that had been placed around coal mines and mineral locations.

Q: What other surveying did you do?

J.M.: In 2006, we carried out an airborne geophysics survey covering about 70% of the country using an Orion P-3 plane owned by the U.S. Naval Research Lab. It collected gravity and magnetic data, which gives you an insight into what the three-dimensional look of a potential ore body is.

In 2007, we carried out a hyperspectral-imaging survey with an instrument mounted on the belly of a former British bomber. Hyperspectral imaging [imaging across the electromagnetic spectrum] allows you to map different rocks and minerals [each of which reflects sunlight uniquely] from 50,000 feet above the ground. It allows us to confirm a number of sites with potential deposits.

Q: How did you arrive at the assessment?

J.M.: We integrated the geological, geochemical, and geophysical information with mining history and ran it through a Monte Carlo simulation. We're looking at the known resources, and based upon the geology, we use probability, statistics, and expert judgment to say what there may be.

Q: Can some of this wealth be tapped in the short term?

J.M.: There is a lot of low-hanging fruit. For example, you don't need a lot of mining equipment to mine gold. Another example is brick clays, which can be used for making bricks or ceramics. It's not high-tech, but it can help create jobs.

S.M.: The Afghan government should not touch the mining business. We have to give enough information to potential investors. You will see the full impact when you have 20 investors.

I am very optimistic. If Afghanistan has a few years of calm, allowing the development of its mineral resources, it could become one of the richest countries in the area within a decade.

CREDITS (TOP TO BOTTOM): COURTESY OF JACK MEDLIN; USGS

Published by AAAS

PHYSICS

Invisibility Cloaks for Visible Light Must Remain Tiny, Theorists Predict

Three years ago, physicists unveiled the first invisibility cloak, a ring-shaped device that ferried microwaves around an object and made it undetectable to microwave receivers (*Science*, 20 October 2006, p. 403). Since then, scientists have pushed to make a cloak for shorter-wavelength visible light. But those efforts will never lead to something you can hide in, one team of researchers predicts. The researchers say a cloak for visible light would be so small it could hide only objects almost too tiny to be seen. "It would be about the size of a dot on a piece of paper," says Steven Johnson, an applied mathematician at the Massachusetts Institute of Technology in Cambridge. But the limit may not apply to some types of cloaks, other experts counter.

Scientists have made great strides in cloaking. In May 2006, theorist John Pendry of Imperial College London and colleagues proposed a cloak that consisted of a ring of "metamaterial": a material whose electromagnetic properties are patterned on scales shorter than the electromagnetic waves it channels. Five months later, David Smith and colleagues at Duke University in Durham, North Carolina, produced one for microwaves. By April 2009, two other groups had fashioned tiny cloaks for infrared light.

Along the way, there have been plenty of doubts. For example, Pendry's original cloak worked at only one wavelength because it relied on a metamaterial that "resonates" with light, much as an organ pipe rings with sound of a fixed frequency. Some argued that no cloak could work at a range of frequencies. But in 2008, Pendry and a colleague devised a "carpet cloak," which produces a hidden hump on a reflective surface instead of a hidden hole in space and works over a range of wavelengths. The infrared devices reported last year were "broadband" carpet cloaks.

Even so, a broadband cloak cannot be much bigger than the wavelengths at which it works, Johnson and colleagues argue. In a paper in press at *Physical Review Letters*, they consider a simple scenario in which a pulse of light with a range of wavelengths descends on a flat object covered by a cloaking layer. If the object were not there, the light pulse would take more time to reach the surface and bounce back. So to hide the object, the cloak must delay the light pulse. And for the cloak to do that correctly over the entire wavelength range, its thickness must increase in proportion to the height of the hidden object, Johnson argues.

The thicker the cloaking layer, however, the longer the light pulse will remain in the material and the more light the cloak will absorb or scatter. If the cloak is too thick, that light loss becomes noticeable. Johnson and colleagues estimate that researchers might someday beat down the losses enough to cloak a meter-sized object at microwave wavelengths. At optical wavelengths, the losses are orders of magnitude too high to conceal such a large object, they say. A cloak for infrared or visible light cannot be more than a few micrometers across, they conclude.

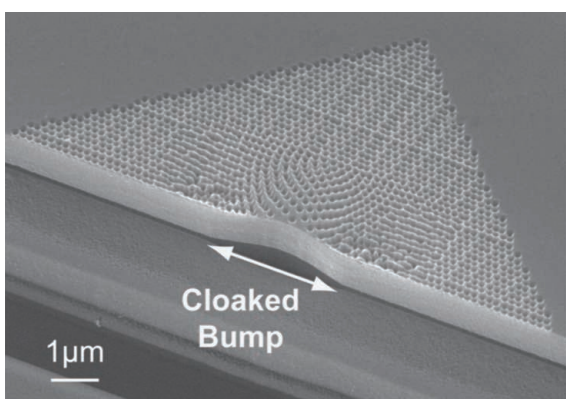

Small wonder. This micrometer-sized cloak can hide a tiny object from nearly visible infrared light. The light actually flows through the slab of silicon and reflects from its edge back into the material.

Not everyone is convinced. Johnson's argument applies only to resonant systems, Pendry contends; it does not prove you cannot make a large nonresonant cloak. "It's not Moses descending from the mountain and saying you can't do it," Pendry says. "It's a rider saying that there may be some complications." Johnson says the result is general.

Cloaking is only one application for the concept of "transformation optics" that Pendry has pioneered, and others could prove more important. Still, it would be disappointing if all you could hide in your personal invisibility cloak were an eyelash.

–ADRIAN CHO

CREDIT: J. VALENTINE *ET AL.*, *NATURE MATERIALS LETTERS* 8 (JULY) © 2009 MACMILLAN PUBLISHERS LTD.

ScienceInsider

From the *Science* Policy Blog

The U.S. Supreme Court says that the government shouldn't have banned the planting of **genetically modified alfalfa** pending completion of an environmental review. http://bit.ly/alfalfa-ruling

The American Heart Association has banned drug company scientists from making scientific presentations at its upcoming meeting in what some researchers say is an overreaction to concerns about **conflicts of interest** in research. http://bit.ly/cme-rules

Partners in a worldwide effort to harness nuclear fusion as a source of power have imposed a 31 July deadline on themselves for approving the design, schedule, and cost of the **ITER fusion reactor**. It's the latest attempt to manage the mounting price tag of the project. http://bit.ly/iter-baseline-delay

A $1 billion tax-credit program to jumpstart the languishing U.S. biotech industry is now open for business. For many companies, the **Therapeutic Discovery Project Program** will actually mean a cash grant to help develop a drug or therapeutic. http://bit.ly/biotech-tax-credit

Two Japanese foundations have honored four scientists for their research achievements. The Inamori Foundation has awarded its 2010 Kyoto Prize to Shinya Yamanaka and László Lovász, and the Asahi Glass Foundation named James Hansen and Robert Watson the 2010 winners of its Blue Planet Prize. http://bit.ly/kyoto-prize and http://bit.ly/blue-planet

An internal investigation has concluded that **Peter Duesberg**, a molecular virologist at the University of California, Berkeley, was within his rights when he wrote in a paper since retracted that there is no evidence of a deadly AIDS epidemic in South Africa. http://bit.ly/duesberg

Blood banks are being advised to tell patients with **chronic fatigue syndrome** not to donate because they may pass on a virus suspected of causing the elusive syndrome. http://bit.ly/blood-banks

See the full postings and more at **news.sciencemag.org/scienceinsider**.

Published by AAAS

MANTLE DYNAMICS

Another Quarry Sighted In the Great Mantle Plume Hunt?

Mantle plumes—tall columns of hot rock rising to feed volcanic hot spots like Hawaii—are either fundamental components of Earth's heat-shedding machinery that reshape the surface and perhaps trigger mass extinctions, or they are figments of some geophysicists' imaginations. Every report that someone has caught sight of a plume in seismic images of the mantle has been greeted by roughly equal portions of support and derision (*Science*, 4 December 2009, p. 1330).

The latest claim is faring a bit better. The report of the detection of the most realistic-looking plume yet "is a very, very nice piece of work," says seismologist Jeannot Trampert of the University of Utrecht in the Netherlands. "This is a new way forward," but—there's still no escaping the buts—"it's a tough problem. There are still a lot of assumptions."

The appeal of the new work is that it is rooted directly in data. Previous plume claims involved so-called tomographic imaging. A seismic wave passing through a hot plume would be slowed so that it arrived at a distant seismometer later than a seismic wave that missed the plume. Tomographers would combine seismic travel times to create images of Earth's interior in much the way radiologists combine x-ray absorptions to create computed tomography images of human interiors. But just where the putative plume images came from, critics contended, was not clear. A signal created by an unrelated slow spot elsewhere in the mantle could have smeared into an adjacent area and could be taken for a plume, they said.

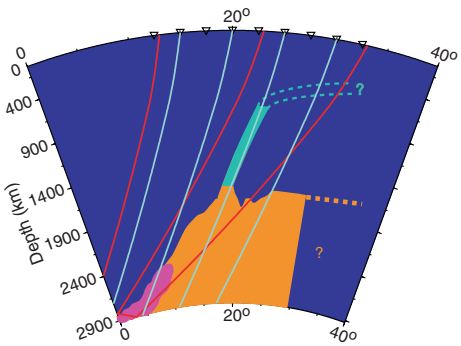

Plume ho? Seismic waves (red and blue-green lines) passing up through the lower mantle may have detected a plume (blue-green column).

The new work, by seismologists Daoyuan Sun, Donald Helmberger, and Michael Gurnis of the California Institute of Technology (Caltech) in Pasadena, also uses travel times but includes the opticslike behavior of seismic waves as well. As the Caltech group discusses in its 4 May paper in *Geophysical Research Letters*, seismic waves—like light waves—are diffracted when they graze any sharp change in seismic properties. The effect showed up in the complex shapes of seismic waves that rose along a narrow, sharp-edged zone of lower seismic velocity in the lower mantle just off the southern tip of Africa.

By modeling exactly what sort of mantle feature could create the observed complex shapes of waves, the Caltech group homed in on the most realistic-looking plume yet reported. As geophysical theory calls for, the Caltech group's African feature is conical, sharp-edged, and about 150 kilometers across. All previously reported plume images were fuzzy and several times wider.

"There is definitely something there, something small-scale," says seismologist Christine Thomas of Münster University in Germany. "It's a direct observation; you can see [sharp edges] with your eye" in unprocessed data, unlike tomographic images that require massive processing. "Whether it's a plume," she says, "I don't know."

The picture is still incomplete. Scientists can't tell whether the small, sharp-edged feature extends into the upper mantle because no waves passed that way. They can't gauge its length without better knowledge of the difference between seismic velocities in its interior and in the surrounding mantle. And seismologist Edward Garnero of Arizona State University in Tempe even asks, "How do you know [the plume] is not somewhere else along the path followed by the seismic wave?" Helmberger says that's unlikely but can't rule it out.

Everyone agrees on the need for more data from seismic waves grazing the suspected plume. "The problem is there aren't that many earthquakes," Thomas says. All in all, Garnero says, "the question may be extremely difficult to answer."

–RICHARD A. KERR

CLIMATE CHANGE

Critics Are Far Less Prominent Than Supporters

A new analysis of 1372 climate scientists who have participated in major climate science reviews or taken public positions on their main conclusions confirms what many researchers have said for years: Those who believe in anthropogenic climate change rank, on average, much higher in the scientific pecking order than do those who take issue with the idea.

The co-authors examined lists of scientists who have signed statements in support or opposition to the main findings over the years of the Intergovernmental Panel on Climate Change, namely, that the planet is warming and humans are largely responsible. They categorized the scientists as either "convinced" or "unconvinced" and then analyzed how many papers involving climate they had published. "Unconvinced" scientists comprised only 2% of the top 50 researchers ranked by number of climate publications and 3% of the top 100. Among scientists with 20 or more papers on climate, the so-called convinced group had an average of 172 citations for their top paper compared with 105 for the unconvinced.

But the paper, published this week in the *Proceedings of the National Academy of Sciences*, faces several criticisms. The first is that the grouping of researchers into "unconvinced" and "convinced" fails to capture the nuances of scientific views on the subject. That makes the paper a "pathological politicization of climate science," says Roger Pielke Jr. of the University of Colorado, Boulder. Pielke also objects to applying the "unconvinced" label to anyone who signed a paper opposing immediate cuts in greenhouse gas emissions. "So you are a 'climate skeptic' if you have a certain view on climate policy?" he asks. "Bizarre."

Critics say the results reflect the cliquishness or biases inherent in peer-reviewed science. "We are being "black-listed," as best I can tell, by our colleagues," says John Christy of the University of Alabama, Huntsville, who was in the "unconvinced" group.

Co-author Jim Prall, a computer support professional at the University of Toronto in Canada, says, "It would be helpful to have lukewarm [as] a third category." But he defends the peer-review system, noting that journal editors, although not perfect, "know the field better than any one else."

–ELI KINTISCH

Published by AAAS

ScienceNOW

From *Science*'s Online Daily News Site

Scientists Score in Ranking Soccer Stars

If you're new to World Cup soccer madness and wondering which team is tops, science has an answer.

Luís Amaral, a complex-systems engineer at Northwestern University in Evanston, Illinois, and an avid soccer fan, wanted to measure team and player performance in a way that takes into account the complex interactions within the team and each player's contribution. Applying the kinds of mathematical techniques used to map Facebook friends and other networks, Amaral and colleagues created software that can trace the ball's flow from player to player. The program assigns points for precise passing and for passes that ultimately lead to a shot at the goal, then calculates a skill index for each team and player.

When the researchers analyzed data from the 2008 UEFA European Football Championship, the indices closely matched the tournament's outcome and the overall consensus of sports reporters, coaches, and other experts who weighed in on the performances, Amaral and colleagues reported in *PLoS ONE*. http://bit.ly/soccer-science

Still No 'Mammoth-Killer'

Proponents of the idea that an exploding comet wiped out mammoths, giant sloths, and other megafauna 12,900 years ago have pointed to unusual organic debris in the soil from this period—debris, they say, that could have formed only in extreme wildfires raging across North America. But in a new study, a team argues that this debris is just fungal remains and bug poop.

Using four kinds of microscopy, Andrew Scott of Royal Holloway, University of London in Egham, U.K., found a good match between the odd, honeycombed debris, known as carbonaceous spherules, and so-called fungal sclerotia, balls that fungi form to hibernate through times of environmental stress. When the sclerotia are charred at relatively low temperatures, the resemblance increases. Some of the more elongate particles are "certainly fecal pellets, probably from termites," says Scott. What's more, the 12,900-year-old spherules were heated in low-intensity natural wildfires, if that, the team reported in *Geophysical Research Letters*. "There's certainly no evidence they're related to intense fire from a comet impact," says Scott.

But comet proponents say Scott and others have yet to explain an unusual feature in some carbonaceous spherules: nanodiamonds, nanometer-size bits of diamond that they say could have formed only in the extreme conditions of an impact. http://bit.ly/mammoth-killer

A World Without Flowers

A world without flowering plants wouldn't just be drab, it would be hotter and drier, particularly in parts of the tropics, a new study concludes.

Paleontologist C. Kevin Boyce and climate modeler Jung-Eun Lee of the University of Chicago in Illinois rejiggered climate models, cutting out the moisture released to the atmosphere through the leaves of flowering plants, or angiosperms—the group that includes elms, oaks, tulips, and roses.

The effects were complex, but the biggest impact occurred in tropical areas of South America, the pair reported in the *Proceedings of the Royal Society B*. Average annual rainfall declined by 300 millimeters. In the eastern Amazon basin, the length of the wet season decreased by nearly 3 months. The extent of the wettest rainforests, which receive more than 100 millimeters of rain per month, shrank by 80%. Biodiversity would also suffer, as less precipitation usually translates into fewer species of animals and plants. http://bit.ly/no-flowers

Read the full postings, comments, and more at **news.sciencemag.org/sciencenow**.

Chimpanzees Kill for Land

After at least 5 million years of separate evolutionary history, chimpanzees and humans still have one thing in common: Males of both species kill each other over territory, according to a study in *Current Biology*.

From 1999 to 2008, a team led by primatologist John Mitani of the University of Michigan, Ann Arbor, and David Watts of Yale University followed male chimpanzees in the Ngogo group in Kibale National Park in Uganda whenever the chimpanzees would stop their usual noisy social behavior to form patrols of several males, about once every 2 weeks or so. In 18 cases, the researchers observed the Ngogo chimpanzees ambush a solitary male—often an infant—and kill it by pummeling it and biting it, says Mitani. In three other cases, the primatologists did not witness the attacks but found the beaten, torn bodies of chimpanzees after they heard an attack, or they observed the Ngogo males eating a freshly killed infant chimpanzee.

In most cases, the Ngogo males took over new territory after a kill. Experts say these land grabs may give the chimpanzees access to more fruit trees or to females that live there. http://bit.ly/killer-chimps

A male chimpanzee attacks and kills a male from a different group.

CREDITS: (LEFT, PHOTO) CHRISTIAN CHARISIUS/REUTERS; (ILLUSTRATION) JORDI DUCH; (RIGHT) PHOTOS.COM; (BOTTOM) JOHN MITANI (2)

Published by AAAS

Different roads to gas. Gas from deep shale can turn up beneath both rural and urban landscapes.

Natural Gas From Shale Bursts Onto the Scene

New technologies have sparked a rush of drilling in the United States, but environmental concerns and economic unknowns could still keep shale gas from becoming a bridge to clean energy

ENGINEERING INGENUITY IS UNLOCKING A vast storehouse of natural gas buried beneath American soil from Texas to New England. Drillers are turning their instruments from the vertical to horizontal and then blasting the rock that tightly holds the gas with high-pressure chemical brews. This "fracing" (pronounced and sometimes spelled "fracking") is finally making gas trapped in shale a profitable resource. That change, in turn, has driven up declining U.S. gas production, rescuing the American natural gas industry from seemingly inevitable depletion.

The sudden great promise of clean, homegrown shale gas has all kinds of people excited. National-security types see it as a replacement for foreign oil and gas, environmentalists as a replacement for dirty coal and even oil. And because it yields only 45% of the carbon dioxide emissions of coal, advocates of taming global warming see it as a temporary crutch while carbon-free energy sources are developed and deployed. Everyone seems to agree with a March study by IHS Cambridge Energy Research Associates in Massachusetts that concluded that shale gas "provides the potential to transform North America's energy landscape."

The problem is that word "potential." Every link in the chain between the newly abundant domestic energy source and its transformative impact is still shrouded in uncertainty. How much gas is there? What will it cost to extract? What government policies will be needed to direct the natural gas revolution toward reducing greenhouse gas emissions? No one's sure. And a rising tide of NUMBY—not under my backyard—that's greeting shale gas in the Northeast could hobble the revolution (see sidebar, p. 1625).

How to unleash the gas

The newly applied technology of shale gas extraction is letting drillers go straight to the source. Conventional deposits of oil and gas are actually the final resting places of far-traveled hydrocarbons that were generated in deeper "source beds" of organic-rich rock. Drill into a conventional reservoir, and out flows oil and gas.

By contrast, shale gas—a so-called unconventional resource—never left its birthplace. It's still in the source bed whose organic matter gave rise to the gas. Because the pores in the fine-grained shale are not well connected, the rock is too impermeable to let the gas go. Drill into it—as drillers occasionally did—and you get barely a fizzle.

But all that shale gas began to look more and more tantalizing as conventional U.S. natural gas resources dwindled. After drillers had sunk millions of wells into North America's conventional oil and gas reservoirs, U.S. natural gas production—which had soared for three-quarters of a century—peaked in the early 1970s and promptly went into decline. The easy gas was quickly becoming a thing of the past.

Conventional gas production will never recover, but the two basic tools drillers needed to unleash unconventional shale gas were already on hand, waiting to be combined and refined. From the offshore oil and gas industry, they borrowed horizontal drilling. The ability to drill straight down and then bend the hole made it possible to drain much more of a reservoir from a single offshore drilling platform. Onshore, horizontal drilling out to 2.5 kilometers from a drill site can multiply the length of a single well within a gas-bearing shale layer by five or 10 times.

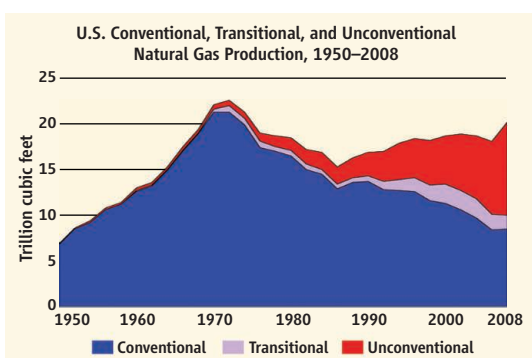

Gas comeback. Unconventional gas (red) has been more than replacing declining conventional gas (blue).

CREDITS (TOP TO BOTTOM): RUHRFISCH/WIKIMEDIA COMMONS; COURTESY RICHARD NEHRING, NEHRING ASSOCIATES

Published by AAAS

Not Under My Backyard, Thank You

A 3 June blowout 145 kilometers northeast of Pittsburgh, Pennsylvania, paled beside the catastrophe in the Gulf of Mexico. But it was the most dramatic harbinger yet of a revolution in the natural gas industry that will bring the threat of environmental disaster to millions of people's backyards, both figuratively and literally. Now that drillers have figured out how to extract gas trapped in shale rock (see main text, p. 1624), a new and perhaps more hazardous style of drilling is coming to parts of the country unfamiliar with the ways of the oil and gas industry.

To those outside the industry, the scariest part of the new drilling might be the way drillers unleash the gas. They drill straight down, turn the drill to go horizontally, and then pump in chemically treated water to pressurize a horizontal section of the well until surrounding rock fractures and begins to give up its gas. Many local residents and environmentalists have worried that this "fracing" (pronounced and sometimes written "fracking") might propagate fractures upward into overlying aquifers so that escaping gas, chemicals, and brine will contaminate groundwater.

There is certainly some sort of problem. In January 2009, somehow gas got into a residential water well near Dimock, Pennsylvania, and exploded. There's general agreement that nearby shale drilling had something to do with it, but it's not clear how. Driving fractures from a shale gas well up into an aquifer is "pretty inconceivable," geologist Ian Duncan of the University of Texas (UT), Austin, said at a seminar in Washington, D.C., in April. In fact, "we don't think [the Dimock gas] is coming from the Marcellus," says hydrogeologist Daniel Soeder of the Department of Energy's National Energy Technology Laboratory in Morgantown, West Virginia. "There have been isolated cases of gas occurring in water wells," he says, but isotopic analysis has shown that the gas is the shallow crustal equivalent of marsh gas rather than deep shale gas. Drilling and fracing may have triggered release of this biological gas, he says, but there are many other concerns about shale gas drilling.

The biggest concern for many is the water that pressurizes the well during fracing. The process takes 12 million to 16 million liters of water per well. Supplying such amounts can be a challenge in dry regions, but the larger problem is often what to do with it after fracing, when most of it comes back up the well. To improve performance, drillers may add as many as a dozen chemicals up to about 2% by volume, such as biocides to keep down corrosive bacteria. The fracing fluid also picks up naturally occurring chemicals, primarily salts from deep brines.

Drillers either inject the wastewater into deep wells, treat and release it, or recycle it, but spills do occur. The Dimock area had a series of them in 2009, for example. And the 3 June blowout in Pennsylvania spewed drilling fluid, brine, and gas into a forest for 16 hours (without igniting).

Shale gas extraction can have other drawbacks. A drill site covering 2 hectares turns into a heavy industrial zone, even if it's in the suburban Fort Worth part of the Barnett Shale in Texas. More than 100 big water-tanker trucks might have to come and go for each of 20 or more wells at a site. Although drillers can drain more than 500 hectares from a single site, "it still makes quite a mess," says analyst Richard Smead of Navigant Consulting Inc. in Houston, Texas.

In response to the upsurge in shale gas drilling, the Pennsylvania Legislature is moving to strengthen pertinent regulations. New York state has greatly tightened licensing requirements on drilling in about 10% of the Marcellus in the state, effectively ruling out drilling in a prime source of New York City drinking water. And in March, the U.S. Environmental Protection Agency launched a multimillion-dollar study of potential ill effects of fracing on water quality and public health.

"It's all manageable," says oil and gas analyst Michelle Foss of UT Austin, assuming everyone does the right thing. "Industry needs to get its act together and try to minimize things that would not be good," she says. Companies may have cut corners in their haste to drill. And "the states need to get their houses in order" too, she says. Better late than never. **–R.A.K.**

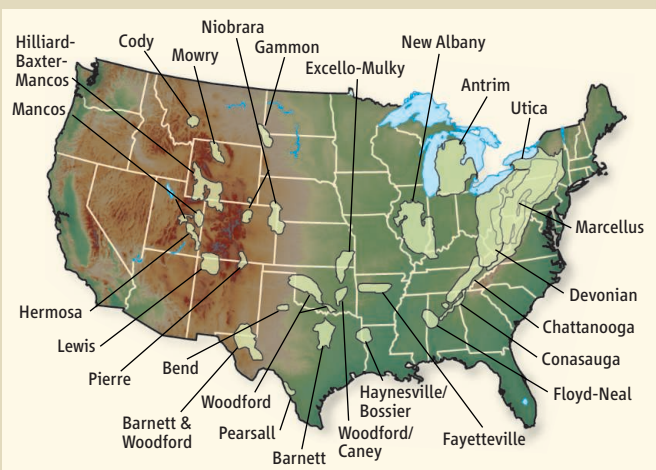

Shale gets around. Shale gas basins range from Montana to New York.

CREDIT: ADAPTED FROM *MODERN SHALE GAS DEVELOPMENT IN THE UNITED STATES: A PRIMER*, U.S. DEPARTMENT OF ENERGY

The other tool was hydraulic fracturing, or fracing. Drillers pressurize a horizontal section of a well by rapidly pumping in 3 million or 4 million gallons of water (plus a bit of fine sand and chemicals) to pressures of up to 7000 kilopascal. The extreme pressure creates a football-shaped cloud of fractured shale 300 meters long, the fractures remaining propped open by sand grains. Repeat up to 30 times in one well and drill tens of wells from a single site, and you could free up enough gas to make a tidy profit.

Hitting the mother lode

When the price of natural gas began to climb along with that of oil early in the decade, newly equipped shale gas drillers went to work. In 2000, shale gas was 1% of the U.S. gas supply; now it is 20%. Production from the Barnett Shale under Fort Worth, Texas, increased 3000% from 1998 to 2007. And unconventional gas—from shale, low-permeability sandstone, and coal beds—rose to more than 50% of U.S total production. By 2009, total production was back up almost to the 1970 peak, thanks largely to shale gas.

With gas gushing from the Barnett Shale and increasingly from other shale basins (see map, above), those sizing up America's natural gas resources took notice. Last June, the Potential Gas Committee, a nonprofit organization of experts, announced that shale gas was largely responsible for boosting PGC's estimate of the country's total available future supply of gas by 35% from its previous estimate just 2 years earlier. The natural gas resource had reached the highest level in the committee's 44-year history. That would be a 100-year supply at the current rate of consumption, industry ads touted.

The changes in the natural gas industry could be big. A June 2009 study by Navigant Consulting Inc. in Houston, Texas, found that gas production companies believed that they could be producing 300 billion cubic meters of shale gas a year—equal to half of today's total U.S. gas production—in little more than a decade. And thanks in large part to shale

Online
sciencemag.org
Podcast interview with author Richard A. Kerr.

Published by AAAS

gas, "natural gas is more than a bridge fuel; [it] is part of the long-term energy solution," James Mulva, chair and CEO of ConocoPhillips, said at a major oil and gas gathering last March in Houston.

Enter uncertainty

Despite all the glowing testimonials, every shale gas analysis has its caveats. The Navigant estimate of future production, for example, "represents what producers say they could do if everything works," says Richard Smead, a Navigant analyst, but "there are so many issues."

For one, experts question how much gas is actually in the ground and how much of that can be extracted. "The [shale gas] resource is quite large," says analyst Richard Nehring of Nehring Associates in Colorado Springs, Colorado, "but how large is it?" Resource estimates are usually reported as an average, he notes, but that conceals the range of uncertainty. PGC's 100-year supply "could be 50 years to 125 years of supply at present rates," he says. And production will peak and decline rather than hold steady for 50 years or 125 years and then suddenly disappear. Nehring recently estimated that U.S. and Canadian gas production will likely peak sometime between the 2020s and the 2040s, depending in large part on how much shale gas there is.

Ultimate source. This shale is rich with organic matter that gave rise to gas, but shale is too impermeable to let go of its gas.

Narrowing the resource uncertainties will take a while. "At this stage of the game, we have very little experience with shale gas," notes Nehring. "Predictions of well performance over 15 to 20 years are based on 6 to 24 months of experience." Yet flow from a new well can decline by 60% to 80% during the first year of production alone. "We don't know if they'll keep diving or level off," says geologist Richard Pollastro of the U.S. Geological Survey in Denver.

Future shale gas production will also depend on the profits to be made from extracting the gas. Production took off as the U.S. price of gas soared toward $14 per million British thermal units (MBtu). Since that peak, the price has fallen to about $4.50 per MBtu. Some shale gas producers might be making money from some wells at the current price, Navigant's Smead says, but "it's not sustainable; it's not good for growth."

On the debit side of the ledger, the cost of producing shale gas could soar once drillers have depleted the obvious "sweet spots" where geology has made the gas particularly abundant and relatively easy to extract. For example, the Marcellus Shale now under development runs 1000 kilometers from eastern Kentucky halfway across New York state, but the difficulty and expense of getting gas out varies from location to location. Without further technological change, production could become considerably more costly in the future.

How much shale gas actually gets used in coming decades also depends on how it fits into the U.S. energy economy. To see how gas might perform as a "bridge" to a low-carbon energy future, resource economists Stephen Brown, Alan Krupnick, and Margaret Walls of Resources for the Future in Washington, D.C., ran a range of scenarios in the National Energy Modeling System, which was developed by the U.S. Department of Energy and modified by RFF.

The energy model predicted prices and consumption across U.S. energy markets under various assumptions about the size of U.S. shale gas resources and the nature of government energy policy, among other factors. The researchers used it to explore scenarios in which the shale gas resource was either moderately large or very large and in which the country either had or lacked a low-carbon cap-and-trade policy with carbon dioxide emission targets similar to those in legislation passed in the U.S. House of Representatives.

Simply having a shale gas bonanza, the modeling suggested, doesn't solve all energy problems. In the absence of a low-carbon policy, more abundant shale gas "just gives you cheap energy," says Brown, and everyone "just consumes more"—although gas burns more cleanly than conventional fossil fuels do and is a domestic fuel rather than a foreign one. Some coal is displaced from the energy mix, but so are zero-emission nuclear energy and renewables. As a result, both energy consumption and carbon dioxide emissions increase slightly. With a low-carbon policy in place, however, things are different. In that case, the model showed, abundant shale gas fills the need for a low-carbon fuel, somewhat decreasing the cost of meeting emission goals in the law. Even if shale gas is less abundant, the low-carbon policy still helps nuclear energy and renewables to replace coal.

Shale gas "is a bridge if we want it to be," Brown concludes. But given all the uncertainties, he says, putting a price on emitted carbon—using cap-and-trade or a carbon tax—is preferable to letting the government promote one technological solution over another. The government could easily guess wrong, he notes.

Ingenuity and perseverance have unleashed a natural gas revolution in America and someday perhaps worldwide. But the revolution's first test is already in the offing. Financial arrangements that have encouraged continued shale gas drilling despite low prices will begin to expire in the next year or so. Drillers are said to be slowing the frenetic pace of sinking wells that's required just to maintain production. And a blowout that struck a well in the Marcellus Shale earlier this month serves as a reminder that environmental concerns could still sway a jittery public to favor leaving the gas inside the rock.

–RICHARD A. KERR

Long reach. Horizontal drilling can extend shale gas wells several kilometers from a few-hectare drill site.

CREDITS (TOP TO BOTTOM): COURTESY AMERICA'S NATURAL GAS ALLIANCE; COURTESY ALL CONSULTING

Published by AAAS

PSYCHOLOGY

A WEIRD View of Human Nature Skews Psychologists' Studies

Relying on undergraduates from developed nations as research subjects creates a false picture of human behavior, some psychologists argue

Suppose you're a psychologist at a research university, trying to figure out what drives human behavior. You have devised simple, clever experiments in which people play economic games or perceive visual illusions, and you would like large sample sizes. How will you find subjects? For generations of psychologists, the answer has been straightforward: Use the pool of thousands of undergraduates at your university.

But although undergrads from wealthy nations are numerous and willing subjects, psychologists are beginning to realize that they have a drawback: They are WEIRDos. That is, they are people from Western, educated, industrialized, rich, and democratic cultures. In a provocative review paper published online in *Behavioral and Brain Sciences* (*BBS*) last week, anthropologist Joseph Henrich and psychologists Steven Heine and Ara Norenzayan of the University of British Columbia in Canada argue that WEIRDos aren't representative of humans as a whole and that psychologists routinely use them to make broad, and quite likely false, claims about what drives human behavior.

"A lot of psychologists assume that one group of humans is as good as the next for their experiments, and that results from these studies apply more broadly. We show that this assumption is wrong," says Heine. "WEIRD subjects are some of the most psychologically unusual people on the planet."

There's little doubt that psychologists have relied on WEIRDos. In a 2008 paper in *American Psychologist*, Jeffrey Arnett of Clark University in Worcester, Massachusetts, analyzed all empirical papers published in six top-tier psychology journals between 2003 and 2007 and found that the United States alone provided 68% of study subjects, with a further 27% coming from the United Kingdom, Canada, Australia, New Zealand, or Europe. Psychology undergraduates were the sole subjects in 67% of U.S. studies and 80% of studies in other countries. Overall, 96% of subjects were WEIRDos.

This would be fine if WEIRDos were representative of people from other cultures, but they are not, Henrich, Heine, and Norenzayan argue in the *BBS* paper. Although cultural variation is sometimes assumed to be superficial, Heine says that cultures differ in fundamental aspects such as reasoning styles, conceptions of the self, the importance of choice, notions of fairness, and even visual perception. For example, in the Muller-Lyer illusion (see figure), most people in industrialized societies think line A is shorter than line B, though the lines are equally long. But in small-scale traditional societies, the illusion is much less powerful or even absent.

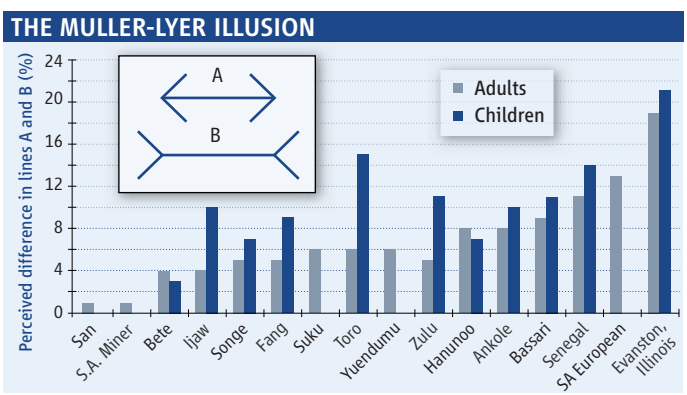

In the eye of the beholder. People in industrialized societies often think line A is shorter than line B, but that illusion is weaker or absent in some small-scale societies, whose members perceive the lines as equally long.

The reliance on WEIRD data has led to a biased picture of human psychology, says Heine. Social psychologists, for example, talk of the "fundamental attribution error," or the tendency to explain people's behavior in terms of internal personality traits rather than external, situational factors (attributing an instance of angry behavior to an angry temperament, for example). Yet outside WEIRD societies, this error looks a lot less fundamental, says Henrich, as people pay more attention to the context in which behavior occurs, so someone's anger might be construed as simply reflecting an irritating day.

Textbooks also frequently describe people as valuing a wide range of options when making choices, being analytical in their reasoning, being motivated to maintain a highly positive self-image, and having a tendency to rate their capabilities as above average. Again, the review article contends, this picture breaks down for people from non-WEIRD societies: These groups tend to place less importance on choice, be more holistic in their reasoning, and be less concerned with seeing themselves as above average. And although WEIRDos stand apart from the rest of the world in these and other respects, Americans stand even further away, with U.S. undergraduates further away still—"an outlier in an outlier population," as the *BBS* authors put it. "We will never figure out human nature by studying American undergrads," says Henrich.

Other researchers welcome this central message but caution that the differences observed in crosscultural studies may themselves be problematic. "Not only do psychologists use WEIRD people, they also use weird, highly artificial experiments," says Nicolas Baumard, an anthropologist at the University of Oxford in the United Kingdom. So the cultural variation those experiments detect may simply reflect the way experiments are construed by various groups rather than deep differences. Heine counters that many crosscultural findings have been replicated with a range of methods, suggesting that the differences are robust.

Henrich, Heine, and Norenzayan recommend that psychologists explicitly discuss whether their findings can be generalized and make data on subjects available so population effects can be more easily detected. Researchers should also try to build links to diverse subject pools, perhaps drawing on contacts made by economists and public-health researchers in non-WEIRD societies. The Internet also provides another way of reaching out, though potentially biasing research away from WEIRD people toward wired people.

The accumulated data on WEIRDos may still prove to have enduring value, argues cultural psychologist Paul Rozin of the University of Pennsylvania, as the world becomes more globalized. "The U.S. is in the vanguard of the global world and may provide a glimpse into the future," he says. For now, however, psychologists should remember that WEIRDos remain weird.

–DAN JONES

Dan Jones is a freelance writer in Brighton, U.K.

CREDIT: (ADAPTED FROM) M. SEGALL, *ET AL.*, *THE INFLUENCE OF CULTURE ON VISUAL PERCEPTION*, THE BOBBS-MERRILL COMPANY (1966)

Published by AAAS

ID checker. Mark O'Neill's insect-identification software may soon appear on cell phones.

BIODIVERSITY

Pushing DAISY

In his spare time, an entrepreneurial engineer-cum-entomologist teams up with a museum to develop an automated insect-identification computer program

Ever since he was a small child, Mark O'Neill has been captivated by the small things in life: insects. He remembers vividly the impressive Brown Hawker dragonflies that inhabited the wet meadow across the road from his childhood home in Lincolnshire, England, and the devil's coach horse beetles and puss moth caterpillars that used to abound in the garden. "When I was about 5, I got the idea that I could use large bumblebees to power paper aircraft," recalls O'Neill. "The idea failed miserably, but I became adept at harnessing bumblebees using cotton thread." That unusual skill continues to pay dividends as he now develops transponders for tracking bees for the technology company that he founded, Tumbling Dice, which is based in Newcastle-upon-Tyne in the United Kingdom.

Although O'Neill isn't a formally trained entomologist—his background is in physics and engineering—his fascination with insects has also brought him to develop an image-based insect-identification computer program, the Digital Automated Identification System (DAISY), in his spare time. The program compares digital photographs of insects' morphological features with a database of shapes and markings gathered from taxonomic records, in much the same way detectives use computer databases to match crime-scene fingerprints or a suspect's face from security cameras.

The idea is simple, but once DAISY is fully loaded with enough insect records, it should save taxonomists hours of painstaking research. In doing so, DAISY may help combat the problems associated with a growing shortage of trained taxonomists. It also promises to bring greater rigor to biodiversity studies, experts say, as traditional taxonomy methods rely on written descriptions in field notes to distinguish between species, using words that are sometimes not expressive enough for the task. "Taxonomists are forced to use subjective designations about how something looks, which is why DAISY's approach is so valuable," says paleontologist Norman MacLeod of the Natural History Museum (NHM) in London.

O'Neill has been developing DAISY for the past 18 years, struggling to find funding and collaborators—mainly because of his nontraditional background and position outside the academic world, he believes. But this insect-identification system has begun to prove itself in pilot trials around the world. MacLeod has been impressed enough by the results—and with O'Neill on both a personal and a professional level—that he has persuaded NHM to back DAISY with significant funding in the coming years. O'Neill "is one of the most interdisciplinary scientists that I have ever worked with," MacLeod says. "Mark lives and breathes entomology—growing caterpillars at home—but he is also an advanced IT specialist. He is decidedly unique."

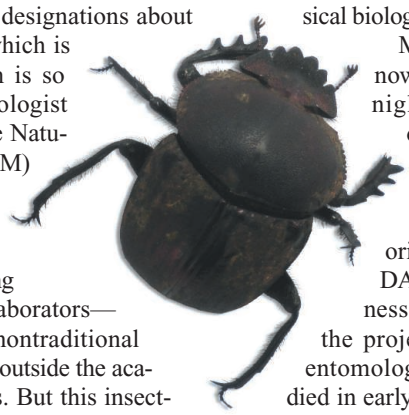

CREDITS: COURTESY MARK O'NEILL

DAISY takes roots

O'Neill wasn't actually around when the initial seed for DAISY was planted. That came about as a result of a conversation between the late entomologist Ian Gauld, formerly at NHM, and ecologist Kevin Gaston of the University of Sheffield in the United Kingdom. While stranded overnight at a Costa Rican airport in 1988, the pair pondered how a technological society might solve one aspect of the "taxonomic bottleneck": how a lot of biodiversity work isn't carried out simply because the people and resources required to identify known species are not available. They decided that they needed to automate species identification, and so the concept of DAISY was born.

A few years later, O'Neill came onboard to work alongside Gauld on the project, bringing his technology expertise to the table. O'Neill had acquired his information-technology and computer-programming skills while studying physics and engineering. He ultimately completed a Ph.D. in engineering in 1992 at University College London. O'Neill says he chose to study these subjects, despite his lifelong passion for entomology, because they were academically his strongest areas. "My physics and engineering background has helped me to contribute more to entomology than would have been the case had I trained as a classical biologist," he says.

More than 2 decades have now passed since that late-night conversation in the departures lounge in Costa Rica, and DAISY is still in the backwaters. Gauld, who had been awarded the original funding to work on DAISY, was slowed by illness for many years, leaving the project without a prominent entomologist to champion it. (He died in early 2009.) And O'Neill says he's also partly to blame for the slow progress. "I'm afraid that I am a bit of a 'back-room boy,' meaning that I have invested a lot more time in developing DAISY as opposed to advocating it," he says.

But O'Neill has a fully operational, UNIX-based version of the software now. It has been used for projects at several universities in the

Published by AAAS

United Kingdom and overseas, including the University of Oxford, Newcastle University, and the University of Costa Rica. Wherever O'Neill has taken the project, he seems to have left a lasting impression. "Mark is one of the brightest and most enthusiastic people I have ever met," says entomologist Paul Hanson of the University of Costa Rica in San José, who provided specimens for O'Neill to test DAISY on during a field trip to Costa Rica.

During that test, and many others, DAISY performed extremely well, says O'Neill. In the Costa Rican test, DAISY was able to identify more than 40 species of hawkmoths (*Xylophanes*) with an accuracy of 95% (increasing to 98% if the program was allowed to reject tricky specimens). In another study, in which DAISY was asked to identify 60 species of biting midges (Ceratopogonidae), the program had a 90% success rate, far better than a group of undergraduate zoologists at Sheffield, who identified only 20%.

These high success rates result from the sophisticated self-learning algorithm at the heart of DAISY, called a Self-Organizing Map, which, once trained to recognize an insect from a set of images from taxonomic records, can do so again automatically. Also, unlike fingerprint recognition, which matches only between seven and 10 spots of an image, DAISY's algorithm uses every bit of each image presented to it in order to make an ID.

Taking a gamble

O'Neill has repeatedly failed to secure grants for DAISY from research councils or other science agencies, even after the encouraging test results of the past few years. As a result, from February 2000, when the initial Darwin Initiative grant awarded to Gauld ended, until the recently announced NHM commitment, DAISY was completely unfunded. "I think in the U.K., and possibly in the U.S. as well, research grants are often awarded to well-known scientists and institutions without assessing the potential of the field as a whole," O'Neill says. In order to maintain excellence, he contends, it is sometimes necessary to gamble on relative unknowns and people whose ideas are unorthodox.

It seems NHM is willing to take that gamble; the museum recently announced that it will back DAISY for the next 3 to 5 years. The numbers are still being crunched, but the financial support is expected to be on the order of hundreds of thousands of dollars. And NHM's involvement in DAISY doesn't end there. It will feed its world-renowned taxonomical records into the system. Currently, about 7000 of the museum's 70 million records have been uploaded to DAISY. "We are in the process of formulating a strategy for ramping up the amount of resources we put into the digitization of the NHM collections," says MacLeod. By 2012, from his own personal effort, MacLeod expects to be able to double, or maybe even triple, the number of images that are currently uploaded to DAISY. "If I'm able to attract others to work with me, then that figure will be even larger," he says.

For comparison, another insect-identification technique called DNA bar-coding, which uses a short DNA sequence from a standard position in the mitochondrial genome to automatically identify species, currently has bar codes representing 100,000 insect species at its disposal. When the infrastructure is in place for DAISY, it will complement DNA bar-coding and help to address the immense task facing biologists of understanding the diversity of life on the planet. "Our current knowledge of species diversity is shockingly inadequate for the critical tasks that confront biodiversity science—the exploration of patterns in nature, the management of natural resources, and the conservation of life," says biologist Paul Hebert of the University of Guelph in Canada, who came up with the idea of DNA bar-coding.

Insect input. Norman MacLeod will upload images of museum specimens to DAISY.

Hebert agrees that DAISY can also address that problem, though he notes that it has limitations. "I think that DAISY will have an important role to play in the identification of taxonomic groups," he says. "Its most serious constraint relates to its reliance on current taxonomic knowledge to provide the training sets required for species identification; DAISY is designed to deliver identifications, not to probe taxonomic terra incognita, like DNA bar-coding promises."

Hanson acknowledges that DNA bar-coding is powerful but feels that DAISY has been unfairly overlooked as a result. "It is distressing to what extent the latest fashions can dominate funding in science," he says. He can see the advantages of both techniques. DNA bar-coding is more widely applicable than DAISY, he says, as it can be used on specimens with a simple morphology, such as nematodes or microbes, or in the event you have only a small piece of an insect. DAISY, on the other hand, is a more straightforward, faster, and cheaper technique (although DNA bar-coding costs have decreased and are now estimated at about $1 per specimen). However, DAISY's unique selling point is that it has the potential to be used by the general public to aid biodiversity studies.

Indeed, O'Neill has grand plans to make DAISY readily available for "citizen science." He is currently adding a Web-based platform for DAISY, which will make it possible for members of the public to identify insects using an Internet-enabled mobile phone. He's also experimenting with future commercial applications of DAISY, such as identifying the model numbers of consumer products and distinguishing among species of protists called foraminifera, which could be used to find new deposits of oil.

Motivated by the NHM funding, O'Neill's progress has increased tremendously, and he expects to have a pilot version of the Web-based DAISY, hosted on the museum's Web site, running by the end of the summer. He hopes that it will be used by professional and hobby entomologists, as well as by anyone with a passing curiosity about what type of butterfly they're looking at on a country walk. "This will be DAISY's crowning glory," says O'Neill, "giving the public a powerful tool to understand the world around them."

–SARAH REED

CREDITS: COURTESY MARK O'NEILL (INSETS); NATURAL HISTORY MUSEUM, LONDON

Published by AAAS

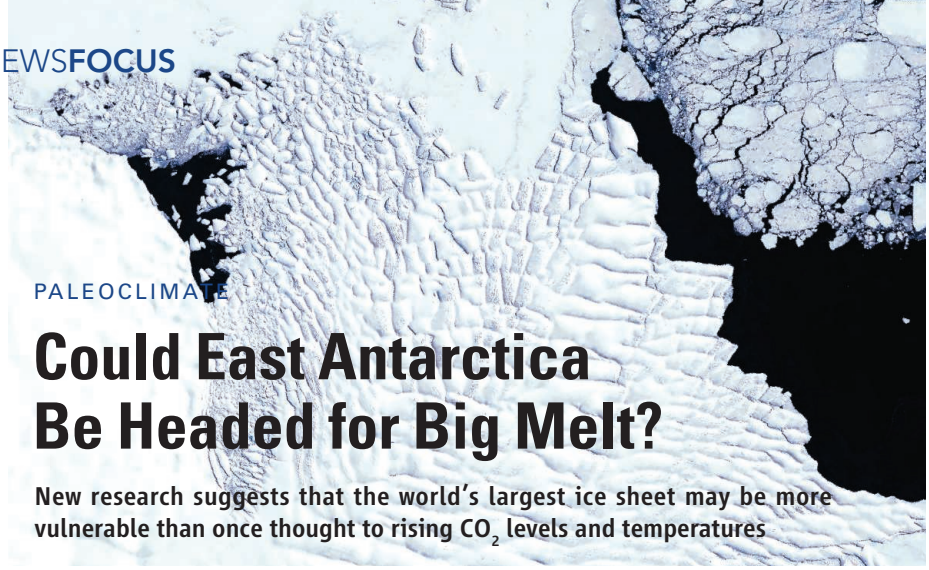

PALEOCLIMATE

Could East Antarctica Be Headed for Big Melt?

New research suggests that the world's largest ice sheet may be more vulnerable than once thought to rising CO_2 levels and temperatures

Cracked up. East Antarctica's Totten Glacier may be stretching and thinning.

The Orangeburg Scarp, a band of hard, crusty sediment teeming with tiny plankton fossils, runs from Florida to Virginia under tobacco fields, parking lots, shopping centers, and Interstate 95, the major highway along the U.S. East Coast. It marks an ancient shoreline where waves eroded bedrock 3 million years ago. That period, the middle Pliocene, saw carbon dioxide (CO_2) levels and temperatures that many scientists say could recur by 2100. The question is: Could those conditions also result in Pliocene-epoch sea levels within the next 10 to 20 centuries, sea levels that may have been as much as 35 meters higher than they are today? The answer, say climate scientists, may lie 17,000 kilometers away in East Antarctica.

The East Antarctic Ice Sheet is the world's largest, a formation up to 4 kilometers thick and 11 million km^2 in area that covers three-quarters of the southernmost continent. Its glaciers were thought to sit mostly above sea level, protecting them from the type of ocean-induced losses that are affecting the West Antarctic Ice Sheet. But studies of ancient sea levels that focus on the Orangeburg Scarp and other sites challenge that long-held assumption. Not everybody believes the records from Orangeburg. But combined with several other new lines of evidence, they support the idea that parts of East Antarctica could indeed be more prone to melting than expected.

"That's pretty incredible when you think about it," says Maureen Raymo, a marine geologist at Boston University who studies Pliocene records. "It implies that the East Antarctic Ice Sheet is not quite as stable as we think it is."

Three studies, using different remote-sensing methods, show that East Antarctica has already begun to lose ice. A survey of laser altimetry data from the ICESat satellite, published in *Nature* in October 2009, found ice thinning in several spots along the East Antarctic coast at annual rates as high as nearly 2 meters. Another study, published in *Nature Geoscience* in November 2009, used the gravity-sensing GRACE satellites and found two areas along the East Antarctic coast each losing about 13 km^3 of ice per year. A 2008 study in *Nature Geoscience* that compared ice flux off the edges of the continent with new accumulation of snow in the interior found a loss of about 10 km^3 of ice per year at two areas.

These amounts pale in comparison to the 150 km^3 or so of ice vanishing each year from West Antarctica. But all three studies point to a handful of hot spots—including, most strongly, Totten Glacier, which is losing up to 1.9 meters of thickness per year. If East Antarctica were to start losing weight, Totten is exactly where it should happen, researchers say, because of its distinctive subglacial landscape. Seeing Totten at risk marks a sea change in the way that people think of East Antarctica, whose topography is the least-known landscape on Earth.

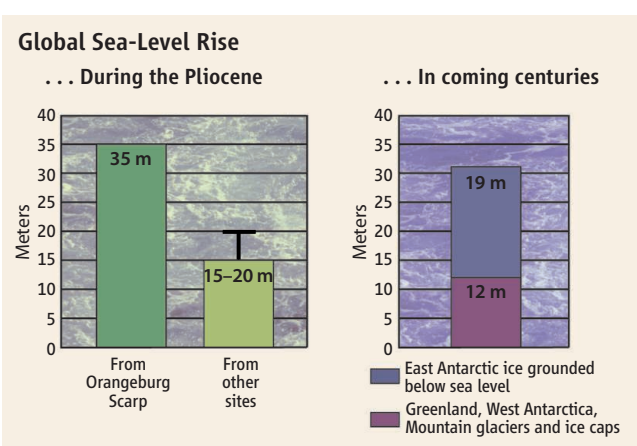

High water. A partial melting in East Antarctica, records indicate, raised sea levels during the Pliocene—and could do so in the future.

Donald Blankenship, a glaciologist at the University of Texas, Austin, has spent the past 2 decades compiling what data there are. He now oversees parts of a multinational survey, called ICECAP, which is using ice-penetrating radar and other sensors flown on aircraft to map the subglacial topography. "Most of these basins weren't particularly well surveyed; some weren't surveyed at all," Blankenship says.

The surveys now in progress, he says, show these basins to be "good and deep." And that's bad news. One survey, published last year in *Tectonophysics* by Fausto Ferraccioli of the British Antarctic Survey, finds the bed of East Antarctica's Wilkes Basin far lower than thought, with two long troughs plunging as far as 1400 meters below sea level. A soon-to-be-published interpolation of older radar data, using undulations in the ice surface to refine the bed topography, suggests that the much larger Aurora Basin, which includes Totten Glacier, is connected to the ocean by troughs that sit 500 to 1000 meters below sea level. These troughs deepen as they head inland, to as low as 2000 meters below sea level in one spot.

The new data are worrisome, says Jason Roberts of the Australian Antarctic Division (AAD) in Hobart, Tasmania. "That's the classic scenario where if you do get melting, you get a deepening grounding line of the ice sheet, which makes it more susceptible to further retreat," he says. "It's much more potentially vulnerable to climate change than we would have thought."

Events in West Antarctica provide a glimpse into what happens when even small amounts of deep, warm water reach glaciers that sit in deepening beds. Pine Island, Smith, Thwaites, and a handful of other glaciers along the coast of West Antarctica's Amundsen Sea are collectively hemorrhaging 100 km^3 of ice annually.

It's too early to know what the ice loss in East Antarctica really means, says Isabella Velicogna, a remote-sensing specialist at NASA's Jet Propulsion Laboratory in Pasadena, California. "What is important is to see what's generating the mass loss," she says. Reductions in snowfall, for example, might reflect short-term weather cycles that could reverse at any time. But thinning caused by accelerating glaciers—as seen in

CREDITS (TOP TO BOTTOM): COURTESY BRAD HERRIED, ANTARCTIC GEOSPATIAL INFORMATION CENTER, ORIGINAL LIMA IMAGE PROVIDED BY NSF, NASA, USGS, BAS; H. J. DOWSETT, T. M. CRONIN, TIMOTHY NAISH, DUNCAN YOUNG, AND SCIENCE

Published by AAAS

West Antarctica—would warrant concern.

Finding out whether Totten is accelerating will be difficult, says Neal Young, an AAD glaciologist who has studied the region for 40 years. Totten sits beyond helicopter range from Australia's Casey Station, and Young says "huge crevasses that would swallow up big buildings" make it extremely tricky to land field parties by airplane.

Young was part of an Australian team that rode Caterpillar tractors 200 kilometers to Totten in 1987—the first of only two human visits to the glacier's lower reaches—and measured Totten's velocity in nine places. Heavy snowfall and rapidly shifting surface features have prevented satellites from remeasuring velocity precisely enough to confirm whether Totten has sped up. And thick sea ice prevents icebreakers from getting near enough to look for warm ocean currents that could erode the glacier underneath.

Even so, the patterns of thinning reported last year suggest that it may have accelerated near the ice fronts of Totten and nearby Vanderford Glacier, causing them to stretch. Both glaciers have thinned most strongly at their ocean margins, where ice is sliding fastest. Thinning is substantially less in adjacent, slow-moving areas. "The answer is in the ocean and the dynamics of the glacier," Young says. "I think the floating ice tongue on Totten has thinned, leading to [increases in speed] that are propagating inland."

All of this suggests that CO_2 levels expected by 2030 and temperatures predicted by midrange models for 2100 could eventually—over a millennium or longer—raise global sea level by 25 to 30 meters. That's well above the 10 to 15 meters predicted from the melting of Greenland and West Antarctica, and a magnitude that would displace hundreds of millions more people.

Plenty of uncertainties remain, though. The best ice-sheet models don't predict East Antarctica losing anywhere near that much ice. But refined topographic maps expected from ICECAP in the next 18 months could change this. "If there are really deep, [narrow] basins around the edges of the continent that the model doesn't know about, then we could be underestimating the potential for retreat," says Robert DeConto, an ice-sheet modeler at the University of Massachusetts, Amherst, who published a model in March 2009 in *Nature* that successfully reproduces 5 million years of ice fluctuations in West Antarctica.

The biggest question is whether Pliocene sea levels really ever reached the heights indicated by studies of the Orangeburg Scarp. "[Pliocene sea level] is a poorly constrained number," Raymo says. "The error bars could be anywhere from 10 to 40 meters above present levels."

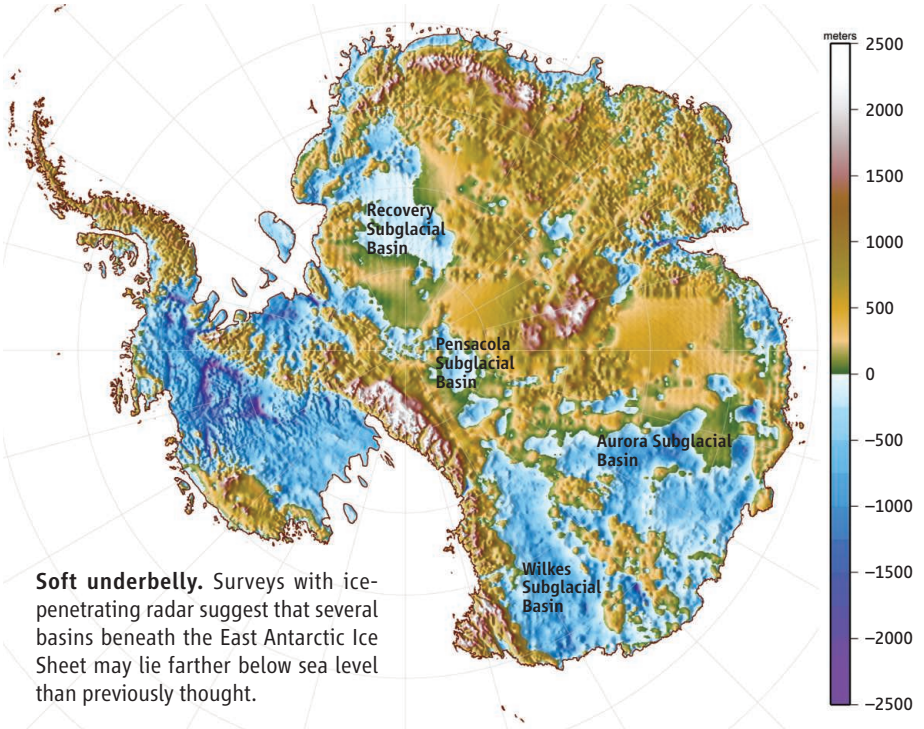

Soft underbelly. Surveys with ice-penetrating radar suggest that several basins beneath the East Antarctic Ice Sheet may lie farther below sea level than previously thought.

Timothy Naish of Victoria University of Wellington, New Zealand, hopes that a technique called backstripping will reduce these errors. Rock cores drilled from ancient coastlines show a sequence of erosion faces in which rising seas periodically chewed away at sediments. Stacked atop one another in time, such a sequence of water lines allows researchers to better correct for tectonic rise or fall, which can skew sea-level estimates.

Preliminary results of cores drilled from the Chesapeake Bay in the United States and Wanganui Basin in New Zealand suggest lower sea levels than Orangeburg would imply. "Twenty-five meters is an absolute upper number," says Naish, who works with Kenneth Miller of Rutgers University, Piscataway, in New Jersey. "We think the number is nearer to 15 to 20 meters." That estimate implies that there was some melting in East Antarctica, but not as much.

Another confounding factor is that ice-sheet melting produces uneven rises in sea level. The meltwater is redistributed to reflect changes in Earth's gravity field caused by the disappearance of a fixed ice sheet. "Sea level is a complex stew," says geophysicist Jerry Mitrovica of Harvard University, who is collaborating with DeConto and Raymo. "The bathtub model is only going to get you partway there." Just 5000 years ago, as Ice Age glaciers were still melting, for example, sea levels in New Jersey were 9 meters lower than at present—whereas those in Argentina were 5 meters higher.

Differences this large could distort interpretation of the world's handful of Pliocene sea-level records. Raymo and collaborators hope that Mitrovica and DeConto can reconcile ice-sheet masses with sea levels around the world by plugging more numbers into their models. Paul Hearty, a collaborator at the University of North Carolina, Wilmington, is looking for sea-level records in Australia and the Azores. Raymo is constructing a Web-based wiki that she hopes will attract sea-level records from around the globe.

Others are directly investigating the history of East Antarctica's low-lying basins for indications of what happened to their ice during the Pliocene. Early this year, a team with the Ocean Drilling Program extracted seven cores from the sea floor in front of Wilkes Basin. Investigators are picking those layers apart this summer in search of clues about how well the ice in Wilkes Basin held together during the Pliocene.

Together, these efforts will begin to address the bigger question of what the loss of ice in East Antarctica, if it's occurring, actually means for the world's inhabitants. "Nobody expected it," says Velicogna. "And if we just think that nothing is going to happen there, we're making a mistake."

–DOUGLAS FOX

Douglas Fox is a freelance writer based in San Francisco, California.

CREDIT: DUNCAN YOUNG

Published by AAAS

Faith against illness 1636

Breeding perennial grains 1638

SPORE Essay 1648

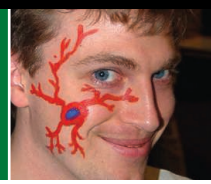

LETTERS | BOOKS | POLICY FORUM | EDUCATION FORUM | PERSPECTIVES

LETTERS

edited by Jennifer Sills

Time for a Sea Change in Chinese Collaboration

THE EXCAVATION OF *NANHAI 1*, A SONG DYNASTY SHIP OFF THE COAST OF CHINA BY RESEARCHers based in Guangzhou, Guangdong Province (News Focus, L. Jiao, "Unprecedented excavation brings Maritime Silk Road to life," 23 April, p. 424) is one of the most exciting recent developments in research on Song Dynasty seagoing trade and technology. Scholarship on this topic has been under way for decades. In 1974, a Song Dynasty ship was unearthed and studied in Quanzhou, Fujian Province. In combination with many other sources of evidence, the find provided rich information on China's early engagement with other societies (*1*, *2*).

Experts from and on Quanzhou should have a part in the *Nanhai 1* research. Unfortunately, collaboration between cities in China can be especially difficult, both in research and education. As an urban planner who has worked for 17 years on historic preservation in Quanzhou, I have observed the city's efforts to obtain UNESCO World Heritage status on the basis of its importance to China's Maritime Silk Road, an effort in which no Chinese city has yet succeeded. UNESCO encourages multiple jurisdictions to apply together for one "property" when the heritage is extended across many geographic locations. To be successful, the Chinese central government must do more to facilitate collaboration among Quanzhou, Guangzhou, and other port cities in China and abroad that contributed to the trade.

DANIEL B. ABRAMSON

Urban Design and Planning, University of Washington, Seattle, 98105 WA, USA. E-mail: abramson@uw.edu

References

1. The Song Dynasty in China (http://afe.easia.columbia.edu/song/out/trade.htm).
2. R. Pearson, L. Min, L. Guo, *Int. J. Hist. Archaeol.* **6**,23 (2002).

Benefits of Self-Reporting

W. F. LAURANCE AND O. VENTER ("MEASURING forest changes," Letters, 30 April, p. 569) question whether, under the proposed REDD mechanism (reducing emissions from deforestation and forest degradation), developing countries should be responsible for producing their own estimates of changes in forest carbon stocks. Instead, they propose that an independent organization should be given this task, and mention the UNEP World Conservation Monitoring Centre as a possible candidate for this role.

We note that the practice within the framework convention on climate change (UNFCCC) has been that countries report, in accordance with specified standards, on their own greenhouse gas emissions (*1*). Independent review teams composed of experts nominated by the Parties then verify that country reports correctly apply the IPCC methodology for estimating emissions (*2*).

There are strong indications that the Parties to the UNFCCC will follow a similar approach for REDD (*3*, *4*). Each independent review team is mandated to make use of "technical information" from third parties. Ensuring that the teams have access to any available independent forest monitoring data would strengthen the verification process.

This approach has the merit of promoting the development of accurate monitoring systems within countries, which are themselves an important component of good forest management, while also retaining a strong element of independent verification. For these reasons, we suggest that Laurance and Venter's proposal to replace developing countries' role in the process may not be in the long-term interests of promoting reduced emissions from forests in developing countries.

JONATHAN M. HUTTON* AND BARNEY DICKSON

United Nations Environment Programme World Conservation Monitoring Centre, 219 Huntingdon Road, Cambridge CB3 0DL, UK.

*To whom correspondence should be addressed. E-mail: jon.hutton@unep-wcmc.org

References

1. "Updated UNFCCC reporting guidelines on annual inventories following incorporation of the provisions of decision 14/CP.11" (UNFCCC Subsidiary Body for Scientific and Technological Advice, FCCC/SBSTA/2006/9, 2006); unfccc.int/resource/docs/2006/sbsta/eng/09.pdf.
2. "Review of the implementation of commitments and of other provisions of the Convention. National communications: Greenhouse gas inventories from Parties included in annex I to the Convention" (UNFCCC Conference of the Parties, FCCC/CP/2002/8, 2003); unfccc.int/resource/docs/cop8/08.pdf.
3. A. Angelsen *et al.*, *Reducing Emissions from Deforestation and Forest Degradation (REDD): An Options Assessment Report* (Meridian Institute, Washington, DC, 2009); www.REDD-OAR.org.
4. D. J. Baker *et al., Environ. Sci. Pol.* **13**, 249 (2010).

Consequences of Legal Ivory Trade

THE POLICY FORUM BY S. WASSER *ET AL.* ("Elephants, ivory, and trade," 12 March, p. 1331) overlooks several points that bear on the issue of whether the Convention on International Trade in Endangered Species (CITES) should allow legal ivory sales.

There is no proof that the elephant population is dropping. The two citations given offer no clear evidence. The IUCN Red List categorizes *Loxodonta africana* as "vulnerable," below two levels of higher threat, and

CREDIT: ZHANG WANXING

Published by AAAS

its population trend is described as "increasing" (*1*).

We agree with the statement that "most of Africa lacks adequate controls for protection of elephants," but rather than target legal ivory sales, CITES should take steps to increase anti-poaching and trade enforcement. Legal ivory sales have not been shown to stimulate poaching (*2*–*4*), despite widespread media claims that link the two. Focus on this issue takes attention away from other factors that drive illegal killings, such as unregulated domestic markets, ivory demand, corruption, and human-elephant conflict.

Wasser *et al*. state that "[i]n the absence of data, precautionary principles should be applied." Yet precautionary principles can be manipulated to suit one's purposes. The authors assume that a legal trade might lead to irreversible elephant losses. What if the assumption were the opposite—that not allowing trade would lead to increased poaching? This scenario is hardly far-fetched. In the absence of legal supply, ivory demand will inevitably be met by killing elephants illegally.

The authors state, accurately, that "one-off" sales introduce uncertainty into the marketplace, but they do not acknowledge that there is another way to reduce uncertainty other than having no sales: Allow a regular, annually recurrent sale to settle the markets, reduce prices, and lower motivation to poach and buy illegal ivory.

We believe that both no sales and "one-off" sales are harmful for elephant conservation and, given sufficient institutional support and political will, a normalized legal ivory trade would save elephant lives.

JOHN F. WALKER[1]* AND DANIEL STILES[2]

[1]Kent, CT 06757, USA. [2]Diani Beach, 80401, Kenya.

*To whom correspondence should be addressed. E-mail: johnfwalker@charter.net

References

1. The IUCN Red List of Threatened Species, *Loxodonta africana* (www.iucnredlist.org/apps/redlist/details/12392/0).
2. D. Stiles, *Environ. Conserv*. **34**, 309 (2004).
3. E. Bulte, R. Damania, G. van Kooten, *J. Wildlife Manage*. **71**, 613 (2007).
4. T. Milliken, R. W. Burn, L. Sangalakula, *The Elephant Trade Information System (ETIS) and the Illicit Trade in Ivory* (CoP15, Doc. 44.1, TRAFFIC, Cambridge, MA, 2009); www.cites.org/eng/cop/15/doc/E15-44-01A.pdf.

Response

WALKER AND STILES ARGUE THAT ELEPHANT populations are not declining. The facts say otherwise. *Loxodonta africana* numbers have plummeted by more than 50% continent-wide in the past 40 years, a reduction now compounded by increases in range loss, conflict with humans, and resurgence in poaching (*1*). Illegal killing from 2000 to 2007 was highest in central Africa (63% of carcasses were illegally killed) followed by eastern (57%), western (33%), and southern Africa (19%) (*2*). Poaching reduced one of the Democratic Republic of the Congo's (DRC's) largest populations of forest elephants by nearly half between 1996 and 2006 (*3*). Elephant populations in Chad and Central African Republic declined by more than 80% in the past 5 and 20 years, respectively (*4*, *5*). The Selous Game Reserve population in Tanzania has declined by 30% since 2006, amidst escalated poaching (*2*, *6*). Because average tusk size has progressively decreased over the past three decades (*7*, *8*), more elephants must be killed for the same volume of ivory; this has accelerated the trend toward population collapse.

Walker and Stiles next argue that legal trade does not increase illegal trade, and CITES should focus on enforcement instead of targeting legal trade. We disagree. The appeal of the market mechanism for managing wildlife stocks presumes well-functioning institutions with unambiguous ownership of the stocks. Chronic problems such as poaching, corruption, and inadequate regulation and enforcement capacity show that this assumption is false. The problem will be exacerbated if CITES' promotion of legal trade increases illegal trade by signaling an opening market. The ETIS (*9*) report to CITES rejected such a relationship for the first one-off ivory sale in 1999 but acknowledged that illegal ivory trade increased substantially in 2009 after the 2008 sale. The Elephant Trade Information System (ETIS) analysis used adjusted amounts of seizures that markedly differed from unadjusted values, incorporated a smoothing technique that blunted peaks and troughs, and excluded a major increase in poaching in DRC during 2004 (*10*). This obscured a recurring pattern where each proposal for one-off ivory sales appears to have instigated a rise in poaching.

Walker and Stiles believe that a regular, legal trade should be established and enforced. We are not suggesting that legal sales will always lead to irreversible losses, but rather that illegal trade currently is too uncontrolled to justify the risk. When the distinction between legal and illegal ivory is uncertain, increasing the legal supply raises the probability that more ivory will be provided through illegal trade. Illegal dealers will see an expanding market due to increased allowable trade, and will endeavor to maintain their share of that market. Moreover, growing demand for ivory will outstrip

CORRECTIONS AND CLARIFICATIONS

News Focus: "The coastal Indus looks west" by A. Lawler (28 May, p. 1100). The story incorrectly identified two distances on page 1100. Lothal is approximately 250 kilometers from Dholavira, which in turn is approximately 650 kilometers from Mohenjo Daro. In addition, Kanmer dig director Toshiki Osada is at the Research Institute for Humanity and Nature in Kyoto, which is part of the National Institutes for the Humanities, based in Tokyo. Also, the subheadline on page 1100 should have read that the Indus society shipped goods to the west, not the east.

News Focus: "Laser fusion energy poised to ignite," by D. Clery (14 May, p. 808). Hiroshi Azechi's statement that "NIF will prove that ignition takes place at laboratory temperatures, irrespective of the heating method" should read "NIF will prove that ignition takes place in laboratories, irrespective of the heating method."

Reports: "Altered histone acetylation is associated with age-dependent memory impairment in mice" by S. Peleg *et al*. (7 May, p. 753). There were 2229 genes, but the text misstates the numbers that were up-regulated and down-regulated. It should have read, "In 3-month-old mice, 2229 genes (1977 up-regulated versus 252 down-regulated) were differentially expressed." The body of table S1 is correct, but the title contains the same mistake.

TECHNICAL COMMENT ABSTRACTS

Comment on "30,000-Year-Old Wild Flax Fibers"

C. Bergfjord, S. Karg, A. Rast-Eicher, M.-L. Nosch, U. Mannering, R. G. Allaby, B. M. Murphy, B. Holst

Kvavadze *et al*. (Brevia, 11 September 2009, p. 1359) identified fiber samples as 30,000-year-old flax based on a comparison with modern flax fibers analyzed by compound microscope and on the presence of dislocations/nodes in the fibers. We argue that this evidence is not sufficient to identify the fibers as flax.

Full text at www.sciencemag.org/cgi/content/full/328/5986/1634-b

Response to Comment on "30,000-Year-Old Wild Flax Fibers"

Eliso Kvavadze, Ofer Bar-Yosef, Anna Belfer-Cohen, Elisabetta Boaretto, Nino Jakeli, Zinovi Matskevich, Tengiz Meshveliani

Bergfjord *et al*. express doubts regarding our identification of flax fibers on the basis of the morphology of their internal layers. The authors use microphotographs and descriptions of the outer layers of fibers as arguments for their claims. Morphology and structure of the outer and inner parts of fibers are radically different, however, rendering their reservations misplaced.

Full text at www.sciencemag.org/cgi/content/full/328/5986/1634-c

any potential sustainable legal supply given increasing purchasing power of Asian consumers and limited maximum growth rates of elephant populations, particularly when poaching is already mining populations of progressively younger individuals. If seizures are assumed to represent ≤10% of ivory shipped (*11*), the average 19,000 kg of annual ivory seizures over the past decade (*9*) would require 190,000 kg of "legal" ivory sold annually just to meet levels of demand presently supplied through illegal trade.

We contend that any legal trade at this time is an untenable risk that complicates law enforcement and distracts from the need to reduce demand. Although reducing demand is possible, elephants could be seriously depleted in the interim because (i) verified natural mortality and controlled culls are insufficient to meet current demand; (ii) proceeds from ivory sales cannot be guaranteed to return to local communities as incentive for in situ conservation; and (iii) education campaigns are finding it difficult to suppress the growing desire and purchasing power for luxury goods in end-user countries.

Analogous arguments apply to most other trade species, including sharks, blue fin tuna, polar bears, and corals. CITES should therefore reset its priorities, more explicitly apply the precautionary principle, and insist upon open data access and peer review. Only then will it ensure the long-term viability of species and trade.

SAMUEL WASSER,[1]* KATARZYNA NOWAK,[2] JOYCE POOLE,[3,4] JOHN HART,[5] RENE BEYERS,[6] PHYLLIS LEE,[4,7] KEITH LINDSAY,[4] GARDNER BROWN,[1] PETTER GRANLI,[3] ANDREW DOBSON[2]

[1]University of Washington, Seattle, WA 98195, USA. [2]Princeton University, Princeton, NJ 08540, USA. [3]ElephantVoices, Sandefjord, 3236, Norway. [4]Amboseli Trust for Elephants, Kenya. [5]Tshuapa-Lomami-Lualaba Project, Kinshasa, Democratic Republic of the Congo. [6]University of British Columbia, Vancouver, BC V6T 1Z4, Canada. [7]University of Stirling, Stirling K94LA, UK.

*To whom correspondence should be addressed. E-mail: wassers@u.washington.edu

References and Notes

1. J. J. Blanc *et al.*, *African Elephant Status Report 2007* (IUCN, Gland, Switzerland, 2007).
2. CITES, "Monitoring of illegal hunting in elephant range states" (CoP15, Doc. 44.2, 2009); www.cites.org/eng/cop/15/doc/E15-44-02.pdf.
3. R. Beyers, thesis, University of British Columbia, Vancouver, BC (2008); https://circle.ubc.ca/handle/2429/960.
4. P. Bouché *et al.*, *Afr. J. Ecol.*, 10.1111/j.1365-2028.2009.01202.x (23 December 2009).
5. D. Potgieter, N. Taloua, B. Djimet, M. Fay, L. Holm, *Dry Season Aerial Total Count, Zakouma National Park, Chad 4–8 March 2009* (Wildlife Conservation Society Technical Report, 2009).
6. CITES, "Report of the Panel regarding the proposal of the United Republic of Tanzania" (CoP15 Doc. 68 A6a); www.cites.org/eng/cop/15/doc/E15-68A06a).pdf.
7. E. J. Millner-Gulland, J. R. Beddington, *Proc. R. Soc. London Ser. B* **252**, 29 (1993).
8. CITES, "Report of the Panel regarding the proposal of Zambia" (CoP15 Doc. 68 A6b); www.cites.org/eng/cop/15/doc/E15-68A06b).pdf.
9. T. Milliken, R. W. Burn, L. Sangalakula, *The Elephant Trade Information System (ETIS) and the Illicit Trade in Ivory* (CoP15, Doc. 44.1, TRAFFIC, Cambridge, MA, 2009); www.cites.org/eng/cop/15/doc/E15-44-01A.pdf.
10. C. A. Apobo, *Rapport sur le Braconnage D'Eléphant et sur le Commerce de l'Ivoire dans et a la Périphérie de la Réserve de Faune à Okapis (RFO) Ituri, RDC* (ICCN Report, Wildlife Conservation Society, Democratic Republic of Congo, 2004).
11. S. K. Wasser *et al.*, *Conserv. Biol.* **22**, 1065 (2008).

Letters to the Editor

Letters (~300 words) discuss material published in *Science* in the previous 3 months or issues of general interest. They can be submitted through the Web (www.submit2science.org) or by regular mail (1200 New York Ave., NW, Washington, DC 20005, USA). Letters are not acknowledged upon receipt, nor are authors generally consulted before publication. Whether published in full or in part, letters are subject to editing for clarity and space.

Published by AAAS

Comment on "30,000-Year-Old Wild Flax Fibers"

C. Bergfjord,[1] S. Karg,[2] A. Rast-Eicher,[3] M.-L. Nosch,[4] U. Mannering,[4] R. G. Allaby,[5] B. M. Murphy,[6] B. Holst[1]*

Kvavadze *et al*. (Brevia, 11 September 2009, p. 1359) identified fiber samples as 30,000-year-old flax based on a comparison with modern flax fibers analyzed by compound microscope and on the presence of dislocations/nodes in the fibers. We argue that this evidence is not sufficient to identify the fibers as flax.

Kvavadze *et al*. (*1*) recently described fiber samples found in a series of Upper Paleolithic layers at Dzudzuana Cave in Georgia. Based on radiocarbon (^{14}C) dating of accompanying material (bone and charcoal), the authors dated the fibers to 30,000 years ago. The authors also report that the fiber samples are flax based on comparison of white light compound microscope images of the samples with (i) similar images of modern flax, (ii) scanning electron microscopy images of modern flax, and (iii) an interference microscopy image of an ancient sample reported to be flax. The authors claim that "some of the characteristic features of the flax fibers structure are their considerable thickness" and that "they consist of multiple longitude segments" [Supporting Online Material (SOM) for (*1*)]. Kvavadze *et al*. further state that "[a]pplying these criteria, flax fibers are easily separated from other plant fibers" [SOM for (*1*)]. Unfortunately, this statement is not correct. Although it is easy to distinguish cotton from flax [by polarization microscopy (*2*), for example], it can be very difficult to distinguish between different types of bast fibers. Bast fibers can be extracted from plant stalks or tree bark (cotton is not a bast fiber). Bast fibers have a characteristic cross-section appearance with a central opening (lumen) surrounded by the cell wall (*3*). Bast fibers used for textiles include flax, hemp, nettle, ramie (an Asian nettle variety), jute, and more rarely, wood. Flax tends to have a smaller overall diameter and a smaller lumen than other bast fibers. This is often a very good indicator for identification. However, the flax lumen is not always narrow, and other bast fibers can show narrow lumen too, so this is not a conclusive identification criterion (*4*). A comparison of thickness measurements of several types of bast fibers, including flax, show that the overlap is so large that thickness cannot be taken as a conclusive criterion [see for example (*4*, *5*)].

The "multiple longitude segments" Kvavadze *et al*. mention are the areas of the fibers located between what is normally referred to as dislocations, nodes, or kinks (*6*). The first description of dislocations is attributed to von Höhnel (*7*), who described "ring markings" as a result of "tension in the tissues." The cause(s) of dislocations are still debated, but they are common in many plant fibers. Catling and Grayson (*4*) write that "Whatever the cause, there is no doubt that dislocations occur in every species examined during the course of this work." As early as 1957, Tobler (*8*) noted that "the significance of dislocations for diagnostic purposes has completely disappeared" [see also (*6*, *9*)].

Kvavadze *et al*. state that another important diagnostic property is the particular structure of the fiber extremities, noting that those of flax fibers are "completely straight (as if truncated)" [SOM for (*1*)]. However, Catling and Grayson (*4*) present images of fiber cell ends for a range of plants. They showed 11 different ends for flax alone and concluded that these ends are not a useful character for the identification of plant fibers. Kvavadze *et al*. finally state that "[t]he structure of the flax fibers is linear, while that of cotton is smooth" [SOM for (*1*)]. By "linear," we assume they are referring to the fact that the fibers are not round but have a polygonal cross section. This cross-sectional shape can, however, also be found in many other bast fibers. Herzog (*5*), for example, writes that "based on the experience of many years I would not ascribe the cross section appearance of flax the importance of a characteristic or distinguishing feature (the same applies to hemp)."

For the reasons explained above, white light compound microscopy alone is not a failsafe method for identifying flax fibers. The presence of a lumen and the dislocations in the fiber samples only provide evidence that they are bast fibers. The fiber samples may be flax, but they have not been proven to be so. As an illustration, Fig. 1 shows white light and polarization microscopy images of modern domesticated flax (*Linum usitatissimum*), nettle (*Urtica dioica*), and hemp (*Cannabis sativa*) fibers, respectively. The similarity between these fiber images and the images of the fiber samples published in (*1*) is evident.

We contend that for a conclusive identification of flax, other analytical methods are necessary. An ideal method would be DNA analysis, but it is generally difficult to extract DNA even from modern bast fibers (*10*). The removal of the fibers from the plant stem (retting) involves exposure to water, thus increasing the likelihood of extensive hydrolytic damage to the DNA (*11*, *12*). The presence of crystals in the associated tissue of the fibers can provide clues to their identity. For example, calcium oxalate crystals are present in ramie and hemp but not in flax (*4*). Polarization microscopy can also be used to separate hemp from flax, nettle, and ramie based on the microfibrilliar orientation (*13*). A conclusive method for identifying flax fibers that works well even with very little fiber material is x-ray microdiffraction. This method can identify very slight species-dependent differences in the cell wall structure, including the organization of well-oriented cellulose fibrils. It often works well even on damaged fibers, in which degraded surface features can obscure the results of light and electron microscopy. Müller *et al*. (*14*) were the first to apply this method to plant bast fibers. They successfully identified flax and ramie (and also, unexpectedly, cotton) fibers from caves of the Dead Sea region. For a further discussion of characterization criteria for bast fibers, we also refer to (*15*).

In conclusion, Kvavadze *et al*. (*1*) present white light compound microscopy images of fiber samples with a clearly visible lumen and dislocations. Based on these two features, the fiber samples can be identified only as bast fibers. Any further conclusions about the nature of these fibers will require additional investigations with other techniques.

[1]Department of Physics and Technology, University of Bergen, Allegaten 55, 5007 Bergen, Norway. [2]Environmental Archaeology and Archaeometry, The National Museum of Denmark, Ny Vestergade 11, 1471 Copenhagen, Denmark. [3]Archeotex, Kirchweg 58, 8755 Ennenda, Switzerland. [4]The Danish National Research Foundation's Centre for Textile Research, SAXO Institute, University of Copenhagen, Njalsgade 102, 2300 Copenhagen, Denmark. [5]Plant Evolution Research, Warwick HRI, University of Warwick, Wellesbourne, CV35 9EF Warwick, UK. [6]Institute of Experimental and Applied Physics, University of Kiel, Olshausenstrasse 40, 24098 Kiel, Germany.

*To whom correspondence should be addressed. E-mail: bodil@cantab.net

References

1. E. Kvavadze *et al*., *Science* **325**, 1359 (2009).
2. B. Luniak, *The Identification of Textile Fibers* (Pitman, London, 1953).
3. D. Cutler, T. Botha, D. W. Stevenson, *Plant Anatomy: An Applied Approach* (Blackwell, Oxford, 2008).
4. D. Catling, J. Grayson, *Identification of Vegetable Fibres* (Archtype, London, 2004).
5. A. Herzog, *Mikrophotographischer Atlas der Technisch Wichtigen Pflanzenfasern* (Akademie-Verlag, Berlin, 1953).
6. L. G. Thygesen, M. Eder, I. Burgert, *J. Mater. Sci.* **42**, 558 (2007).
7. F. von Höhnel, *Jahrb. Wissensch. Bot.* **15**, 313 (1884).
8. F. Tobler, in *Handbuch der Planzenantomie*, K. Linsbauer, Ed. (Gebr. Bornträger, Berlin, 1957), pp. 22–27.
9. S. Khalili, D. E. Akin, B. Pettersson, G. Henriksson, *J. Appl. Bot.* **76**, 133 (2002).
10. M. Dunbar, T. M. Murphy, *J. Forensic Sci.* **54**, 108 (2009).

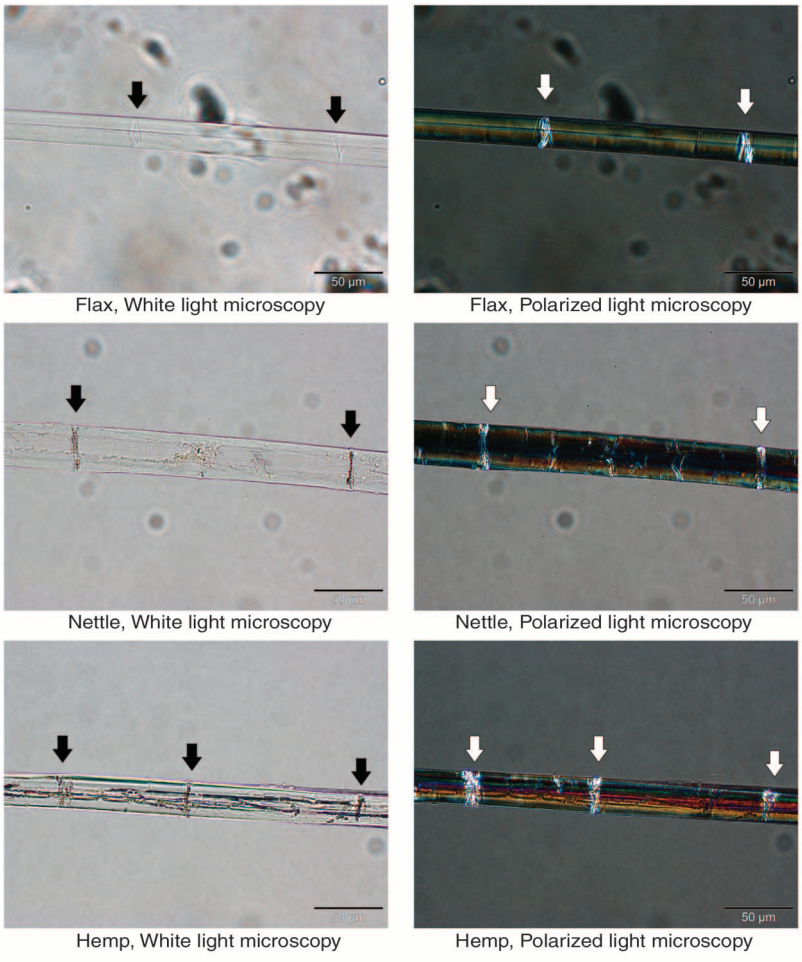

Fig. 1. Images of modern fibers from flax, nettle, and hemp acquired with an Olympus BX-51P compound microscope. Dislocations (arrows) are clearly visible in all three fibers. Note the narrow lumen in flax. This is typical but does not always occur. The polarized light images were taken with the analyzer and polarizer perpendicular to each other.

11. T. Lindahl, *Nature* **362**, 709 (1993).
12. M. Hofreiter, D. Serre, H. N. Poinar, M. Kuch, S. Pääbo, *Nat. Rev. Genet.* **2**, 353 (2001).
13. N. Petraco, T. Kubic, *Color Atlas and Manual of Microscopy for Criminologists, Chemists and Conservators* (CRC Press, Boca Raton, FL, 2004).
14. M. Müller *et al.*, *Appl. Phys., A Mater. Sci. Process.* **89**, 877 (2007).
15. U. Körber-Grohne, A. Feldtkeller, *Pflanzliche Rohmaterialien und Herstellungstechniken der Gewebe, Netze, Geflechte sowie anderer Produkte aus den neolithischen Siedlungen Hornstaad, Wangen, Allensbach und Sipplingen am Bodensee* (Thesis, Stuttgart, 1998).

23 December 2009; accepted 1 June 2010
10.1126/science.1186345

Response to Comment on "30,000-Year-Old Wild Flax Fibers"

Eliso Kvavadze,[1] Ofer Bar-Yosef,[2]* Anna Belfer-Cohen,[3] Elisabetta Boaretto,[4] Nino Jakeli,[5] Zinovi Matskevich,[2] Tengiz Meshveliani[5]

Bergfjord *et al*. express doubts regarding our identification of flax fibers on the basis of the morphology of their internal layers. The authors use microphotographs and descriptions of the outer layers of fibers as arguments for their claims. Morphology and structure of the outer and inner parts of fibers are radically different, however, rendering their reservations misplaced.

We reported the identification of wild flax fibers based on the morphology of the internal layers of the fibers, which were exposed due to the chemical treatment applied in palynological sample preparation (*1*). The morphology of the internal layers is considerably different from the structure of the outer layers of the flax fibers. This is substantiated through a series of laboratory experiments that tested recent plant material of different taxons. Exposure of the internal structure of modern flax fibers was achieved by subjecting the fibers to damage procedures analogous to the treatment of palynological samples in which chemically active substances such as potassium hydroxide, acetic anhydrite, sulphuric acid, and others were employed.

Following this procedure, we identified the taxonomic characteristics of various basts. These characteristics are missing in the outer layers of fibers, yet can be consistently used for identification of fossilized plant fibers. We noticed in the case of flax that each fiber consists of multiple segments of equal length. The segments are clearly visible and are distinctly separated from each other by deep linear grooves. The fibers' surface is not smooth but rather linear. The end of the short fiber segments is always straight, as if cut across. These features were observed during the study of more than a thousand modern flax samples, as well as several thousand ancient fibers uncovered by archaeological investigations.

During the next step of our analysis (*1*), we compared the internal structure of the flax fibers with the internal structure of other plant fibers, including nettle, hemp, and cotton—species most commonly used for textile production. The comparison demonstrated clear differences in the morphology of the inner layers of each of the plants, as visible in Fig. 1. In nettle fibers, the segments are of uneven length and lack deep grooves with straight borders. The internal structure of hemp is generally not segmented. Also, the surface morphology is different, and fiber extremities are not straight. Thus, our results are in accordance with the opinion that the internal structure of fibers (similarly to other vegetative or generative parts of plants) is a reliable criterion for their taxonomic identification (*2*, *3*).

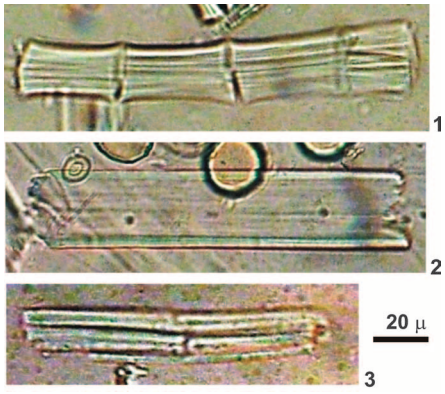

Fig. 1. Modern fibers from the collections of the Institute of Paleobiology, National Museum of Georgia. 1, flax; 2, hemp; 3, nettle. The photos were taken using light microscope E. Leitz (Wetzlar).

We cannot agree with the conclusion of Bergfjord *et al*. (*4*) that light microscopy does not allow the identification of various bast fibers. The research history of bast fibers demonstrates the opposite. Light microscopy has revealed time and again the essential characteristic traits of fiber morphology and allowed plant identification (*5*–*11*). The use of different methods, such as DNA analysis, x-ray microdiffraction, and polarization microscopy is undoubtedly suitable for the verification of bast fibers. But so is the identification of plant fibers as palynomorphs, demonstrated through numerous laboratory experiments comparing modern and archaeological samples (*12*).

[1]Institute of Paleobiology, National Museum of Georgia, Tbilisi, 380007, Georgia. [2]Department of Anthropology, Peabody Museum, Harvard University, Cambridge, MA, 02138, USA. [3]Institute of Archaeology, Hebrew University, Jerusalem 91905, Israel. [4]Radiocarbon Dating and Cosmogenic Isotopes Laboratory, Kimmel Center for Archaeological Science, Weizmann Institute of Science, Rehovot, 76100, Israel, and Department of Land of Israel Studies and Archaeology, Bar-Ilan University, Ramat Gan 59100, Israel. [5]Georgian State Museum, Department of Prehistory, Tbilisi, 380105, Georgia.

*To whom correspondence should be addressed. E-mail: obaryos@fas.harvard.edu

References

1. E. Kvavadze *et al*., *Science* **325**, 1359 (2009).
2. K. Esau, *Anatomy of Seed Plants*, ed. 2 (Mir, Moskow, 1980).
3. N. Myer-Melikian, *Botanical J.* **85**, 69 (2000).
4. C. Bergfjord *et al*., *Science* **328**, 1634 (2010); www.sciencemag.org/cgi/content/full/328/5986/1634-b.
5. K. G. Isakadze, *Sapeikro sakme sakartveloshi (Textile Making in Georgia)* (Ganatleba, Tbilisi, 1970).
6. *Identification of Textile Materials* (Textile Institute, Manchester, ed. 7, 1985).
7. E. Kvavadze, G. Narimanishvili, in *Abstracts of 7th EPPC (European Palaeobotany and Palynology Conference), Sept. 6–11* (Prague, 2006), pp. 77–78.
8. E. Kvavadze, L. Rukhadze, V. Nikolaishvili, L. Mumladze, *Vegetation History and Archaeobotany* **17** (S1), 217 (2008).
9. E. Kvavadze *et al*., in *Problems of Palaeobiology II,* G. Mchedlidze, Ed. (Georgian National Museum Press, Tbilisi, 2008), pp. 12–23.
10. G. Makharadze *et al*., *Analebi* **3**, 436 (2009).
11. E. Kvavadze, I. Gagoshidze, *Vegetation History and Archaeobotany* **17** (S1), 211 (2008).
12. E. Kvavadze *et al*., paper presented at the 4th Workshop on Non-Pollen Palynomorphs, Besançon, France, 16 to 19 June 2010.

29 January 2010; accepted 1 June 2010
10.1126/science.1187161

MEDICINE

Paths Out of Illness via Faith

Esther M. Sternberg

Miracle Cures
Saints, Pilgrimage, and the Healing Powers of Belief
by Robert A. Scott
University of California Press, Berkeley, 2010. 265 pp. $24.95, £16.95. ISBN 9780520262751.

At a time when issues of religion and science can so easily ignite passions at both ends of the spectrum of true believers, it is refreshing to see the topics treated in an objective and scholarly manner. Robert Scott's *Miracle Cures* presents a thorough sociological analysis of unexplained cures that, over the centuries from medieval through modern times, have been alleged to occur at shrines, by saints, and through pilgrimages. Fascinating in its depth, thoroughness, and detailed accounts of medieval life, the book is a good read despite the numerous footnotes and the clearly textbook-style chapter structure. Indeed, dealing with a subject as potentially controversial as this one the author does well to extensively document his point of view. His position is consistently nonjudgmental and open; he states in the prologue:

> I do not dismiss, negate, or supplant the views of religious believers but instead extend the modern understanding of what transpires in the body and mind when the faithful report that they gain relief from their suffering by appealing to saints.
>
> My only real quarrel is with those who dismiss all such claims of cure as hogwash.

Scott (Center for Advanced Study in the Behavioral Sciences at Stanford University) does not set out to debunk or substantiate these claims of miracle cures, but rather analyzes them from a sociological point of view. In this he succeeds. The book's first chapters set the stage in Christian Europe with detailed descriptions of medieval life, conditions of poverty, malnutrition, poor hygiene, and crowding. He suggests that these could have led to and fostered the many ills rampant in the population, which he surveys. Once the stage has been set, Scott introduces the characters in the drama: the saints to whom medieval people turned for help and salvation. There are several ah-ha moments in the book when these characters are seen through a sociologist's eyes. Thus, it appears that medieval Christians accepted as fact that there were certain things that saints could do and other actions that lay beyond their powers. For example, they could cure blindness but could not reattach a limb. Scott also deconstructs the system by which miracle cures and sightings of apparitions were disseminated. He likens that to a modern public relations campaign, in which it is always humans who do the disseminating. In comparing the process to our modern publicity machines, Scott does not disparage the system or the event, but simply analyzes the methods involved.

The author similarly analyzes the why and what of pilgrimages: why would an individual undertake such a daunting task, when in those times going on a pilgrimage was no small feat, involving extensive preparation and considerable risk? Scott suggests a variety of motivations, which range from the serious (seeking cures for illness, escaping dire circumstances, the draw of the supernatural, and devotion to their faith) to the mundane: "an excuse to travel" or "the prospect of a partially subsidized vacation!" Such insights allow the reader to relate to the material and understand it in more personal terms.

Having set the stage and added the characters, Scott introduces the action: the healing of ills. But first he discusses the illnesses for which people sought cures (drawing on the records of healing shrines in England and France, such as that of Thomas Becket in Canterbury). He uses statistics to illustrate an interesting phenomenon that appears to have repeated itself at many shrines: an initial large number of sightings and miracle cures is followed by a drop-off over time. Offering another comparison with the modern day, he likens this phenomenon to the effects often seen when new drugs are introduced to the market: after an early peak, efficacy declines with time. Scott cites William of Canterbury's explanation for this phenomenon: "once a saint has performed enough miracles to command veneration, he withdraws gracefully and leaves the task to other, more recently canonized saints." But the reader has already grasped that Scott is leading up to a more modern explanation, which he expands upon in later chapters: the placebo effect. And in fact, this pattern is a typical feature of neural habituation that could accompany the placebo effect.

This is not to say that Scott dismisses all such miracle cures as just the placebo effect. He devotes three chapters to discussing the effects of stress on illness, belief on healing, and the social world on both. These provide an excellent summary of the modern body of work that in recent years has elucidated not only that the mind and emotions have a very powerful effect on health and illness but also how this effect occurs.

Taken together, the structure Scott provides—outlining exactly how medieval pilgrims left oppressing situations and were then exposed during their journey to social support, clean water, and fresh, healthy food—makes a strong case for the effectiveness of the simple act of going on a pilgrimage as a healthy endeavor, which could have begun the course of healing. The added power of belief in healing, through the placebo effect and the many nerve chemicals and brain hormones released in such states, almost ensures that people who engaged in such activities would feel much better, if not be cured from illnesses that would today be considered "self-limiting" under the right circumstances.

Continuing to draw the faithful. Pilgrims attending a mass at Lourdes, France.

CREDIT: LIONEL BONAVENTURE/AFP/GETTY IMAGES

Implicitly, *Miracle Cures* suggests that a parallel situation might be propelling some of the resurgence of modern-day seeking of spiritual solutions for physical ills. Although the physical conditions fostering illness in the developed world today are a far cry from those in medieval times, we are certainly exposed to a vast array of emotional stresses, which may trigger or worsen many illnesses. The power of belief and the lifestyle and social changes that go along with it may indeed assist many in their search for healing.

10.1126/science.1191479

The reviewer is the author of *Healing Spaces: The Science of Place and Well-Being*. Web site: www.esthersternberg.com

ECOLOGY

Asking Why Who Is Where

Devorah Bennu

Komodo dragon (*Varanus komodoensis*).

Why are there no dragons in Europe? Why are frogs so rarely found on oceanic islands? Well, the answers are complicated. But we can understand this complexity through theories of biogeography. Whereas physicists are still searching for the grand unified theory that will tie general relativity to quantum mechanics, biologists already have an overarching theory for the history of life on Earth. Biogeography explains the relationships between the theory of evolution and the planet on which known life evolved. In *Here Be Dragons*, Dennis McCarthy (Buffalo Museum of Science) explains how these observations all fit together: how movements of the continental plates, oceanic currents, and global climate patterns profoundly affect the evolution and geographic distribution of plant and animal species through both time and space.

As McCarthy recounts the history and development of the discipline that came to be known as biogeography, the reader catches a glimpse of how a scientific field develops. McCarthy describes some of the mysteries that inspired early workers in the field: There were the puzzling distribution patterns of many animal and plant fossils. For example, remains of the Permian freshwater reptile *Mesosaurus* (one of the first reptiles to return to the water) are only found on the southernmost portions of South America and Africa. There was the question of why isolated land masses, such as South America, Australia, and New Zealand, are modern-day sanctuaries for "living fossils" (extant taxa that appear to have changed little over many millions of years and closely resemble their ancient relatives). In the narrative of his famous voyage, Charles Darwin mused at length about the curious relationship between geographic location and the sorts of animals he found; he speculated, for example, about why the organisms of the Galápagos Islands were exclusively "created on American types of organisation" (*1*).

Naturalist Alfred Russel Wallace provided some answers. In a paper that can be seen as "the beginning of modern biogeography," he noted that "[e]very species has come into existence coincident both in space and time with a pre-existing closely allied species" (*2*). Later, he described the distributional divide between Asian and Australian species that runs through the straits separating the South Pacific islands of Borneo and Sulawesi—the striking biotic barrier now known as Wallace's Line. Geographer Alfred Wegener provided additional clues when, in the early 20th century, he recognized that the world's continents neatly fit together, almost like jigsaw pieces, forming a supercontinent—an observation that formed one basis for plate tectonics. When viewed against the backdrop of mobile continents, many peculiar biological distribution patterns could be explained.

Here Be Dragons
How the Study of Animal and Plant Distributions Revolutionized Our Views of Life and Earth
by Dennis McCarthy
Oxford University Press, Oxford, 2009. 242 pp. $29.95, £16.99. ISBN 9780199542468.

Recently, our understanding of the world has been deepened through studies of genetic variation among species, in addition to their physical and geographic discrepancies: a new discipline known as phylogeography. Forming a fascinating feedback loop, molecular systematics provides greater insight into the intricate reciprocal interactions between evolutionary and geological history. For example, DNA analyses revealed that the two genera of Galápagos iguanas (marine and land) are roughly 10 to 20 million years old, while their island homes are only 3 to 4 million years old. The explanation for this discrepancy is that the Galápagos, like many oceanic archipelagos, are perched over a rupture in Earth's crust through which basaltic lavas flow onto the sea floor. These eruptions create seamounts that sometimes grow so large that they eventually emerge from the waters as volcanic islands. The islands will eventually be carried off the underlying rupture and disappear into a watery grave. But before they do, they are colonized by insects, birds, and adventurous plants that will evolve and adapt to fit the demands of their new home. And a younger seamount may pop above the sea nearby and thus provide a still newer home to offspring of these island-hopping species. Once again, biogeographic theory explains the patterns.

Not all islands, however, are volcanic mountaintops rising from the sea, covered with youthful, rapidly evolving species. Some, like New Zealand, are remote continental fragments that are haunted by ancient Gondwanan passengers, such as the reptilian tuataras (whose sphenodontian cousins died alongside the dinosaurs) and primitive *Leiopelma* frogs (whose closest relatives lived during the Jurassic). Yet other islands are found in the depths of the oceans, where perpetual darkness and crushing pressure isolate deep-sea creatures such as hydrothermal vent tubeworms, much as bodies of water or mountain ranges can isolate terrestrial animals.

After investigating how geography and evolution go hand in hand for animals and plants, McCarthy turns his curious eye toward humans. His penultimate chapter (the longest in the book) offers an overview of how we evolved, why we managed to colonize the entire planet, and how geography influenced our skin color and the development of our myriad idiosyncrasies in language and culture.

Throughout, the author supports his arguments with maps and family trees, although readers with a more academic interest in the topics he discusses will find his reference list of primary literature frustratingly short. McCarthy writes engagingly and generally with an admirable clarity. *Here Be Dragons* offers an entertaining airplane read. It provides a quick but enthusiastic summary of the fascinating field of biogeography, and it leaves us wanting more. The book delivers on its promise that we will never look at the world in the same way again.

The reviewer writes the blog Living the Scientific Life (Scientist, Interrupted). Web site: http://scienceblogs.com/grrlscientist

References and Notes

1. C. Darwin, *Journal and Remarks*, vol. 3 of *The Narrative of the Voyages of H. M. Ships* Adventure *and* Beagle (Henry Colburn, London, 1839); now known as *Voyage of the Beagle*.
2. A. R. Wallace, *Ann. Mag. Nat. Hist*. **16** (2nd ser.), 184 (September 1855); www.victorianweb.org/science/science_texts/wallace_law.html.

10.1126/science.1189901

Published by AAAS

AGRICULTURE

Increased Food and Ecosystem Security via Perennial Grains

Perennial grains hold promise, especially for marginal landscapes or with limited resources where annual versions struggle.

J. D. Glover,[1]* J. P. Reganold,[2] L. W. Bell,[3] J. Borevitz,[4] E. C. Brummer,[5] E. S. Buckler,[6] C. M. Cox,[1] T. S. Cox,[1] T. E. Crews,[7] S. W. Culman,[8] L. R. DeHaan,[1] D. Eriksson,[9] B. S. Gill,[10] J. Holland,[11] F. Hu,[12] B. S. Hulke,[13] A. M. H. Ibrahim,[14] W. Jackson,[1] S. S. Jones,[15] S. C. Murray,[14] A. H. Paterson,[16] E. Ploschuk,[17] E. J. Sacks,[18] S. Snapp,[8] D. Tao,[12] D. L. Van Tassel,[1] L. J. Wade,[19] D. L. Wyse,[20] Y. Xu[21]

Despite doubling of yields of major grain crops since the 1950s, more than one in seven people suffer from malnutrition (*1*). Global population is growing; demand for food, especially meat, is increasing; much land most suitable for annual crops is already in use; and production of nonfood goods (e.g., biofuels) increasingly competes with food production for land (*2*). The best lands have soils at low or moderate risk of degradation under annual grain production but make up only 12.6% of global land area (16.5 million km^2) (*3*). Supporting more than 50% of world population is another 43.7 million km^2 of marginal lands (33.5% of global land area), at high risk of degradation under annual grain production but otherwise capable of producing crops (*3*). Global food security depends on annual grains—cereals, oilseeds, and legumes—planted on almost 70% of croplands, which combined supply a similar portion of human calories (*4*, *5*). Annual grain production, though, often compromises essential ecosystem services, pushing some beyond sustainable boundaries (*5*). To ensure food and ecosystem security, farmers need more options to produce grains under different, generally less favorable circumstances than those under which increases in food security were achieved this past century. Development of perennial versions of important grain crops could expand options.

As highlighted in discussions of biofuel production, perennial crops generally have advantages over annuals in maintaining important ecosystem functions, particularly on marginal landscapes or where resources are limited (*6*) (fig. S1). Perennial grain crops would have similar advantages and also produce food. Compared with annual counterparts, perennial crops tend to have longer growing seasons and deeper rooting depths, and they intercept, retain, and utilize more precipitation (*6*–*10*). Longer photosynthetic seasons resulting from earlier canopy development and longer green leaf duration increase seasonal light interception efficiencies, an important factor in plant productivity (*7*). Greater root mass reduces erosion risks and maintains more soil carbon compared with annual crops (*9*). Annual grain crops can lose five times as much water and 35 times as much nitrate as perennial crops (*10*). Perennial crops require fewer passes of farm equipment and less fertilizer and herbicide (*9*), important attributes in regions most needing agricultural advancement.

Obstacles and Opportunities

Past efforts to develop perennial grain crops were limited by technologies and resources of the time. Efforts in the former Soviet Union and the United States to develop perennial wheat in the 1960s were abandoned in part because of plant sterility and undesirable agronomic characteristics (*11*). More recently, programs have been initiated in Argentina, Australia, China, India, Sweden, and the United States to identify and improve, for use as grain crops, perennial species and hybrid plant populations derived from annual and perennial parents: rice, wheat (see the figure on page 1639), maize, sorghum, pigeon peas, and oilseed crops from the sunflower, flax, and mustard families (*11*–*16*). Additional plant taxa have potential to be developed as perennial grains (*11*).

Plants may face physiological trade-offs between seed productivity and longevity; resources otherwise allocatable to seeds may instead be needed belowground to maintain perenniality. However, this would not necessarily prevent perennial grain crops from being high-yielding and economically viable, for at least two reasons.

First, crops are grown for unique characteristics, of which high potential yield is but one. For example, despite lower yield potential, wheat is grown on more cropland than maize, in part because it can be grown in some environments for which maize is not well suited. Similarly, lower-yield perennial crops could be options where higher-yield annuals cannot reliably achieve full yields. In semiarid regions of sub-Saharan Africa, annual crops often use less than 30% of rainfall owing to high rates of water draining below root zones, evaporation, and runoff, which partly explains the meager 1 metric ton/ha yields of annual grains common in such regions (*8*). Perennial crops can reduce surface and subsurface water losses (*8*, *10*) and be grown on highly erodible sites (fig. S1). For example, perennial types of pigeon peas, important food crops and sources of biologically fixed nitrogen, are grown on steep slopes in regions of Malawi, China, and India (*16*).

Second, because they intercept sunlight over long periods of the year and their roots take up deep-soil water and nutrients, many perennials can sustain greater aboveground production per unit land area than our most widely grown annual crops on fertile land-

[1]The Land Institute, Salina, KS 67401, USA. [2]Department of Crop and Soil Sciences, Washington State University, Pullman, WA 99164, USA. [3]Sustainable Ecosystems–Agricultural Production Systems Research Unit, Commonwealth Scientific and Industrial Research Organization (Australia), Toowoomba, Queensland 4350, Australia. [4]Department of Evolution and Ecology, University of Chicago, Chicago, IL 60637, USA. [5]Institute of Plant Breeding, Genetics, and Genomics, University of Georgia, Athens, GA 30602, USA. [6]U.S. Department of Agriculture–Agricultural Research Service (USDA-ARS) and Institute for Genomic Diversity, Cornell University, Ithaca, NY 14853, USA. [7]Environmental Studies, Prescott College, Prescott, AZ 86301, USA. [8]Kellogg Biological Station, Michigan State University, Hickory Corners, MI 49060, USA. [9]Department of Plant Breeding and Biotechnology, Swedish University of Agricultural Sciences, Alnarp, Sweden. [10]Wheat Genetic and Genomic Resources Center, Kansas State University, Manhattan, KS 66506, USA. [11]USDA-ARS Plant Science Research Unit, North Carolina State University, Raleigh, NC 27695, USA. [12]Food Crops Research Institute, Yunnan Academy of Agricultural Sciences, Kunming 650205, China. [13]USDA-ARS Sunflower Research Unit, Northern Crop Science Laboratory, Fargo, ND 58105, USA. [14]Department of Soil and Crop Sciences, Texas A&M University, College Station, TX 77843, USA. [15]Department of Crop and Soil Sciences, Washington State University, Mount Vernon, WA 98273, USA. [16]Plant Genome Mapping Laboratory, University of Georgia, Athens, GA 30602, USA. [17]Cátedra de Cultivos Industriales, Facultad de Agronomía, Universidad de Buenos Aires, C1417DSE Buenos Aires, Argentina. [18]Department of Crop Sciences, University of Illinois, Urbana, IL 61801, USA. [19]Charles Sturt University, E. H. Graham Centre for Agricultural Innovation, Wagga Wagga, New South Wales 2678, Australia. [20]Department of Agronomy and Plant Genetics, University of Minnesota, St. Paul, MN 55108, USA. [21]Global Maize Program, International Maize and Wheat Improvement Center, Apartado 0660, Mexico DF, Mexico.

*Author for correspondence. E-mail: glover@landinstitute.org

Published by AAAS

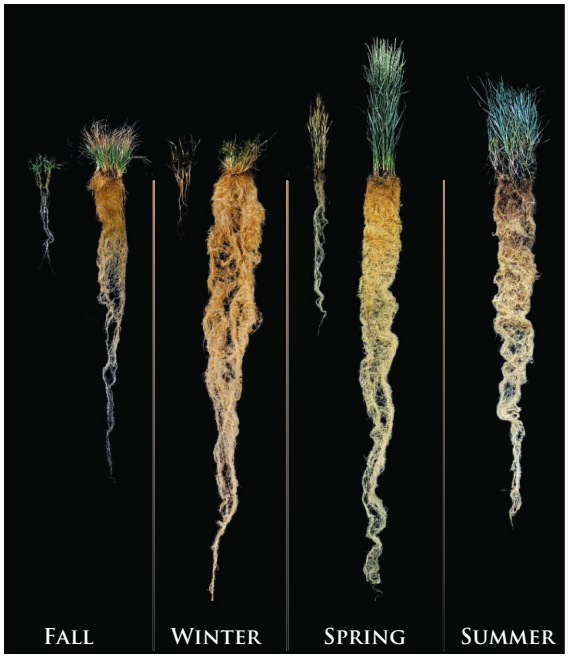

Annual wheat versus perennial intermediate wheatgrass. Seasonal development of annual winter wheat (left of each panel) and its wild perennial relative, intermediate wheatgrass (right of each panel). Plant breeding programs are working to domesticate intermediate wheatgrass (*Thinopyrum intermedium*) and to develop perennial wheat by crossing it with wheat (*11*, *13*).

scapes (*7*, *9*). For example, with no fertilizer inputs and without the benefits of centuries of domestication, the perennial grass *Miscanthus* has 61% greater annual solar radiation interception efficiency by the plant canopy and can produce 59% more aboveground biomass than heavily fertilized, highly domesticated annual maize (*7*, *17*). Regrowth of perennial crop stems and leaves after seed harvest may allow for additional harvests of biomass for livestock feed or biofuels (*13*).

Plant breeding programs must combine multiple desirable traits in perennial grain crops, including (i) reliable regrowth and high grain yield and quality over multiple years; (ii) adaptation to abiotic stresses, such as water and nutrient deficiencies; and (iii) resistance to pests and diseases. Management practices, such as use of fertilizers to minimize nutrient deficiencies, can decrease some pressures. Perennial grain crops could expand opportunities to rotate perennial and annual crops or to grow multiple crops together (*16*), important strategies in reducing pests and diseases. For some traits, perennial crops have advantages over annual counterparts. Wild perennials are often used as sources of disease resistance in annual crop breeding. Offspring from crosses between annual wheat and its perennial relatives are often resistant to diseases to which annual wheat is susceptible (*18*).

Use of molecular markers associated with desirable traits can accelerate breeding programs by allowing plant breeders to characterize and exploit plant genetic variation more effectively (*19*). The ability to determine genotypes of large numbers of plants, covering the entire genome rapidly and inexpensively, can facilitate the combining of desirable genes without the need for field evaluation over many years and in every selection cycle. Naturally occurring genes that permit exchange of DNA between chromosomes of different species or genera can be used to obtain offspring with desirable traits from both parents (*20*). Plant breeders can use genetic modification to introduce new genes, to modify existing genes, or to interfere with gene expression in specific cases. Classically trained plant breeders and agronomists will be needed to fully realize opportunities offered by these innovations.

Additional Needs

Plant breeding innovations can accelerate development of perennial grains. Greater progress, though, requires (i) the initiation and acceleration of breeding programs around the world, with more personnel, land, and technological capacity; (ii) expansion of ecological and agronomic research of improved perennial germplasm; (iii) coordination of global activities through germplasm and scientific exchanges; (iv) prioritization of global regions for introduction of perennial grains; and (v) training of scientists and students in the breeding, ecology, and management of perennial crops.

Perennial grain crops could help meet a wide array of domestic and international challenges (e.g., food security, climate change, and energy supply) (*21*) addressed by U.S. federal agencies, including the Departments of Agriculture and Energy and the Agency for International Development. State agricultural institutions, agencies, and commissions could support perennial grain breeding programs to meet regional needs. International organizations and national governments can assist plant breeding programs in regions of the world most in need of agricultural advancement. The International Rice Research Institute, for example, initiated perennial rice research (*12*) that was subsequently transferred to scientists in China with funding from China's National Natural Science Foundation. As happened during the Green Revolution, private philanthropies can play key roles in supporting transformative plant breeding programs.

Large investments have been committed to developing technologies for biofuel conversion of perennial crops because of their ecological advantages over annual sources, despite their potential to displace food crops. With similar commitments for developing food-producing perennial grains, we estimate that commercially viable perennial grain crops could be available within 20 years.

References and Notes

1. Food and Agricultural Organization of the United Nations (FAO), *The State of Food Insecurity in the World 2009* (Progress Report, FAO, Rome 2009).
2. H. C. J. Godfray *et al.*, *Science* **327**, 812 (2010).
3. H. Eswaran, F. Beinroth, P. Reich, *Am. J. Altern. Agric.* **14**, 129 (1999).
4. C. Monfreda, N. Ramankutty, J. A. Foley, *Global Biogeochem. Cycles* **22**, GB1022 (2008).
5. S. L. Pimm, *The World According to Pimm* (McGraw-Hill, New York, 2001).
6. D. Tilman *et al.*, *Science* **325**, 270 (2009).
7. F. G. Dohleman, S. P. Long, *Plant Physiol.* **150**, 2104 (2009).
8. J. S. Wallace, *Agric. Ecosyst. Environ.* **82**, 105 (2000).
9. J. D. Glover *et al.*, *Agric. Ecosyst. Environ.* **137**, 3 (2010).
10. G. W. Randall *et al.*, *J. Environ. Qual.* **26**, 1240 (1997).
11. T. S. Cox, J. D. Glover, D. L. Van Tassel, C. M. Cox, L. R. DeHaan, *Bioscience* **56**, 649 (2006).
12. E. J. Sacks, J. P. Roxas, M. T. Sta Cruz, *Crop Sci.* **43**, 120 (2003).
13. L. W. Bell, F. Byrne (nee Flugge), M. A. Ewing, L. J. Wade, *Agric. Syst.* **96**, 166 (2008).
14. E. L. Ploschuk, G. A. Slafer, D. A. Ravetta, *Ann. Bot.* (London) **96**, 127 (2005).
15. D. Eriksson, thesis, Swedish University of Agricultural Sciences, Alnarp, Sweden (2009).
16. S. S. Snapp, R. B. Jones, E. M. Minja, J. Rusike, S. N. Silim, *HortScience* **38**, 1 (2003).
17. Although comparisons of yields and environmental benefits of fully developed perennial grain crops with those of annual grain crops receiving similar inputs would be ideal, breeders must first develop perennial grains. In the meantime, studies illustrating environmental benefits and productivity of perennial crops currently in use (albeit not for grain production) provide useful information on the potential of future perennial grain crops.
18. C. M. Cox, K. A. Garrett, T. S. Cox, W. W. Bockus, T. Peters, *Plant Dis.* **89**, 1235 (2005).
19. Y. Xu, J. H. Crouch, *Crop Sci.* **48**, 391 (2008).
20. L. Qi, B. Friebe, P. Zhang, B. S. Gill, *Chromosome Res.* **15**, 3 (2007).
21. J. D. Glover, C. M. Cox, J. P. Reganold, *Sci. Am.* **297**, 82 (2007).
22. This work is primarily based on discussions at the Sackler Forum, London, UK (December 2009); International Perennial Grain Breeding Workshop, Kunming, China (September 2009); International Maize and Wheat Improvement Center, Mexico City, Mexico (September 2009); and The Land Institute's Graduate Fellowship Workshop, Salina, Kansas, USA (June 2008). L. R. Klein and L. Young made helpful comments on an earlier draft. Funding from Texas Corn Producers Board (S.C.M.) and Cooperative Research Centre for Future Farm Industries, Australia (L.J.W.).

Supporting Online Material

www.sciencemag.org/cgi/content/full/328/5986/1638/DC1

10.1126/science.1188761

ECOLOGY

Time to Tap Africa's Livestock Genomes

We need to better understand and exploit the genetic diversity of Africa's indigenous livestock breeds—before they fade away.

Olivier Hanotte,[1] Tadelle Dessie,[2] Steve Kemp[3]

If you travel across rural Africa looking for livestock such as cows, pigs, and goats, rather than scenic or wildlife wonders, you will be struck by the extraordinary diversity of its indigenous breeds (*1*). But the visual wonders of coat color or horn shape are only the tip of the iceberg. Looking deeper, a world of Darwinian adaptations—from the ability to tolerate parasites to robust milk production—waits to be discovered, understood, and used. The scientific community has largely ignored these adaptations. Now, however, we have the opportunity, by combining genomic and geo-environmental data, to unravel African livestock adaptations and to use this information to aid sustainable breeding improvements and development. But we must act soon: The genetic diversity of Africa's indigenous livestock is now threatened by a range of economic and demographic forces.

Tailor-made. Acting now to characterize and exploit the unique genomes and adaptations of Africa's livestock, such as the Maasai Zebu cattle (above), could help breed new genotypes tailored to changing local environments.

Genetic studies are revealing the origins of today's African livestock. It is a complex history that includes human-driven migration, dispersion, crossbreeding, and trading (*2*). Africa's proximity to the major livestock domestication centers in the Near East, as well as oceanic currents and weather patterns linking the East African coast to South and Southeast Asia, have offered multiple opportunities for livestock introductions. Human migrations, such as the spread of Bantu-speaking people from their stronghold in western and Central Africa to the southern part of the continent, and the Islamization of eastern and northern Africa, further favored dispersion of livestock. Last but not least, European influences added a layer of livestock genetic diversity from the north.

Throughout its history, this diversity has been shaped by subtle combinations of human and natural selection. In contrast to modern European breeds, which have been selected for productivity, in Africa selection has been driven primarily by sociocultural concerns and the need for livestock to survive in heterogeneous environments. Livestock are closely intertwined with African societies, providing nutrition, transport, and labor. Researchers estimate that 70% of Africa's rural poor keep livestock and some 200 million people rely on these animals for their livelihoods. They play a central role in nearly all African agro-ecological production systems, showing how remarkably adapted they have become to local environments. To succeed, Africa's livestock breeds have also had to survive an extraordinary diversity and intensity of disease and climatic challenges.

The unique genetic make-up and adaptations of African livestock are now endangered. "Exotic" cattle breeds from the developed world, for instance, are displacing indigenous cattle across the African continent. This is due to pressure to increase short-term productivity, fueled by changing demography and rising demand for livestock products. The result is a livestock sector increasingly dependent on external inputs such as veterinary intervention and feed. This trend threatens to exclude a majority of rural farmers from livestock production and raises questions about long-term sustainability. Perhaps more seriously, it also drives an irreversible loss of the unique adaptations of indigenous livestock, reducing options for future productivity improvements that could benefit local farmers.

Fortunately, the fields of genetics and genomics (*3*–*5*) offer a new start for the sustainable improvement of African livestock productivity. Landscape genomics links genome-wide information to geo-environmental resource analysis to identify potentially valuable genetic material. Typically, researchers will perform a genome-wide scan on a number of animals from populations living in different habitats or across an ecological cline (from dry to wet areas, for instance). Regions where livestock face selection pressure from environmental conditions, such as drought, are expected to show higher genomic divergence across habitats compared to the "neutral" genome background. The assumption is that an animal genotype living in a specific habitat will show signatures of selection in its genome for "habitat traits" under natural selection; the added effect of human selection will point to genome regions linked to productivity traits. The approach has been successfully applied to characterizing the genomes of northeast Mediterranean goat breeds (*6*).

Selection based on genome-wide analyses is transforming livestock breeding in the developed world. It tackles breeding improvement by aiming to capture all the genetic variation at a trait and then using the information to assess the breeding value of an animal. It progresses in two steps: Investigators estimate the effect of all markers in a set of "reference" animals that are both phenotyped and genotyped; then, they use the genomic information obtained from the reference animals to estimate the breeding value of animals that are not phenotyped (*7*). Breeders are applying the technology to dairy cattle in at least four improvement pro-

[1]School of Biology, University of Nottingham, Nottingham NG7 2RD, UK. [2]International Livestock Research Institute (ILRI), Post Office Box 5689, Addis Ababa, Ethiopia. [3]University of Liverpool, School of Biological Sciences, Biosciences Building, Liverpool L69 7ZB, UK and ILRI, Post Office Box 30709, Nairobi, Kenya. E-mail: olivier.hanotte@nottingham.ac.uk

Published by AAAS

grams (*8*), and beef and poultry breeders are exploring applications in their sectors.

Although many challenges remain, combining the two approaches offers the opportunity to tailor individual indigenous African livestock genotypes both to present needs and to future environmental conditions. We need to encourage multidisciplinary livestock research and support the development of genome sequencing projects of different African livestock species, populations, and environments. In parallel, there is an urgent need to begin phenotypic characterization of indigenous livestock population in situ over a large geographic scale.

These tasks will require substantial new funding for Africa's livestock sector at the national and international levels. It will also require a shift in our thinking. We need to make greater use of the exquisitely well-adapted livestock already living in Africa—rather than relying on the blunt instrument of importing ill-adapted exotic breeds.

References

1. *DAGRIS 2007. Domestic Animal Genetic Resources Information System* (*DAGRIS*), S. Kemp, Y. Mamo, B. Asrat, T. Dessie, Eds. (International Livestock Research Institute, Addis Ababa, Ethiopia), http://dagris.ilri.cgiar.org.
2. U.N. Food and Agriculture Organization (FAO), www.fao.org/docrep/010/a1250e/a1250e00/htm (2007).
3. S. Manel, M. K. Schwartz, G. Luikart, P. Taberlet, *Trends Ecol. Evol.* **18**, 189 (2003).
4. S. Joost *et al*., *Mol. Ecol.* **16**, 3955 (2007).
5. T. H. Meuwissen, B. J. Hayes, M. E. Goddard, *Genetics* **157**, 1819 (2001).
6. L. Pariset, S. Joost, P. Ajmone-Marsan, A. Valentini, *BMC Genet.* **10**, 7 (2009).
7. T. H. Meuwissen, *Genet. Sel. Evol.* **41**, 35 (2009).
8. B. J. Hayes, P. J. Bowman, A. J. Chamberlain, M. E. Goddard, *J. Dairy Sci.* **92**, 433 (2009).

10.1126/science.1186254

MEDICINE

Tackling Two Diseases with HDL

A lipoprotein that transports cholesterol to the liver also controls the proliferation of myeloid stem cells.

Göran K. Hansson and Magnus Björkholm

High-density lipoproteins (HDLs) transport cholesterol from peripheral tissues to the liver, helping to protect against diseases such as atherosclerosis. On page 1689 in this issue, Yvan-Charvet *et al*. present an entirely new role for HDL in regulating stem cell proliferation in the bone marrow (*1*). A relationship between cellular cholesterol content, HDL, and cells of the myelomonocytic lineage opens up the possibility that disorders characterized by the proliferation of immature white blood cells could be treated by targeting cholesterol transport in these cells.

The human pluripotent hematopoietic stem cell in bone marrow can give rise to lymphocytes, erythrocytes, granulocytes, monocytes, and platelets. Proliferative capacity is maintained during differentiation, although the end products released into the blood no longer divide. In one of the lineages, hematopoietic stem cells differentiate into granulocyte-monocyte progenitors, which become neutrophils or monocytes in a process driven by growth factors.

Many cell surface receptors assemble in membrane "rafts" that contain a high content of cholesterol and glycolipids. These rafts enhance receptor oligomerization and signaling in many cell types (*2*). In hematopoietic progenitor stem cells, growth factor receptors are organized in lipid rafts to promote receptor signaling and consequently, cell proliferation and migration (*3*). Because cholesterol overload can cause havoc in cells, its concentration is regulated by several mechanisms. Excess cholesterol is removed by ATP binding cassette (ABC) transporters in the plasma membrane, which move cholesterol to extracellular HDL particles at the cell surface (*4*) (see the figure).

Yvan-Charvet *et al*. analyzed mice lacking two ABC cassette transporter genes *Abca1* and *Abcg1* (*Abca1*$^{-/-}$ *Abcg1*$^{-/-}$ mice). These animals displayed an increase in the number of neutrophils and monocytes in the blood (leukocytosis) and an increase in hematopoietic stem cells, common myeloid progenitor cells, and granulocyte-monocyte progenitor cells in the bone marrow. These expansions were due to increased cell proliferation resulting from increased responsiveness to the hematopoietic growth factors interleukin-3 (IL-3) and granulocyte-macrophage colony-stimulating factor (GM-CSF).

ABC cassette transporters as well as lipoprotein receptors are highly expressed in

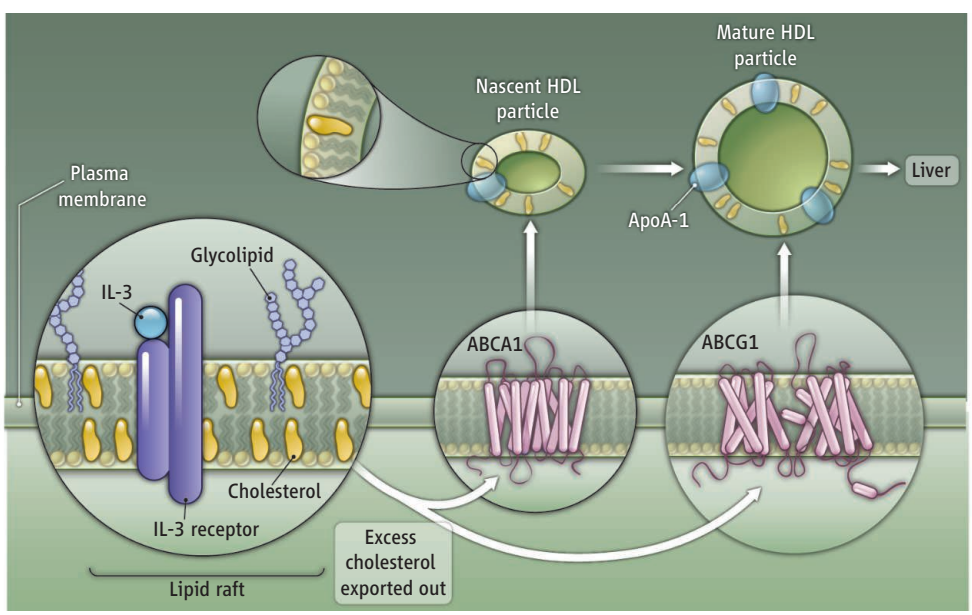

CREDIT: Y. GREENMAN/*SCIENCE*

HDL and cell proliferation. In mammalian cells, cholesterol, glycolipids, and proteins (such as growth factor receptors) are organized in lipid rafts in the plasma membrane. ABCA1 transports excess cholesterol from membranes to nascent HDL particles, and ABCG1 transports cholesterol to mature HDL particles. HDL particles are then taken up by the liver. When cholesterol is removed from a hematopoietic (myeloid) stem cell in this way, membrane rafts disassemble, receptor signaling (such as through the IL-3 receptor) is hampered, and receptor-dependent outcomes such as cell proliferation are reduced.

Center for Molecular Medicine and Department of Medicine, Karolinska Institutet, SE-17176 Stockholm, Sweden. E-mail: goran.hansson@ki.se

hematopoietic cells (*5*, *6*) and indeed, cells lacking *Abca1* and *Abcg1* had an increase in lipid rafts due to accumulated cholesterol. Addition of HDL to cells lacking these ABC transporters reversed the increase in lipid rafts when cholesterol was mobilized (perhaps by alternative efflux mechanisms that are not yet fully understood) from cell membranes to HDL particles.

Patients with myeloproliferative diseases display an expansion of myeloid precursor cells and enlarged spleens and livers due to infiltration of myeloid cells. Yvan-Charvet *et al*. observed this phenotype in the $Abca1^{-/-}$ $Abcg1^{-/-}$ mice and in wild-type mice whose bone marrow was replaced with that transplanted from $Abca1^{-/-}$ $Abcg1^{-/-}$ mice. To determine if this condition could be reversed if cholesterol efflux was promoted, Yvan-Charvet *et al*. transplanted bone marrow from $Abca1^{-/-}$ $Abcg1^{-/-}$ mice into recipients that were engineered to produce high amounts of the HDL protein apolipoprotein A-1 (apoA-1). The myeloproliferative disorder was not observed, suggesting that cholesterol efflux through ABC transporters to HDL controls myeloid cell proliferation.

These experiments point to a cholesterol dependent mechanism for controlling receptor function. As hematopoietic growth factor receptors in stem cells organize in membrane rafts, the availability of cholesterol for raft formation modulates receptor function. Membrane cholesterol can come either from lipoprotein uptake or local synthesis in the cell and is balanced by elimination of cholesterol from the cell. This balance depends on ABCA1 and ABCG1 transporters that mobilize cholesterol from the membrane, and on HDL particles that act as cholesterol acceptors. Lack of ABCA1 and ABCG1 results in increased raft formation, whereas addition of HDL reduces rafts. Increased raft formation helps to cluster receptors for IL-3 and GM-CSF, leading to increased responsiveness to these hematopoietic growth factors and to increased proliferation of myeloid precursor cells.

Myeloproliferative neoplasms are potentially life-threatening conditions that include chronic myeloid leukemia, primary myelofibrosis, polycythemia vera (excess blood cells), and essential thrombocythemia (excess platelets). Myeloid precursor proliferation is usually increased in these conditions. Although imatinib and second-generation tyrosine kinase inhibitors, directed against the oncogenic BCR-ABL fusion protein, have revolutionized the treatment for patients with chronic myeloid leukemia, additional therapeutic approaches are needed in myeloproliferative neoplasms. Modulation of cellular cholesterol content by increasing HDL concentration could be an attractive strategy.

In atherosclerosis, leukocytosis is observed (*7*), but the reason has been unclear. The results of Yvan-Charvet *et al*. suggest that individuals with hypercholesterolemia may develop leukocytosis because of increased proliferation of myeloid progenitors in the bone marrow. Again, the cholesterol efflux pathway could be an interesting target for therapy.

References

1. L. Yvan-Charvet *et al*., *Science* **328**, 1689 (2010); published online 20 May 2010 (10.1126/science.1189731).
2. D. Lingwood, K. Simons, *Science* **327**, 46 (2010).
3. B. Giebel *et al*., *Blood* **104**, 2332 (2004).
4. A. R. Tall, *J. Intern. Med.* **263**, 256 (2008).
5. S. Vitols *et al*., *Lancet* **326**, 1150 (1985).
6. S. D. Peeters *et al*., *Exp. Hematol.* **34**, 622 (2006).
7. D. L. Feldman *et al*., *Arterioscler. Thromb.* **11**, 985 (1991).

10.1126/science.1191663

CLIMATE CHANGE

Dry Times Ahead

The climate of the western United States could become much drier over the course of this century.

Jonathan Overpeck[1] and Bradley Udall[2]

In the past decade, it has become impossible to overlook the signs of climate change in western North America. They include soaring temperatures, declining late-season snowpack, northward-shifted winter storm tracks, increasing precipitation intensity, the worst drought since measurements began, steep declines in Colorado River reservoir storage, widespread vegetation mortality, and sharp increases in the frequency of large wildfires. These shifts have taken place across a region that also saw the nation's highest population growth during the same period.

The climate changes in western North America, particularly the Southwest, have outstripped change elsewhere on the continent, save perhaps in the Arctic. In the past decade, many locations, notably in the headwaters region of the Colorado River, have been more than 1°C warmer than the 20th-century average. This warming has been the primary driver in reducing late-season snowpack and the annual flow of the Colorado River (*1*, *2*). These reductions, coupled with the most severe drought observed since 1900, have caused the biggest regional water reservoirs—Lake Powell and Lake Mead—to decline from nearly full in 1999 to about 50% full in 2004; there has been no substantial recovery since. All of these changes, as well as dramatic warming and drying elsewhere in the region and deep into Mexico, are consistent with projected anthropogenic climate change, but seem to be occurring faster than projected by the most recent national (*2*) and international (*3*) climate change assessments; this could indicate that substantially more severe warming and drying lies ahead.

The land surface of the West is also changing at a rate that is unprecedented since systematic monitoring began in the 20th century. Background tree mortality rates in western U.S. forests have increased rapidly in recent decades (*4*), and more than a million hectares of piñon pine mortality in the Southwest has been linked to a combination of record warm temperatures and drought not seen previously in the past 100 years (*5*). Moreover, the background forest mortality across western North America is accelerating, most likely as a result of climate change (*4*). Even the low-altitude Southwestern deserts are showing signs of widespread drought-induced plant mortality (*6*). A clear link with record regional warming again implicates global warming in driving what has been termed "global-change-type drought" (*5*) and unprecedented vegetation impacts. Similarly, the exceptional warming and associated snowpack declines have led to an accelerating increase in the frequency of large wildfires (*7*).

The warming and snowpack reductions can be confidently attributed to anthropogenic global warming (*1*–*3*), but the cause of the recent and ongoing drought is harder to nail down. Drought is not unusual in western North America, and much worse droughts occurred prior to the 20th century (*8*, *9*). The cause of the current drought could be natural,

[1]Climate Assessment of the Southwest, University of Arizona, 845 N. Park Avenue, Suite 532, Tucson, AZ 85721, USA. [2]Western Water Assessment, University of Colorado, 325 Broadway R/PSD, Boulder, CO 80305, USA. E-mail: jto@email.arizona.edu; bradley.udall@colorado.edu

Signs of change. Recent drops in water levels in major reservoirs fed by the Colorado River, such as Lake Mead, may be a sign of things to come as climate change takes hold in western North America.

CREDIT: WIKIMEDIA COMMONS

with impacts exacerbated by the record warming (*9*). On the other hand, global warming theory and modeling has projected an increase in drought frequency (*3*).

It would be quite useful to scientists and decision-makers alike to know the extent to which the ongoing drying of the region is natural or anthropogenic. If we know the cause, it becomes much easier to assess what the future holds for western North America. According to climate models, global warming should lead to a continued progressive drying out of the region as it warms up and winter storm tracks shift north. Thus, it is both reassuring and troubling that observed recent climate change in the West matches these projections (*2*, *10*). Warming is bad enough, but when it is coupled to a continued reduction in winter snow and rainfall, the situation will only get worse (*3*, *11*).

Equally troubling is the observed high rate of recent climate change in western North America. This indicates that the West, like the Arctic, could be unusually sensitive to greenhouse gas emissions. However, the region's high rate of recent change could also be due to an unusual confluence of anthropogenic and natural processes that may or may not coincide into the future.

Either way, it is sobering to consider published projections of future Colorado River flow given continued anthropogenic climate change: All studies published thus far point to continued declines in the river's flow. Even assuming modest reductions in greenhouse gas emissions (i.e., assuming the Intergovernmental Panel on Climate Change's Special Report on Emission Scenarios' A1B scenario), the average annual flow of the Colorado could decrease by 20% by 2050 (*12*). At the same time, the risk of all Colorado reservoir storage (3 to 5 years' worth of water) drying up could increase to 3 chances in 10 (*13*). Such change would have profound implications for the southwestern cities (such as Los Angeles, San Diego, Phoenix, Salt Lake City, and Denver) and the agricultural production areas (for example, in southern California and Arizona) that depend on water from the Colorado River.

The above scenario does not take into account the possibility that projected anthropogenic change could coincide with a "megadrought." The tree-ring record shows that droughts lasting decades have routinely gripped western North America. The cause of these droughts lies in the oceans (*14*–*16*), but the origin of their unusual persistence remains enigmatic. As western North America currently endures its worst drought since 1900, it is important to realize that this drought might be nothing compared to what is possible in the future if megadrought and even hotter temperatures coincide.

What can be done in the face of an increasingly hot and arid western North America? Scientists and decision-makers in the West are already talking seriously about climate change adaptation strategies, particularly with respect to water resources and ecosystems management, and efforts to develop such strategies may be essential to the sustainability of the region. Both climate change and natural megadrought would likely force the West to adapt to less water and more widespread landscape transformation, so a "no-regrets" approach is to plan for such change. Improved climate science will enable better projections of future climate, and close partnerships with decision-makers throughout the region will enable the development of strategies to cope with the projected range of future climate change.

We know more about what might lie ahead for western North America than for many other regions in the world. This knowledge should ultimately translate into confidence in developing coping strategies. Moreover, western North America has vast potential for solar, wind, and geothermal renewable energy production. These resources could produce substantial regional economic benefits that will help offset the inevitable costs associated with adapting to, and slowing, climate change.

References and Notes

1. T. P. Barnett *et al.*, *Science* **319**, 1080 (2008).
2. T. R. Karl, J. M. Melillo, T. C. Peterson, Eds. *Global Climate Change Impacts in the United States* (Cambridge Univ. Press, New York, 2009).
3. *Climate Change 2007: The Physical Science Basis. Contribution of Working Group I to the Fourth Assessment Report of the Intergovernmental Panel on Climate Change*, S. Solomon *et al.*, Eds, Cambridge Univ. Press, Cambridge, 2007.
4. P. J. van Mantgem *et al.*, *Science* **323**, 521 (2009).
5. D. D. Breshears *et al.*, *Proc. Natl. Acad. Sci. U.S.A.* **102**, 15144 (2005).
6. J. R. McAuliffe, E. P. Hamerlynck, *J. Arid Environ.* **74**, 885 (2010).
7. A. L. Westerling *et al.*, *Science* **313**, 940 (2006).
8. C. Woodhouse, J. Overpeck, *Bull. Am. Meteorol. Soc.* **79**, 2693 (1998).
9. E. R. Cook *et al.*, *J. Quat. Sci.* **25**, 48 (2010).
10. S. A. McAfee, J. L. Russell, *Geophys. Res. Lett.* **35**, L17701 (2008).
11. R. Seager *et al.*, *Science* **316**, 1181 (2007).
12. Ray *et al.*, Colorado Water Conservation Board, 2008 (http://cwcb.state.co.us/Home/ClimateChange/ClimateChangeInColoradoReport).
13. B Rajagopalan *et al.*, *Water Resour. Res.* **45**, W08201 (2009).
14. N. E. Graham *et al.*, *Clim. Change* **83**, 241 (2007).
15. R. Seager *et al.*, *J. Clim.* **22**, 5021 (2009).
16. J. L. Conroy *et al.*, *Geophys. Res. Lett.* **36**, L17703 (2009).

17. NOAA supported this work through its Coping with Drought and Regional Integrated Sciences and Assessments Programs.

10.1126/science.1186591

Published by AAAS

BIOCHEMISTRY

Membrane Protein Gymnastics

A bacterial protein could flip its orientation in the membrane to attain its correct topology.

Christopher G. Tate

The high-resolution crystal structures of many membrane proteins (*1*) have provided a detailed understanding of the fold they adopt within the membrane. However, how a nascent polypeptide chain inserts into the membrane and folds to attain its final structure and orientation (topology) are an enigma. On page 1698 of this issue, Seppälä *et al*. (*2*) describe how a protein with up to five transmembrane domains could flip in the membrane, thus allowing a misinserted protein to attain its correct orientation (see the figure).

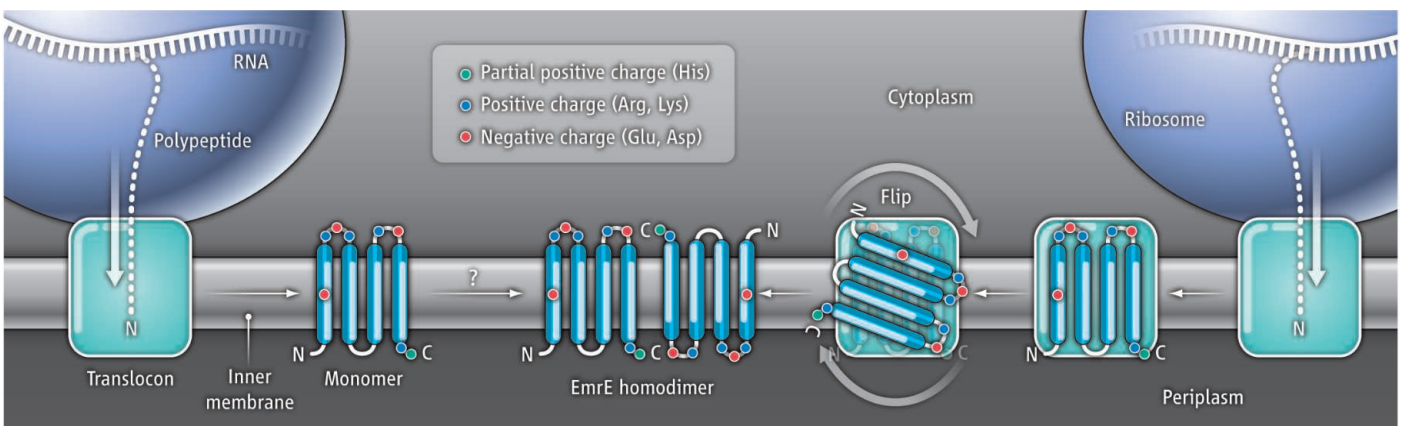

EmrE biosynthesis. The multidrug transporter EmrE is a homodimer consisting of two monomers with opposite topologies (**center**). During synthesis, the nascent polypeptide chain exits the ribosome and enters the translocon; once released into the membrane, EmrE probably cannot change its topology (**left**). However, EmrE could potentially flip in the membrane while associated with the translocon (**right**), perhaps either while the translocon is still associated with the ribosome or after dissociation. The topology of EmrE is determined predominantly by the positively charged residues.

The basic framework for membrane protein synthesis is known. The nascent polypeptide chain exits the ribosome and enters the translocon (*3*), a protein complex that provides a channel that allows the polypeptide to insert into the lipid bilayer. In the textbook model of a membrane protein, the portion inside the lipid bilayer is hydrophobic, and hydrophilic regions lie outside the membrane. Implicit within this paradigm is that a protein maintains its orientation once inserted into the membrane. This makes biochemical sense because this means that, for example, a hormone binding site on a receptor remains where it should be—on the outside of the cell. It is also what would be predicted from biophysics, because the energy required to tumble a protein in the membrane is prodigious; at some point in the process, all the hydrophilic parts of the protein surface would have to pass through the hydrophobic center of the membrane. It is also generally accepted that a major determinant of topology is the distribution of positively charged arginine and lysine amino acids within the loops between transmembrane regions (helices), although there are clearly additional factors involved (*4*). The hydrophilic face with the most positively charged residues is invariably cytoplasmic [the "positive inside" rule (*5*)]. By changing the distribution of positively charged residues by mutagenesis, it is possible to change the topology of a membrane protein. It is even possible to engineer a membrane protein that is topologically frustrated, adopting a mixture of the two possible orientations, because there is a similar distribution of positive charges between both hydrophilic faces of the membrane protein (*6*). There are also rare examples of membrane proteins that adopt this dual topology in vivo, including the bacterial protein EmrE (*7*).

EmrE is a multidrug transporter located in the inner membrane of *Escherichia coli*. It is functional as a dimer, with each monomer containing four transmembrane α helices. The monomers are thought to be arranged in an antiparallel orientation, with each monomer having opposite topology (*7*), although this is still debated (*8*). The distribution of positively charged residues in EmrE is similar between the two hydrophilic faces of the protein, as expected for a dual-topology protein. However, if the charge distribution is altered so that all the monomers have their N termini either intracellular (facing the cytoplasm) or extracellular (facing the periplasm), then the transport of substrates is substantially decreased. The expression of the topologically fixed mutant forms of EmrE with opposite orientations regains function (*9*). But does it matter where in the EmrE transporter the topological determinants are placed?

As a protein is inserted into the membrane N terminus first, then topological determinants should in theory be at the N terminus and would be expected to have little effect if placed at the C terminus. Seppälä *et al*. engineered a form of EmrE whose topology could be changed by adding a single arginine (Arg) or lysine (Lys) residue. The orientation of each mutant was then tested by coexpression with mutants of defined orientation that could not form active homodimers. Surprisingly, it did not matter whether the positively charged residue was inserted at the N or C terminus of EmrE, or even after an additional transmembrane α helix was engineered at the C terminus. Thus, it appears that if the first four transmembrane α helices are already synthesized and have taken up the wrong orientation in the membrane, then placing a single Arg or Lys residue at either terminus, or at the end of a fifth transmembrane α helix, corrected the topology to give a functional protein.

MRC Laboratory of Molecular Biology, Hills Road, Cambridge CB2 0QH, UK E-mail: cgt@mrc-lmb.cam.ac.uk

Published by AAAS

The inescapable conclusion is that a membrane protein containing four or five transmembrane helices, when associated with the translocon, remains in a topologically uncommitted state and can "flip" within the membrane to change its topology. There has been circumstantial evidence suggesting this for a number of membrane proteins for many years (*10*), but Seppälä *et al*. provide the first systematic analysis that suggests the phenomenon. But how can membrane protein flipping, when associated with the translocon, be reconciled with the energy required for tumbling within a membrane? Is it the privileged, protected environment within the translocon that permits such topological gymnastics? This would require a translocon pore size with a diameter of ~50 Å, which is consistent with biochemical data (*11*) but which is too large to be encompassed within a single translocon, thus implying the requirement for oligomers. However, the structure of a eukaryotic translocon (Sec61 complex) bound to a ribosome that is actively translocating a polypeptide chain supports the theory that it functions as a monomer (*12*), although higher oligomeric states could exist transiently during membrane protein biosynthesis. Structures of the ribosome bound to the translocon containing a nascent polypeptide chain may provide some answers, but considerable work on the dynamics of membrane protein synthesis will be required to interpret these snapshots of the process. Engineering topological reporter proteins such as EmrE constitutes an important addition to this field, which should eventually lead to a better understanding of how membrane proteins fold.

References

1. K. R. Vinothkumar, R. Henderson, *Q. Rev. Biophys.* **42**, 1 (2010).
2. S. Seppälä, J. S. Slusky, P. Lloris-Garcerá, M. Rapp, G. von Heijne, *Science* **328**, 1698 (2010); published online 27 May 2010 (10.1126/science.1188950).
3. B. Van den Berg *et al*., *Nature* **427**, 36 (2004).
4. K. Xie, R. E. Dalbey, *Nat. Rev. Microbiol.* **6**, 234 (2008).
5. G. von Heijne, *Nature* **341**, 456 (1989).
6. G. Gafvelin, G. von Heijne, *Cell* **77**, 401 (1994).
7. V. M. Korkhov, C. G. Tate, *Acta Crystallogr. D* **65**, 186 (2009).
8. S. Schuldiner, *Biochim. Biophys. Acta* **1794**, 748 (2009).
9. M. Rapp, S. Seppälä, E. Granseth, G. von Heijne, *Science* **315**, 1282 (2007); published online 25 January 2007 (10.1126/science.1135406).
10. W. Dowhan, M. Bogdanov, *Annu. Rev. Biochem.* **78**, 515 (2009).
11. B. D. Hamman *et al*., *Cell* **89**, 535 (1997).
12. T. Becker *et al*., *Science* **326**, 1369 (2009); published online 29 October 2009 (10.1126/science.1178535).

10.1126/science.1193065

PHYSICS

When Does Photoemission Begin?

H. W. van der Hart

Ultrafast spectroscopy and multielectron calculations reveal complex electron dynamics occurring just before an atom emits a photoelectron.

The process of photoemission was one of the effects that led to the formulation of quantum mechanics. If an atom or surface absorbs sufficient energy from incoming light, it can transfer that energy to an electron, which is then emitted. Theories of photoemission mainly focus on energetics—the temporal or dynamic aspects are ignored—but complex electron interactions occur that will create a slight delay between light absorption and electron emission. This time delay has been poorly understood for a fundamental reason: We cannot "see" an atom absorbing a photon. At best, we can follow subsequent emission events and use them to establish a "time zero" when the light was absorbed. A practical challenge has been that the time delay is extremely short, and only recently have direct experiments been feasible with the advent of lasers that emit pulses on the attosecond (as, 10^{-18} s) time scale. On page 1658 of this issue (*1*), Schultze and co-workers present measurements of time delays between different photoemission processes generated by the same ultrashort light pulse. This finding not only allows further studies of the timing of photoemission but also provides a new way to investigate electron interactions in atoms.

The complex dynamics of atomic photoemission has a simple origin—the emission of a negatively charged electron changes the neutral atom into a positive ion. The energy levels of the remaining electrons are different in the positive ion, and as the electrons adjust to their new energy levels, they release energy that is transferred to the outgoing electron. The time needed for this transfer is the origin of the small time delays.

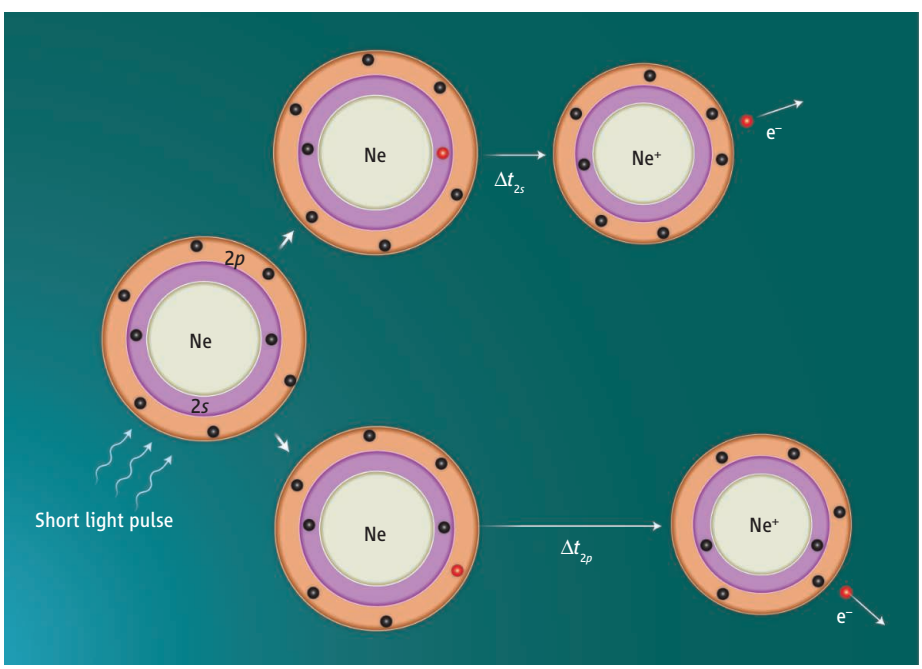

Electron hesitation. Schematic diagram of a photoemission process for Ne. An incoming photon of an ultrashort light pulse is absorbed by either a 2*s* (top row) or a 2*p* (bottom row) electron. After photoabsorption, the electron escapes, while the orbitals of the other electrons adjust to the new surroundings as the atom becomes an ion. This adjustment leads to a time delay Δt in the emission of the electron, which is longer for emission of a 2*p* electron than for emission of a 2*s* electron.

Centre for Theoretical Atomic, Molecular, and Optical Physics, School of Mathematics and Physics, Queen's University Belfast, Belfast BT7 1NN, UK. E-mail: h.vanderhart@qub.ac.uk

Published by AAAS

Schultze *et al*. studied two ionization processes induced by the same ultrashort pulse, emission of a 2*s* electron, and emission of a 2*p* electron from a Ne atom (see the figure). It takes 20 attoseconds longer for a 2*p* electron to be emitted than for a 2*s* electron. The natural orbit time of 2*p* electrons in Ne is about 100 as, so photoemission time delays could affect the interpretation of ultrafast measurements.

The current demonstration of delays in photoemission is an example of the new physics emerging from the capability to generate ultrashort light pulses. Previous experiments have probed responses of a single electron to a light field. For example, ultrafast spectroscopy can be used to relate the kinetic energy of a photoelectron to the vector potential associated with a light field (*2*) and to observe coherent scattering electronic wave packets with the so-called quantum stroboscope (*3*).

The photoemission delays observed by Schultze *et al*. arise from multielectron dynamics, which are substantially more difficult to interpret than single-electron dynamics. The main mechanism for the energy transfer is the repulsive force between the electrons, so photoemission delays are a signature of the collective dynamics of the electron cloud. Schultze *et al*. also performed electronic structure calculations (multiconfiguration Hartree-Fock studies) for Ne and demonstrated a time delay between different photoemission processes. An absolute time delay was established for He by direct solution of the Schrödinger equation.

The neon atom has eight electrons in the outer 2*s* and 2*p* shells. Although two electrons can be described with remarkable precision (*4*), a future challenge for the ultrafast atomic physics community is to investigate how the response of such a large electron cloud can be decomposed into the response of individual electron pairs and look for correlations in electron motion. Recent theoretical studies have demonstrated how two coupled electrons may move in unison on the ultrashort time scale, for example, in doubly excited states in the He atom (*5*) or in an isolated configuration in the C^+ ion (*6*). Further theoretical work is required to extend such a treatment to the response of a full atomic cloud.

The application of attosecond light-pulse technology to measurements of collective electron dynamics in atoms will also require a change in our view of atomic structure. The splitting of energy levels caused by electron-electron interactions is well known. This energy-centered view of atomic structure, found in standard textbooks [e.g., (*7*)] can now be complemented by an alternate view, in which the underlying electron dynamics takes center stage.

The time resolution at which atomic and electronic motion can be observed has increased greatly over the past decades. Femtosecond (10^{-15} s) spectroscopy allowed molecular dynamics to be observed (*8*). Recent advances here have enabled observations of vibrations in even the lightest molecules [H_2, D_2, and D_2^+ (*9*–*11*)] and observation of signatures of multielectron dynamics in CO_2 (*12*). Atoms now form the next frontier. The delay in photoemission in atoms, and the differences in this delay for different electron shells, is a great example of the new physics revealed by crossing this frontier. Attosecond light-pulse technology is now enabling experiments that can be exploited to determine ultrafast collective electron dynamics.

References

1. M. Schultze *et al*., *Science* **328**, 1658 (2010).
2. R. Kienberger *et al*., *Nature* **427**, 817 (2004).
3. J. Mauritsson *et al*., *Phys. Rev. Lett.* **100**, 073003 (2008).
4. J. S. Parker *et al*., *Phys. Rev. Lett.* **96**, 133001 (2006).
5. T. Morishita *et al*., *Phys. Rev. Lett.* **98**, 083003 (2007).
6. M. A. Lysaght *et al*., *Phys. Rev. Lett.* **102**, 193001 (2009).
7. M. Weissbluth, *Atoms and Molecules* (Academic Press, San Diego, 1978).
8. A. H. Zewail, *J. Phys. Chem.* **97**, 12427 (1993).
9. S. Baker *et al*., *Science* **312**, 424 (2006).
10. T. Ergler *et al*., *Phys. Rev. Lett.* **97**, 103004 (2006).
11. W. A. Bryan *et al*., *Phys. Rev. A* **76**, 053402 (2007).
12. O. Smirnova *et al*., *Nature* **460**, 972 (2009).

10.1126/science.1191842

IMMUNOLOGY

IgA Changes the Rules of Memory

Pathogens and bacteria that normally live in the gut induce different immune responses.

Andrea Cerutti[1,2]

The human intestinal mucosa is exposed to a complex ecosystem of harmless bacteria (commensals) that are excluded from the sterile environment of the body by an antibody isotype called immunoglobulin A (IgA) (*1*). Characterizing the dynamics of this immune response has been problematic because of constant immune stimulation by such bacteria. On page 1705 of this issue, Hapfelmeier *et al*. (*2*) use a reversible system of gut bacterial colonization in mice to show that responses to commensals lack cardinal features of systemic (extramucosal) IgG responses to pathogenic bacteria.

[1]Catalan Institute for Research and Advanced Studies, IMIM–Hospital del Mar, Barcelona Biomedical Research Park, 08003 Barcelona, Spain. [2]The Immunology Institute, Department of Medicine, Mount Sinai School of Medicine, New York, NY 10029, USA. E-mail acerutti@imim.es; andrea.cerutti@mssm.edu

Commensal microbes form a diverse community in the gut, estimated to exceed the host's eukaryotic cell number by an order of magnitude (*3*). Commensals break down otherwise indigestible food components, generate essential nutrients, and "educate" the local immune system. Intestinal B cells maintain this mutualistic relationship by producing IgA, an isotype that induces a weak inflammatory response compared to IgG in blood (*1*).

The poor inflammatory activity of IgA permits the intestinal mucosa to impede the entry of bacteria into the body without inducing inflammatory damage of the epithelial barrier (*1*). If invading pathogens breach this barrier, circulating IgG rapidly recruits innate immune cells with phagocytic function (granulocytes, monocytes) through the activation of an inflammatory reaction. With the help of IgG, these innate effector cells clear invading bacteria in a matter of hours.

Systemic IgG responses emerge 5 to 7 days after the immune system encounters a pathogen. IgG provides protection against secondary challenges by generating long-lived memory B cells that circulate like sentinels and produce massive amounts of IgG upon reencountering bacteria (*4*), and plasma cells, which release IgG from the bone marrow into the circulation (*5*). Key features of IgG memory by these cells are the quick increase and higher affinity of secondary responses, and the synergistic effect of repeated exposures. Bacterial products also enhance the half-life of serum IgG by activating memory B cells (*6*). Does intestinal IgA follow the same dynamics as systemic IgG?

To address this question, Hapfelmeier *et al*. directly introduced a mutant strain of the bacteria *Escherichia coli* into the intestine of otherwise germ-free mice. This bacterial

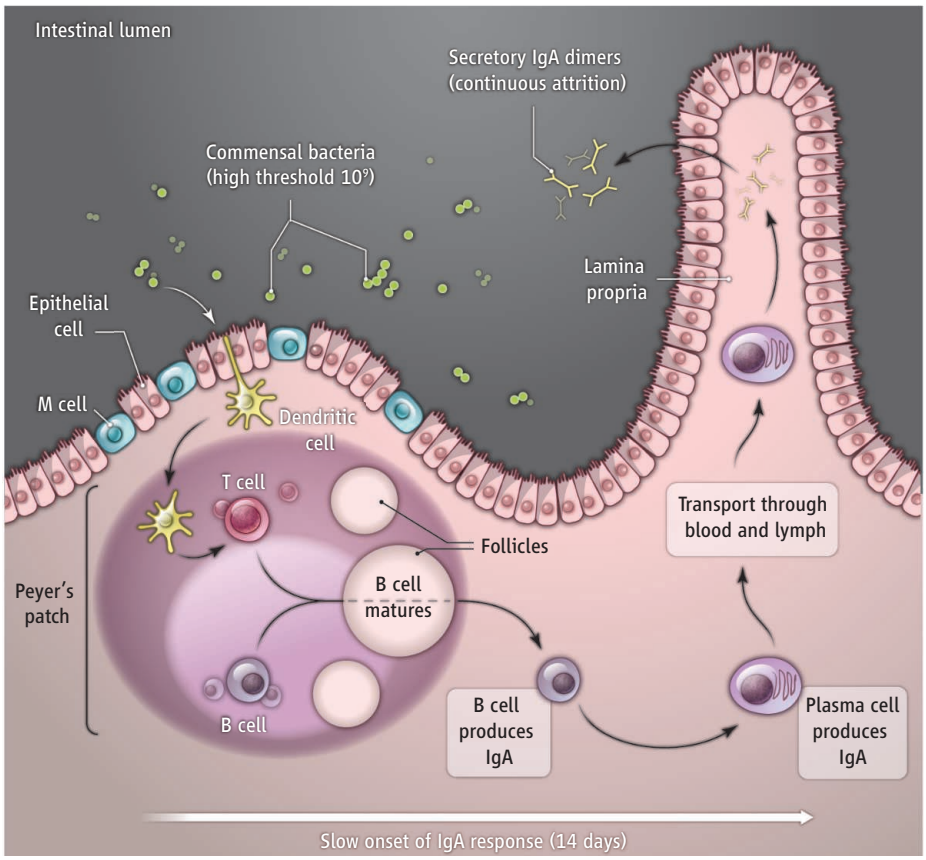

CREDIT: Y. GREENMAN/SCIENCE

Intestinal IgA dynamics. Dendritic cells sample commensal bacteria from the intestinal lumen and migrate to follicles, where they present antigen to T cells. T cells and dendritic cells in the follicles stimulate B cells to mature and produce IgA. B cells then enter lymphatic and blood vessels. After about 14 days, they enter the lamina propria and differentiate into long-lived (more than 16 weeks) plasma cells that release IgA dimers. Dimers enter the intestinal lumen and function as secretory IgA. Exposure to a different commensal rapidly attenuates an ongoing response (attrition).

strain (HA107) cannot divide and therefore provides a highly controlled and "reversible" situation in which a bacterial presence is initiated but cannot persist, and thus eventually disaappears. Strikingly, reversible colonization with HA107 induced as much total IgA production as irreversible colonization with multiple strains of other commensal bacteria. This IgA response was specific to HA107, indicating that intestinal IgA dynamics could be effectively examined without the background of continuous immune stimulation by commensal bacteria.

Intestinal IgA responses to HA107 had a slow onset (more than 14 days), which may reflect the time needed for specific IgA-producing plasma cells to move from inductive sites (follicles) of intestinal lymphoid tissues (Peyer's patches) to the effector site of the intestinal lamina propria (see the figure) (*1*). Intestinal IgA responses also had a very high threshold for induction (10^9 bacteria), which was independent of preexisting natural IgA antibodies or competition with other endogenous commensal bacteria. This may be afforded by specialized microfold epithelial cells (M cells) and transepithelial dendritic cells that sample only tiny amounts of commensal bacteria from the intestinal lumen to initiate local immunity (*7*).

Similar to systemic IgG responses (*5*), intestinal IgA responses had a sustained half-life (more than 16 weeks), in contrast to the short duration of germinal centers (where B cells mature) in intestinal follicles. One possibility is that commensal bacteria "hidden" within these follicles stimulate B cells through signals that do not require germinal centers (*8*), such as T cell–independent signals from primary follicular dendritic cells (*9*). Alternatively, epithelial, dendritic, and stromal cells lodged in the lamina propria may provide maturation and survival signals to IgA-secreting plasma cells (*10*).

Unlike systemic memory IgG responses, intestinal memory IgA responses did not show a synergistic increase in strength (prime-boost effect), but displayed additive increases after each challenge. Moreover, exposure of mice colonized with HA107 to bacteria different from HA107 limited the persistence of HA107-specific IgA memory. This attrition suggests that the intestine adapts its memory IgA response to the predominant commensal species present in the lumen at any given time, perhaps to compensate for the space constraints of plasma cells in the lamina propria.

The mechanism underlying IgA attrition remains unknown, but may relate to properties specific to intestinal B cells and/or T cells. In this regard, intestinal IgA responses require a subset of regulatory T cells usually involved in the negative regulation of other T cells (*11*, *12*). The signals from this subset of T cells that help B cells in intestinal follicles may be qualitatively different from those signals delivered by helper T cells to B cells in nonintestinal follicles during systemic IgG responses. Intestinal IgA responses may also involve a larger component of T cell–independent signals from innate immune cells and stromal cells (*13*, *14*), which could account for the limited diversity in the IgA antibodies observed by Hapfelmeier *et al*.

The lack of canonical IgG memory characteristics such as the prime-boost effect in intestinal IgA responses has important implications for developing effective vaccines against mucosal pathogens, including HIV. One prediction is that induction of long-lasting IgA-mediated protection will require the development of creative vaccine-delivery strategies to ensure sustained stimulation of intestinal B cells. These strategies could include embedding appropriate immunogens in stable components of our microbiota, edible probiotic bacteria, or genetically modifying foods, such as transgenic plants, that express the appropriate stimulatory antigen (*15*).

References

1. A. Cerutti, M. Rescigno, *Immunity* **28**, 740 (2008).
2. S. Hapfelmeier *et al*., *Science* **328**, 1705 (2010).
3. A. J. Macpherson, N. L. Harris, *Nat. Rev. Immunol.* **4**, 478 (2004).
4. L. J. McHeyzer-Williams, M. G. McHeyzer-Williams, *Annu. Rev. Immunol.* **23**, 487 (2005).
5. A. Radbruch *et al*., *Nat. Rev. Immunol.* **6**, 741 (2006).
6. N. L. Bernasconi, E. Traggiai, A. Lanzavecchia, *Science* **298**, 2199 (2002).
7. M. Chieppa, M. Rescigno, A. Y. Huang, R. N. Germain, *J. Exp. Med.* **203**, 2841 (2006).
8. T. Obata *et al*., *Proc. Natl. Acad. Sci. U.S.A.* **107**, 7419 (2010).
9. M. E. El Shikh, R. M. El Sayed, A. K. Szakal, J. G. Tew, *J. Immunol.* **182**, 3482 (2009).
10. B. P. O'Connor *et al*., *J. Exp. Med.* **199**, 91 (2004).
11. Y. Cong, T. Feng, K. Fujihashi, T. R. Schoeb, C. O. Elson, *Proc. Natl. Acad. Sci. U.S.A.* **106**, 19256 (2009).
12. M. Tsuji *et al*., *Science* **323**, 1488 (2009).
13. M. Tsuji *et al*., *Immunity* **29**, 261 (2008).
14. B. He *et al*., *Immunity* **26**, 812 (2007).
15. D. Tokuhara *et al*., *Proc. Natl. Acad. Sci. U.S.A.* **107**, 8794 (2010).

10.1126/science.1192488

Published by AAAS

SPORE* SERIES WINNER

Resources for Anyone Interested in the Brain

Games, information, and discussions with scientists bring neuroscience knowledge to all hands.

Eric H. Chudler

The high incidence of neurological and mental illness in our society makes it likely that children will know someone who has been affected by a disease or disorder of the nervous system. For example, 50 million people in the United States are affected by neurological illnesses and it costs more than $460 billion to treat these individuals (*1*). The high economic and emotional costs of these disorders make it imperative that we understand the implications of these issues and communicate this to the public, as a knowledgeable public can make healthier life-style choices that may reduce the burden of these conditions. Moreover, a science-literate electorate may support and advocate for biomedical research.

With these issues in mind, the "Neuroscience for Kids" Web site (http://faculty.washington.edu/chudler/neurok.html) was created in 1997 with the primary goal to help children, adolescents, teenagers, and their teachers learn about the nervous system. Neuroscience for Kids was initiated with development of the Web site and evaluation of the Web site's efficacy in changing attitudes about science and increasing knowledge about neuroscience. Although the title of the site includes the word "Kids," the resource can be used by the general public as an introduction to the field of neuroscience.

Early construction of the Web site was a collaborative effort between research neuroscientists and middle school science teachers. Scientists translated recent research papers into simple language or provided ideas for experiments, activities, and demonstrations. Middle school teachers reviewed this work to ensure readability, style, and content before the material was made public. Teachers also wrote articles, lesson plans, and experiments that were reviewed by researchers for scientific accuracy. Care has been taken to align the materials with the AAAS *Benchmarks for Science Literacy* (*2*) to increase the acceptance of the resource by classroom teachers (*3*). The goal has been to develop a storehouse of materials to motivate precollege students to learn more about science.

University of Washington Brain Awareness Week Open House participant.

Neuroscience for Kids has always been focused on content rather than on the latest browser enhancements. This approach was taken because students and teachers are often prohibited from downloading software from the Internet onto school or personal computers. Since its inception, Neuroscience for Kids has undergone substantial changes to improve its navigation and visual appeal. Since 2002, videos have been added to the site, including the BrainWorks television program (*4*) and Flash animations to illustrate concepts. Nevertheless, it is impossible to please everyone, and the extensive depth of the site sometimes makes materials difficult to find.

The content-rich environment of Neuroscience for Kids offers users hundreds of individual Web pages to explore at their own pace as they learn about neuroscience. The resource can be used for research; students and teachers can find basic information about neuroanatomy, neurophysiology, neuropharmacology, the senses, sleep, mental and neurological illness, neuroscience methods, blood supply, and language. Visitors can interact with online activities and demonstrations illustrating a variety of neuroscientific concepts. For example, a set of interactive visual illusions allows students to manipulate figures and background images as they explore their own perceptions (http://faculty.washington.edu/chudler/chvision.html).

Many students use Neuroscience for Kids to locate ideas for local and regional science fairs. In addition to providing science fair project ideas, the Web site has suggestions and best practices for the development of project hypotheses, data collection, data analysis, and visual displays.

A unique feature of Neuroscience for Kids is the "Neuroscientist Network" that consists of a group of 19 neuroscientists from different institutions. Through e-mail, students and teachers can ask these neuroscientists questions about neuroanatomy, neurophysiology, the educational requirements to become a neuroscientist, and careers in neuroscience. Responses are sent back through personal e-mail messages and posted to the Web site for others to read.

Offline games, demonstrations, and quizzes permit users to learn in an entertaining environment and to extend their learning beyond the Web site. Many of the activities and demonstrations include open-ended questions that encourage students to perform their own experiments. For example, in an activity using Benham disks, students are presented with classic pattern designs, but are then asked to view the patterns in different lighting conditions, to change the pattern design, and to spin the disks in different directions and speeds. These investigations are designed to help students inquire independently or in groups and to develop their own hypotheses about what they experience.

Students and teachers can also send free neuroscience-related postcards by e-mail (see the figure on page 1649) or request a monthly, electronic Neuroscience for Kids newsletter. The newsletter is sent to about 9600 people (students, teachers, school administrators, and scientists) with information about new additions to the Web site. It also includes upcoming events, such as television programs and museum exhibits, book reviews, interesting

Department of Bioengineering, University of Washington, Seattle, WA 98195, USA. E-mail: chudler@u.washington.edu

*SPORE, *Science* Prize for Online Resources in Education; www.sciencemag.org/special/spore/.

Published by AAAS

trivia about the brain, and current popular magazine articles about the nervous system.

The effectiveness of Neuroscience for Kids for changing student attitudes about science and for improving neuroscience content knowledge was evaluated by distributing the Web site (on compact disk) and pre- and post-use questionnaires to 52 teachers and about 3794 middle school students in public and private schools across the United States. Analysis of the responses from students demonstrated that student content knowledge about neuroscience concepts improved significantly after the use of Neuroscience for Kids, but student attitudes toward science, as measured with the Scientific Attitude Inventory SAI II (*5*) remained unchanged (*6*). Further studies are warranted to determine how classroom visits by scientists, laboratory tours, and other informal learning experiences in addition to online resources affect students' content knowledge and attitudes about science.

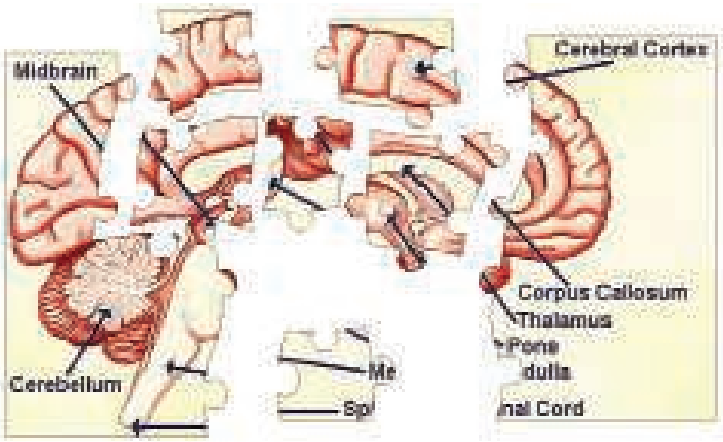

Postcard jigsaw puzzle. A partially completed jigsaw puzzle of a midsagittal section of the human brain. Users piece together the puzzle and then can send an e-mail link to the puzzle to others.

Neuroscience for Kids has been accessed by people from more than 150 different countries. About 150 million files (e.g., Web pages, PDFs, graphics, animations, Flash applications) and 770 GB of information are downloaded from the Web site each year. Portions of the Web site have been translated into Spanish, Slovene, Chinese, Portuguese, Italian, Korean, Dutch, Japanese, and Turkish, and materials translated into Arabic, Hebrew, and Hindi are planned for 2010. Neuroscience for Kids is ranked highly in both Google and Yahoo search engines: For example, the search term "neuroscience" results in hits to Neuroscience for Kids pages in two of the top 10 returns in Google and one of the top 25 returns in Yahoo; "brain" results in the 11th return in a Google search (*7*).

The creation and maintenance of online scientific education materials are not without challenges. Bench scientists have to balance responsibilities in the laboratory with those of developing educational resources. Science outreach and public education are not usually recognized or rewarded by universities and may sometimes be actively discouraged. They rarely influence faculty tenure and promotion decisions, and grants that are available for these projects often are accompanied by low indirect-cost rates. These factors reduce the motivation of scientists to undertake such endeavors and create an academic culture that discourages public engagement (*8*).

Some organizations are working to change this culture. In addition to *Science*'s SPORE award, the Science Educator Award and the Next Generation Award, two awards established by the Society for Neuroscience, are other examples that recognize senior and junior faculty members, and pre- and postdoctoral trainees who contribute to public education. To succeed in shifting the culture of academia to be more welcoming of public education will require financial and administrative support from the top levels of academic institutions. Scientists have many opportunities for community engagement. For example, through Brain Awareness Week (BAW), an international campaign established and supported by the DANA Alliance for Brain Initiatives and the Society for Neuroscience to celebrate education and outreach about the brain, researchers visit neighborhood schools, invite students into laboratories, and present public lectures (see the figure on page 1648). Over the course of its 15-year history, BAW has involved 2600 partners (i.e., universities, kindergarten through 12th-grade schools, hospitals, patient support groups, museums, government agencies, service organizations, and professional associations) in 76 countries (*9*).

Neuroscience for Kids seeks to spark curiosity about science in young students and to encourage them to pursue careers in neuroscience. Concerted efforts by scientists, educators, administrators, and parents may entice young scholars into the mysteries of the nervous system, teach them to ask questions, and give them the confidence to seek answers.

About Dr. Chudler

Eric H. Chudler is a research associate professor in the departments of Bioengineering and of Anesthesiology & Pain Medicine at the University of Washington in Seattle. Chudler's research interests focus on cortical and basal ganglia mechanisms of nociception and pain and on how the cerebral cortex and basal ganglia process information from multiple sensory systems. In addition to his research, Chudler is the director of education and outreach for University of Washington Engineered Biomaterials where he manages several programs for precollege students and for research training opportunities for undergraduate students.

References and Notes

1. Society for Neuroscience, *Brain Facts: A Primer on the Brain and Nervous System* (Society for Neuroscience, Washington, DC, 2008).
2. American Association for the Advancement of Science, *Benchmarks for Science Literacy* (Oxford Univ. Press, New York, 1993).
3. W. Cameron, E. Chudler, *Nat. Rev. Neurosci.* **4**, 763 (2003).
4. E. H. Chudler, B. K. Ross, *Neuroscience Abstr.*, Program no. 29.1 (2007); program available at www.uwtv.org/programs/displayevent.aspx?rID=4909.
5. R. W. Moore, R. L. H. Foy, *J. Res. Sci. Teach.* **34**, 327 (1997).
6. E. H. Chudler, E. Y. Kuwana, M. A. Murray, L. J. Bleeker, *Neurosci. Abstr.* Program no. 22.37 (2002).
7. Google, accessed on 17 February 2010.
8. J. Illes *et al.*, *Nat. Rev. Neurosci.* **11**, 61 (2010).
9. DANA Alliance for Brain Initiatives, www.dana.org/brainweek/reports/.
10. Supported (1997–2005) by a Science Education Partnership Award, National Center for Research Resources, National Institutes of Health (R25RR12312).

10.1126/science.1186935

SCIENCE POLICY

U.S. Science: Bold Initiatives, with a Wary Eye on the Budget

With medical researchers making dramatic new advances, Margaret Hamburg is leading the U.S. Food and Drug Administration (FDA) in developing a robust field of regulatory science to help bring new drugs and therapies more quickly to patients. In an address at the AAAS Forum on Science and Technology Policy, she described the FDA's effort as crucial to public health and a healthy economy.

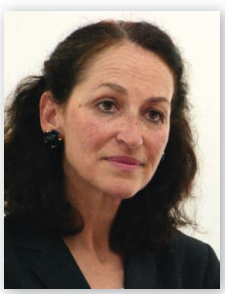

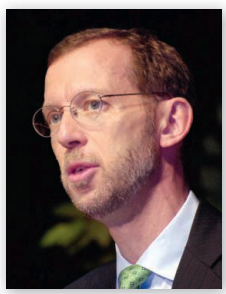

Margaret Hamburg and Douglas W. Elmendorf

Her talk was resolutely optimistic—except for a sobering note near the end. "I have no illusions about how difficult it will be to achieve all of our goals in regulatory science," Hamburg said. "These are difficult times—as a nation we face staggering budget constraints and an array of compelling yet competing priorities for attention and resources."

It was a telling moment. Throughout the 35th annual Forum, public officials, educators, and other science leaders described ambitious initiatives now under way to address global challenges and drive a new generation of economic growth. But a recurring question was whether a weak economy and historic federal deficits will undermine the efforts.

The Forum, held 13 to 14 May in Washington, D.C., attracted over 500 U.S. and foreign participants from government, education, and business. They heard policy leaders talk on a range of critical issues, including energy, national security, the impact of science on society, and U.S.-European science cooperation.

White House science adviser John P. Holdren, in an address that opened the conference, offered a detailed look at President Obama's science-related initiatives. Holdren said that Obama sees science and technology as critical to addressing many of the defining issues of our era—the economy, national security, energy and climate, health, and education.

The fiscal stimulus package directed more than $100 billion into science-related projects, Holdren said. And the administration is proceeding with efforts to double the budgets for the National Science Foundation, the Department of Energy Office of Science, and the National Institute of Standards and Technology.

But the economy is already taking a toll in some sectors, and the pressures could intensify in coming years, speakers said.

In the world-renowned University of California system, state support has been cut by 50% in the past 25 years, and by more than 20% in the past year alone, said Linda Katehi, chancellor of the university's campus at Davis. Diminished support, she said, jeopardizes "the ability of the state to sustain the public research university, and to sustain the mission of educating citizens and sustaining democracy."

Congressional Budget Office Director Douglas W. Elmendorf offered a gloomy assessment of the long-term federal fiscal picture. For the 2011 budget year, Obama has proposed a $3.8 trillion budget, with a deficit estimated at nearly $1.3 trillion. And without a significant change in taxes or spending—or a combination of those—deep deficits will continue for a decade and beyond.

"The gap is so large as to be unsustainable," Elmendorf told the Forum. "The longer it persists, the more drag it creates on people's income and the greater the risk it creates of a government-centered financial crisis."

Patrick J. Clemins, director of the AAAS R&D Budget and Policy Program, said the 2011 budget proposed by the White House shows a clear near-term strategy Obama has proposed a slight decrease in funds for research and development, part of his commitment to a 3-year freeze on non-security discretionary spending. But within the R&D investment portfolio, Clemins said, the White House is increasing funds for priority programs and cutting funds elsewhere.

Hamburg said that the FDA has received new support under Obama. Still, she suggested that policy leaders will be challenged by a future climate that features both promising opportunity and fiscal austerity.

"We live in a time when science and technology are changing our world in dramatic ways," she said. "And with that comes a fundamental question—how do we make sure that we fully translate the potential and promise of that research into real-world products and programs that really matter?"

AAAS

New Dues Rates Approved for 2011

The AAAS Board of Directors has approved a dues increase for 2011. The Board authorizes increases to cover two kinds of expenses: unavoidable costs associated with running AAAS and publishing *Science*, and new expenses that add value to membership. Postage and paper increases and improving online resources are examples of the kinds of expenses the Board anticipated in setting the 2011 rates.

The new rates are effective for membership terms beginning after 31 December 2010. As listed below, they do not include postage or taxes for international members, which are additional.

Regular professional members	$149
Postdocs and K-12 teachers	$99
Emeritus members who receive print *Science*	$115
Students	$75
Patrons	$310
Institutional rate for print for high schools and public libraries	$360
All other institutions receiving print	$990

For further information, including subscription rates for *Science* Online, librarians should contact AAAS or their subscription agents, or go to the *Science* Online Web site.

All members will be advised of the new dues rates on their renewal notices for 2011. Member dues and voluntary contributions form the critical financial base for a wide range of AAAS activities. For more information, contact the AAAS Membership Office at 202-326-6417, or www.aaas.org/membership/.

Published by AAAS

The Last Glacial Termination

G. H. Denton,[1] R. F. Anderson,[2,3]* J. R. Toggweiler,[4] R. L. Edwards,[5]
J. M. Schaefer,[2,3] A. E. Putnam[1]

A major puzzle of paleoclimatology is why, after a long interval of cooling climate, each late Quaternary ice age ended with a relatively short warming leg called a termination. We here offer a comprehensive hypothesis of how Earth emerged from the last global ice age. A prerequisite was the growth of very large Northern Hemisphere ice sheets, whose subsequent collapse created stadial conditions that disrupted global patterns of ocean and atmospheric circulation. The Southern Hemisphere westerlies shifted poleward during each northern stadial, producing pulses of ocean upwelling and warming that together accounted for much of the termination in the Southern Ocean and Antarctica. Rising atmospheric CO_2 during southern upwelling pulses augmented warming during the last termination in both polar hemispheres.

At the peak of the last ice age, expansive ice sheets covered large areas of the Northern Hemisphere (NH) (Fig. 1). The reduction of this continental ice to about its present volume represents one of the largest and most rapid natural climate changes in Earth's recent history. As a consequence, identifying the conditions and processes that triggered this deglaciation has been a major objective of paleoclimate research [supporting online material (SOM)].

The last deglaciation was part of a recurring pattern of ice-sheet growth and decay (Fig. 2). Late Quaternary glacial cycles varied between 80,000 and 120,000 years in length, with an average recurrence interval of about 100,000 years. These cycles have asymmetric signatures, featuring a long cooling interval marked by an oscillating buildup of ice sheets to maximum volume followed by a relatively short warming period. During deglaciations, huge NH ice sheets (Fig. 1) melted away, sea level rose about 120 m (Fig. 2), atmospheric CO_2 increased by about 100 parts per million by volume (ppmv) (Fig. 3K), and interglacial climate emerged across the planet. The relatively rapid transitions from glacial to interglacial conditions have been dubbed terminations (*1*). The last ice recession began in the NH about 20,000 years ago (*2*, *3*), and by 7000 years ago all that was left of the great Laurentide Ice Sheet that had covered northern North America was a small ice cap on Baffin Island (*4*). In Antarctica and the Southern Ocean the last termination began about 18,000 years ago, with interglacial temperature attained close to 11,000 years ago (Fig. 3J).

The retreat of the huge NH ice sheets during the last termination sent bursts of melt water and icebergs into the northern North Atlantic Ocean, where they initiated thousand-year-long intervals of cold stadial climate. Here, we describe a sequence of global environmental changes initiated by those bursts, including the warming of Antarctica. Interhemispheric teleconnections, reinforced by rising atmospheric CO_2, allowed Earth to emerge from the last ice age.

NH Summer Insolation

Based on the proposition that marginal melting dominates mass balance, Milankovitch (*5*) postulated that variations in summer insolation at high latitudes caused waxing and waning of northern ice sheets. That orbital oscillations strongly influenced northern ice sheets is supported by the connection between ice-volume change and the concomitant variations of summer insolation (Fig. 2B) (*6*). Well-dated paleoclimate proxies from Chinese caves (*7*), the Dome Fuji ice core in Antarctica (*8*), and marine sediment cores (*9*) indicate that rising northern summer insolation accompanied terminations. However, increasing northern summer insolation also occurred elsewhere in the glacial record where no terminations took place (Fig. 2B). Moreover, full terminations occurred both when the amplitude of summer insolation change was high [e.g., ter-

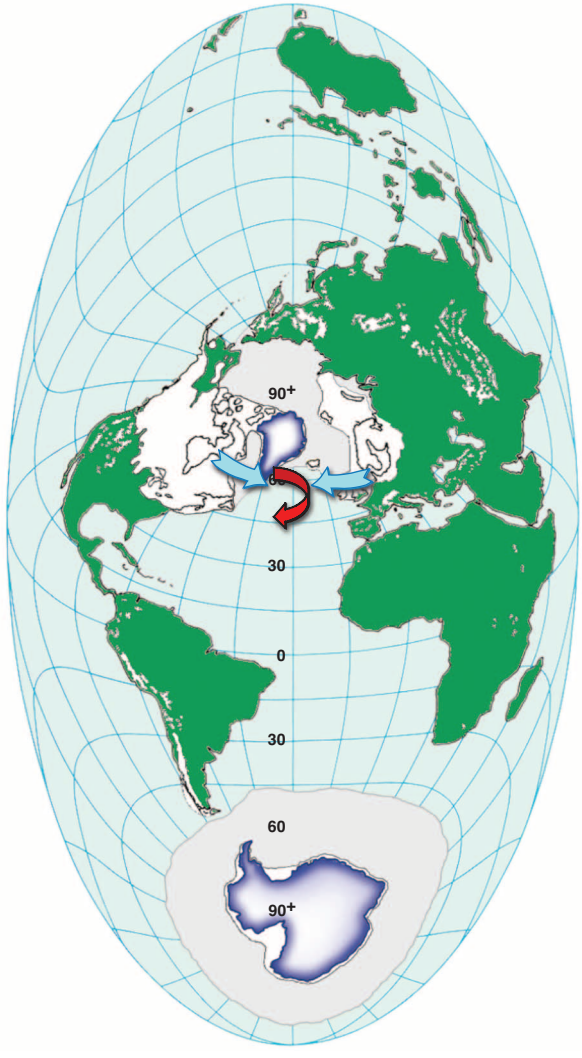

Fig. 1. Representative changes in the volume of continental ice throughout the Late Pleistocene. Global map showing the schematic spatial extent of continental ice sheets (white shading) at the LGM (*61*, *62*). Two large ice sheets (outlined in blue) survived the last termination. One is in Greenland and the other in Antarctica. This map projection emphasizes the proximity of the Laurentide and European ice sheets to areas of deepwater formation in the North Atlantic Ocean (red arrow, indicating a general region without implying a specific mechanism or site of deepwater formation). Blue arrows indicate the supply of freshwater and icebergs. On the Southern Ocean, gray shading indicates maximum extent of winter sea ice (*63*).

[1]Department of Earth Sciences and Climate Change Institute, Bryand Global Sciences Center, University of Maine, Orono, ME 04469, USA. [2]Lamont-Doherty Earth Observatory of Columbia University, Post Office Box 1000, Palisades, NY 10964, USA. [3]Department of Earth and Environmental Sciences, Columbia University, New York, NY 10025, USA. [4]Geophysical Fluid Dynamics Laboratory, National Oceanic and Atmospheric Administration, Princeton, NJ 08542, USA. [5]Department of Geology and Geophysics, University of Minnesota, Minneapolis, MN 55455, USA.

*To whom correspondence should be addressed. E-mail: boba@ldeo.columbia.edu

mination 2 (T2) and T4 (Fig. 2B)] and when it was low [e.g., T1 and T3 (Fig. 2B)]. Therefore, rising insolation alone is insufficient to explain terminations.

Large Ice Sheets

Terminations invariably began when ice sheets were at or close to their greatest area and volume. This striking situation affords an important clue in deciphering their cause(s). Specifically, as described below, a large volume of NH ice represents the essential initial condition for a termination [supporting online material (SOM)]. Raymo (*10*) pointed out that terminations ending in full interglacial climate occurred only after ice sheets achieved what she defined as "excess" volume at glacial maxima, derived from benthic oxygen-isotope ratios in deep-sea cores (Fig. 2B). This "excess" ice must have been tied up in NH ice sheets because the Antarctic sheet contributed only 14 m or less to the total drop of sea level of about 120 m at the last glacial maximum (LGM) (*11*). Figure 1 shows that most northern sheets, of which the Laurentide was by far the largest, were arrayed around the critical North Atlantic deepwater downwelling sites. When at their largest, these sheets expanded across continental shelves, had maximum isostatic depression beneath them, and were drained seaward by ice streams. Ice-sheet sectors with such marine-based configurations were prone to unstable collapse into the adjacent ocean (SOM). Thus, the importance of Raymo's "excess" ice was that it provided the necessary volume in seaward-draining ice systems to produce a collapse into the North Atlantic that was massive and long enough to jump-start a termination via oceanic and atmospheric teleconnections with the Southern Hemisphere (SH), as described below.

Ice drainage systems that emptied into the North Atlantic produced copious quantities of icebergs and meltwater that affected northern overturning circulation [e.g., (*12*, *13*)]. Heinrich (*14*) discovered six distinctive deposits of ice-rafted lithic fragments dating to the last glacial cycle in deep-sea cores collected in the ice-rafting zone centered at ~50°N in the North Atlantic. Layers of detrital dolomitic carbonate, which dominate these deposits, can be traced to Hudson Strait. These carbonate layers record massive outbursts of icebergs that are a testament to episodes of Laurentide ice collapse. In addition to Canadian-sourced detrital carbonate, many of the lithic deposits in the North Atlantic ice-rafting zone contain important contributions from Greenland and European ice sheets (*15*), indicating the significance of these sources as well. The last of these massive outbursts of icebergs is termed Heinrich 1 and occurred near the onset of the last termination. In addition, summer melting during retreat of northern sheets injected fresh water into the North Atlantic. As a prominent example, Toucanne *et al.* (*3*) documented a massive discharge of melt water emanating from margins of European ice sheets through the Channel River between England and France into the North Atlantic early in the last termination, beginning about 20,000 years ago and reaching a maximum between 18,300 and 17,000 years ago. Abrupt expansion of polar planktonic foraminifera shortly before 18,000 years ago accompanied this meltwater pulse (*16*).

During the last termination, such outbursts of meltwater and icebergs produced the Heinrich 1 and Younger Dryas stadials in the North Atlantic region by curtailing northern overturning circulation. In the case of Heinrich stadial 1 [HS1, as defined by (*17*), which is equivalent to the Mystery Interval of Denton *et al.* (*18*)], reduced overturning (Fig. 3F) was initiated and maintained by fresh water supplied by ice melt (*3*) and surges (*13*). Figure 3 illustrates the resulting situation south of the main ice-rafting zone in the subtropical northeast Atlantic near the Iberian Peninsula. There, ice rafting occurred in two pulses during HS1 (Fig. 3D) (*19*). A substantial drop in sea surface temperature (SST) and the expansion of polar planktonic foraminifera preceded the maximum ice-rafting spike (*16*). SST remained low between about 17,800 and 15,000 years ago during HS1 (Fig. 3E). Thus, HS1 featured widespread melt and collapse of Laurentide and European ice, along with cold SST and reduced overturning circulation in the North Atlantic. Figure 3 illustrates that the Younger Dryas stadial (YDS) was in many ways a replicate of HS1.

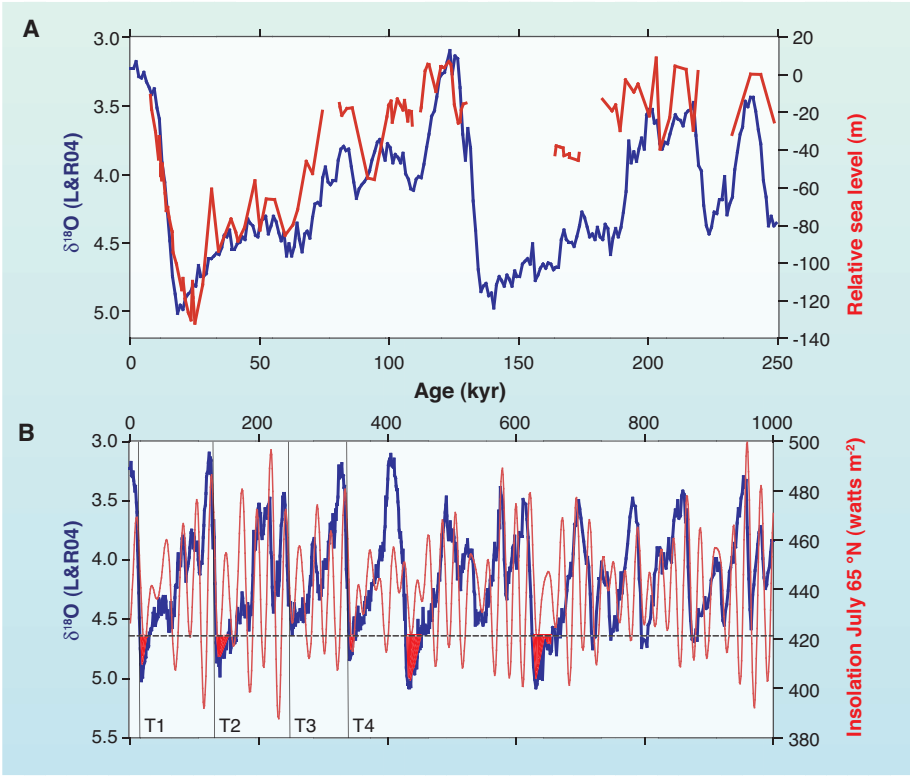

Fig. 2. (**A**) Two proxy records related to global ice volume during the past 250,000 years. The stacked record of the oxygen isotopic composition of benthic foraminifera recovered from 57 deep-sea cores [blue (*9*)] is influenced primarily by global ice volume but also secondarily by changes in the temperature of the deep ocean. Oxygen isotopes are plotted on a reverse scale, such that more-positive values (down) reflect greater volumes of continental ice. Changes in sea level relative to modern conditions (red), which are controlled by the amount of water locked up in continental ice, are estimated by uranium-thorium dating of corals that lived at a known depth (*64*). Before the last glacial cycle, the coral record is limited to high sea levels, but the record is sufficient to illustrate the robust relationship between sea level and the oxygen-isotope signal, which extends back much further in time. (**B**) The stacked oxygen-isotopic record from benthic foraminifera [blue (*9*)] is compared against July insolation at 65°N [red (*65*)] over the past 1,000,000 years. Periods of maximum global ice volume just before major terminations (shaded in red) are referred to in the text as excess ice (*10*). The level beyond which the oxygen-isotope record is shaded is intended to emphasize the point that terminations occur when continental ice volume is at or near its maximum and not to imply that a specific oxygen isotope value is required for a termination to occur. The extended Asian Monsoon record of Cheng *et al.* (*7*) supports the chronology and relationships illustrated here. Terminations 1 to 4, referred to in the text, are identified by vertical black lines.

Sea Ice and Seasonality

Proxy records show that an important consequence of weakened overturning circulation, combined with fresh water–induced stratification, was an expansion of winter sea ice that introduced a highly seasonal climate in the North Atlantic region (*20*–*23*), a result repli-

cated in a model experiment (*24*). Such seasonality arose during stadials because the spread of winter sea ice created Siberian-like conditions, dominated by large temperature swings between winter and summer, in lands adjacent to and downwind of the North Atlantic. For example, mean annual temperatures in Greenland and northern Europe dropped 12° to 17°C below today's values in the YDS (*22*, *25*), partitioned into a 22° to 28°C shift in winter and a 3° to 6°C shift in summer (*20*–*22*). A similar seasonal difference marked northern Europe in HS1 (*23*).

Model results suggest that the expansion of sea ice across the northern North Atlantic, particularly in winter, was the key factor in spreading the impacts of the millennial-scale cold events quickly and efficiently throughout the NH and into the tropics. Chiang and Bitz (*24*) showed that the Intertropical Convergence Zone (ITCZ) in all ocean basins shifted away from the hemisphere with an imposed increased ice cover anomaly such as that on the North Atlantic during the YDS and HS1. Their findings are supported by the observation that the ITCZ and Trade Winds over South America (*26*, *27*) and across the tropical Pacific (*28*, *29*) varied during the last glacial period with a distinct pattern similar to stadial-interstadial switches in the North Atlantic, as well as by the observation that the Atlantic sector of the ITCZ was pushed south so much during HS1 that it rained in Brazil in areas normally arid (*30*). Weakening of the Asian monsoon during the YDS and HS1 (Fig. 3B) coincided with increased precipitation in Indonesia (*31*) and in northern Australia (*32*) as the ITCZ shifted southward. Barnett *et al*. (*33*) linked weakened Asian monsoons to cold and long Asian winters, such as might be imposed in the northern tier of the hemisphere, including Eurasia, as a consequence of a winter sea-ice cover on the northern North Atlantic. Evidence for changes in precipitation during North Atlantic stadials has been found throughout tropical Africa and extending to the southern tip of the continent (*34*). The impact of these events extended well into the SH.

North-South Connections

Full-glacial conditions persisted in Antarctica until about 18 ka (Fig. 3J). The subsequent termination featured two warming pulses separated by the Antarctic Cold Reversal (ACR) (Fig. 3J). Similar features characterized the termination at SH middle latitudes. As atmospheric summer temperature rose about 6°C in the Chilean Lake District (Fig. 3H), Andean glaciers underwent considerable recession; for the first time in more than 50,000 years, a rainforest invaded the lowland (*35*). On both sides of the Pacific Ocean, mid-latitude SST rose in two steps by a total of more than 5°C (Fig. 3G) (*36*–*40*).

The first southern warming pulse coincided with HS1 and the second with the YDS (yellow bands in Fig. 3). Within each of these cold NH stadials, the north featured a slow down or cessation of North Atlantic overturning (Fig. 3F) accompanied by the spread of winter sea ice and cold ocean temperatures (Fig. 3E), with concomitant weakening of the Asian monsoon (Fig. 3B) and a southward shift of the ITCZ. In contrast, the SH featured increasing upwelling in the Southern Ocean (Fig. 3I) accompanied by a rise in atmospheric CO_2 (Fig. 3K) along with rapidly warming ocean temperatures (Fig. 3G). The behavior between the hemispheres was also opposite in the interval between the NH stadials. In the northern Bølling-Allerød, North Atlantic overturning circulation resumed (Fig. 3F), forcing a retreat of winter sea ice and hence a rapid

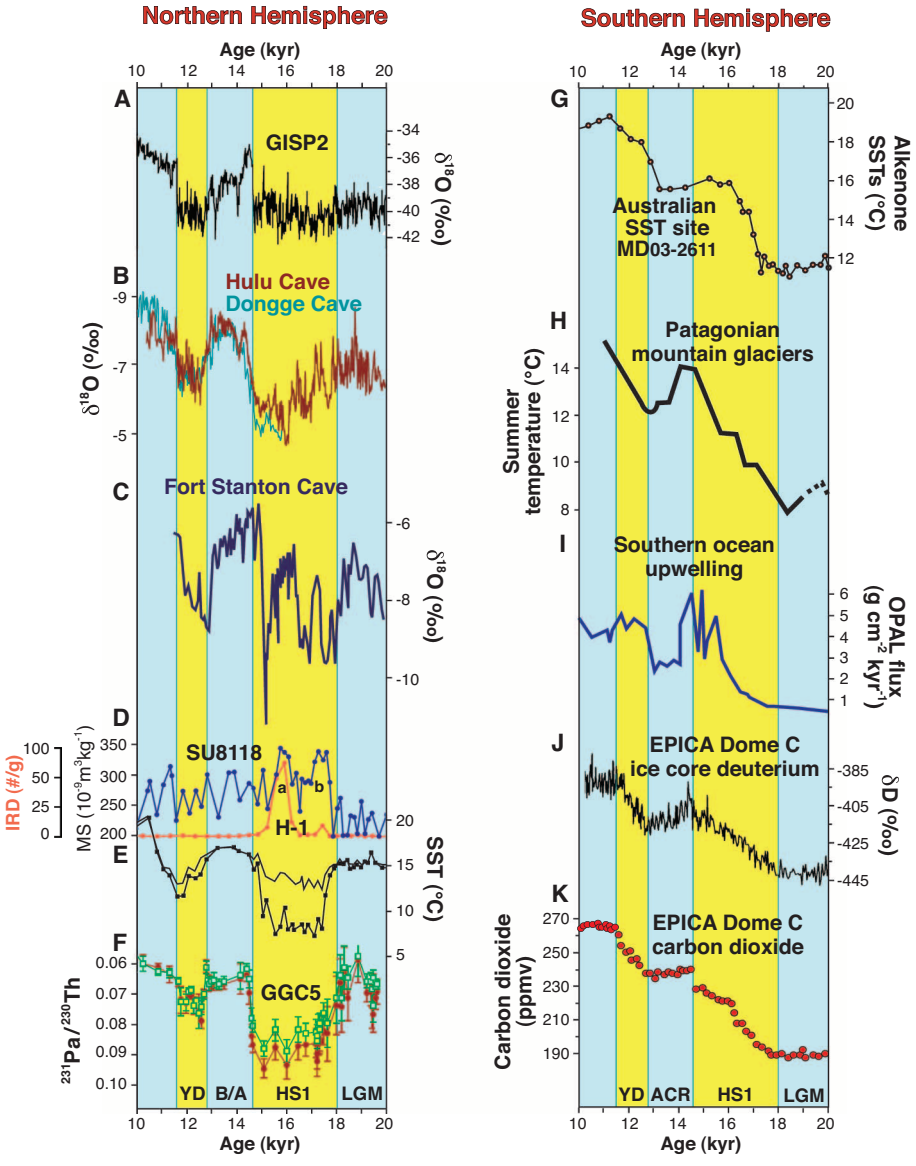

Fig. 3. (**A**) Greenland Ice Sheet Project 2 (GISP2) oxygen isotopes (*66*). (**B**) Chinese monsoon records reconstructed from speleothems [drier is down, wetter up (*67*, *68*)]. (**C**) Precipitation record reconstructed from Fort Stanton Cave, southwestern United States [wetter down, drier up (*69*)]. (**D**) Magnetic susceptibility (MS) and ice-rafted detritus (IRD) from marine sediments located off the coast of Portugal (*19*), where IRD is expressed as the number of grains per gram for the size fraction greater than 150 μm. H-1 is Heinrich Event 1. (**E**) SST based on alkenone unsaturated ratios from North Atlantic marine sediment core SU-8118 (*19*). (**F**) The $^{231}Pa/^{230}Th$ ratios from core GGC5 off the Bermuda Rise, where increasing values (plotted downward) reflect reduced Atlantic overturning circulation (*70*). (**G**) SST from a site south of Australia (36°44′S; 136°3′E) reconstructed by using the alkenone unsaturation index (*37*). (**H**) Summer temperature changes determined from glacier and vegetation fluctuations in the Andes of Patagonia in southern South America (*35*, *71*). (**I**) Biogenic opal flux in the Southern Ocean, interpreted as a proxy for changes in upwelling south of the Antarctic Polar Front (*43*). (**J**) European Project for Ice Coring in Antarctica (EPICA) Dome C (EDC) deuterium record (*72*) as a proxy for temperature in Antarctica. (**K**) EDC CO_2 record (*72*). EPICA deuterium and CO_2 data are plotted on the GISP2 time scale [after (*73*)]. Heinrich stadial 1 (HS1) and the Younger Dryas stadial (YD) are marked with yellow backgrounds, whereas the Bølling-Allerød (B/A), which is contemporary with the Antarctic Cold Reversal (ACR), and LGM have blue backgrounds.

warming of mean annual temperatures (Fig. 3E). The Asian monsoon strengthened (Fig. 3B), and the ITCZ shifted northward. In the south, the termination stalled during the ACR.

There are at least two ways to explain this opposing behavior between the hemispheres. One invokes the oceanic bipolar seesaw by which weakening North Atlantic overturning during HS1 and the YDS reduced northward ocean heat transport (*41*), thereby warming the SH. In addition, reduced North Atlantic overturning would have stimulated deepwater formation in the Southern Ocean, further warming the Southern Ocean and Antarctica during NH stadials (*42*).

A second and complementary mechanism involves a southward shift of the southern westerly wind belt each time the ITCZ was pushed toward the SH by the spread of winter sea ice over the northern North Atlantic (*43*). Such a mechanism would have the advantage of transferring the effects of northern millennial-scale stadial/interstadial events rapidly into the SH. The two processes likely acted synergistically. For example, the bipolar seesaw facilitated the southward shift of the zonal wind systems by changing SST gradients (*44*).

Climate-related shifts in the mean position of the SH westerlies are supported by a number of independent lines of evidence. For example, the latitude of maximum precipitation along the west coast of South America, which coincides with storm tracks that follow the westerlies, was located several degrees north of its present position during the LGM (*45*). Also, during the LGM the SH oceanic Subtropical Front (STF) was situated north of its present position, a condition that has been linked to a northward displacement of the westerlies (*36*, *46*). In contrast to the LGM, a displacement of the SH westerlies to an extreme southerly latitude during terminations is inferred by tracking the STF (*36*) and from estimates of the volume of Agulhas Current water transported into the South Atlantic Ocean, which is controlled by the distance of the STF from the southern tip of Africa (*46*, *47*).

Southward movement of the STF was a contributing factor for the large amplitude and rapid rise of temperatures during HS1 and the YDS within the region between 35°S and 45°S (Fig. 3, G and H) (*17*, *36*–*38*, *40*). This latitude zone also contains the mountain glaciers that began retreating rapidly at ~18 thousand years ago (ka) (*35*). Rapidly warming ocean temperatures "upwind" of the temperate mountain glaciers provided a heat source to stimulate glacier retreat (*38*).

A southward displacement of the SH westerlies during NH stadials would have warmed the Southern Ocean and Antarctica by several mechanisms. A southerly position of the winds would have dissipated sea ice more effectively via northward Ekman transport (*48*), thereby exposing the atmosphere to warmer ocean water. Increased wind-driven upwelling south of the Antarctic Polar Front (Fig. 3I) would have further reduced sea ice cover by bringing to the surface deepwater that was warm enough, although still quite cold, to melt sea ice. A southerly position and increased intensity of the westerlies would have warmed the Southern Ocean and Antarctica by increased southward eddy transport of heat (*49*). Lastly, CO_2 released by increased upwelling would have warmed the SH along with the rest of Earth.

Thus, we speculate that during HS1 and the YDS, cold conditions in northern winters forced the ITCZ southward, strengthening the NH Hadley cell to transport heat more effectively from the tropics to high northern latitudes (*50*). The SH Hadley cell, by contrast, would have been weakened (*50*), as would the subtropical jet (STJ) that forms at the poleward boundary of the Hadley Cell at high altitudes. Weakening of the southern STJ would have allowed more momentum to be transferred by eddies to the SH subpolar jet (*51*), which, because of its barotropic nature, would have strengthened the surface SH westerlies, forcing the changes in the ocean described above.

Essential Elements of a Termination

We now return to the role of large NH ice sheets and summer insolation in the last termination. We first note that the size of the Antarctic Ice Sheet changed little. Most of the minor change was concentrated in the Weddell and Ross embayments, where recession was too late to have had a major effect on the termination (*52*). In the north, recession of the Laurentide and Scandinavian ice sheets was underway at least by 20 ka, as sea level started to rise and as meltwater from European ice sheets and mountain glaciers began to enter the Bay of Biscay (*3*). Presumably this recession was in response to an increase in summer insolation that caused ablation zones to enlarge, intensify, and migrate northward. At the same time, North Atlantic SST remained high and may even have been warming before HS1 (*19*). A critical transition occurred about 18 ka when a combination of ice-sheet melting and surging initiated HS1. At that time, ablation became sufficiently intense and widespread to produce a strong meltwater pulse through the Channel River into the North Atlantic. Shortly thereafter, the continued rise of surface ablation, probably accompanied by basal melting of buttressing ice tongues, triggered surges of ice streams along with massive calving of all marine ice margins. The result was unstable collapse of Laurentide, Greenland, and European ice into the North Atlantic (Fig. 1). It seems reasonable to suggest that ice collapse during HS1 was the longest-lived of the last glacial cycle simply because northern ice sheets were then at or near their largest extent and volume. As a result, isostatic depression was presumably greatest, and therefore the conditions for the operation of marine instability mechanisms (SOM) were likely in place.

Heinrich stadials before the last termination induced changes in the SH similar to those of HS1. For example, they were accompanied by warming in Antarctica and a concomitant rise in atmospheric CO_2 (*53*), by increased upwelling in the Southern Ocean (*43*), and by increased SST in the vicinity of the STF (*38*, *39*). However, those events did not lead to terminations. Previous studies have suggested that terminations did not materialize at those times because Earth's climate system failed to pass a critical threshold (*17*, *40*, *54*). We propose that this threshold involves the two essential elements mentioned above: rising NH summer insolation and large NH ice sheets prone to instabilities. The key factor is that delivery of freshwater to the North Atlantic, which is required to maintain stadial conditions (*13*) and a southward displacement of the SH westerlies, must have persisted for a sufficient duration to raise atmospheric CO_2 above a minimum level necessary to maintain warm conditions globally.

In support of this threshold concept, we note that each of the last four terminations involved extended northern stadial conditions, as indicated by reduced Asian monsoon intensity (*7*). At each termination, the total duration of stadial conditions, excluding brief reversals, was ~5000 years, much greater than for other stadials

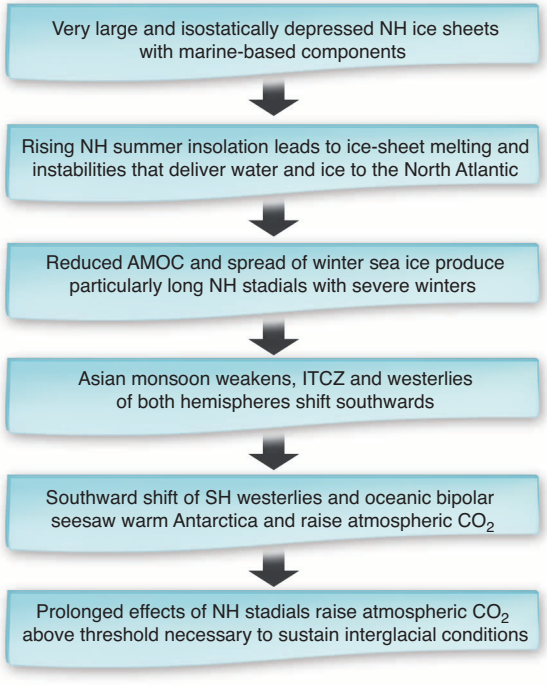

Fig. 4. Essential elements of a termination. Summary of the conditions and processes described in the text that contribute to the termination of a Late Pleistocene ice age (e.g., T1 to T4 in Fig. 2). AMOC indicates Atlantic Meridional Overturning Circulation.

evident in the Asian monsoon record (*7*). We attribute this long duration of stadials at terminations to the presence of exceptionally large NH ice sheets, poised for unstable collapse, at the time of increasing NH summer insolation. In this sense, HS1 nearly brought Earth to this threshold, but the YDS was necessary to complete the termination by raising CO_2 above the level required to achieve interglacial conditions.

Broader Implications

Explaining the near coincidence of the last termination in both polar hemispheres has been a long-standing problem. For example, following Milankovitch's (*5*) reasoning that glaciers at middle to high latitudes wax and wane in response to varying summer insolation, Mercer (*55*) noted that recession of middle-latitude SH mountain glaciers during the last termination, that is, a period of declining local summer insolation intensity from the precession effect (18 to 11 ka), "defies explanation." Broecker (*56*) suggested that changes in atmospheric CO_2 would help resolve this problem by synchronizing the hemispheres, but he could not identify a mechanism that would cause CO_2 to change before NH ice volume.

Our hypothesis addresses this dilemma of coupling the hemispheres during the last termination despite out-of-phase summer insolation signals. We suggest that the combined influence of the oceanic bipolar seesaw and the southward displacement of the SH westerlies, both linked to northern stadials, allowed the high southern latitudes to warm as a result of melting and collapse of NH ice sheets into the North Atlantic. Invoking the same principles, we suggest that a northward displacement of the ITCZ and of the SH westerlies at the onset of the Bølling (~14.7 ka) created the pause in the warming of Antarctica midway through the last termination.

Our hypothesis further points to higher atmospheric CO_2, driven by the reorganization of ocean and atmospheric circulation that accompanied northern stadials, as a key factor to complete the deglaciation (Fig. 4). Specifically, it was the long duration of stadial conditions made possible by large and unstable ice sheets that extracted enough CO_2 from the deep ocean to warm Earth and then to sustain melting of NH ice sheets for several thousand years after NH summer insolation started to decline. We suggest that this combination of factors was instrumental in terminating the last ice age on a global scale. Furthermore, the effects of these long northern stadials could well have been augmented by the consequences of orbitally induced lengthening of summers and shortening of winters in high southern latitudes (*57*).

Our hypothesis also implies widespread reorganizations of atmospheric circulation during the last termination. Changes in the Asian monsoon (Fig. 3B) and in records from lakes [e.g., (*58*)] and speleothems (Fig. 3C) indicate a reorganization of NH winds during North Atlantic stadial periods. Global reorganization of atmospheric circulation forced by such stadial conditions affords a unifying hypothesis for many features of climate variability throughout the last glacial cycle. In addition to explaining key aspects of the last termination, noted above, it provides a mechanism to account for other climate-related signals that have been correlated with stadial-interstadial cycles in Greenland ice cores, such as changes in marine biological productivity and in the intensity of oxygen minimum zones both in the Arabian Sea [e.g., (*59*)] and in the eastern North Pacific [e.g., (*60*)]. It also affords a benchmark for testing and improving climate models, for example, in simulating the response of atmospheric circulation to meridional surface temperature gradients (SOM).

References and Notes

1. W. S. Broecker, J. van Donk, *Rev. Geophys. Space Phys.* **8**, 169 (1970).
2. G. H. Denton, T. J. Hughes, *The Last Great Ice Sheet* (Wiley Interscience, NY, 1981).
3. S. Toucanne *et al.*, *Quat. Sci. Rev.* **28**, 1238 (2009).
4. A. S. Dyke, V. K. Prest, *Geogr. Phys. Quat.* **41**, 237 (1987).
5. M. Milankovitch, *Kanon der Erdbestrahlung und Seine Andwendung auf das Eiszeitenproblem* (Royal Serbian Academy Special Publication 132, Belgrade, Serbia, 1941).
6. G. Roe, *Geophys. Res. Lett.* **33**, L24703 (2006).
7. H. Cheng *et al.*, *Science* **326**, 248 (2009).
8. K. Kawamura *et al.*, *Nature* **448**, 912 (2007).
9. L. E. Lisiecki, M. E. Raymo, *Paleoceanography* **20**, PA1003 (2005).
10. M. E. Raymo, *Paleoceanography* **12**, 577 (1997).
11. G. H. Denton, T. J. Hughes, *Quat. Sci. Rev.* **21**, 193 (2002).
12. R. Knutti, J. Flückiger, T. F. Stocker, A. Timmermann, *Nature* **430**, 851 (2004).
13. Z. Liu *et al.*, *Science* **325**, 310 (2009).
14. H. Heinrich, *Quat. Res.* **29**, 142 (1988).
15. G. C. Bond, R. Lotti, *Science* **267**, 1005 (1995).
16. F. Naughton *et al.*, *Earth Planet. Sci. Lett.* **284**, 329 (2009).
17. S. Barker *et al.*, *Nature* **457**, 1097 (2009).
18. G. H. Denton, W. S. Broecker, R. B. Alley, *PAGES News* **14**, 14 (2006).
19. E. Bard, F. Rostek, J.-L. Turon, S. Gendreau, *Science* **289**, 1321 (2000).
20. G. H. Denton, R. B. Alley, G. C. Comer, W. S. Broecker, *Quat. Sci. Rev.* **24**, 1159 (2005).
21. R. F. B. Isarin, H. Renssen, *Earth Sci. Rev.* **48**, 1 (1999).
22. R. F. B. Isarin, H. Renssen, J. Vandenberghe, *J. Quat. Sci.* **13**, 447 (1998).
23. H. Renssen, R. F. B. Isarin, *Global Planet. Change* **30**, 117 (2001).
24. J. C. H. Chiang, C. M. Bitz, *Clim. Dyn.* **25**, 477 (2005).
25. J. P. Severinghaus, T. Sowers, E. J. Brook, R. B. Alley, M. L. Bender, *Nature* **391**, 141 (1998).
26. H. W. Arz, J. Patzold, G. Wefer, *Quat. Res.* **50**, 157 (1998).
27. L. C. Peterson, G. H. Haug, K. A. Hughen, U. Röhl, *Science* **290**, 1947 (2000).
28. G. Leduc, L. Vidal, K. Tachikawa, E. Bard, *Quat. Res.* **72**, 123 (2009).
29. R. Saikku, L. Stott, R. Thunell, *Quat. Sci. Rev.* **28**, 2374 (2009).
30. X. F. Wang *et al.*, *Nature* **432**, 740 (2004).
31. M. L. Griffiths *et al.*, *Nat. Geosci.* **2**, 636 (2009).
32. J. Muller *et al.*, *Quat. Sci. Rev.* **27**, 468 (2008).
33. T. P. Barnett, L. Dümenil, U. Schlese, E. Roeckner, *Science* **239**, 504 (1988).
34. F. Gasse, F. Chalie, A. Vincens, M. A. J. Williams, D. Williamson, *Quat. Sci. Rev.* **27**, 2316 (2008).
35. G. H. Denton *et al.*, *Geogr. Ann. Ser. A* **81A**, 107 (1999).
36. E. L. Sikes *et al.*, *Paleoceanography* **24**, PA2201 (2009).
37. E. Calvo, C. Pelejero, P. De Deckker, G. A. Logan, *Geophys. Res. Lett.* **34**, L13707 (2007).
38. T. T. Barrows, S. Juggins, P. De Deckker, E. Calvo, C. Pelejero, *Paleoceanography* **22**, PA2215 (2007).
39. J. Kaiser, F. Lamy, D. Hebbeln, *Paleoceanography* **20**, PA4009 (2005).
40. F. Lamy *et al.*, *Earth Planet. Sci. Lett.* **259**, 400 (2007).
41. T. J. Crowley, *Paleoceanography* **7**, 489 (1992).
42. W. S. Broecker, *Paleoceanography* **13**, 119 (1998).
43. R. F. Anderson *et al.*, *Science* **323**, 1443 (2009).
44. J. C. H. Chiang, *Annu. Rev. Earth Planet. Sci.* **37**, 263 (2009).
45. P. I. Moreno, T. V. Lowell, G. L. Jacobson Jr., G. H. Denton, *Geogr. Ann. Ser. A* **81A**, 285 (1999).
46. E. Bard, R. E. M. Rickaby, *Nature* **460**, 380 (2009).
47. F. J. C. Peeters *et al.*, *Nature* **430**, 661 (2004).
48. A. Levermann, J. Schewe, M. Montoya, *Geophys. Res. Lett.* **34**, L12711 (2007).
49. J. A. Screen, N. P. Gillett, D. P. Stevens, G. J. Marshall, H. K. Roscoe, *J. Clim.* **22**, 806 (2009).
50. R. S. Lindzen, A. Y. Hou, *J. Atmos. Sci.* **45**, 2416 (1988).
51. S. Lee, H. K. Kim, *J. Atmos. Sci.* **60**, 1490 (2003).
52. H. Conway, B. L. Hall, G. H. Denton, A. M. Gades, E. D. Waddington, *Science* **286**, 280 (1999).
53. J. Ahn, E. J. Brook, *Science* **322**, 83 (2008); published online 11 September 2008 (10.1126/science.1160832).
54. E. W. Wolff, H. Fischer, R. Rothlisberger, *Nat. Geosci.* **2**, 206 (2009).
55. J. H. Mercer, in *Climate Processes and Climate Sensitivity*, J. E. Hansen, T. Takahashi, Eds. (American Geophysical Union, Washington, DC, 1984), pp. 307–313.
56. W. S. Broecker, *Prog. Oceanogr.* **11**, 151 (1982).
57. P. Huybers, G. Denton, *Nat. Geosci.* **1**, 787 (2008).
58. L. Benson, M. Kashgarian, M. Rubin, *Palaeogeogr. Palaeoclimatol. Palaeoecol.* **117**, 1 (1995).
59. M. A. Altabet, M. J. Higginson, D. W. Murray, *Nature* **415**, 159 (2002).
60. J. D. Ortiz *et al.*, *Geology* **32**, 521 (2004).
61. W. S. Broecker, G. H. Denton, *Sci. Am.* **262**, 48 (1990).
62. J. I. Svendsen *et al.*, *Quat. Sci. Rev.* **23**, 1229 (2004).
63. R. Gersonde, X. Crosta, A. Abelmann, L. Armand, *Quat. Sci. Rev.* **24**, 869 (2005).
64. W. G. Thompson, S. L. Goldstein, *Quat. Sci. Rev.* **25**, 3207 (2006).
65. A. Berger, M. F. Loutre, *Quat. Sci. Rev.* **10**, 297 (1991).
66. M. Stuiver, P. M. Grootes, *Quat. Res.* **53**, 277 (2000).
67. Y. J. Wang *et al.*, *Science* **294**, 2345 (2001).
68. D. X. Yuan *et al.*, *Science* **304**, 575 (2004).
69. Y. Asmerom, V. Polyak, S. J. Burns, *Nat. Geosci.* **3**, 114 (2010).
70. J. F. McManus, R. Francois, J. M. Gherardi, L. D. Keigwin, S. Brown-Leger, *Nature* **428**, 834 (2004).
71. J. Strelin, G. H. Denton, *Proceedings of the XVI Congreso Geologico Argentino*, Asociación Geológica Argentina, La Plata, Argentina, 20 to 23 September 2005, article 269.
72. E. Monnin *et al.*, *Science* **291**, 112 (2001).
73. T. M. Marchitto, S. J. Lehman, J. D. Ortiz, J. Flückiger, A. van Geen, *Science* **316**, 1456 (2007).

74. Comments from W. S. Broecker and three anonymous reviewers improved this manuscript. S. Birkel assisted in drafting the figures. Work described in this paper was funded by a grants/cooperative agreement from the National Oceanic and Atmospheric Administration and by the Gary C. Comer Science and Education Foundation. The views expressed herein are those of the authors and do not necessarily reflect the views of NOAA or any of its subagencies. This is Lamont-Doherty Earth Observatory contribution number 7368.

Supporting Online Material

www.sciencemag.org/cgi/content/full/328/5986/1652/DC1
SOM Text
References

10.1126/science.1184119

Plants Integrate Information About Nutrients and Neighbors

James F. Cahill Jr.,[1]* Gordon G. McNickle,[1] Joshua J. Haag,[1]† Eric G. Lamb,[2] Samson M. Nyanumba,[1] Colleen Cassady St. Clair[1]

All organisms are challenged by the need to find patchy resources efficiently, resulting in the evolution of diverse foraging strategies (*1*). Plants exhibit a variety of behaviors in response to environmental stimuli (*2*), including altering the spatial distribution of their roots as a function of resource patchiness (*3*). Competitors also induce behavioral changes in plants, including increased (*4*) or decreased (*5*) root growth.

Because it is unknown whether plants synthesize these different types of information, we measured patterns of root growth of *Abutilon theophrasti* (Malvaceae) while manipulating both resource distributions and competition (*6*). Our goal was to determine whether root foraging behavior was an additive response to multiple forms of environmental information or whether plants used novel behaviors under different combinations of conditions.

A. theophrasti seedlings received one of six factorial combinations of soil heterogeneity (uniform, patch-center, and patch-edge) and competition treatments (alone versus with competition) (Fig. 1). In all treatments, one focal individual was planted on one side of the mesocosm. A second individual (of the same species) was planted on the opposite side (with competition), but not in the alone treatment. Soil nutrients were distributed homogenously throughout the soil [uniform (Fig. 1, A and D)], concentrated in a single patch in the middle of the mesocosm [patch-center (Fig. 1, B and E)], or concentrated in a single patch near the mesocosm edge on the outside of the focal plant [patch-edge (Fig. 1, C and F)]. Root distributions were recorded with a mini-rhizotron camera over 8 weeks of growth. We then removed the plant shoots and injected dyes of different colors into each root system. Root identity (focal versus competitor) was determined on the basis of color (*7*). We measured the distribution of the focal plant's roots in the soil; root and shoot biomass were also measured.

We analyzed presence or absence of focal plant roots in each location in the soil (Fig. 1, lines) and maximum rooting breadth (Fig. 1, bars) by using mixed models. In each analysis, soil heterogeneity and competition served as fixed effects and mesocosm as a random effect. For the presence-absence data, the model also included distance from stem as a fixed effect and mesocosm as a random effect.

The likelihood of a focal plant root occurring in a given soil location was influenced by a three-way interaction among distance from stem, heterogeneity, and competition ($P = 0.04$, table S1), whereas the maximum rooting breadth was influenced by an interaction between heterogeneity and competition ($P = 0.075$, table S2). When grown alone, plants adopted a broad rooting strategy regardless of the distribution of resources (Fig. 1, A to C), indicating that resource distributions alone did not alter root placement, consistent with prior work on *A. theophrasti* (*8*).

In contrast, competitors reduced both the likelihood of focal plant roots occurring far from the stem and focal plant rooting breadth, but these effects were moderated by nutrient distributions (Fig. 1 and table S2). In uniform soil with competition, plants had the most restricted root distribution (Fig. 1D), resulting in spatial soil segregation among the two plants. In the patch-center treatment with a competitor, plants had a broader root distribution (Fig. 1E), where plant roots overlapped in the patch and thus were not segregated. In the patch-edge treatment with competition, the root distribution of the focal plant roots was intermediate in breadth (Fig. 1E).

These data suggest root placement for this species is determined by a hierarchical set of decision rules dependent on presence or absence of a neighbor. First, if a plant grew alone, it adopted a broad foraging strategy that was agnostic with respect to resource distributions (Fig. 1, A to C). Second, if neighbors were present, a restricted foraging strategy was adopted that was modified by resource distributions (Fig. 1, D to F). This effect was most pronounced when nutrients were more abundant in the same direction as the competitor (Fig. 1, D to F).

Thus, plants nonadditively integrate information about both resource and neighbor-based cues in the environment. If such complex behaviors are widespread, they may influence spatial segregation and territoriality, niche differentiation and species coexistence, and the basic understanding of plant behavioral ecology.

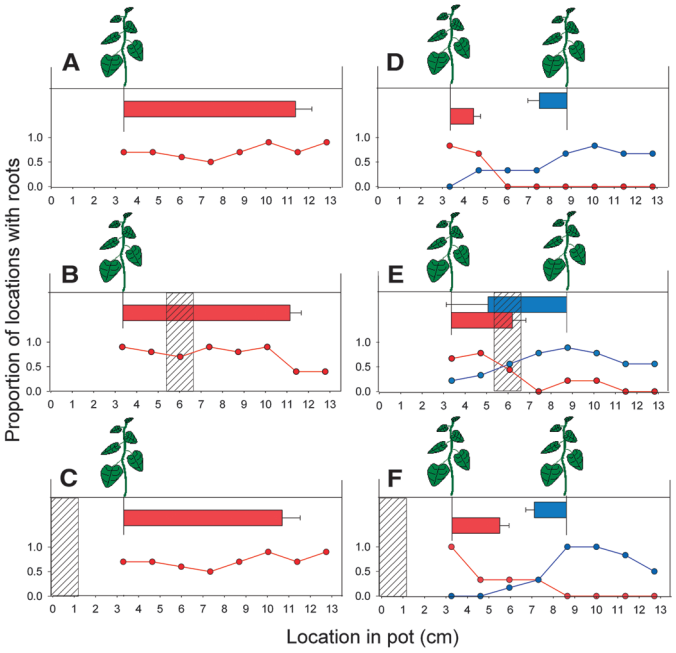

Fig. 1. The annual plant *A. theophrasti* was planted into six combinations of soil heterogeneity (uniform, patch-center, and patch-edge) and competition (alone versus with a competitor) treatments. **(A)** Alone uniform, **(B)** alone patch-center, **(C)** alone patch-edge, **(D)** competition uniform, **(E)** competition patch-center, and **(F)** competition patch-edge. Hatched areas denote nutrient patches (when present). Plant illustrations indicate the location of focal and competitor plants. Red data obtained from the focal plant; blue, data from the competitor (when present). The horizontal bars represent average root breadth (±1 SE), and the lines at the bottom of each frame indicate the proportion of replicates with focal plant roots in each location in the pot.

References and Notes

1. D. W. Stephens, J. S. Brown, R. C. Ydenberg, *Foraging: Behavior and Ecology* (Univ. Chicago Press, Chicago, 2007).
2. R. Karban, *Ecol. Lett.* **11**, 727 (2008).
3. A. Hodge, *New Phytol.* **162**, 9 (2004).
4. M. Gersani, J. S. Brown, E. E. O' Brien, G. M. Maina, Z. Abramsky, *J. Ecol.* **89**, 660 (2001).
5. B. E. Mahall, R. M. Callaway, *Proc. Natl. Acad. Sci. U.S.A.* **88**, 874 (1991).
6. Materials and methods are available as supporting material on *Science* Online.
7. C. Holzapfel, P. Alpert, *Oecologia* **134**, 72 (2003).
8. S. W. Kembel, J. F. Cahill Jr., *Am. Nat.* **166**, 216 (2005).

9. We thank G. Law for assistance with the Biotron plant growth facility, C. Wild for explanations of behavioral theory and trait correlations, and three anonymous reviewers for helpful comments. Supported by a Natural Sciences and Engineering Research Council of Canada Discovery Grant to J.F.C.

Supporting Online Material

www.sciencemag.org/cgi/content/full/328/5986/1657/DC1
Materials and Methods
Fig. S1
Tables S1 to S3
References

17 March 2010; accepted 14 May 2010
10.1126/science.1189736

[1]Department of Biological Sciences, University of Alberta, Edmonton, AB T6G 2E9, Canada. [2]Department of Plant Sciences, University of Saskatchewan, Saskatoon, SK S7N 5A8, Canada.

*To whom correspondence should be addressed. E-mail: jc.cahill@ualberta.ca
†Present address: joshua.j.haag@gmail.com

Delay in Photoemission

M. Schultze,[1,2]* M. Fieß,[2] N. Karpowicz,[2] J. Gagnon,[1,2] M. Korbman,[2] M. Hofstetter,[1] S. Neppl,[3] A. L. Cavalieri,[2] Y. Komninos,[4] Th. Mercouris,[4] C. A. Nicolaides,[4] R. Pazourek,[5] S. Nagele,[5] J. Feist,[5,6] J. Burgdörfer,[5] A. M. Azzeer,[7] R. Ernstorfer,[3] R. Kienberger,[2,3] U. Kleineberg,[2] E. Goulielmakis,[2] F. Krausz,[1,2] V. S. Yakovlev[1,2]*

Photoemission from atoms is assumed to occur instantly in response to incident radiation and provides the basis for setting the zero of time in clocking atomic-scale electron motion. We used attosecond metrology to reveal a delay of 21 ± 5 attoseconds in the emission of electrons liberated from the 2*p* orbitals of neon atoms with respect to those released from the 2*s* orbital by the same 100–electron volt light pulse. Small differences in the timing of photoemission from different quantum states provide a probe for modeling many-electron dynamics. Theoretical models refined with the help of attosecond timing metrology may provide insight into electron correlations and allow the setting of the zero of time in atomic-scale chronoscopy with a precision of a few attoseconds.

The emission of an electron from an atom upon the absorption of an energetic photon (photoemission, or the photoelectric effect) is one of the most elementary quantum-mechanical phenomena (*1*–*3*). In the absence of resonances, the formation of the outgoing wave packet is usually presumed to instantly follow temporal variations of the incident light field. A delayed response, the possibility of which was recognized in the 1950s (*4*, *5*), would have several far-reaching consequences. If a single electron is set free when an atom absorbs a photon, it is, strictly speaking, not a single-electron process. Rather, it is the result of the correlated motion of all the electrons; hence, electron correlations generally affect the properties of the emitted photoelectron (*6*, *7*). As a consequence, comprehensive attosecond-scale temporal characterization of photoemission promises new insights into intra-atomic electron correlations and can bolster theoretical models of dynamic changes of atomic structure (*8*) and of correlated many-electron dynamics.

Furthermore, a delay in photoemission implies a change in the timing of ejection of the electron pulse with respect to the arrival of the photon pulse. This would compromise the accuracy of setting the zero of time for clocking microscopic processes on the atomic time scale. Capturing the outgoing electron with the controlled electric field of a laser pulse (*9*) via attosecond streaking (*10*, *11*) provides the only means of timing the arrival of a photon pulse with a precision comparable to the atomic unit of time. This timing is of fundamental importance because attosecond light pulses (*12*–*15*) presently constitute the most precise trigger for timing electronic processes. Hence the zero of time in atomic-scale chronoscopy, the time-resolved observation of electronic and concomitant processes, is to coincide with the arrival time of this photon pulse. Any unknown delay Δt in the emission of the photoelectron wave packet will result in an apparent shift of the origin of the time arrow (Fig. 1A). This introduces an unknown systematic error in clocking the microscopic motion under scrutiny, preventing us from revealing its details. Reliable absolute timing information would be essential, for example, in understanding the multielectron response of metals and semiconductors to sudden excitations (*16*).

Our measurements reveal a small delay time between the formation of electron wave packets originating from different atomic orbitals. The temporal properties of both wave packets were recorded by means of attosecond streaking (*10*), and the measured spectrograms were found to be shifted with respect to each other along the pump-probe delay axis (henceforth referred to as temporally shifted), as if one of the wave packets were emitted later than the other. Comprehensive quantum simulations show that a delay of one wave packet with respect to the other indeed results in a temporal shift between spectrograms, even though the delay between wave packets and the shift between spectrograms may not be exactly equal to each other. The delay considered here is of a different physical origin than that previously observed in photoemission from a solid (*17*), where a temporal shift was attributed to transport effects that occur before an electron reaches the surface (*18*, *19*).

Attosecond streaking measurements on Ne. Ne was chosen for our study for two reasons. First, its small polarizability precludes the possibility of an artificial temporal shift of the spectrogram due to the Stark effect (*20*). Second, the relatively high photoionization cross-section (*21*) benefits the signal-to-noise ratio (*S*/*N*) of attosecond streaking, which is of crucial importance for achieving the required timing accuracy.

Even the most advanced measurements in photoelectron spectroscopy can only provide energy and angle-resolved probability distributions (*22*, *23*). Probing the photoionization cross-section corresponds to measuring the absolute values of complex-valued matrix elements that quantum mechanics assigns to transitions from a bound atomic state to states where a photoelectron propagates toward the detector. The quantum phase of the matrix element, the energy derivative of which defines the emission timing (*5*), has largely remained experimentally inaccessible (*24*). Our work demonstrates that the energy derivative of the quantum phase, which is closely related to the Wigner-Smith time delay (*4*, *25*), can now be accessed by attosecond streaking.

Pushing attosecond timing metrology into the sub–10-as regime has been enabled by waveform-controlled near–single-cycle pulses (duration ~3.3 fs) of near-infrared (NIR, carrier wavelength ~750 nm) light (*26*). These pulses permit the generation of isolated sub–100-as extreme ultraviolet (XUV) pulses via high-order harmonic generation (*12*, *14*). More importantly for the present study, they increase the XUV photon yield by two orders of magnitude, resulting in an attosecond photon flux (at ~100 eV) in excess of 10^{11} photons/s (*14*). The resulting more than 10-fold improvement in *S*/*N* has advanced the timing accuracy of attosecond streaking to a fraction of the atomic unit of time.

High-order harmonic generation in Ne atoms driven by sub–4-fs NIR pulses yields robust XUV continua in the energy range of 100 to 140 eV, which are stable against substantial changes in the carrier-envelope phase (*14*). This bandwidth supports isolated pulses below 100 as in duration. Simultaneous temporal characterization of photoemission pathways with distinguishable final ionic states calls for recording streaking spectrograms that are well separated in energy and sets a limit on the XUV bandwidth. To fulfill this condition for the photoelectrons arising from the 2*p* and 2*s* subshells of Ne atoms, the spectrum of attosecond pulses is confined with a specially designed lanthanum/molybdenum multilayer XUV mirror and a 150-nm-thick metallic foil. In combination, they act as a bandpass filter centered at 106 eV, with a full width at half maximum of 14 eV, supporting a Fourier-limited XUV pulse duration well below 200 as.

Photoelectrons ejected from Ne atoms by 106-eV attosecond pulses and streaked by the electric field of near–single-cycle NIR pulses were recorded with a time-of-flight spectrometer versus the delay between the XUV and NIR pulses (Fig. 2A). The electron spectrometer

[1]Department für Physik, Ludwig-Maximilians-Universität, Am Coulombwall 1, D-85748 Garching, Germany. [2]Max-Planck-Institut für Quantenoptik, Hans-Kopfermann-Straße 1, D-85748 Garching, Germany. [3]Physik Department, Technische Universität München, James-Franck-Straße, D-85748 Garching, Germany. [4]Theoretical and Physical Chemistry Institute, National Hellenic Research Foundation, 48 Vassileos Constantinou Avenue, Athens 11635, Greece. [5]Institute for Theoretical Physics, Vienna University of Technology, Wiedner Hauptstraße 8-10, 1040 Vienna, Austria. [6]Institute for Theoretical Atomic, Molecular and Optical Physics (ITAMP), Harvard-Smithsonian Center for Astrophysics, Cambridge, MA 02138, USA. [7]Physics and Astronomy Department, King Saud University, Riyadh 11451, Saudi Arabia.

*To whom correspondence should be addressed. E-mail: Martin.Schultze@mpq.mpg.de (M.S.), Vladislav.Yakovlev@physik.uni-muenchen.de (V.S.Y.)

was equipped with an electrostatic lens, enhancing electron counts in the spectral range between 40 and 70 eV. Figure 2B shows the streaking spectrogram reconstructed by the use of an algorithm based on frequency-resolved optical gating (FROG) (*27*–*29*). The measured and calculated spectrograms show excellent agreement. Quantitative comparison of streaked spectral lineouts in Fig. 2D demonstrates the high fidelity with which the characteristics of the emitted electron wave packets can be retrieved (*30*) (Fig. 2C). The evaluated group delay versus frequency reveals that the emission of the electron wave packet from the 2*p* state lags behind that originating from the 2*s* state by approximately 20 as. The linear slope of the group delay representing an energy sweep of the emitted electrons potentially provides more insight into photoemission dynamics. We reproducibly observed a difference between the energy sweeps of the 2*s* and 2*p* wave packets on the order of several thousand attoseconds squared. Simulations show, however, that the retrieved energy sweep, in contrast to the average group delay, is sensitive to the electrostatic lens. Hence, the energy sweeps cannot be reliably inferred from the current measurements.

In addition to the FROG approach, we have developed a simplified procedure in order to extract the delay from a large set of measured attosecond streaking spectrograms [for details, see the caption of Fig. 3 and (*29*)]. Figure 3 summarizes the relative delay extracted from 40 measurements via this method. The result of this analysis agrees within the experimental error with the one obtained with the FROG technique (*29*). We found a clear correlation between the uncertainty of the evaluated delay and the fractional energy carried by a satellite XUV pulse accompanying the main attosecond pulse. Therefore, we selected a set of delay values evaluated from streaking spectrograms acquired with attosecond XUV pulses exhibiting less than 3% satellite pulse content (red diamonds, Fig. 3). These data result in a mean relative delay of 21 as between 2*p* and 2*s* photoelectrons, with a standard deviation of 5 as. In order to exclude any influence of shakeup states on the evaluated delay, the measurements were repeated using an XUV multilayer mirror with a bandwidth of 4.5 eV centered at ~121 eV (supporting Fourier-limited pulses of ~400 as) in another attosecond beamline. The narrower spectrum of these XUV pulses allowed us to spectrally separate the direct 2*s* emission line from most of its much weaker high-order shakeup satellites. The results are also plotted in Fig. 3 (green circles) and found, within our error bars, to be in agreement with the ones achieved with sub–200-as pulses.

The measurements summarized in Fig. 3 were performed by applying streaking laser electric fields of different strength, varying by a factor of 6 in amplitude; that is, by a factor of 36 in intensity. In spite of this large dynamic range, the observed delay shows no dependence on the amplitude of the streaking field. The error

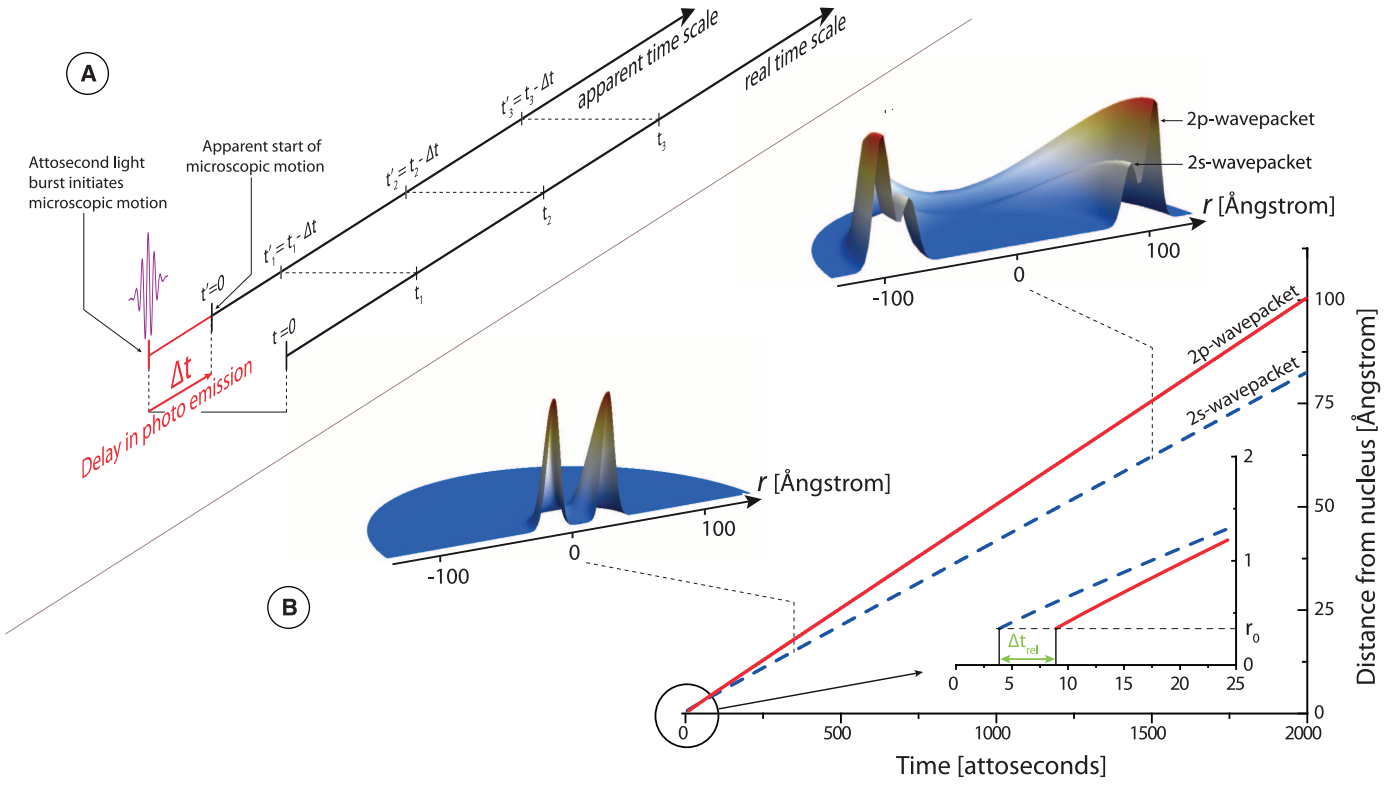

Fig. 1. Attosecond delay in photoemission and its consequences. (**A**) The "real" time scale begins at the maximum of the XUV pulse, whereas the "apparent" time scale in the measurement starts with the release of an electron wave packet and is temporally shifted by a possible delay Δt in photoemission. A delay between the arrival time of the attosecond XUV excitation pulse and the instant of emission would falsify the conclusions reached from measurements with an atomic chronoscope, which is triggered by the emission of an electron wave packet. A microscopic event that occurred at $t = t_{event}$ is indicated by this chronoscope to have apparently happened at $t' = t_{event} - \Delta t$, thereby tainting a comparison between theory and experiment with an unknown systematic error of Δt. (**B**) The surface plots show the spatial distribution of the photoelectron density around the atomic core at $t_1 = 300$ as and $t_2 = 1500$ as after the maximum of the XUV pulse, evaluated by solving the time-dependent Schrödinger equation with the aid of the state-specific expansion approach. As time progresses, the wave packets released from the 2*s* and 2*p* subshells become spatially separated because of their different velocities. Far from the nucleus, where the overlap with ionic orbitals is negligible, their motion can be described semi-classically. Therefore, knowing the average position and velocity of a wave packet that propagates toward the detector, we can illustrate a possible delay in its emission by tracing a classical electron trajectory back to the ion. The red solid and blue dashed lines show the classical trajectories of the 2*p* and 2*s* photoelectrons, respectively. The lines terminate at a distance $r_0 \approx 0.3$ Å, which is equal to the radius of the valence shell. At this distance, the trajectories behave as if they started with a relative delay $\Delta t_{rel} = 5$ as, which is in reasonable agreement with the value obtained by a more rigorous theoretical analysis.

bars are reduced at higher intensities, primarily because of the increased spectral shift.

Theoretical discussion. First, we show that the measured delay of ~20 as cannot be explained by a delayed onset of streaking, which was the dominant effect in (*17*). The streaking NIR field may be significantly screened by bound electrons at small distances from the nucleus. After the absorption of an XUV photon, it takes the positive-energy electron a finite time to leave this screened volume, and this time interval may be different for electrons originating from different orbitals. However, for an atom, this difference cannot exceed a few attoseconds. The characteristic scales can be extracted from the classical trajectories shown in Fig. 1B. If we assume that the 2*s* and 2*p* electrons are set in motion at the same moment, their classical trajectories would acquire a relative delay of 20 as after traveling over 5 Å, whereas significant screening from the streaking field is limited to a distance of less than 1 Å from the nucleus. Furthermore, if screening played a dominant role, the faster 2*p* electrons would be exposed to the streaking field earlier than the slower 2*s* ones, whereas measurements and quantum simulations show that the slower electron is emitted first.

Now we turn our attention to the quantum-mechanical description. First of all, we need a definition for the photoemission delay. Consider a photoelectron wave function $|\psi(t)\rangle$ created by an XUV pulse centered at $t = 0$. The motion of the wave packet after photoionization is conveniently described in a basis of continuum states $|\varepsilon\rangle$, each of which has a well-defined energy ε and describes a wave that propagates in the direction of the detector. In this basis, each probability amplitude has a simple time dependence: $\langle\varepsilon|\psi(t)\rangle = \chi(\varepsilon)e^{-i\frac{\varepsilon}{\hbar}t}$, where the complex-valued function $\chi(\varepsilon)$ fully describes the properties of the wave packet. In this representation, a delay Δt in photoemission, shown as a shift of the electron's trajectory in Fig. 1B, adds $\frac{\varepsilon}{\hbar}\Delta t$ to the phase of $\chi(\varepsilon)$. It is therefore meaningful to define the group delay of the outgoing electron wave packet, in accordance with earlier work (*4*, *5*, *25*), as $\alpha(\varepsilon) = \hbar\frac{d}{d\varepsilon}\arg[\chi(\varepsilon)]$. Analyzing our simulations, we average $\alpha(\varepsilon)$over the bandwidth of the XUV pulse (*29*) and denote the result as $\overline{\alpha}$.

As the first and most important task, we validate the experimental methodology. Intuitively, one expects that a delay in the formation of a wave packet causes a corresponding temporal shift of the streaking spectrogram. This holds true

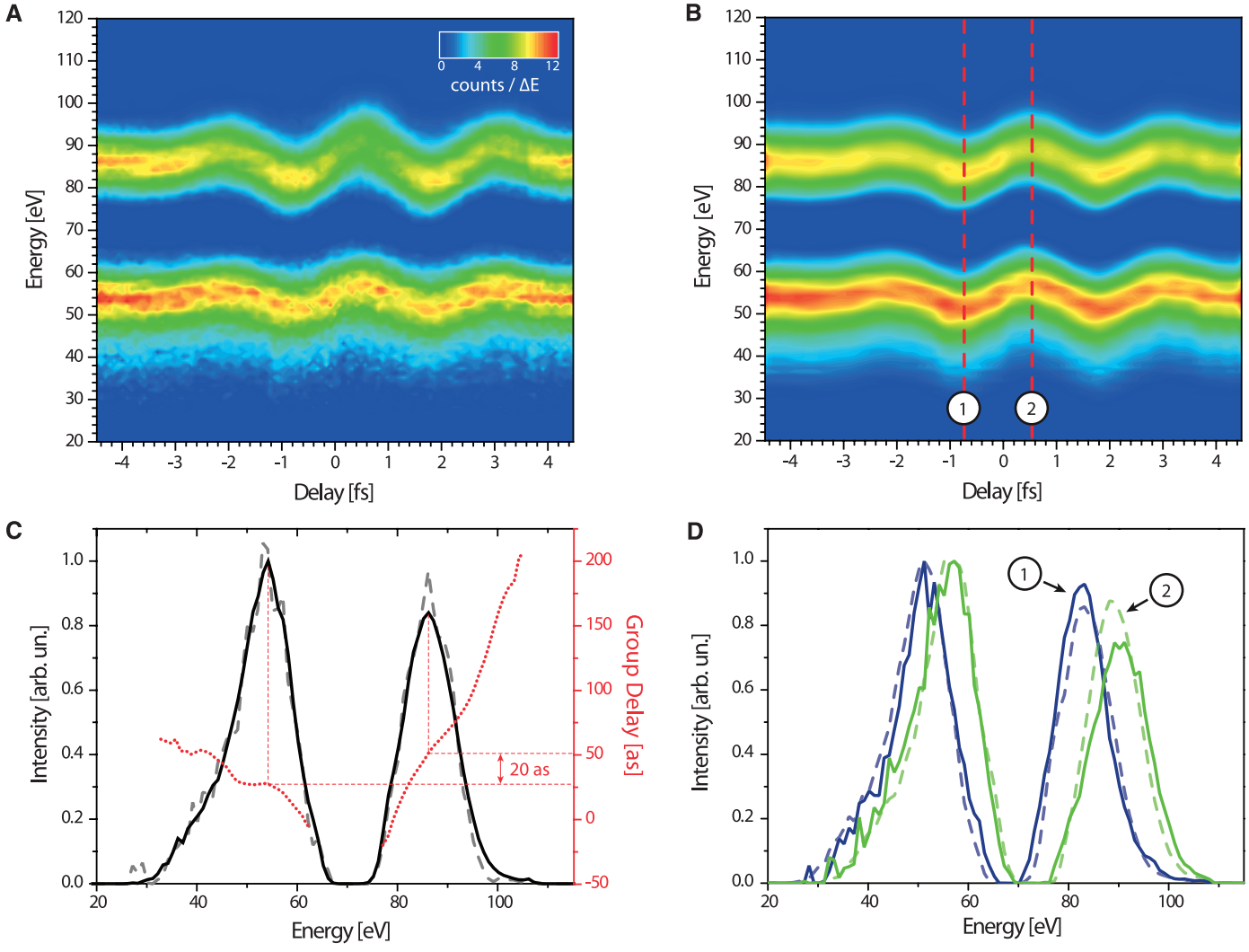

Fig. 2. Attosecond streaking spectrograms (**A** and **B**), evaluated photoelectron wave packets (**C**), and streaked spectra (**D**). The spectrograms in (A) are composed of a series of photoelectron energy spectra recorded by releasing 2*s* and 2*p* electrons from Ne with an attosecond XUV pulse in the presence of a strong NIR few-cycle laser field, as a function of the delay between the XUV and NIR fields. The spectrogram is processed with a FROG algorithm tailored for streaking measurements (*30*). (B) shows the spectrogram reconstructed by this algorithm. The retrieved 2*s* and 2*p* spectra, together with the respective group delays, are plotted in (C) (black solid line and red dotted line, respectively). The reconstructed energy spectra are in excellent agreement with the measured ones (gray dashed line). The average difference between the group delays corresponds to a 20-as retardation of the 2*p* emission with respect to the 2*s* emission. (D) compares reconstructed and measured streaked spectra at two delays, which exhibit the largest positive and negative shifts of the electron energy distribution.

within the Coulomb-Volkov approximation (CVA) (*29*). To quantify the accuracy of the CVA, the single-electron time-dependent Schrödinger equation in three spatial dimensions was numerically solved with an effective potential that modeled Ne (*29*). The analysis of wave packets yielded a spectrally averaged relative group delay of $\overline{\alpha}_{2p} - \overline{\alpha}_{2s} = 4.5$ as. Although the CVA yields the same value of the temporal shift between spectrograms, the numerical solution of the Schrödinger equation results in simulated spectrograms that are shifted with respect to each other by 6.8 as. The origin of this discrepancy lies in the fact that the photoelectron interacts with both the streaking field and the ion, resulting in a quantum motion that is not exactly described by known analytical approaches. Thus, for the current experimental parameters, the small deviations between the electron's exact motion and that modeled via the CVA give rise to a 2-as discrepancy in the relative delay.

Accepting this small discrepancy, many-electron models were applied to investigate the effects of electron correlation. As a first attempt, the multiconfigurational Hartree-Fock method was used to evaluate transition matrix elements from the ground state of Ne to states where the electron wave asymptotically propagated along the direction of the streaking NIR electric field. These matrix elements predict a relative delay of $\overline{\alpha}_{2p} - \overline{\alpha}_{2s} = 4.0$ as. The major drawback of this model is that it does not account for interchannel coupling (*6*). This deficiency was overcome by modeling the interaction with the XUV pulse using the state-specific expansion approach (*31*, *32*). This model accounts for electron correlations before and after photoionization and predicts a relative group delay of $\overline{\alpha}_{2p} - \overline{\alpha}_{2s} = 6.4$ as. Our modeling successfully predicts that the emission of 2*s* electrons precedes that of 2*p* electrons, but the computed relative delay is ~15 as (3 SD) smaller than the measured value.

So far, the theoretical discussion has focused on the relative delay between two photoemission channels, which can be acquired experimentally. Precise determination of the zero of time for allowing us to track the history of microscopic phenomena accurately (Fig. 1A) calls for precise knowledge of the delay between the XUV pulse and an outgoing electron wave packet (henceforth, absolute delay). This can only be inferred from theory. For multielectron systems, such as Ne, physical description of the discrepancies revealed by this work proved to be a challenge. The sensitive experimental test to which time-dependent many-electron models can now be subjected will benefit their development.

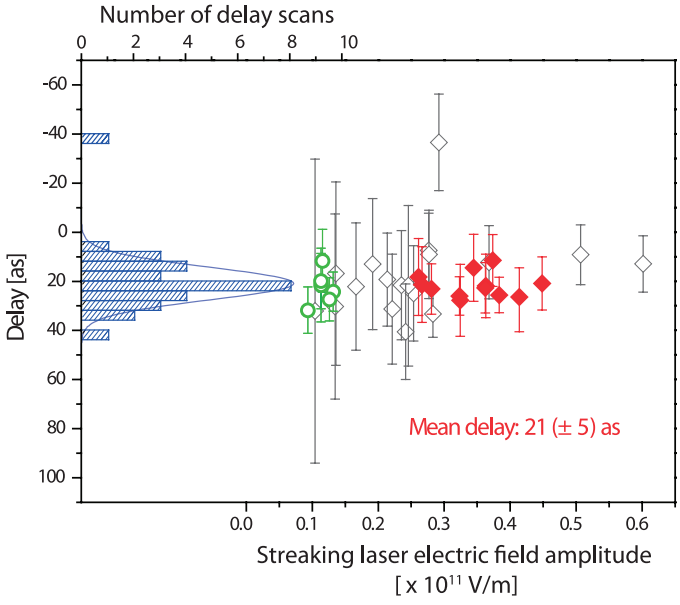

Fig. 3. The relative delay between photoemission from the 2*p* and 2*s* subshells of Ne atoms, induced by sub–200-as, near–100-eV XUV pulses. The depicted delays are extracted from measured attosecond streaking spectrograms by fitting a spectrogram, within the strong-field approximation, with parameterized NIR and XUV fields. Our optimization procedure matches the first derivatives along the time delay dimension of the measured and reconstructed spectrograms, thereby eliminating the influence of unstreaked background electrons [for details on the fitting algorithm, see (*29*)]. From the analysis of a set of spectrograms, the measured delays and associated retrieval uncertainties are plotted against the amplitude of the vector potential applied in the attosecond streak camera. Spectrograms measured in the presence of a satellite attosecond pulse were found to exhibit a less accurate retrieval of the delay value. When a subset of data (red diamonds) that represents scans with less than 3% satellite pulse content was evaluated, a mean delay value of 21 as with a standard deviation of ~5 as was found. The green circles represent the result of analyzing spectrograms recorded with an XUV pulse with narrower bandwidth in order to exclude the potential influence of shakeup states contributing to the electron kinetic energy spectrum.

Meanwhile, it is possible to obtain reliable absolute emission times for He, with which truly ab initio simulations (*33*) can be carried out with the help of supercomputers. Such simulations were performed for the He ($1s^2$) ground state, and for direct ionization with a 100-eV photon, a 5-as temporal shift of the spectrogram was found. Such modeling will allow precise timing calibration of attosecond measurements, once sufficiently powerful attosecond sources will allow the recording of spectrograms for He with sufficiently good statistics in spite of its small photoionization cross-section.

Conclusions and outlook. Establishing the zero of time in atomic chronoscopy is currently tainted with an error of up to several tens of attoseconds. Because attosecond streaking can measure only relative delays between different photoemission channels, the knowledge of absolute delays relies on the predictions of thoroughly tested time-dependent multielectron models. Presently, only two-electron ab initio simulations provide this degree of reliability, but the low photoionization cross-section of He limits (because of low *S*/*N*) the timing accuracy. For more complex systems, phase-sensitive measurements of the photoelectron wave packets via attosecond streaking will put many-electron models of atomic photoionization to comprehensive, highly sensitive tests, which is a prerequisite for gradually improving them and gaining trust in their predictions. These developments will improve our understanding of subatomic electron correlations and will make the absolute timing precision of atomic chronoscopy approach the 1-as frontier.

References and Notes

1. H. Hertz, *Annalen Physik Chem.* **267**, 983 (1887).
2. W. Hallwachs, *Annalen Physik Chem.* **269**, 301 (1888).
3. A. Einstein, *Annalen Physik* **17**, 132 (1905).
4. E. P. Wigner, *Phys. Rev.* **98**, 145 (1955).
5. C. A. A. de Carvalho, H. M. Nussenzveig, *Phys. Rep.* **364**, 83 (2002).
6. A. F. Starace, in *Handbuch der Physik*, W. Mehlhorn, Ed. (Springer, Berlin, 1982), vol. 31.
7. S. T. Manson, *Radiat. Phys. Chem.* **75**, 2119 (2006).
8. M. Y. Ivanov, J. P. Marangos, *J. Mod. Opt.* **54**, 899 (2007).
9. A. Baltuška *et al.*, *Nature* **421**, 611 (2003).
10. R. Kienberger *et al.*, *Nature* **427**, 817 (2004).
11. M. Nisoli, G. Sansone, *Prog. Quantum Electron.* **33**, 17 (2009).
12. G. Sansone *et al.*, *Science* **314**, 443 (2006).
13. M. Schultze *et al.*, *N. J. Phys.* **9**, 243 (2007).
14. E. Goulielmakis *et al.*, *Science* **320**, 1614 (2008).
15. M. Hentschel *et al.*, *Nature* **414**, 509 (2001).
16. A. Borisov, D. Sánchez-Portal, R. Díez Muiño, P. M. Echenique, *Chem. Phys. Lett.* **387**, 95 (2004).
17. A. L. Cavalieri *et al.*, *Nature* **449**, 1029 (2007).
18. A. K. Kazansky, P. M. Echenique, *Phys. Rev. Lett.* **102**, 177401 (2009).
19. C. Lemell, B. Solleder, K. Tőkési, J. Burgdörfer, *Phys. Rev. A* **79**, 062901 (2009).
20. J. C. Baggesen, L. B. Madsen, *Phys. Rev. Lett.* **104**, 043602; and erratum, 209903 (2010).
21. U. Becker, D. A. Shirley, in *VUV and Soft X-Ray Photoionization*, U. Becker, D. A. Shirley, Eds. (Plenum, New York, 1997), chap. 5.
22. A. Rudenko *et al.*, *Phys. Rev. Lett.* **101**, 073003 (2008).
23. J. Mauritsson *et al.*, *Phys. Rev. Lett.* **100**, 073003 (2008).

24. The relative phases of interfering partial waves are accessible to measurement because they determine angular photoelectron distributions; still, this information is not sufficient to retrieve either the energy dependence of a phase in a particular photoionization channel or the relative phase between channels that do not interfere.
25. F. T. Smith, *Phys. Rev.* **118**, 349 (1960).
26. A. L. Cavalieri *et al*., *N. J. Phys.* **9**, 242 (2007).
27. Y. Mairesse, F. Quéré, *Phys. Rev. A* **71**, 011401 (2005).
28. J. Gagnon, E. Goulielmakis, V. S. Yakovlev, *Appl. Phys. B* **92**, 25 (2008).
29. Information on technology and methods is available as supporting material on *Science* Online.
30. J. Gagnon, V. S. Yakovlev, *Opt. Express* **17**, 17678 (2009).
31. C. A. Nicolaides, Th. Mercouris, Y. Komninos, *J. Phys. At. Mol. Opt. Phys.* **35**, L271 (2002).
32. Th. Mercouris, Y. Komninos, C. A. Nicolaides, *Phys. Rev. A* **76**, 033417 (2007).
33. J. S. Parker, B. J. S. Doherty, K. J. Meharg, K. T. Taylor, *J. Phys. At. Mol. Opt. Phys.* **36**, L393 (2003).
34. Supported by the Max Planck Society and the Deutsche Forschungsgemeinschaft Cluster of Excellence: Munich Centre for Advanced Photonics (www.munich-photonics.de) and the King Saud University–Max-Planck-Institut für Quantenoptik collaboration. Supported in part by NSF through TeraGrid resources provided by the National Institute for Computational Sciences and Texas Advanced Computing Center under grant TG-PHY090031. R.P., S.N., and J.B. acknowledge support from the Austrian Science Fund (FWF) under grant FWF-SFB016. J.F. acknowledges support by NSF through a grant to ITAMP. E.G. acknowledges a Marie-Curie Reintegration grant (MERG-CT-2007-208643). R.K. acknowledges support from the Sofia Kovalevskaja award of the Alexander von Humboldt Foundation and an ERC starting grant. We thank A. Maquet and R. Taieb for fruitful discussions.

Supporting Online Material

www.sciencemag.org/cgi/content/full/328/5986/1658/DC1
SOM Text
Fig. S1
References

10 March 2010; accepted 10 May 2010
10.1126/science.1189401

Reconstituting Organ-Level Lung Functions on a Chip

Dongeun Huh,[1,2] Benjamin D. Matthews,[2,3] Akiko Mammoto,[2] Martín Montoya-Zavala,[1,2] Hong Yuan Hsin,[2] Donald E. Ingber[1,2,4]*

Here, we describe a biomimetic microsystem that reconstitutes the critical functional alveolar-capillary interface of the human lung. This bioinspired microdevice reproduces complex integrated organ-level responses to bacteria and inflammatory cytokines introduced into the alveolar space. In nanotoxicology studies, this lung mimic revealed that cyclic mechanical strain accentuates toxic and inflammatory responses of the lung to silica nanoparticles. Mechanical strain also enhances epithelial and endothelial uptake of nanoparticulates and stimulates their transport into the underlying microvascular channel. Similar effects of physiological breathing on nanoparticle absorption are observed in whole mouse lung. Mechanically active "organ-on-a-chip" microdevices that reconstitute tissue-tissue interfaces critical to organ function may therefore expand the capabilities of cell culture models and provide low-cost alternatives to animal and clinical studies for drug screening and toxicology applications.

One of the causes of the high cost of pharmaceuticals and the major obstacles to rapidly identifying new environmental toxins is the lack of experimental model systems that can replace costly and time-consuming animal studies. Although considerable advances have been made in the development of cell culture models as surrogates of tissues and organs for these types of studies (*1*), cultured cells commonly fail to maintain differentiation and expression of tissue-specific functions. Improved tissue organization can be promoted by growing cells in three-dimensional extracellular matrix (ECM) gels (*2*); however, these methods still fail to reconstitute structural and mechanical features of whole living organs that are central to their function. In particular, existing model systems do not recreate the active tissue-tissue interface between the microvascular endothelium and neighboring parenchymal tissues where critical transport of fluids, nutrients, immune cells, and other regulatory factors occur, nor do they permit application of dynamic mechanical forces (e.g., breathing movements in lung, shear in blood vessels, peristalsis in gut, tension in skin, and the like) that are critical for the development and function of living organs (*3*).

Microscale engineering technologies first developed to create microchips, such as microfabrication and microfluidics, enable unprecedented capabilities to control the cellular microenvironment with high spatiotemporal precision and to present cells with mechanical and biochemical signals in a more physiologically relevant context (*4*–*7*). This approach has made it possible to microfabricate models of blood vessels (*8*, *9*), muscles (*10*), bones (*11*), airways (*12*), liver (*13*–*16*), brain (*17*, *18*), gut (*19*), and kidney (*20*, *21*). However, it has not yet been possible to engineer integrated microsystems that replicate the complex physiological functionality of living organs by incorporating multiple tissues, including active vascular conduits, and placing them in a dynamic and mechanically relevant organ-specific microenvironment.

To provide the proof of principle for a biomimetic microsystems approach, we developed a multifunctional microdevice that reproduces key structural, functional, and mechanical properties of the human alveolar-capillary interface, which is the fundamental functional unit of the living lung. This was accomplished by microfabricating a microfluidic system containing two closely apposed microchannels separated by a thin (10 μm), porous, flexible membrane made of poly(dimethylsiloxane) (PDMS). The intervening membrane was coated with ECM (fibronectin or collagen), and human alveolar epithelial cells and human pulmonary microvascular endothelial cells were cultured on opposite sides of the membrane (Fig. 1A). Once the cells were grown to confluence, air was introduced into the epithelial compartment to create an air-liquid interface and more precisely mimic the lining of the alveolar air space. The compartmentalized channel configuration of the microdevice makes it possible to manipulate fluid flow, as well as delivery of cells and nutrients, to the epithelium and endothelium independently.

During normal inspiration, intrapleural pressure decreases, causing the alveoli to expand; this pulls air into the lungs, resulting in stretching of the alveolar epithelium and the closely apposed endothelium in adjacent capillaries (Fig. 1B). We mimicked this subatmospheric, pressure-driven stretching by incorporating two larger, lateral microchambers into the device design. When vacuum is applied to these chambers, it produces elastic deformation of the thin wall that separates the cell-containing microchannels from the side chambers; this causes stretching of the attached PDMS membrane and the adherent tissue layers (Fig. 1A, right versus left). When the vacuum is released, elastic recoil of PDMS causes the membrane and adherent cells to relax to their original size. This design replicates dynamic mechanical distortion of the alveolar-capillary interface caused by breathing movements.

These hollow microchannels were fabricated by soft lithography in conjunction with a new method that uses chemical etching of PDMS (*22*) to form the vacuum chambers. Fabrication begins with alignment and permanent bonding of a 10-μm-thick porous PDMS membrane (containing 10-μm-wide pentagonal pores) and two PDMS layers containing recessed microchannels (Fig. 1C). A PDMS etching solution composed of tetrabutyl-

[1]Wyss Institute for Biologically Inspired Engineering at Harvard University, Boston, MA 02115, USA. [2]Vascular Biology Program, Departments of Pathology and Surgery, Children's Hospital Boston, and Harvard Medical School, Boston, MA 02115, USA. [3]Department of Medicine, Children's Hospital Boston, Boston, MA 02115, USA. [4]School of Engineering and Applied Sciences, Harvard University, Cambridge, MA 02138, USA.

*To whom correspondence should be addressed. E-mail: don.ingber@wyss.harvard.edu

ammonium fluoride and N-methylpyrrolidinone is then pumped through the side channels (Fig. 1D). Within a few minutes, PDMS etchant completely dissolves away portions of the membrane in the side channels, creating two large chambers directly adjacent to the culture microchannels. The entire integrated device is only 1 to 2 cm in length, with the central channels only millimeters in width (Fig. 1E), and thus, it is fully amenable to high-density integration into a highly multiplexed microdevice in the future.

Reconstitution of a functional alveolar-capillary interface. When human alveolar epithelial cells and microvascular endothelial cells were introduced into their respective channels, they attached to opposite surfaces of the ECM-coated membrane and formed intact monolayers composed of cells linked by continuous junctional complexes containing the epithelial and endothelial junctional proteins, occludin and vascular endothelial cadherin (VE-cadherin), respectively (Fig. 2A). These cells remained viable for prolonged periods (>2 weeks) after air was introduced into the epithelial microchannel and the alveolar cells were maintained at an air-liquid interface (fig. S1). Addition of air to the upper channel resulted in increased surfactant production by the epithelium (Fig. 2B and fig. S1), which stabilizes the thin liquid layer in vitro as it does in whole lung in vivo, such that no drying was observed. This was also accompanied by an increase in electrical resistance across the tissue layers (Fig. 2C) and enhanced molecular barrier function relative to cells cultured under liquid medium (Fig. 2D). These differences in barrier integrity and permeability likely result from strengthening of intercellular junctions in air-liquid interface culture (*12*), and from the observed changes in pulmonary surfactant production that can influence alveolar-capillary barrier function (*23*). Moreover, the low level of protein permeability (2.1%/hour for fluorescently labeled albumin) exhibited by cells cultured at the air-liquid interface (Fig. 2D) closely approximated that observed in vivo (1 to ~2%/hour) (*24*). It should be noted that although we mimic the alveolar microenvironment by generating an air-liquid interface in contact with the apical surface of epithelium in our microdevice, there is likely a large variation in the microscale properties of this interface in vivo. Thus, it would be difficult to interpret these results in any way other than functional measures at this time. Our results clearly show that the epithelial cells not only remained viable but also increased their surfactant production, enhanced their structural integrity, and restored normal barrier permeability in this biomimetic microsystem.

The microfluidic device was then integrated with computer-controlled vacuum to produce cyclic stretching of the tissue-tissue interface to mimic physiological breathing movements (movie S1). The level of applied strain ranged from 5% to 15% to match normal levels of strain observed in alveoli within whole lung in vivo, as previously described (*25*). Vacuum application generated uniform, unidirectional mechanical strain across the channel length, as demonstrated by measured displacements of fluorescent quantum dots immobilized on the PDMS membrane (Fig. 2E and movie S2). Membrane stretching also resulted in cell shape distortion, as visualized by concomitant increases in the projected area and length of the adherent cells in the direction of applied tension (Fig. 2F and movie S3).

The permeability of the alveolar-capillary barrier to fluorescent albumin remained unchanged during cyclic stretching over 4 hours with physiological levels of strain (5 to ~15%) or after preconditioning with 10% strain for varying amounts of time (fig. S1). Application of physiological cyclic strain (10% at 0.2 Hz) also induced cell alignment in the endothelial cells in the lower compartment (fig. S2 and movie S4) and, hence, mimicked physiological responses previously observed in cultured endothelium and in living blood vessels in vivo (*26*, *27*). Cyclic stretching caused some pulsatility in the fluid flow, but this unsteady effect was negligible due to the small channel size and low stretching frequency (see SOM text). Thus, this microdevice extends far beyond previously described cell stretching systems by permitting the application of cyclic stretch and fluid shear stress to two opposing cell layers

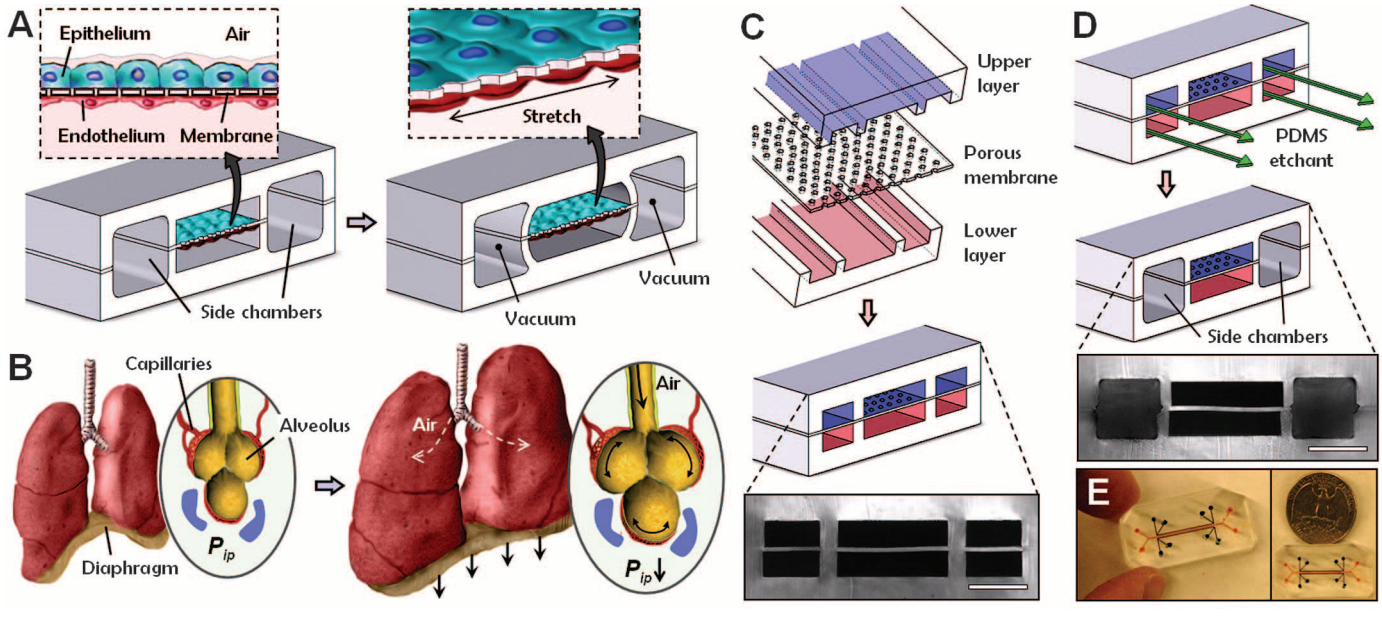

Fig. 1. Biologically inspired design of a human breathing lung-on-a-chip microdevice. (**A**) The microfabricated lung mimic device uses compartmentalized PDMS microchannels to form an alveolar-capillary barrier on a thin, porous, flexible PDMS membrane coated with ECM. The device recreates physiological breathing movements by applying vacuum to the side chambers and causing mechanical stretching of the PDMS membrane forming the alveolar-capillary barrier. (**B**) During inhalation in the living lung, contraction of the diaphragm causes a reduction in intrapleural pressure (P_{ip}), leading to distension of the alveoli and physical stretching of the alveolar-capillary interface. (**C**) Three PDMS layers are aligned and irreversibly bonded to form two sets of three parallel microchannels separated by a 10-μm-thick PDMS membrane containing an array of through-holes with an effective diameter of 10 μm. Scale bar, 200 μm. (**D**) After permanent bonding, PDMS etchant is flowed through the side channels. Selective etching of the membrane layers in these channels produces two large side chambers to which vacuum is applied to cause mechanical stretching. Scale bar, 200 μm. (**E**) Images of an actual lung-on-a-chip microfluidic device viewed from above.

separated by a permeable and flexible ECM, while simultaneously enabling analysis of tissue barrier permeability and transport.

Recapitulation of whole-organ responses. We then explored whether this microsystem could recapitulate more complex integrated organ-level responses observed in whole living lung, such as pulmonary inflammation, by incorporating blood-borne immune cells in the fluid flowing through the vascular channel. Pulmonary inflammatory responses involve a highly coordinated multistep cascade, including epithelial production and release of early-response cytokines, activation of vascular endothelium through up-regulation of leukocyte adhesion molecules [e.g., intercellular adhesion molecule–1 (ICAM-1)], and subsequent leukocyte infiltration into the alveolar space from the pulmonary microcirculation (*28*–*30*). Because cytokines are produced by cells of the lung parenchyma, we simulated this process by introducing medium containing the potent proinflammatory mediator, tumor necrosis factor–α (TNF-α), into the alveolar microchannel in the presence of physiological mechanical strain and examined activation of the underlying microvascular endothelium by measuring ICAM-1 expression.

TNF-α stimulation of the epithelium substantially increased endothelial expression of ICAM-1 within 5 hours after addition (Fig. 3A and fig. S3), whereas physiological cyclic strain had no effect on ICAM-1 expression. The activated endothelium also promoted firm adhesion of fluorescently labeled human neutrophils flowing in the vascular microchannel, which do not adhere to the endothelium without TNF-α stimulation (Fig. 3B and movies S5 and S6). Real-time, high-resolution, fluorescent microscopic visualization revealed that soon after adhering, the neutrophils flattened (fig. S3) and migrated over the apical surface of the endothelium until they found cell-cell junctions, where they underwent diapedesis and transmigrated across the capillary-alveolar barrier through the membrane pores over the period of several minutes (Fig. 3C and movie S7). Phase-contrast microscopic visualization on the opposite side of the membrane revealed neutrophils crawling up through the spaces between neighboring cells and emerging on the surface of the overlying alveolar epithelium (Fig. 3D), where they remained adherent despite active fluid flow

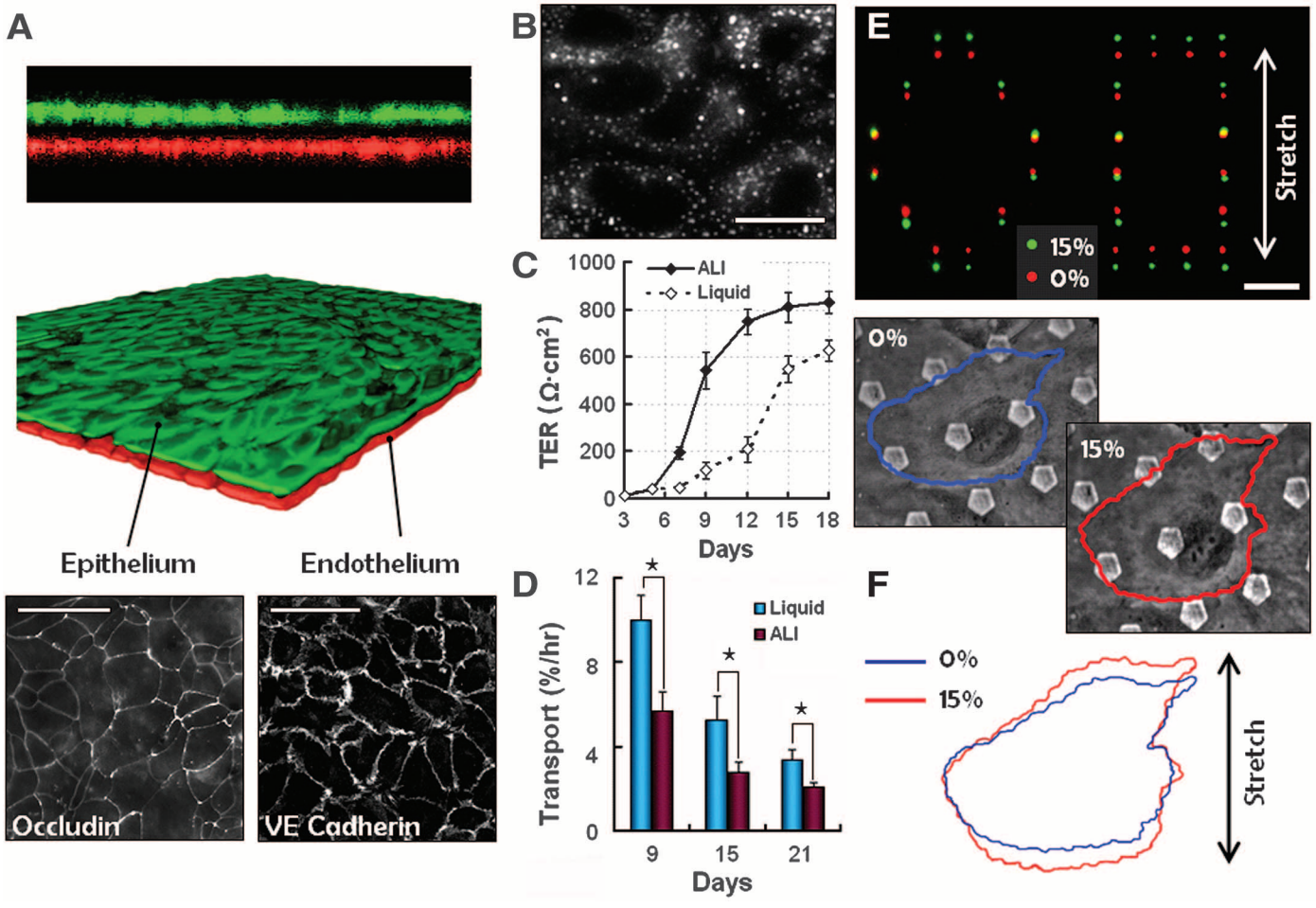

Fig. 2. On-chip formation and mechanical stretching of an alveolar-capillary interface. (**A**) Long-term microfluidic coculture produces a tissue-tissue interface consisting of a single layer of the alveolar epithelium (epithelium, stained with CellTracker Green) closely apposed to a monolayer of the microvascular endothelium (endothelium, stained with CellTracker Red), both of which express intercellular junctional structures stained with antibodies to occludin or VE-cadherin, separated by a flexible ECM-coated PDMS membrane. Scale bar, 50 μm. (**B**) Surfactant production by the alveolar epithelium during air-liquid interface culture in our device detected by cellular uptake of the fluorescent dye quinacrine that labels lamellar bodies (white dots). Scale bar, 25 μm. (**C**) Air-liquid interface (ALI) culture leads to a greater increase in transbilayer electrical resistance (TER) and produces tighter alveolar-capillary barriers with higher TER (>800 Ω·cm^2), as compared with the tissue layers formed under submerged liquid culture conditions. (**D**) Alveolar barrier permeability measured by quantitating the rate of fluorescent albumin transport is significantly reduced in ALI cultures compared with liquid cultures (*$P < 0.001$). Data in (C) and (D) represent the mean ± SEM from three separate experiments. (**E**) Membrane stretching–induced mechanical strain visualized by the displacements of individual fluorescent quantum dots that were immobilized on the membrane in hexagonal and rectangular patterns before (red) and after (green) stretching. Scale bar, 100 μm. (**F**) Membrane stretching exerts tension on the cells and causes them to distort in the direction of the applied force, as illustrated by the overlaid outlines of a single cell before (blue) and after (red) application of 15% strain. The pentagons in the micrographs represent microfabricated pores in the membrane. Endothelial cells were used for visualization of cell stretching.

and cyclic stretching. Similar adhesion and transmigration of neutrophils were observed in response to alveolar stimulation with other proinflammatory cytokines, such as interleukin-8. These sequential events successfully replicate the entire process of neutrophil recruitment from the microvasculature to the alveolar compartment, which is a hallmark of lung inflammation.

We also demonstrated that this system could mimic the innate cellular response to pulmonary infection of bacterial origin. Living *Escherichia coli* bacteria constitutively expressing green fluorescent protein (GFP) were added to the alveolar microchannel. The presence of these pathogens on the apical surface of the alveolar epithelium for 5 hours was sufficient to activate the underlying endothelium, as indicated by capture of circulating neutrophils and their transmigration into the alveolar microchannel. Upon reaching the alveolar surface, the neutrophils displayed directional movement toward the bacteria, which they then engulfed over a period of a few minutes (Fig. 3E and movies S8 and S9), and the phagocytic activity of the neutrophils continued until most bacteria were cleared from the observation area. We specifically excluded the air-liquid interface in the experiments shown in Fig. 3 because inflammatory cytokines are produced by the epithelial tissue, and alveoli often become filled with fluid exudate during early stages of lung infections. These results show that this bioinspired microdevice can effectively recapitulate the normal integrated cellular immune response to microbial infection in human lung alveoli. It also can be used to visualize these cellular responses in real time by high-resolution microscopic imaging during mechanical stimulation, which has been difficult in most existing cell stretching systems.

Identification of novel mechanosensitive responses to nanoparticulates. We also explored the potential value of this lung-on-a-chip system for toxicology applications by investigating the pulmonary response to nanoparticulates delivered to the epithelial compartment. Despite the widespread use of nanomaterials, much remains to be learned about their risks to health and the environment (*31*–*33*). Existing toxicology methods rely on oversimplified in vitro models or lengthy and expensive animal testing.

When nanoparticles are delivered to the alveoli of the lung in an aerosol, they are deposited in a thin fluid layer supported by surfactant on the surface of the epithelium. To mimic delivery of airborne nanoparticles into the lung using our microdevice, we injected nanoparticle solution into the alveolar microchannel and then gently aspirated the solution to leave a thin liquid layer containing nanoparticles covering the epithelial surface. When alveolar epithelial cells were exposed for 5 hours to 12-nm silica nanoparticles that are commonly used to model the toxic effects of ultrafine airborne particles (*34*–*36*), the underlying endothelium in the microvascular channel became activated and exhibited high levels of ICAM-1 expression (Fig. 4A). Although physiological breathing movements (10% cyclic strain) had no effect on ICAM-1 expression on their own, mechanical stretching significantly augmented endothelial expression of ICAM-1 induced by the silica nanoparticles (Fig. 4A). Moreover, this effect was sufficient to induce endothelial capture

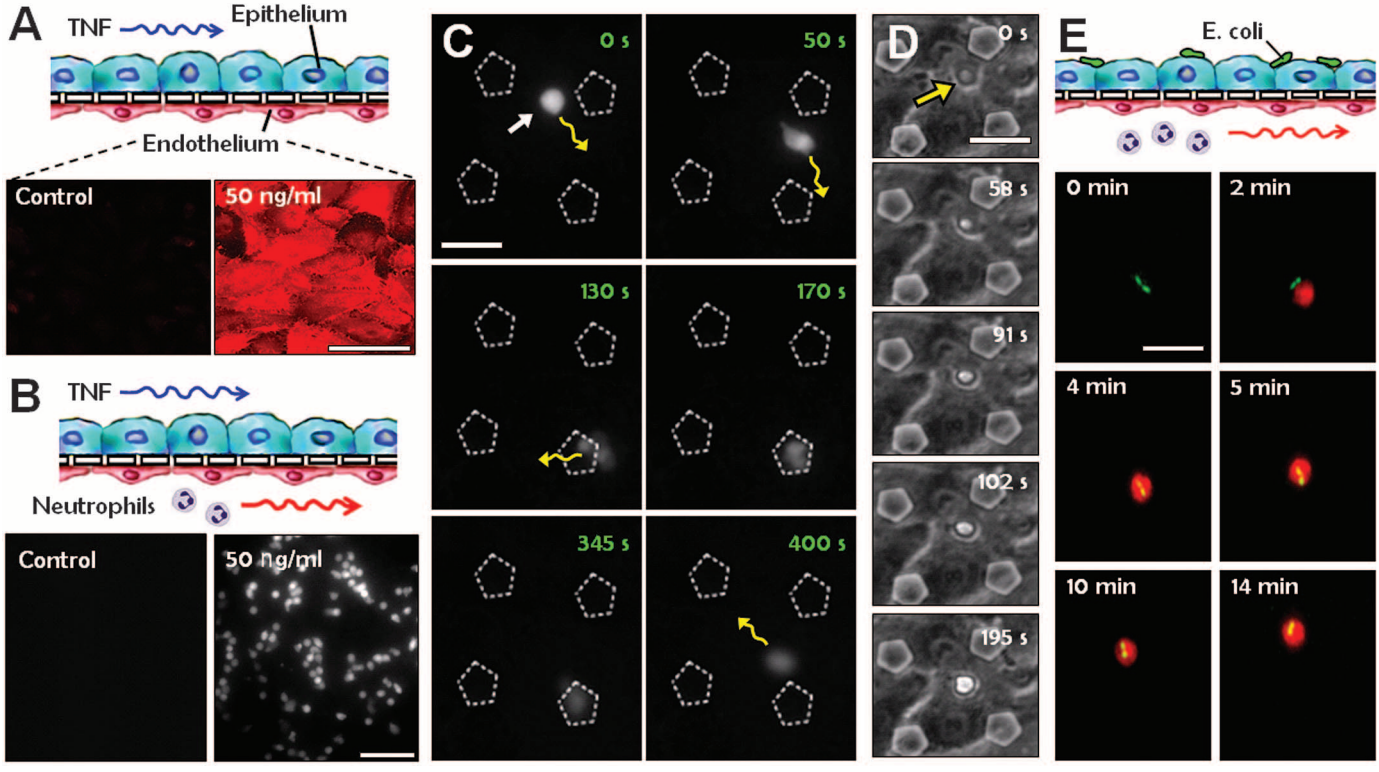

Fig. 3. Reconstitution and direct visualization of complex organ-level responses involved in pulmonary inflammation and infection in the lung-on-a-chip device. (**A**) Epithelial stimulation with TNF-α (50 ng/ml) up-regulates ICAM-1 expression (red) on the endothelium; control shows lack of ICAM-1 expression in the absence of TNF-α treatment. Cells were stretched with 10% strain at 0.2 Hz in both cases. (**B**) Fluorescently labeled human neutrophils (white dots) adhere avidly to the activated endothelium within 1 min after introduction into the vascular channel. (**C**) Time-lapse microscopic images showing a captured neutrophil (white arrow) that spreads by firm adhesion and then crawls over the apical surface of the activated endothelium (not visible in this view; direction indicated by yellow arrows) until it forces itself through the cell-cell boundary within about 2 min after adhesion (times indicated in seconds). During the following 3 to 4 min, the neutrophil transmigrates through the alveolar-capillary barrier by passing through a pentagonal pore in the PDMS membrane, and then it moves away from the focal plane, causing it to appear blurry in the micrographs. (**D**) Phase-contrast microscopic images show a neutrophil (arrow) emerging from the apical surface of the alveolar epithelium at the end of its transmigration over a period of ~3 min; thus, complete passage takes approximately 6 min in total. (**E**) Time-lapse fluorescence microscopic images showing phagocytosis of two GFP-expressing *E. coli* (green) bacteria on the epithelial surface by a neutrophil (red) that transmigrated from the vascular microchannel to the alveolar compartment. Scale bar, 50 μm in (A) and (B), 20 μm in (C) to (E).

of circulating neutrophils (Fig. 4A) and to promote their transmigration across the tissue-tissue interface and their accumulation on the epithelial surface (fig. S4).

Nanoparticles have been previously shown to induce lung inflammation by stimulating pulmonary epithelial cells to produce proinflammatory cytokines and by causing endothelial cells to express ICAM-1 and recruit circulating leukocytes (*31*–*33*, *37*). However, our results extend this observation by providing evidence to suggest that breathing motions might greatly accentuate the proinflammatory activities of silica nanoparticles and contribute substantially to the development of acute lung inflammation. This finding also could be relevant for the design of artificial lung motions in positive-pressure lung ventilator devices, which can sometimes induce dangerous inflammatory responses in the clinic. This effect of mechanical stress would never have been detected in conventional culture models based on static cultures, including Transwell culture systems, that fail to incorporate mechanical force regimens.

Next, various nanomaterials were added to the alveolar microchannel, and the cellular oxidative stress response was quantitated by measuring intracellular production of reactive oxygen species (ROS) using microfluorimetry (*31*). When the ultrafine (12 nm) silica nanoparticles were added to the alveolar epithelium in the absence of mechanical distortion, there was little or no ROS production. However, when the cells were subjected to physiological levels of cyclic strain (10% at 0.2 Hz), the same nanoparticles induced a steady increase in ROS production that increased by a factor of more than 4 within 2 hours (Fig. 4B), and this response could be inhibited with the free radical scavenger, N-acetylcysteine (NAC) (fig. S5). ROS levels in the underlying endothelium also increased by a factor of almost 3 over 2 hours, but initiation of this response was delayed by about 1 hour compared with the epithelium (fig. S5). Experiments with carboxylated Cd/Se quantum dots (16 nm) produced similar results (fig. S6), whereas cyclic strain alone had no effect on ROS even when applied for 24 hours (fig. S7). Nanomaterial-induced ROS production also increased in direct proportion to the level of applied strain (Fig. 4C). In contrast, exposure of alveolar epithelial cells to 50-nm superparamagnetic iron nanoparticles under the same conditions only exhibited a small transient increase in ROS production (Fig. 4D).

Indeed, this mechanical strain–induced oxidative response appeared to be specific for the silica nanoparticles and carboxylated quantum dots, because it was not induced by treatment with various other nanomaterials, including single-walled carbon nanotubes, gold nanoparticles, polystyrene nanoparticles, or polyethylene glycol–coated quantum dots (fig. S8 and table S1). On the other hand, we found that longer exposure to silica nanoparticles alone for 24 hours induced similar

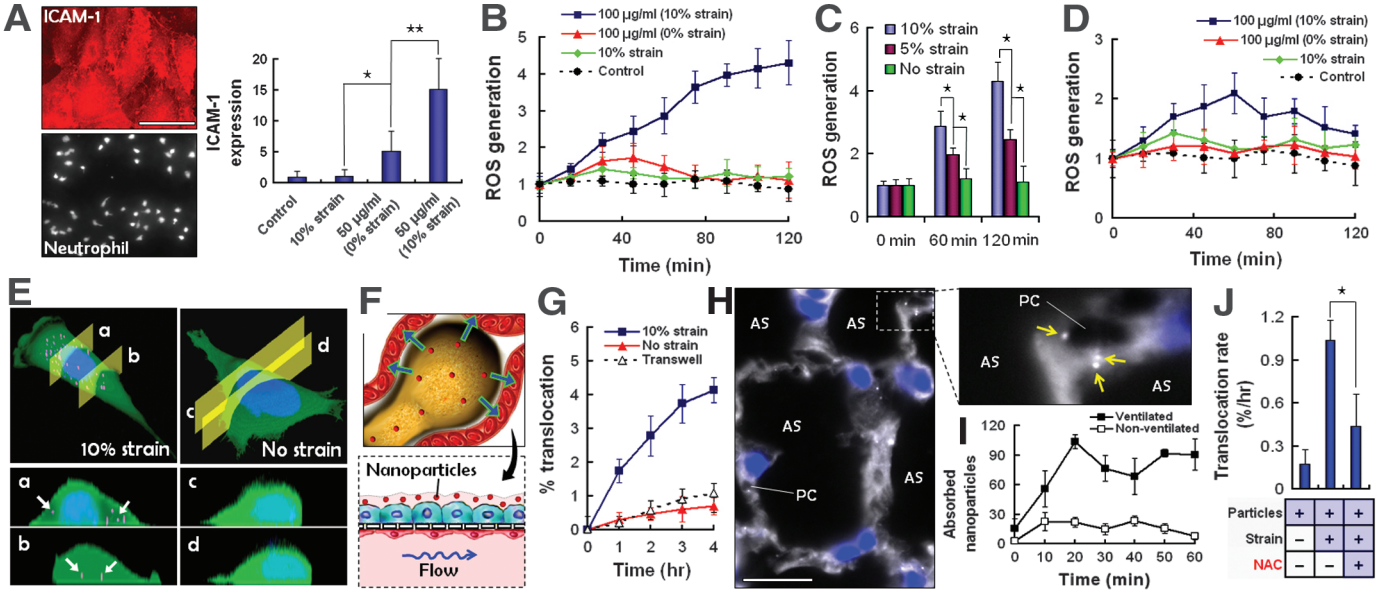

Fig. 4. Microengineered model of pulmonary nanotoxicology. (**A**) Ultrafine silica nanoparticles introduced through an air-liquid interface overlying the alveolar epithelium induce ICAM-1 expression (red) in the underlying endothelium and adhesion of circulating neutrophils (white dots) in the lower channel. Scale bar, 50 μm. Graph shows that physiological mechanical strain and silica nanoparticles synergistically up-regulate ICAM-1 expression (*P < 0.005; **P < 0.001). (**B**) Alveolar epithelial cells increase ROS production when exposed to silica nanoparticles (100 μg/ml) in conjunction with 10% cyclic strain (square) (P < 0.0005), whereas nanoparticles (triangle) or strain (diamond) alone had no effect on intracellular ROS levels relative to control cells (circle); ROS generation was normalized to the mean ROS value at time 0. (**C**) The alveolar epithelium responds to silica nanoparticles in a strain-dependent manner (*P < 0.001). (**D**) Addition of 50-nm superparamagnetic nanoparticles produced only a transient elevation of ROS in the epithelial cells subjected to 10% cyclic strain (P < 0.0005). (**E**) Application of physiological mechanical strain (10%) promotes increased cellular uptake of 100-nm polystyrene nanoparticles (magenta) relative to static cells, as illustrated by representative sections (a to d) through fluorescent confocal images. Internalized nanoparticles are indicated with arrows; green and blue show cytoplasmic and nuclear staining, respectively. (**F**) Transport of nanomaterials across the alveolar-capillary interface of the lung is simulated by nanoparticle transport from the alveolar chamber to the vascular channel of the lung mimic device. (**G**) Application of 10% mechanical strain (closed square) significantly increased the rate of nanoparticle translocation across the alveolar-capillary interface compared with static controls in this device (closed triangle) or in a Transwell culture system (open triangle) (P < 0.0005). (**H**) Fluorescence micrographs of a histological section of the whole lung showing 20-nm fluorescent nanoparticles (white dots, indicated with arrows in the inset at upper right that shows the region enclosed by the dashed square at higher magnification) present in the lung after intratracheal injection of nebulized nanoparticles and ex vivo ventilation in the mouse lung model. Nanoparticles cross the alveolar-capillary interface and are found on the surface of the alveolar epithelium, in the interstitial space, and on the capillary endothelium. PC, pulmonary capillary; AS, alveolar space; blue, epithelial nucleus; scale bar, 20 μm. (**I**) Physiological cyclic breathing generated by mechanical ventilation in whole mouse lung produces an increase by a factor of more than 5-fold in nanoparticle absorption into the blood perfusate when compared to lungs without lung ventilation (P < 0.0005). The graph indicates the number of nanoparticles detected in the pulmonary blood perfusate over time, as measured by drying the blood (1 μl) on glass and quantitating the number of particles per unit area (0.5 mm^2). (**J**) The rate of nanoparticle translocation was significantly reduced by adding NAC to scavenge free radicals (*P < 0.001).

high levels of ROS production even in the absence of mechanical strain (fig. S7), confirming findings of past pulmonary nanotoxicology studies that analyzed the effects of ultrafine silica nanoparticles in static cell cultures (*34*). Taken together, these data suggest that physiological mechanical stresses due to breathing might act in synergy with nanoparticles to exert early toxic effects or accelerate nanoparticle toxicity in the lung.

Mechanical strain enhanced cellular uptake of nanoparticulates in the alveolar epithelium and underlying endothelium. For example, confocal microscopic analysis revealed that the number of fluorescent nanoparticles (100 nm in diameter) or their aggregates present within the intracellular compartment of alveolar epithelial cells was much greater for the first hour after exposure when cells were subjected to physiological breathing movements (Fig. 4E). More than 70% of cells within mechanically active epithelium and endothelium internalized nanoparticles, whereas this fraction was lower by a factor of 10 in the absence of strain (fig. S9).

Modeling nanoparticle transport from alveoli into the lung vasculature. Increasing in vivo evidence suggests that nanomaterials introduced into the alveolar space have the capacity to cross the alveolar-capillary barrier and enter the pulmonary circulation, potentially affecting other organs and causing systemic toxicity (*31*, *33*). When we introduced fluorescent nanoparticles (20 nm in diameter) into the alveolar microchannel and monitored nanoparticle translocation across the alveolar-capillary barrier in air-liquid interface culture by measuring the fraction of particles retrieved from the underlying microvascular channel by continuous fluid flow (Fig. 4F), we observed only a low level of nanoparticle absorption under static conditions. The level was similar to that measured with a static Transwell culture system containing a rigid, porous, ECM-coated membrane lined with opposing layers of alveolar epithelium and capillary endothelium (Fig. 4G). In contrast, there was an increase by more than a factor of 4 in nanoparticle transport into the vascular compartment when our microdevice experienced physiological breathing motions (10% strain at 0.2 Hz) (Fig. 4G). This was striking given that transport of fluorescent albumin remained unchanged under similar loading conditions (fig. S1). Thus, strain-induced increases in nanoparticle absorption across the alveolar-capillary barrier are not due to physical disruption of cell-cell junctions and simple convective transport. Instead, they more likely result from altered transcellular translocation or from a change in paracellular transport that somehow selectively permits passage of these nanoparticulates while restricting movement of small molecules, such as albumin. The presence of an air-liquid interface on the epithelial surface did not appear to produce substantially higher mechanical stresses or change nanoparticle absorption across the alveolar-capillary barrier in our microdevice. An air-liquid interface has been previously shown to exert higher stress on cells (*12*, *38*); however, those studies focused mainly on the deleterious effects of a moving air-liquid interface (e.g., as might occur with a mucus plug), which generates much larger forces that are more relevant to small-airway closure and reopening.

To determine the physiological relevance of these observations, we conducted similar studies in a whole mouse lung ventilation-perfusion model, which enables intratracheal injection of nebulized nanoparticles and monitoring of nanoparticle uptake into the pulmonary vasculature ex vivo (fig. S10). When 20-nm nanoparticles were injected into whole breathing mouse lung, they were delivered into the deep lung, and histological analysis revealed that they reached the surface of the alveolar epithelium, as well as the underlying interstitial space and microvasculature (Fig. 4H). These findings confirm that these nanoparticles are transported across the alveolar-capillary barrier in vivo, as we observed in vitro. When we monitored the number of absorbed nanoparticles collected from the pulmonary venous circulation after nanoparticle injection into the whole perfused lung, we found that nanoparticle transport from the alveoli into the microvasculature was significantly increased in the presence of cyclic breathing in vivo (Fig. 4I), just as we observed in the lung mimic device in vitro (Fig. 4G). Similar studies carried out with Transwell systems that represent the state of the art for in vitro analysis of tissue barrier permeability only exhibited low levels of nanoparticle translocation (Fig. 4G).

This mechanical force–induced increase in nanoparticle translocation was reduced significantly when the cells were incubated with the antioxidant NAC (Fig. 4J). This finding implies that elevated intracellular production of ROS due to a combination of mechanical strain and nanoparticle exposure might be responsible for the observed increase in barrier permeability to these nanoparticles. We also found that preconditioning of endothelial cells with physiological levels of shear stress (15 dyne/cm^2) slightly increased the rate of nanoparticle translocation in the presence of mechanical stretch (fig. S11), presumably due to a shear-induced increase in endothelial permeability, as previously demonstrated by others (*39*). Taken together, these results highlight the advantages of our microengineered device over existing in vitro model systems and provide evidence that the inherent mechanical activity of the living lung may contribute substantially to the transport of airborne nanoparticulates from the alveolar space into the bloodstream.

Biomimetic microsystems as replacements for animal testing. Development of cell-based biochips that reproduce complex, integrated organ-level physiological and pathological responses could revolutionize many fields, including toxicology and development of pharmaceuticals and cosmetics that rely on animal testing and clinical trials. This human breathing lung-on-a-chip microdevice provides a proof of principle for this novel biomimetic strategy that is inspired by the integrated chemical, biological, and mechanical structures and functions of the living lung. This versatile system enables direct visualization and quantitative analysis of diverse biological processes of the intact lung organ in ways that have not been possible in traditional cell culture or animal models.

There are still differences between our lung mimic device and the alveolar-capillary barrier in vivo (e.g., barrier thickness, cellular composition, lack of alveolar macrophages, and changes in air pressure and flow), and the transformed lung cells used in our study might not fully reproduce the responses of native alveolar epithelial cells. However, our data clearly demonstrate that this biomimetic microsystem can reconstitute multiple physiological functions observed in the whole breathing lung. Specifically, the lung mimic device reconstitutes the microarchitecture of the alveolar-capillary unit, maintains alveolar epithelial cells at an air-liquid interface, exerts physiologically relevant mechanical forces to the entire structure, and enables analysis of the influence of these forces on various physiological and pathological lung functions, including interactions with immune cells and pathogens, epithelial and endothelial barrier functions, and toxicity and absorption of nanoparticulates across this critical tissue-tissue interface. Existing in vitro mechanical stimulation models fail to offer any of these integrated capabilities, and the fact that our system allows one to study all of these complex physiological phenomena in a single device makes it even more novel. Moreover, this microdevice represents an innovative and low-cost screening platform that could potentially replace in vivo assays, or substantially improve the outcome of animal and clinical studies, by enhancing the predictive power of in vitro or in silico computational models.

Microengineering approaches developed in this research also might offer new opportunities to more accurately model critical tissue-tissue interfaces and specialized physical microenvironments found in other organs, such as the gut, kidney, skin, and bone marrow, as well as in human cancers. These biomimetic microsystems are miniaturized (Fig. 1E) and can be easily multiplexed and automated. Hence, with simplified designs and careful choice of biocompatible device materials, they might be useful for high-throughput analysis and screening of cellular responses to drugs, chemicals, particulates, toxins, pathogens, or other environment stimuli relevant to pharmaceutical, cosmetic, and environmental applications. Furthermore, these microengineering approaches might open the possibility of integrating multiple miniaturized organ model systems into a single device to recapitulate interactions between different organs and enable more realistic in vitro assays of the whole body's response to drugs and toxins (*19*, *40*, *41*).

References and Notes

1. J. C. Davila, R. J. Rodriguez, R. B. Melchert, D. Acosta Jr., *Annu. Rev. Pharmacol. Toxicol.* **38**, 63 (1998).

2. F. Pampaloni, E. G. Reynaud, E. H. K. Stelzer, *Nat. Rev. Mol. Cell Biol.* **8**, 839 (2007).
3. D. E. Ingber, *FASEB J.* **20**, 811 (2006).
4. G. M. Whitesides, E. Ostuni, S. Takayama, X. Y. Jiang, D. E. Ingber, *Annu. Rev. Biomed. Eng.* **3**, 335 (2001).
5. A. Khademhosseini, R. Langer, J. Borenstein, J. P. Vacanti, *Proc. Natl. Acad. Sci. U.S.A.* **103**, 2480 (2006).
6. J. El-Ali, P. K. Sorger, K. F. Jensen, *Nature* **442**, 403 (2006).
7. I. Meyvantsson, D. J. Beebe, *Annu. Rev. Anal. Chem.* **1**, 423 (2008).
8. M. Shin *et al.*, *Biomed. Microdevices* **6**, 269 (2004).
9. J. W. Song *et al.*, *Anal. Chem.* **77**, 3993 (2005).
10. M. T. Lam, Y. C. Huang, R. K. Birla, S. Takayama, *Biomaterials* **30**, 1150 (2009).
11. K. Jang, K. Sato, K. Igawa, U. I. Chung, T. Kitamori, *Anal. Bioanal. Chem.* **390**, 825 (2008).
12. D. Huh *et al.*, *Proc. Natl. Acad. Sci. U.S.A.* **104**, 18886 (2007).
13. A. Carraro *et al.*, *Biomed. Microdevices* **10**, 795 (2008).
14. P. J. Lee, P. J. Hung, L. P. Lee, *Biotechnol. Bioeng.* **97**, 1340 (2007).
15. M. J. Powers *et al.*, *Biotechnol. Bioeng.* **78**, 257 (2002).
16. S. R. Khetani, S. N. Bhatia, *Nat. Biotechnol.* **26**, 120 (2008).
17. J. W. Park, B. Vahidi, A. M. Taylor, S. W. Rhee, N. L. Jeon, *Nat. Protoc.* **1**, 2128 (2006).
18. S. G. Harris, M. L. Shuler, *Biotechnol. Bioprocess Eng.* **8**, 246 (2003).
19. G. J. Mahler, M. B. Esch, R. P. Glahn, M. L. Shuler, *Biotechnol. Bioeng.* **104**, 193 (2009).
20. R. Baudoin, L. Griscom, M. Monge, C. Legallais, E. Leclerc, *Biotechnol. Prog.* **23**, 1245 (2007).
21. K. J. Jang, K. Y. Suh, *Lab Chip* **10**, 36 (2010).
22. S. Takayama *et al.*, *Adv. Mater.* **13**, 570 (2001).
23. I. Frerking, A. Günther, W. Seeger, U. Pison, *Intensive Care Med.* **27**, 1699 (2001).
24. K. J. Kim, A. B. Malik, *Am. J. Physiol. Lung Cell. Mol. Physiol.* **284**, L247 (2003).
25. K. G. Birukov *et al.*, *Am. J. Physiol. Lung Cell. Mol. Physiol.* **285**, L785 (2003).
26. T. Iba, B. E. Sumpio, *Microvasc. Res.* **42**, 245 (1991).
27. C. K. Thodeti *et al.*, *Circ. Res.* **104**, 1123 (2009).
28. J. G. Wagner, R. A. Roth, *Pharmacol. Rev.* **52**, 349 (2000).
29. M. I. Hermanns *et al.*, *Cell Tissue Res.* **336**, 91 (2009).
30. D. Wong, K. Dorovini-Zis, *J. Neuroimmunol.* **39**, 11 (1992).
31. A. Nel, T. Xia, L. Mädler, N. Li, *Science* **311**, 622 (2006).
32. V. L. Colvin, *Nat. Biotechnol.* **21**, 1166 (2003).
33. G. Oberdörster, E. Oberdörster, J. Oberdörster, *Environ. Health Perspect.* **113**, 823 (2005).
34. W. S. Lin, Y. W. Huang, X. D. Zhou, Y. F. Ma, *Toxicol. Appl. Pharmacol.* **217**, 252 (2006).
35. D. Napierska *et al.*, *Small* **5**, 846 (2009).
36. R. Merget *et al.*, *Arch. Toxicol.* **75**, 625 (2002).
37. N. L. Mills *et al.*, *Nat. Clin. Pract. Cardiovasc. Med.* **6**, 36 (2009).
38. A. M. Bilek, K. C. Dee, D. P. Gaver 3rd, *J. Appl. Physiol.* **94**, 770 (2003).
39. H. W. Sill *et al.*, *Am. J. Physiol.* **268**, H535 (1995).
40. A. Sin *et al.*, *Biotechnol. Prog.* **20**, 338 (2004).
41. C. Zhang, Z. Q. Zhao, N. A. Abdul Rahim, D. van Noort, H. Yu, *Lab Chip* **9**, 3185 (2009).
42. We thank C. K. Thodeti for his help with ROS assays; G. M. Whitesides and P. Cherukuri for providing carbon nanotubes, gold nanoparticles, and helpful comments; N. Korin for helpful discussions; R. Ruch for providing alveolar epithelial cells; R. Mannix for his imaging assistance; and M. Butte for help with neutrophil isolation. This work was supported by grants from NIH (R01-ES016665), the American Heart Association (0835618D), the Department of Defense (W81XWH-05-1-0115), and the Wyss Institute for Biologically Inspired Engineering at Harvard University; D.H. is a recipient of a Wyss Technology Development Fellowship, and D.E.I. is a recipient of a Department of Defense Breast Cancer Innovator Award. A patent on the device described is pending.

Supporting Online Material

www.sciencemag.org/cgi/content/full/328/5986/1662/DC1
Materials and Methods
SOM Text
Figs. S1 to S11
Table S1
References
Movies S1 to S9

16 February 2010; accepted 7 May 2010
10.1126/science.1188302

REPORTS

4D Electron Tomography

Oh-Hoon Kwon and Ahmed H. Zewail*

Electron tomography provides three-dimensional (3D) imaging of noncrystalline and crystalline equilibrium structures, as well as elemental volume composition, of materials and biological specimens, including those of viruses and cells. We report the development of 4D electron tomography by integrating the fourth dimension (time resolution) with the 3D spatial resolution obtained from a complete tilt series of 2D projections of an object. The different time frames of tomograms constitute a movie of the object in motion, thus enabling studies of nonequilibrium structures and transient processes. The method was demonstrated using carbon nanotubes of a bracelet-like ring structure for which 4D tomograms display different modes of motion, such as breathing and wiggling, with resonance frequencies up to 30 megahertz. Applications can now make use of the full space-time range with the nanometer-femtosecond resolution of ultrafast electron tomography.

For nearly a century, the determination of three-dimensional (3D) structures of a crystalline specimen, with redundancy in the repeating units of the architecture, has primarily depended on x-ray and electron-based methods. Recently, with the combination of electron microscopy techniques and fast computation methods, electron tomography has become a powerful tool for 3D structural determination of nanoscopic noncrystalline materials (*1*, *2*) and biological assemblies such as viruses, bacteria, and cells (*3*–*5*). Historically, several initial advances were made (*5*), but the first examples of the approach were published with different variants in the 1960s: reconstruction of 3D biostructures (of high symmetry) from one or more projections (*6*, *7*), reconstruction of an asymmetric protein structure from a sufficient number of projections (*8*), and average reprojection calculated from a tilt series of images (*9*). However, decades of advances in computation methods were required to bring the field into the state of the art in high-resolution electron tomography with applications in many fields (*10*–*12*), which include the impressive methods of energy-filtering for mapping a specific element or site (*13*–*16*) and the use of the high-angular annular dark field (HAADF) for suppressing the diffraction contrast of crystalline materials (*17*, *18*). In all of these studies, the tomograms obtained are those of a static object representing the time-averaged equilibrium state of the structure.

To visualize the dynamics, the dimension of time must be integrated into any electron tomogram that spans a whole tilt series. Furthermore, the time resolution in every step must be high enough to capture the motion of the object, ideally reduced to the atomic scale. This simultaneous real-space and real-time resolution can be obtained using ultrafast electron microscopy (UEM) (*11*, *19*). However, in UEM a snapshot represents a time frame of the 2D projection of the object under investigation, making invisible the spatial information in the dimension along the optical axis of the microscope. This is because of the large focus depth in the specimen.

Here, we report the development of 4D electron tomography. The tomograms are constructed from nearly 4000 projections for a whole series of tilt angles and time steps. The methodology is demonstrated in the imaging of multiwalled carbon nanotubes (MWNTs), with the time resolution being independent of the video camera response time of milliseconds, thus enabling the visualization of non-equilibrium, fleeting structures on the femtosecond to millisecond time scale. For the nanotubes, the 4D tomograms in a movie display the mechanical motions and morphological dynamics of the object, a

Physical Biology Center for Ultrafast Science and Technology, Arthur Amos Noyes Laboratory of Chemical Physics, California Institute of Technology, Pasadena, CA 91125, USA.

*To whom correspondence should be addressed. E-mail: zewail@caltech.edu

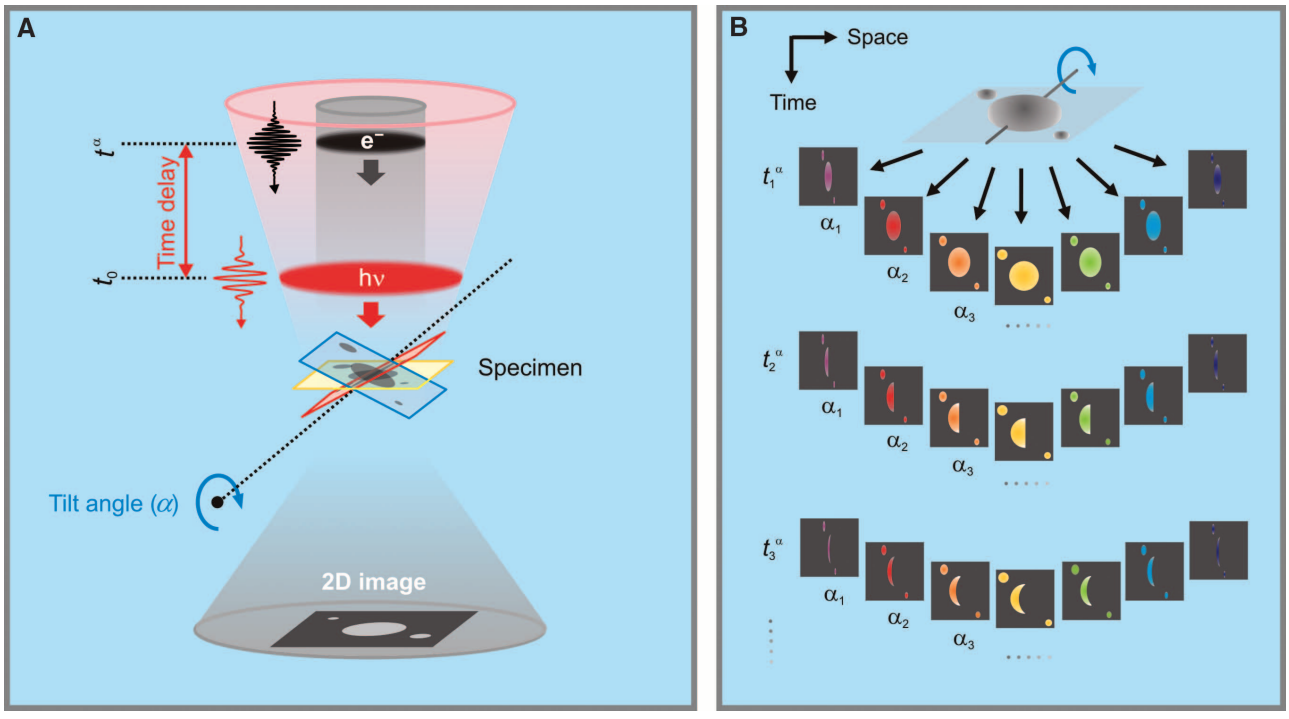

Fig. 1. (**A**) Schematic representation of time-resolved 4D electron tomography. The heating pulse initiates (at t_0) the structural change and acts as a clocking pulse, whereas the time-delayed electron packet (at t^{α}), with respect to the clocking pulse, images the structure at a given tilt angle (α). (**B**) A series of 2D images at various projection angles and time steps are taken to construct the tomograms. In this work, increments of 1° and scannings from −58° to +58° were used to define α and its range; the time scale ranged from femtoseconds to microseconds. The number of total spatiotemporal projections made was near 4000, and these were used to construct the tomographic movies of the object in motion; see text.

bracelet-like structure. For comparison, the dynamics for the same object were investigated for the 2D projections. The complex structures involved exhibit various resonances of motions after laser-driven impulsive heating, and it is possible to obtain their frequencies and the pertinent segmental structure responsible for their dynamics.

Shown in Fig. 1A is a schematic representation of the approach. In addition to the known methodology of UEM (*20*, *21*), here a specimen-tilt arrangement is configured to enable the recording of various 2D projections of an object at a given time. The frames are taken for each degree of tilt with time steps of femtoseconds or nanoseconds, as dictated by the time scale of the motions involved. The concept is illustrated in Fig. 1B, which depicts the construction of tomograms from the 2D projections at different angles and times. Because of the various dimensions involved, we note that at a given time each 2D projection represents a 3D frame (including time), whereas a 3D tomogram when constructed from all the 2D projections represents a 4D frame.

In these studies, two laser systems were used, depending on the time scale of interest. The structural change was initiated through the use of a heating (clocking) pulse, and the images were recorded using the electron (probing) pulse. The timing was controlled by changing the delay time of the electron pulses relative to the heating pulse, either optically (using a delay stage) in the femtosecond mode or electronically in the nanosecond mode. Each time frame was constructed stroboscopically in a few seconds. The electrons were accelerated to 200 kV, giving a de Broglie wavelength of 2.5 pm. The data processing and analysis involved extensive computations, as described below.

For the carbon nanotubes used in this study (*22*), the diffraction contrast in the bright-field images at different tilt angles was nearly absent, thus satisfying the condition for the projection requirement (*10*)—that is, the contrast in images arises dominantly from changes in specimen density or thickness. Accordingly, we took a series of bright-field images of various 2D projections by single-axis tilting (*23*) of the specimen and constructed a 3D tomogram at a well-defined time, t_i^{α}, where i denotes a given time step and α denotes the tilt angle defined with respect to the electron beam. Such tomograms were generated for a whole series of time delays. The stroboscopic buildup of the tomogram is ideal in this configuration, as the specimen returns to the original structure for any α or any i setting.

In generating the tomograms, the tilt series of images was aligned with respect to reference landmarks and a precise tilt axis (*24*); as in conventional tomography, median filtering was used to assist in the image alignment procedure. By using the iterative algebraic algorithm ART or SIRT (*25*), the 3D (volume) tomograms were reconstructed from the aligned images. We then used a series of such time frames of 3D tomograms to make a movie, which displays the temporal evolution of the morphological and mechanical motions. The resonance and local motions become identifiable from changes of volume density selected in the tomograms. Note that the time interval between successive clocking pulses can be chosen to ensure complete heat dissipation and damping out of the mechanical motions before the arrival of each clocking pulse.

In Fig. 2A, we present two time frames of the 3D structures obtained from representative, reconstructed 4D tomograms at t = 50 ps (left) and t = 25 ns (right); at earlier times, in femtosecond frames, there was no noticeable change. The tomograms show the nanoscale tubular structure and the microscale spiral ring, the "bracelet-like" structure. From the tomographic reconstruction, it can be seen that bright-field imaging reproduced the object structure and that the morphology of the sample is preserved. Cross sections of different carbon nanotubes show that the tubular structure has a diameter of 10 ± 2 nm (Fig. 2B); at this magnification and binning, the single-pixel resolution is 4.6 nm. To confirm the general structure, we also obtained transmission electron microscopy (TEM) images at α = 0° (Fig. 2C). These images—which display the support of the bracelet by other tubes, without a substrate—have features that are consistent with the reconstructed tomograms. At higher magnifications, we find that the thickest tube has an average outer diameter of 55 nm and inner diameter of 12 nm for a hollow channel; a narrower tube

has an outer diameter of 28 nm and an inner diameter of 9 nm. From the tomographic volume reconstruction, the 28-nm tube turned out to be attached to the spiral ring of the 55-nm one (Fig. 2A).

Representative time frames of 2D projections of the nanotubes taken at several delay times are displayed in Fig. 3A (*26*). At positive times spanning the nanosecond and microsecond time regime, after $t = 0$, visual changes are clear in the difference images (Fig. 3B). With time, the bracelet begins to move after the heating pulse, and with these and other micrographs of equal time steps we made a movie of such mechanical motions (movie S1, covering the period from –100 ns to 1.9 μs). No noticeable change was observed in images obtained before the arrival of the heating pulse, indicating that the bracelet had returned to its original spatial configuration. Moreover, because each time frame was formed stroboscopically by accumulating ~10^4 snapshots (at a repetition rate of 3 kHz for a few seconds), the revealed motion was reversible, reverting to the at-rest position after each heating pulse. There was no sign of structural fatigue or deformation observed during the course of the experiments. The average dose for each 2D projection image was ~15 e^-/nm^2 at the maximum number of electrons in the nanosecond pulse; for the femtosecond pulse, this number was lower by two orders of magnitude. The total dose for the entire tomographic recording was ≤10^5 e^-/nm^2, which is at least two orders of magnitude smaller than that reported to cause deformation of MWNTs (*27*, *28*).

Figure 3C depicts the temporal behavior obtained from 2D images, as identified by the arrows shown in the frame at negative time (Fig. 3A). Plotted is the displacement from the original position along the transverse directions of the tube, which exhibits the oscillatory behavior shown. The oscillations have well-defined resonance frequencies of 29.9, 13.5, 5.9, and 3.5 MHz, and some near 21 MHz, as quantified in Fig. 3D by taking the fast Fourier transform (FFT) of the displacements. After 1 μs, the two prominent modes at 13.5 and 3.5 MHz survive. Because the images are 2D representations of an originally imaged 3D structure in motion, it is difficult to fully elucidate the nature of the modes involved, which raises the question of whether these resonances result from the wiggling around the anchored tubes or from the breathing resonance of the ring.

Figure 4, A and B, shows the evolution of 4D tomograms of the object for two sets of view angles at representative early time frames and at longer times, respectively. At each time, such tomograms were generated from the sets of 2D projections taken at a series of tilt angles with steps of 1°, from −58° to +58° (*29*). For comparison, we also constructed movies of 2D projections taken at different tilt angles: −55°, 0°, and +55° (movie S1). From the reconstructed 4D tomograms in Fig. 4, it is possible to visualize the complicated motions and to dissect some normal modes in 3D coordinates. There are two prominent time scales of the motion. At early

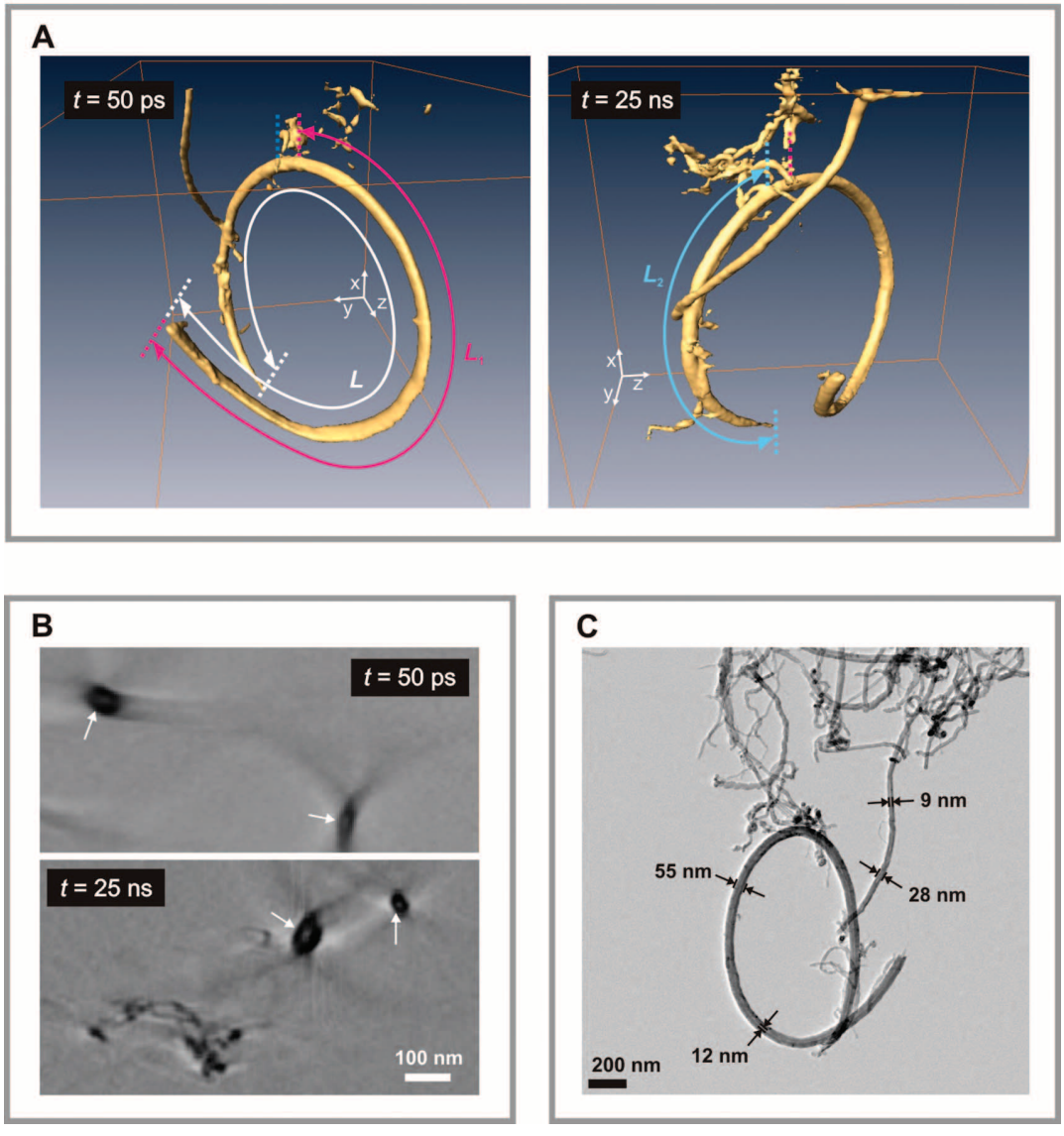

Fig. 2. Tomograms and images resolved in time. (**A**) Representative time frames of 3D volume images taken at $t = 50$ ps and 25 ns for the MWNT specimen. The bracelet shape (radius 620 nm) and the detailed tubular morphology are displayed; from the 3D volume models, the length of the ring (L) was measured to be 4.4 μm. Around the anchored region of the ring, L_1 and L_2 are the lengths of the long and short segments, respectively. The 3D isosurface rendering was made with the Amira visualization program. (**B**) Cross section of tomographic images. Shown are 4.6-nm-thick 2D slices in the xy plane, perpendicular to the optical axis, at $t = 50$ ps (top) and 25 ns (bottom). The dark regions indicated by arrows represent nanometer-thick carbon walls; the light area is the vacant space in the tomograms. Tubular features with hollow channels of diameter ~10 nm are well resolved. (**C**) TEM image of a MWNT specimen. A typical projection image at $\alpha = 0°$ is given with the dimensions indicated. Despite the initial femtosecond excitation, all motions in the object begin on the picosecond time scale because of the nature of structural change (*26*).

times (Fig. 4A), the volumes in black describe the original configuration of the object, whereas those in beige depict the new configuration displaced from the original position. One can identify the early-time resonance "breathing-type" motion, because by 75 ns the reversal for the volume density of the bracelet was obtained. At longer times, the bracelet resonates on a slower time scale; the reversal of the motion is clear, as highlighted by changes in color coding and by the directions of arrows shown in Fig. 4B.

Specifically, at t = 5 ns, the two ends of the ring begin to move (Fig. 4A), and in 15 ns, the displacement of the specimen from the at-rest position is observed for the whole ring. At t = 30 ns, the bending motion of the ring is revealed; the two ends move in the same direction, whereas the middle part of the ring moves in the opposite direction. This bent-ring configuration restores the structure nearly to its original position at t = 75 ns. The time scale of motions revealed in the tomograms corresponds to those obtained independently using 2D images at a given tilt angle, such as $\alpha = 0°$ (insets, Fig. 4A). On the microsecond time scale (e.g., from 1950 to 2090 ns), the bracelet wiggles, as evident from changes in the volume density, which show displacement in the same direction (Fig. 4B). In the next 140 ns, the direction of motion is reversed, revealing that the resonance motion is a wiggling of the whole bracelet around the anchored position.

The breathing period of ~70 ns corresponds to the 13.5-MHz resonance obtained in the FFT analysis (Fig. 3D). To estimate Young's modulus (Y) of the tube, we assumed that the frequencies of the open ring are derivable from a beam undergoing bending motions, similar to a previous analysis of nanotubes (*30*). This assumption is justified when one notices the direction of displacement at, for example, 30 ns in Fig. 4A. The Euler-Bernoulli equation (*31*) for elastic beams with natural frequencies, f_n, is given by

$$f_n = \frac{\beta_n^2}{8\pi L^2}\sqrt{\frac{(D_o^2 + D_i^2)Y}{\rho}} \qquad (1)$$

where L, D_o, D_i, and ρ denote the length, the outer diameter, the inner diameter, and the density of the MWNT, respectively; β_n is a constant for the nth mode. For simplicity, the free-ends boundary condition was adopted with $\beta_1 = 4.730$.

For D_o = 55 nm, D_i = 12 nm, and L = 4.4 μm, all values were easily retrieved from the images, and using the observed value of f_1 = 13.5 MHz, Young's modulus was calculated to be 61 GPa. This value is in the range reported for carbon nanotubes, from ~1 TPa for $D_o < 10$ nm to ~100 GPa for tubes of larger diameter (*30*, *32*); for bent tubes, smaller Y values are expected because of wrinkles or ripples on the inner arc. Knowing that Y = 61 GPa, and using the boundary condition of a clamped-free beam ($\beta_1 = 1.875$), we can deduce the frequencies for segments of the bracelet; for L_1 = 1.4 μm and L_2 = 2.8 μm (Fig. 2A), one obtains 5.3 and 21.4 MHz, respectively. These frequencies are in agreement with those obtained (5.9 and ~21 MHz) in the FFT analysis (Fig. 3D), supporting the assignment of f_1 = 13.5 MHz to the global motion of the ring and the others to local ones. The tomographic visualization in Fig. 4B indicates that the oscillation at 3.5 MHz (period = 300 ns) is

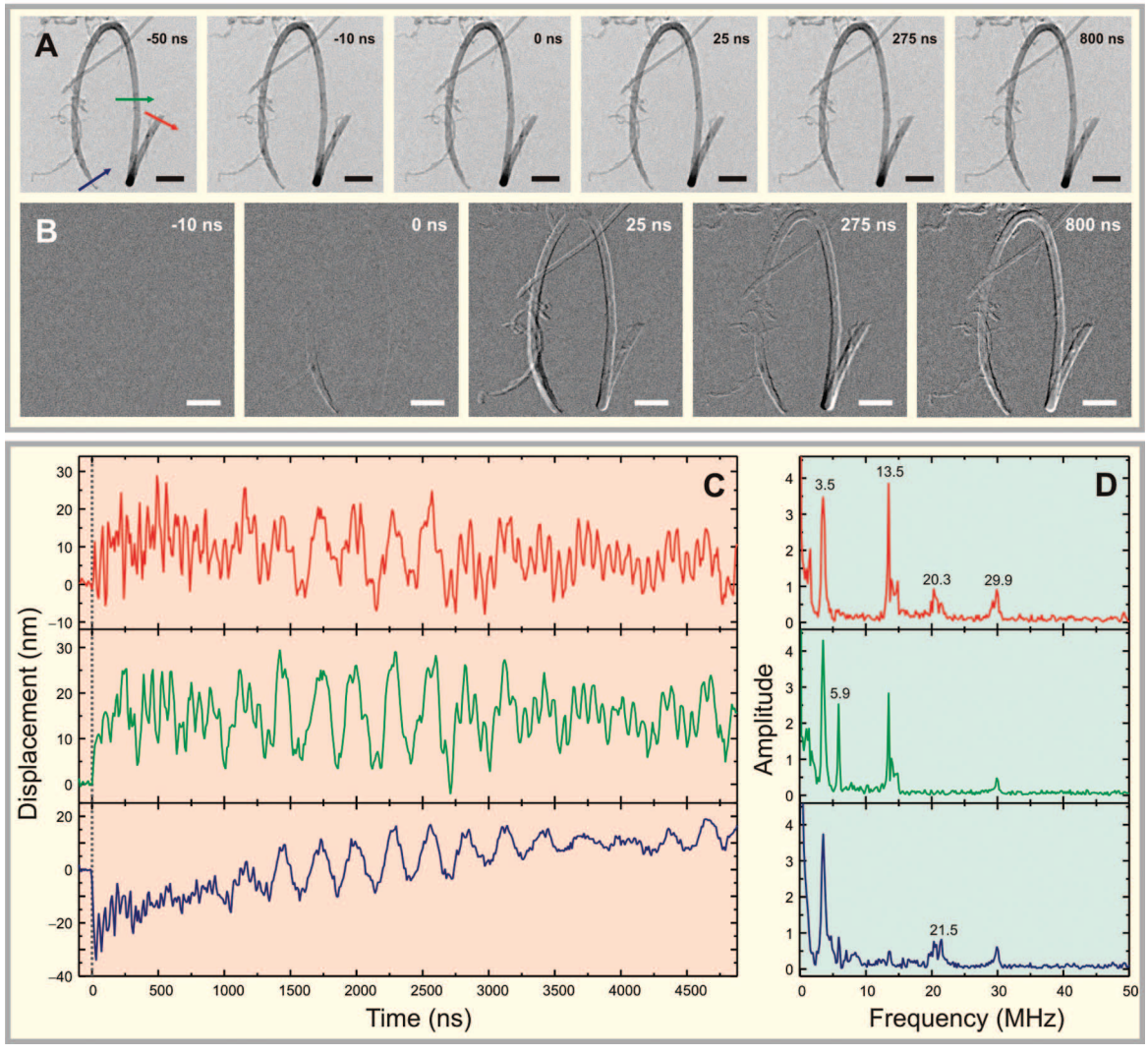

Fig. 3. Dynamics of 2D image projections. (**A**) Snapshots of images recorded stroboscopically at different time delays, as indicated at the upper right of each image. (**B**) Difference images relative to the frame at t = −50 ns, showing projected motions of the MWNT specimen. In the difference images, the regions of white or black indicate the motions involved, whereas the gray regions indicate that the contrast is unchanged from that of the reference frame. Scale bars, 200 nm. (**C**) Oscillatory motions from the time-dependent displacements along three representative transverse cross sections of the MWNT specimen; they are indicated as arrows in the image at t = −50 ns, with the color code indicated. (**D**) FFTs of the displacements in the time regime of 0 to 4.9 μs with a sampling rate of 10 ns for each of the displacements shown. As such, the tomograms would decipher 4D dynamical structures from matrix-isolated conformational structures in cryoelectron microscopy (*37*).

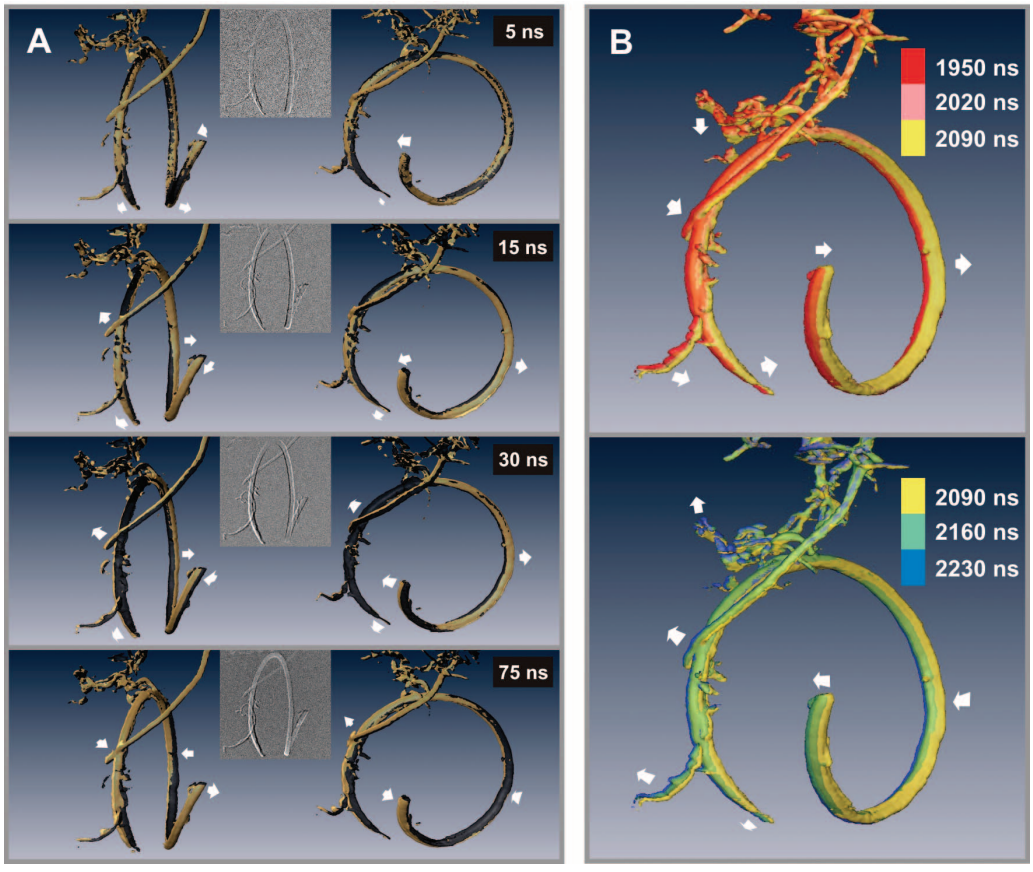

Fig. 4. 4D tomographic visualization of motion. (**A**) Representative 3D volume snapshots of the nanotubes at relatively early times. Each 3D rendered structure at different time delay (beige) is shown at two view angles. A reference volume model taken at t = 0 ns (black) is merged in each panel to highlight the resolved nanometer displacements. Arrows in each panel indicate the direction of motion. (**B**) The time-dependent structures visualized at later times and with various colors to indicate different temporal evolution. The wiggling motion of the whole bracelet is highlighted with arrows. From these tomograms, movies were constructed in the two different time domains (movies S2 and S3). Note that the time scale given here is chosen to display clearly the objects' motions, as opposed to the early ultrashort time domain (see text).

due to the wiggling motion of the ring that is supported by the bundle of nanotubes shown in the tomograms. Note that thermal vibrations (*33*) give rise, from room temperature to 1000°C, to amplitudes ranging from 0.5 to 1.0 nm, in contrast to the large amplitudes of tens of nanometers reported here for heating in the far-from-equilibrium state. In future work, it should be possible to map the microscopic forces involved by comparison with large-scale computer simulations of mechanical motions, including the influence of defects and fatigue on nanoscale materials properties.

4D electron tomography, which unites the power of volume imaging with time resolution, reveals the structural and morphological dynamics of a 3D object. In the application demonstrated here, for a complex ring structure in the non-equilibrium state, the tomographic movie displays the motions in different parts of the object on various time scales. The modes involved are those of breathing, due to segmental bending, and wiggling of the ring around the tethered position. Considering the three domains of electron microscopy—real space, Fourier space, and energy space—the introduction of energy resolution to tomography would constitute a fourth dimension of measurement (*15*), but here the integration of tomography with time represents the fundamental four coordinates of space and time. In this report, the proof-of-principle was made using stroboscopic ultrafast electron tomography, but it should also be possible to use the technique of single-particle (tomographic) imaging together with single-pulse recording, provided that this recording is made before radiation damage can occur. The methodology promises to have wide-ranging applications in materials and biological sciences.

References and Notes

1. P. A. Midgley, R. E. Dunin-Borkowski, *Nat. Mater.* **8**, 271 (2009).
2. H. Friedrich, P. E. de Jongh, A. J. Verkleij, K. P. de Jong, *Chem. Rev.* **109**, 1613 (2009).
3. V. Lučić, F. Förster, W. Baumeister, *Annu. Rev. Biochem.* **74**, 833 (2005) and references therein.
4. R. McIntosh, D. Nicastro, D. Mastronarde, *Trends Cell Biol.* **15**, 43 (2005).
5. J. Frank, Ed., *Electron Tomography: Methods for Three-Dimensional Visualization of Structures in the Cell* (Springer, New York, ed. 2, 2010) and references therein.
6. D. J. De Rosier, A. Klug, *Nature* **217**, 130 (1968).
7. R. A. Crowther, L. A. Amos, J. T. Finch, D. J. De Rosier, A. Klug, *Nature* **226**, 421 (1970).
8. W. Hoppe, R. Langer, G. Knesch, C. Poppe, *Naturwissenschaften* **55**, 333 (1968).
9. R. G. Hart, *Science* **159**, 1464 (1968).
10. P. A. Midgley, E. P. W. Ward, A. B. Hungría, J. M. Thomas, *Chem. Soc. Rev.* **36**, 1477 (2007) and references therein.
11. A. H. Zewail, J. M. Thomas, *4D Electron Microscopy: Imaging in Space and Time* (Imperial College Press, London, 2009) and references therein.
12. P. W. Hawkes, J. C. H. Spence, Eds., *Science of Microscopy* (Springer, New York, 2006), vol. 1.
13. P. A. Midgley, M. Weyland, *Ultramicroscopy* **96**, 413 (2003).
14. J. J. Cha *et al.*, *Nano Lett.* **7**, 3770 (2007).
15. M. H. Gass, K. K. K. Koziol, A. H. Windle, P. A. Midgley, *Nano Lett.* **6**, 376 (2006).
16. C. Colliex *et al.*, *Philos. Trans. R. Soc. London Ser. A* **367**, 3845 (2009).
17. J. M. Thomas *et al.*, *Angew. Chem. Int. Ed.* **43**, 6745 (2004).
18. H. Li, H. L. Xin, D. A. Muller, L. A. Estroff, *Science* **326**, 1244 (2009).
19. A. H. Zewail, *Science* **328**, 187 (2010) and references therein.
20. B. Barwick, H. S. Park, O.-H. Kwon, J. S. Baskin, A. H. Zewail, *Science* **322**, 1227 (2008).
21. O.-H. Kwon, B. Barwick, H. S. Park, J. S. Baskin, A. H. Zewail, *Nano Lett.* **8**, 3557 (2008).
22. MWNTs (average diameter of 50 nm) were purchased and dispersed in cyclohexane. After ultrasonication, the solution was delivered to a bare copper grid (300 mesh), using a micropipette, and allowed to dry for immobilization of the tubes. MWNTs sitting on the middle of the grid square were selected to ensure the maximum range of tilt angles.
23. Q. S. Zheng, M. B. Braunfeld, J. W. Sedat, D. A. Agard, *J. Struct. Biol.* **147**, 91 (2004).
24. C. O. S. Sorzano *et al.*, *BMC Bioinformatics* **10**, 124 (2009).
25. C. Messaoudi, T. Boudier, C. O. Sanchez Sorzano, S. Marco, *BMC Bioinformatics* **8**, 288 (2007).
26. For structural change, the heating was carried out with excitation at 519 and 532 nm for 220-fs and 10-ns pulses, respectively. The fluence varied from 2.5 mJ/cm^2 (for femtosecond experiments) to 100 mJ/cm^2 (for nanosecond experiments); the repetition rate varied from 200 kHz to 3 kHz. Upon absorption of the pulse energy by the specimen, lattice phonons are formed in a few picoseconds (*34*). Consequently, the irradiated region heats up rapidly after phonon-phonon interactions on a time scale of tens of picoseconds. The initial temperature was deduced to be ~1000°C from knowledge of the optical and thermal properties of the specimen and the fluence, using a simple 1D heat-flow scheme (*35*). The impulsive thermal stress induces mechanical vibrations in the material, and the initial motions by heat-induced expansion are then transferred into longitudinal and flexural modes in 3D.

27. F. Banhart, *J. Mater. Sci.* **41**, 4505 (2006).
28. V. H. Crespi, N. G. Chopra, M. L. Cohen, A. Zettl, S. G. Louie, *Phys. Rev. B* **54**, 5927 (1996).
29. The extent of displacement may vary depending on the tilt angle, because the local thickness of the specimen along the axis of the excitation may change. However, the skin depth of the MWNT ring specimen for the 532-nm light is deduced to be 2 μm [absorption coefficient $\alpha = 1.0 \times 10^4$ cm^{-1} (*35*)], which exceeds the largest local thickness along the ring specimen at a tilt angle of 35°. In addition, the absorption cross section of MWNTs is reported to be weakly dependent on the polarization of the incident beam for thick tubes (*36*). To further suppress any polarization dependence, we set the polarization of the optical excitation beam so that it was not along the long axis of the tube. Consequently, the heat gradient and thermal stress are uniform for the tilt angles recorded in this study.
30. P. Poncharal, Z. L. Wang, D. Ugarte, W. A. de Heer, *Science* **283**, 1513 (1999).
31. L. Meirovich, *Elements of Vibration Analysis* (McGraw-Hill, New York, ed. 2, 1986).
32. X.-L. Wei, Y. Liu, Q. Chen, M.-S. Wang, L.-M. Peng, *Adv. Funct. Mater.* **18**, 1555 (2008).
33. M. M. J. Treacy, T. W. Ebbesen, J. M. Gibson, *Nature* **381**, 678 (1996).
34. G. V. Hartland, *Annu. Rev. Phys. Chem.* **57**, 403 (2006).
35. T. Nakamiya *et al.*, *Thin Solid Films* **517**, 3854 (2009).
36. C. Ni, P. R. Bandaru, *Carbon* **47**, 2898 (2009).
37. S. Jonic, C. Vénien-Bryan, *Curr. Opin. Pharmacol.* **9**, 636 (2009).
38. Supported by NSF (grant DMR-0964886) and Air Force Office of Scientific Research (grant FA9550-07-1-0484) in the Physical Biology Center for Ultrafast Science and Technology supported by Gordon and Betty Moore Foundation at Caltech. A patent application has been filed by Caltech based on the methodology presented herein.

Supporting Online Material

www.sciencemag.org/cgi/content/full/328/5986/1668/DC1
Movies S1 to S3

5 April 2010; accepted 19 May 2010
10.1126/science.1190470

Measurement of the Instantaneous Velocity of a Brownian Particle

Tongcang Li, Simon Kheifets, David Medellin, Mark G. Raizen*

Brownian motion of particles affects many branches of science. We report on the Brownian motion of micrometer-sized beads of glass held in air by an optical tweezer, over a wide range of pressures, and we measured the instantaneous velocity of a Brownian particle. Our results provide direct verification of the energy equipartition theorem for a Brownian particle. For short times, the ballistic regime of Brownian motion was observed, in contrast to the usual diffusive regime. We discuss the applications of these methods toward cooling the center-of-mass motion of a bead in vacuum to the quantum ground motional state.

In 1907, Albert Einstein published a paper in which he considered the instantaneous velocity of a Brownian particle (*1*, *2*). By measuring this quantity, one could prove that "the kinetic energy of the motion of the centre of gravity of a particle is independent of the size and nature of the particle and independent of the nature of its environment." This is one of the basic tenets of statistical mechanics, known as the equipartition theorem. However, because of the very rapid randomization of the motion, Einstein concluded that the instantaneous velocity of a Brownian particle would be impossible to measure in practice.

We report here on the measurement of the instantaneous velocity of a Brownian particle in a system consisting of a single, micrometer-sized SiO_2 bead held in a dual-beam optical tweezer in air, over a wide range of pressures. The velocity data were used to verify the Maxwell-Boltzmann velocity distribution and the equipartition theorem for a Brownian particle. The ability to measure instantaneous velocity enables new fundamental tests of statistical mechanics of Brownian particles and is also a necessary step toward the cooling of a particle to the quantum ground motional state in vacuum.

The earliest quantitative studies of Brownian motion were focused on measuring velocities, and they generated enormous controversy (*3*, *4*). The measured velocities of Brownian particles (*3*) were almost 1000-fold smaller than what was predicted by the energy equipartition theorem. Recent experiments with fast detectors that studied Brownian motion in liquid (*5*–*7*) and gaseous (*8*–*10*) environments observed nondiffusive motion of a Brownian particle.

Einstein's theory predicts that $\langle[\Delta x(t)]^2\rangle = 2Dt$, where $\langle[\Delta x(t)]^2\rangle$ is the mean square displacement (MSD) in one dimension of a free Brownian particle during time t, and D is the diffusion constant (*11*). The diffusion constant can be calculated by $D = k_B T/\gamma$, where k_B is Boltzmann's constant, T is the temperature, and γ is the Stokes friction coefficient. The mean velocity measured over an interval of time t is $\bar{v} \equiv \sqrt{\langle[\Delta x(t)]^2\rangle}/t = \sqrt{2D}/\sqrt{t}$. This diverges as t approaches 0 and therefore does not represent the real velocity of the particle (*1*, *2*).

The equation $\langle[\Delta x(t)]^2\rangle = 2Dt$, however, is valid only when $t >> \tau_p$; that is, in the diffusive regime. Here, $\tau_p = m/\gamma$ is the momentum relaxation time of a particle with mass m. At very short time scales ($t << \tau_p$), the dynamics of a particle are dominated by its inertia, and the motion is ballistic. The dynamics of a Brownian particle over all time scales can be described by a Langevin equation (*12*). The MSD of a Brownian particle at very short time scales is predicted to be $\langle[\Delta x(t)]^2\rangle = (k_B T/m)t^2$, and its instantaneous velocity can be measured as $v = \Delta x(t)/t$, when $t << \tau_p$ (*13*).

For a 1-μm-diameter silica (SiO_2) sphere in water, τ_p is about 0.1 μs and the root mean square (rms) velocity is about 2 mm/s in one dimension. To measure the instantaneous velocity with 10% uncertainty, one would require 2-pm spatial resolution in 10 ns, far beyond what is experimentally achievable today (*7*). Because of the lower viscosity of gas, compared with liquid, the τ_p of a particle in air is much larger. This lowers the technical demand for both temporal and spatial resolution. The main difficulty of performing high-precision measurements of a Brownian particle in air, however, is that the particle will fall under the influence of gravity. We overcome this problem by using optical tweezers to simultaneously trap and monitor a silica bead in air and vacuum, allowing long-duration, ultra–high-resolution measurements of its motion.

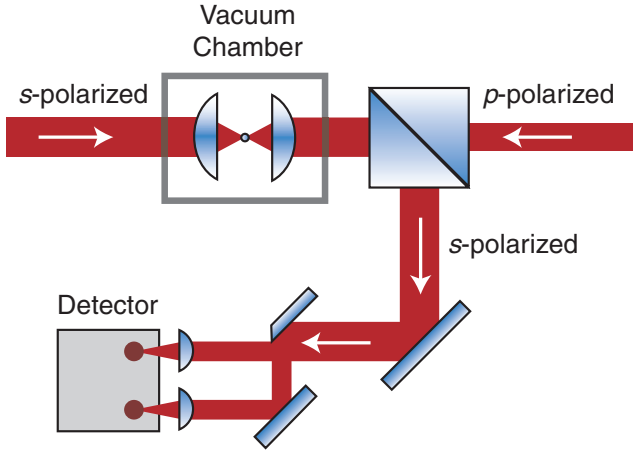

Fig. 1. Simplified schematic showing the counterpropagating dual-beam optical tweezers, and a novel detection system that has a 75-MHz bandwidth and ultralow noise. The *s*-polarized beam is reflected by a polarizing beam-splitter cube after it passes through a trapped bead inside a vacuum chamber. For detection, it is split by a mirror with a sharp edge. The *p*-polarized beam passes through the cube.

Center for Nonlinear Dynamics and Department of Physics, University of Texas at Austin, Austin, TX 78712, USA.

*To whom correspondence should be addressed. E-mail: raizen@physics.utexas.edu

For small displacements, the effect of optical tweezers on the bead's motion can be approximated by a harmonic potential. The MSD of a Brownian particle in an underdamped harmonic trap in air can be obtained by solving the Langevin equation (*14*)

$$\langle[\Delta x(t)]^2\rangle = \frac{2k_BT}{m\omega_0^2}\left[1 - e^{-t/2\tau_p}\left(\cos\omega_1 t + \frac{\sin\omega_1 t}{2\omega_1\tau_p}\right)\right] \quad (1)$$

where ω_0 is the resonant frequency of the trap and $\omega_1 \equiv \sqrt{\omega_0^2 - 1/(2\tau_p)^2}$. The normalized velocity autocorrelation function (VACF) of the particle is (*14*)

$$\psi(t) = e^{-t/2\tau_p}\left(\cos\omega_1 t - \frac{\sin\omega_1 t}{2\omega_1\tau_p}\right) \quad (2)$$

In the simplified scheme of our optical trap and vacuum chamber (Fig. 1), the trap is formed inside a vacuum chamber by two counterpropagating laser beams focused to the same point by two identical aspheric lenses with focal lengths of 3.1 mm and numerical apertures of 0.68 (*15*). The two 1064-nm-wavelength laser beams are orthogonally polarized, and their frequencies differ by 160 MHz to avoid interference. The scattering forces exerted on the bead by the two beams cancel, and the gradient forces near the center of the focus create a three-dimensional harmonic potential for the bead. When the bead deviates from the center of the trap, it deflects both trapping beams. The position of the bead is monitored by measuring the deflection of one of the beams, which is split by a mirror with a sharp edge. The difference between the two halves is measured by a fast balanced detector (*7*, *16*).

The lifetime of a bead in our trap in air is much longer than our measurement times over a wide range of pressures and trap strengths. We have tested it by trapping a 4.7-μm bead in air continuously for 46 hours, during which the power of both laser beams was repeatedly changed from 5 mW to 2.0 W. The trap becomes less stable in vacuum. The lowest pressure at which we have trapped a bead without extra stabilization is about 0.1 Pa.

For studying the Brownian motion of a trapped bead, unless otherwise stated, the powers of the two laser beams were 10.7 and 14.1 mW (*15*), the diameter of the bead was 3 μm, the temperature of the system was 297 K, and the air pressure was 99.8 or 2.75 kPa. The trapping was stable and the heating due to laser absorption was negligible under these conditions. In typical samples of position and velocity traces of a trapped bead (Fig. 2), the position traces of the bead at these two pressures appear to be very similar. On the other hand, the velocity traces are clearly different. The instantaneous velocity of the bead at 99.8 kPa changes more frequently than that at 2.75 kPa, because the momentum relaxation time is shorter at higher pressure.

Figure 3 shows the MSDs of a 3-μm silica bead as a function of time. The measured MSDs fit with Eq. 1 over three decades of time for both pressures. The calibration factor α = position/voltage of the detection system is the only fitting parameter of Eq. 1 for each pressure. τ_p and ω_0 are obtained from the measured normalized VACF. The two values of α obtained for these two pressures differ by 10.8%. This is because the vacuum chamber is distorted slightly when the pressure is decreased from 99.8 to 2.75 kPa. The measured MSDs are completely different from those predicted by Einstein's theory of Brownian motion in a diffusive regime. The

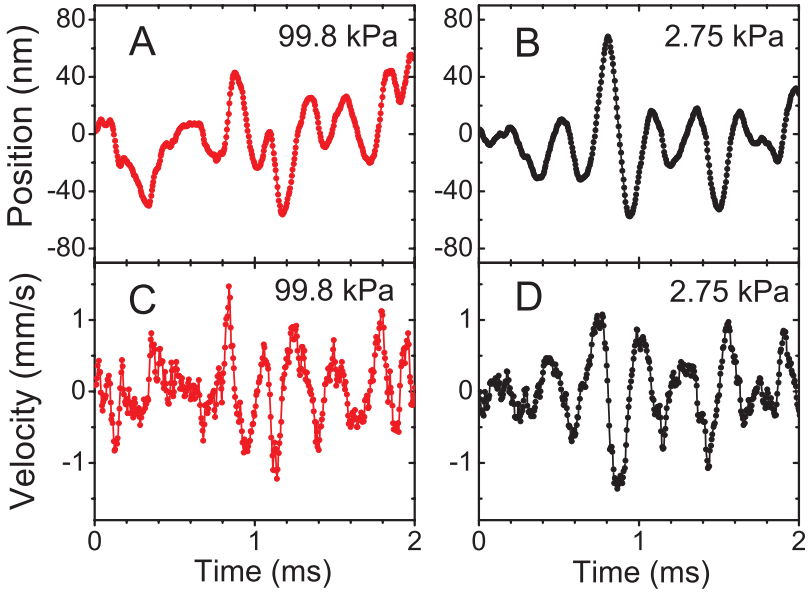

Fig. 2. One-dimensional trajectories of a 3-μm-diameter silica bead trapped in air at 99.8 kPa (**A**) and 2.75 kPa (**B**). The instantaneous velocities of the bead corresponding to these trajectories are shown in (**C**) and (**D**).

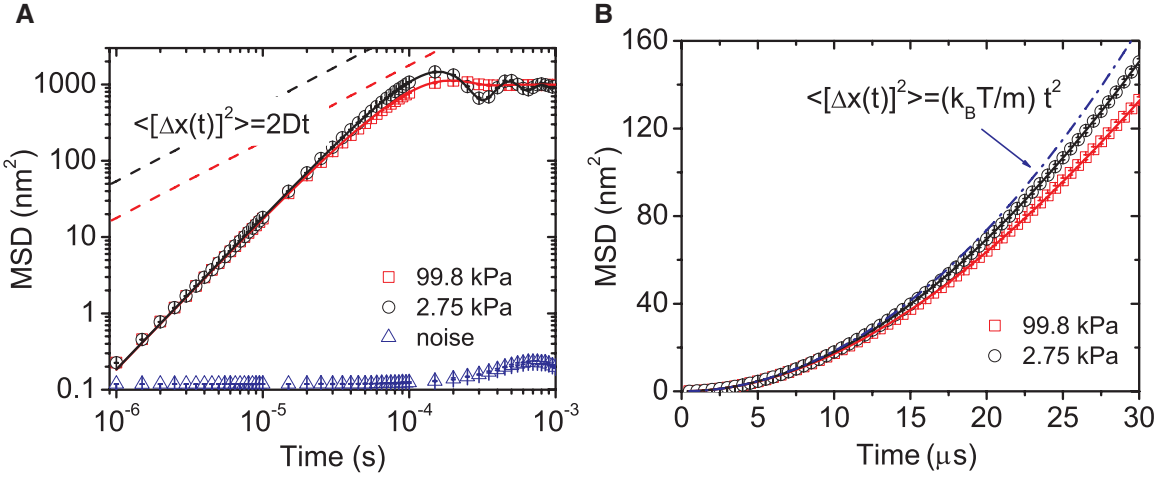

Fig. 3. (**A**) The MSDs of a 3-μm silica bead trapped in air at 99.8 kPa (red square) and 2.75 kPa (black circle). They are calculated from 40 million position measurements for each pressure. The "noise" signal (blue triangle) is recorded when there is no particle in the optical trap. The solid lines are theoretical predictions of Eq. 1. The prediction of Einstein's theory of free Brownian motion in the diffusive regime is shown in dashed lines for comparison. (**B**) MSDs at short time scales are shown in detail. The dash-dotted line indicates ballistic Brownian motion of a free particle.

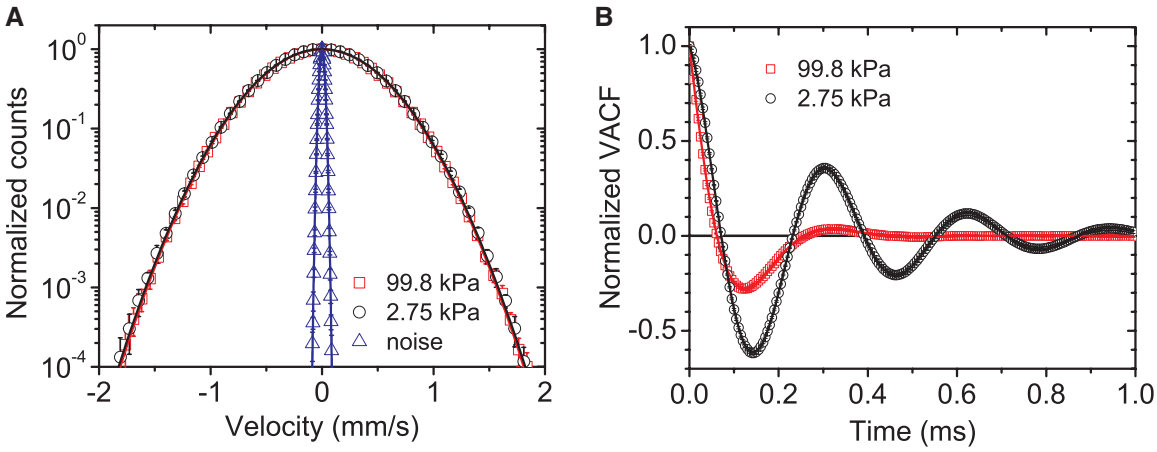

Fig. 4. (**A**) The distribution of the measured instantaneous velocities of a 3-μm silica bead. The statistics at each pressure is calculated from 4 million instantaneous velocities. The solid lines are Maxwell-Boltzmann distributions. We obtained v_{rms} = 0.422 mm/s at 99.8 kPa (red square) and v_{rms} = 0.425 mm/s at 2.75 kPa (black circle) from the measurements. The rms value of the noise (blue triangle) is 0.021 mm/s. (**B**) The normalized velocity autocorrelation functions of the 3-μm bead at two different pressures. The solid lines are fittings with Eq. 2.

slopes of measured MSD curves at short time scales are double those of the MSD curves of diffusive Brownian motion in the log-log plot (Fig. 3A). This is because the MSD is proportional to t^2 for ballistic Brownian motion, whereas it is proportional to t for diffusive Brownian motion. In addition, the MSD curves are independent of air pressure at short time scales, which is predicted by $\langle[\Delta x(t)]^2\rangle = (k_B T/m)t^2$ for ballistic Brownian motion, whereas the MSD in the diffusive regime does depend on the air pressure. At long time scales, the MSD saturates at a constant value because of the optical trap. Figure 3B displays more detail of the Brownian motion at short time scales. It clearly demonstrates that we have observed ballistic Brownian motion.

The distributions of the measured instantaneous velocities (Fig. 4A) agree very well with the Maxwell-Boltzmann distribution. The measured rms velocities are v_{rms} = 0.422 mm/s at 99.8 kPa and v_{rms} = 0.425 mm/s at 2.75 kPa. These values are very close to the prediction of the energy equipartition theorem, $v_{rms} = \sqrt{k_B T/m}$, which is 0.429 mm/s. As expected, the velocity distribution is independent of pressure. The rms value of the noise signal is 0.021 mm/s, which means we have 1.0 Å spatial resolution in 5 μs. This measurement noise is about 4.8% of the rms velocity. Figure 4A represents direct verification of the Maxwell-Boltzmann distribution of velocities and the equipartition theorem of energy for Brownian motion. For a Brownian particle in liquid, the inertial effects of the liquid become important. The measured rms velocity of the particle will be $v_{rms} = \sqrt{k_B T/m^*}$ in the ballistic regime, where the effective mass m^* is the sum of the mass of the particle and half of the mass of the displaced fluid (*17*). This is different from the equipartition theorem. To measure the true instantaneous velocity in liquid as predicted by the equipartition theorem, the temporal resolution must be much shorter than the time scale of acoustic damping, which is about 1 ns for a 1-μm particle in liquid (*17*).

Figure 4B shows the normalized VACF of the bead at two different pressures. At 2.75 kPa, one can see the oscillations due to the optical trap. Equation 2 is independent of the calibration factor α of the detection system. The only independent variable is time t, which we can measure with high precision. Thus the normalized VACF provides an accurate method to measure τ_p and ω_0. By fitting the normalized VACF with Eq. 2, we obtained $\tau_p = 48.5 \pm 0.1$ μs, $\omega_0 = 2\pi \cdot (3064 \pm 4)$ Hz at 99.8 kPa and $\tau_p = 147.3 \pm 0.1$ μs, $\omega_0 = 2\pi \cdot (3168 \pm 0.5)$ Hz at 2.75 kPa. The trapping frequency changed by 3% because of the distortion of the vacuum chamber at different pressures. For a particle at a certain pressure and temperature, τ_p should be independent of the trapping frequency. We verified this by changing the total power of the two laser beams from 25 to 220 mW. The measured τ_p changed less than 1.3% for both pressures, thus proving that the fitting method is accurate, and the heating due to the laser beams (which would change the viscosity and affect τ_p) is negligible. We can also calculate the diameter of the silica bead from the τ_p value at 99.8 kPa (*18*). The obtained diameter is 2.79 μm. This is within the uncertainty range given by the supplier of the 3.0-μm silica beads. We used this value in the calculation of MSD and normalized VACF.

The ability to measure the instantaneous velocity of a Brownian particle will be invaluable in studying nonequilibrium statistical mechanics (*19*, *20*) and can be used to cool Brownian motion by applying a feedback force with a direction opposite to the velocity (*21*, *22*). In a vacuum, our optically trapped particle should be an ideal system for investigating quantum effects in a mechanical system (*16*, *23*–*25*) because of its near-perfect isolation from the thermal environment. Combining feedback cooling and cavity cooling, we expect to cool the Brownian motion of a bead starting from room temperature to the quantum regime, as predicted by recent theoretical calculations (*24*, *25*). We have directly verified the energy equipartition theorem of Brownian motion. However, we also expect to observe deviation from this theorem when the bead is cooled to the quantum regime. The kinetic energy of the bead will not approach zero even at 0 K because of its zero-point energy. The rotational energy of the bead should also become quantized.

References and Notes

1. A. Einstein, *Zeit. f. Elektrochemie* **13**, 41 (1907).
2. A. Einstein, *Investigations on the Theory of the Brownian Movement*, R. Fürth, Ed., A. D. Cowper, Transl. (Methuen, London, 1926), pp. 63–67.
3. F. M. Exner, *Ann. Phys.* **2**, 843 (1900).
4. M. Kerker, *J. Chem. Educ.* **51**, 764 (1974).
5. B. Lukić *et al.*, *Phys. Rev. Lett.* **95**, 160601 (2005).
6. Y. Han *et al.*, *Science* **314**, 626 (2006).
7. I. Chavez, R. Huang, K. Henderson, E.-L. Florin, M. G. Raizen, *Rev. Sci. Instrum.* **79**, 105104 (2008).
8. P. D. Fedele, Y. W. Kim, *Phys. Rev. Lett.* **44**, 691 (1980).
9. J. Blum *et al.*, *Phys. Rev. Lett.* **97**, 230601 (2006).
10. D. R. Burnham, P. J. Reece, D. McGloin, Brownian dynamics of optically trapped liquid aerosols. In press; preprint available at http://arxiv.org/abs/0907.4582.
11. A. Einstein, *Ann. Phys.* **17**, 549 (1905).
12. P. Langevin, *C. R. Acad. Sci. (Paris)* **146**, 530 (1908).
13. G. E. Uhlenbeck, L. S. Ornstein, *Phys. Rev.* **36**, 823 (1930).
14. M. C. Wang, G. E. Uhlenbeck, *Rev. Mod. Phys.* **17**, 323 (1945).
15. Materials and methods are available as supporting material on *Science* online.
16. K. G. Libbrecht, E. D. Black, *Phys. Lett. A* **321**, 99 (2004).
17. R. Zwanzig, M. Bixon, *J. Fluid Mech.* **69**, 21 (1975).
18. A. Moshfegh, M. Shams, G. Ahmadi, R. Ebrahimi, *Colloids Surf. A Physicochem. Eng. Asp.* **345**, 112 (2009).
19. R. Kubo, *Science* **233**, 330 (1986).
20. G. M. Wang, E. M. Sevick, E. Mittag, D. J. Searles, D. J. Evans, *Phys. Rev. Lett.* **89**, 050601 (2002).
21. A. Hopkins, K. Jacobs, S. Habib, K. Schwab, *Phys. Rev. B* **68**, 235328 (2003).
22. D. Kleckner, D. Bouwmeester, *Nature* **444**, 75 (2006).
23. A. Ashkin, J. M. Dziedzic, *Appl. Phys. Lett.* **28**, 333 (1976).
24. D. E. Chang *et al.*, *Proc. Natl. Acad. Sci. U.S.A.* **107**, 1005 (2010).
25. O. Romero-Isart, M. L. Juan, R. Quidant, J. Ignacio Cirac, *N. J. Phys.* **12**, 033015 (2010).

26. M.G.R. acknowledges support from the Sid W. Richardson Foundation and the R. A. Welch Foundation grant number F-1258. D.M. acknowledges support from El Consejo Nacional de Ciencia y Tecnología (CONACYT) for his graduate fellowship (206429). The authors would also like to thank E.-L. Florin and Z. Yin for helpful discussions and I. Popov for his help with the experiment.

Supporting Online Material

www.sciencemag.org/cgi/content/full/science.1189403/DC1
Materials and Methods

10 March 2010; accepted 10 May 2010
Published online 20 May 2010;
10.1126/science.1189403
Include this information when citing this paper.

Glass Transition Dynamics and Surface Layer Mobility in Unentangled Polystyrene Films

Zhaohui Yang,[1] Yoshihisa Fujii,[1] Fuk Kay Lee,[1,2] Chi-Hang Lam,[2] Ophelia K. C. Tsui[1]*

Most polymers solidify into a glassy amorphous state, accompanied by a rapid increase in the viscosity when cooled below the glass transition temperature (T_g). There is an ongoing debate on whether the T_g changes with decreasing polymer film thickness and on the origin of the changes. We measured the viscosity of unentangled, short-chain polystyrene films on silicon at different temperatures and found that the transition temperature for the viscosity decreases with decreasing film thickness, consistent with the changes in the T_g of the films observed before. By applying the hydrodynamic equations to the films, the data can be explained by the presence of a highly mobile surface liquid layer, which follows an Arrhenius dynamic and is able to dominate the flow in the thinnest films studied.

For polymers, glass transition temperature, T_g, is an important technological parameter because it is the temperature at which most polymers freeze into a solidlike glassy state (*1*). Studies over the past 15 years show that the T_g of nanometer polymer films can vary substantially with the film thickness, h, when h is decreased below 50 nm (*2*–*8*). Although the T_g of polymer films has been found to both increase (*6*) and decrease (*4*–*8*) with decreasing film thickness, the latter has drawn vastly more attention because of the often bigger size of the effect, especially in freely standing polystyrene (PS) films (*8*). According to conventional views, the presence of a solid substrate can decrease the configurational space available for the polymers to perform translational motions. Frictional forces between the polymer and the substrate surface can also slow down the dynamics. On the other hand, relaxation of the constraints to molecular motions at the polymer free surface can enhance the mobility. The overall dynamics of the films, and hence the T_g, should be a result of the interplay between all these effects. The most cited model for the thickness dependence $T_g(h)$ of polymer films, namely the layer model (*4*, *6*, *7*, *9*), portrays the films to consist of a highly mobile surface layer on top of a less mobile, largely bulklike inner layer. Although there have been increasing experiments supporting the existence of a surface mobile layer on polymer films, notably for PS (*9*–*11*), its physical properties, including how its thickness depends on temperature, T, and the polymer thickness, h, as well as the mechanism by which it alters the dynamics of the films at the glass transition, are still controversial.

Keddie *et al*. (*7*) hypothesized that the surface mobile layer exists below the bulk T_g ($T_{g,bulk}$), and when the temperature T is increased toward $T_{g,bulk}$, its thickness diverges critically, following $\sim(1 - T / T_{g,bulk})^{-\nu}$, where ν is a constant between 0.56 and 1 (*2*–*4*, *6*, *7*, *12*–*14*). As a result, thinner films can be filled with the surface mobile layer and melt at a lower temperature. Herminghaus *et al*. (*12*, *13*) proposed that the T_g of the films is determined by the fastest surface capillary mode that can penetrate the whole film. As the film thickness decreases, the required wave vector, and hence the relaxation rate of the fastest mode, increases. So, thinner films require a lower temperature to melt. To fit the $T_g(h)$ data, however, the model still requires the existence of a critically thickening surface mobile layer. Mechanisms that are completely independent of a free surface have also been proposed. By using molecular dynamics simulations, Varnik *et al*. (*15*) showed that an enhancement in the glass transition dynamics could be produced by confining the polymers between two repulsive, impenetrable walls. Long *et al*. (*16*) put forward another model on the premise that liquids undergoing the glass transition contain simultaneous fast and slow domains. Upon cooling, the slow domains grow at the expense of the fast ones; the glass transition occurs when the slow domains percolate through the film. Because the percolation threshold is bigger in two dimensions than in three dimensions, the T_g can be lower in thin films. Although the above views for the mechanism of T_g reduction are diversified, they can all provide a good description to the observed $T_g(h)$ with an appropriate choice of the model parameters. Therefore, measurements additional to $T_g(h)$ are necessary to distinguish the prevailing mechanism.

The T_g of polymer films is usually determined by the discontinuous jump in the thermal expansivity in a temperature scan (*4*–*7*). Only a handful of experiments have measured the viscosity (*6*), which provides a straightforward measure of the rapid slowing down at the glass transition. In this study, we measured the viscosity of unentangled, short-chain PS films coated on silicon by monitoring the evolution of the surface structure of the films upon annealing by atomic force microscopy (AFM) (*17*, *18*). The PS used has a weight-average molecular weight of 2.4 kg/mol and a polydispersity index of 1.06 (*19*). Figure 1, A and B, shows the topographic image of an $h = 4$ nm film upon annealing at 328 K for 2 and 24 hours, respectively. Although the temperature used in obtaining these images is 9 K below the T_g of the bulk polymer ($T_{g,bulk} = 337 \pm 2$ K, as determined by multiple thermal expansivity measurements on an $h = 120$ nm film upon cooling), visible features can be seen on the film surface within 2 hours of annealing, and by 24 hours, well-defined holes are developed across the film. These should be contrasted with the corresponding images obtained from an $h = 79$ nm film (Fig. 1, C and D), where no morphological development is discernible with the same annealing conditions. To understand the difference, we examined the evolution in the power spectral density (PSD) of the $h = 4$ nm films upon annealing. Figure 1E shows a sequence of PSD (open circles) obtained from one annealed at 334 K. The solid lines represent the best fit of the data to equations (S1a and S1b) derived from a model assuming the surface dynamics to be

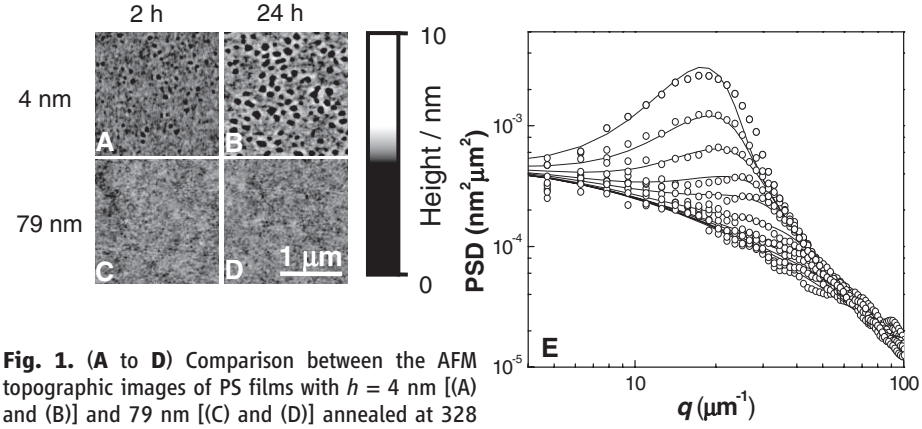

Fig. 1. (**A** to **D**) Comparison between the AFM topographic images of PS films with $h = 4$ nm [(A) and (B)] and 79 nm [(C) and (D)] annealed at 328 K and annealing times of 2 and 24 hours, respectively. Scale bar, 1 μm. (**E**) Power spectral density of a 4-nm film upon annealing at 334 K for various times (from bottom to top): 0, 15, 30, 60, 90, 210, 600, 1080, 2100, 3840, and 7200 s (open circles). The solid lines denote the least-square fit of the data to eq. S1, as detailed in (*19*).

[1]Department of Physics, Boston University, Boston, MA 02215, USA. [2]Department of Applied Physics, Hong Kong Polytechnic University, Hong Kong.

*To whom correspondence should be addressed. E-mail: okctsui@bu.edu.

governed by thermal equilibration of the surface capillary modes. The value of the viscosity of the film, η, deduced is only ~10^{-5} times the bulk value. On the other hand, a low viscosity value is in keeping with the large disparity in morphological development noted between the two films.

Figure 2A depicts the measured η versus T of PS films with various thicknesses (symbols). The viscosity of the thickest (h = 79 nm) film displays an excellent agreement with the published value of the bulk polymer (*20*) (dashed line). In contrast, the viscosity of the thinner films is significantly reduced, especially at low temperatures. The temperature dependence of the viscosity of a glass-forming liquid is conventionally related to its T_g by the Vogel-Fulcher-Tammann (VFT) relation (*1*).

$$\eta(T) = \eta(\infty)\exp\left(\frac{B}{T - T_K}\right) \quad (1)$$

In Eq. 1, B is a constant and T_K is the Kauzmann temperature, that is, the theoretical temperature at which the configurational entropy of an ergodic, supercooled liquid vanishes (*1*). For our polymer in bulk, T_K is 288 K, or 49 K below $T_{g,bulk}$, and B is 1620 K (*20*). As an initial attempt to connect our result to the T_g, we fit the VFT relation to the data in Fig. 2A and display the result by solid lines. In obtaining the fits, we varied both T_K and η(∞) while keeping B equal to the bulk value. The fitted lines describe the data reasonably well. Shown in Fig. 2B are the fitted values of T_K for different films. As seen, they are almost constant, close to $T_{g,bulk} - 48$ K at large h, but decrease rapidly with decreasing h for h < ~20 nm. We find that the data of T_K can be fitted to the equation (solid line in Fig. 2B)

$$T_K(h) = \frac{T_g(\infty)}{(1 + h_0/h)} - \Delta T \quad (2)$$

where $T_g(\infty)$, ΔT, and h_0 are constant fitting parameters. The first term on the right side, which incorporates the dependence in h, coincides with the generic $T_g(h)$ dependence found for all supported (*12*, *13*) and freely standing films with $M_w \leq 378$ kg/mol (*4*). The fitted value of h_0, 0.6 ± 0.1 nm when $T_g(\infty)$ is fixed to $T_{g,bulk}$, matches reasonably well with that obtained by modeling the experimental $T_g(h)$ data to $T_g(h) = T_g(\infty)/(1 + h_0/h)$ (*12*). The fitted value of ΔT (48 ± 3 K) also agrees well with the value known for the bulk polymer. Our result thus shows that the reduction in $T_K(h)$ by viscosity measurements agrees quantitatively with the reduction in $T_g(h)$ by thermal expansivity measurements. Notwithstanding the good agreement between the measurements and Eqs. 1 and 2, the ensuing implications are limited because the physical origins of Eqs. 1 and 2 are largely empirical and still controversial (*1*, *13*).

Our main analysis begins when we replot the viscosity data as η/h^3 versus $1/T$ in Fig. 3A. We find that all the data deviating from the bulk η-T curve collapse onto the straight line corresponding to the following Arrhenius dependence (solid line in Fig. 3A)

$$\frac{3\eta}{h^3} = (165 \pm 7\,\mathrm{Pa{\cdot}s{\cdot}m^{-3}})\exp\left(\frac{(185 \pm 3)\mathrm{kJ/mol}}{RT}\right) \quad (3)$$

where R is the ideal gas constant. For ease of view, we have labeled all such data by filled symbols and the rest by open symbols. All the data for the 2.3 nm ≤ h ≤ 9 nm films collapse onto the Arrhenius line, whereas for the h > 9 nm films, that happens only at sufficiently low temperatures, with the onset temperature (denoted by the arrows in Fig. 3A) increasing with decreasing h. In Fig. 3B, we replot the data as η versus $1/T$ while preserving the same data-labeling scheme. One can see that the data that do not fall on Eq. 3 (open symbols) collapse into the bulk curve noted above. These observations suggest that the films can be separated into two regions, with one responsible for the collapse to the Arrhenius dependence seen in Fig. 3A and one for the collapse to the bulk curve seen in Fig. 3B.

We consider a bilayer film consisting of a homogeneous mobile layer at the free surface (with viscosity η_t and thickness h_t) and a bulklike inner layer (with viscosity η_b and thickness $h_b \equiv h - h_t$). In this experiment, the surface topography on the film produces inhomogeneities in the Laplace and conjoining pressures and thereby pressure gradient, ∇P, parallel to the film (*21*). To find the flow pattern of the bilayer, we solve the Navier-Stokes equation for the system under a uniform pressure gradient, ∇P, parallel to the film, which is valid here as $qh << 1$. By assuming the no-slip boundary condition at both the bottom and intermediate interfaces and the interfacial tension between the two layers to be zero, we find the fluid velocity profile in the film, $v(z)$, to be given by:

$$v(z) = \frac{-\nabla P}{2\eta_b}[z^2 - 2(h_b + h_t)z](z < h_b)$$

$$\text{and } v(z) = \frac{-\nabla P}{2\eta_t}\left[(z - h_b)^2 - 2h_t(z - h_b) - \frac{\eta_t}{\eta_b}h_b(2h_b + h_t)\right](z > h_b) \quad (4)$$

A typical solution described by Eq. 4 is shown in the inset of Fig. 3B. The total (flow) mobility of the film, defined as $(\int_0^h v(z)\,dz)/(-\nabla P)$ (*22*), is given by

$$M_{tot} = \frac{h_b^3}{3\eta_b} + \frac{h_t^3}{3\eta_t} + \frac{h_t h_b(h_b + h_t)}{\eta_b} \quad (5)$$

The first two terms are simply the mobility of individual layers (denoted by M_b and M_t below) if the other layer were absent. The third is a coupling term, which under the experimental conditions is found to be always negligible. So our result shows that $M_{tot} \cong M_b + M_t$. In this experiment, what we measure is the relaxation rates of the capillary modes, which are directly related to M_{tot} (see eq. S1b); the viscosity, on the other hand, is a derived parameter, calculated by using $\eta = h^3/(3M_{tot})$ (*21*, *23*). It follows that in a bilayer film, the measured viscosity is an effective one given by

$$\eta_{eff} \equiv \frac{h^3}{3M_{tot}} \cong \frac{h^3}{3(M_t + M_b)} \quad (6)$$

From Eq. 6, we see that the quantity being plotted in Fig. 3A is ~M_{tot}^{-1}. The fact that the data for all the films with h ≤ ~9 nm collapse onto the same line means that the M_{tot} of those films is the same, independent of h. Independence of M_{tot} on h means that the thinner films transport materials as effectively as the thicker films, contrary to the convention that they should be less effective. Our result can be explained if the mobility M_{tot} is dominated by the top layer so that $M_{tot} \cong M_t$. Any other explanation must entail the artificial relation $\eta_{eff} \sim h^3$ and thereby more contrived arguments.

We have used Eq. 6 to calculate the expected values of η_{eff} by using the experimental film thickness, values of M_t^{-1} given by Eq. 3, and $M_b = h^3/(3\eta_{bulk})$, where η_{bulk} is the viscosity of the bulk polymer (*17*, *20*). The result, displayed by the solid lines in Fig. 3B, agrees remarkably well with the measurements without any adjustable parameters. This simple result shows that the two divergent trends (namely either Arrhenius or bulklike) found of the viscosity of the films are caused by the total mobility M_{tot} being almost

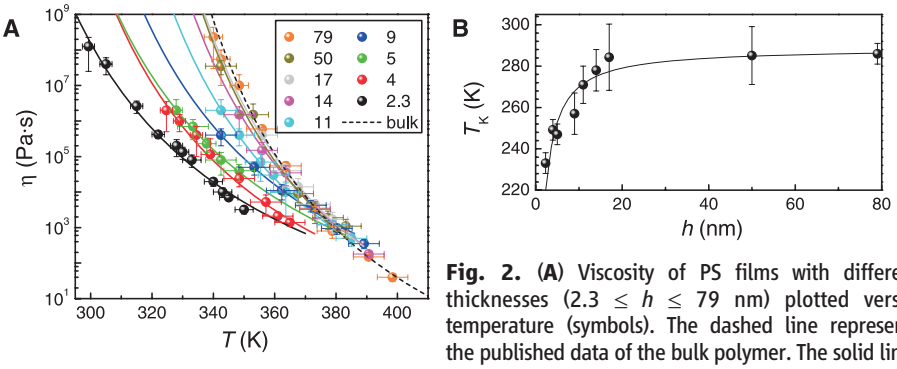

Fig. 2. (**A**) Viscosity of PS films with different thicknesses (2.3 ≤ h ≤ 79 nm) plotted versus temperature (symbols). The dashed line represents the published data of the bulk polymer. The solid lines are the least-square fits of the VFT relation to the data. (**B**) The fitted values of T_K obtained by fitting the data shown in Fig. 2A plotted as a function of the film thickness (solid circles). The solid line is the least-square fit to Eq. 2.

always dominated by either M_t or M_b. Such a drastic crossover from the $M_{tot} \cong M_b$ to the $M_{tot} \cong M_t$ behavior is attributable to the vastly stronger temperature dependence of $M_b(T)$ (VFT) than $M_t(T)$ (Arrhenius). In the above analysis, we have assumed the mobile layer to be thin, with $h_t \cong 0$, whereby $M_b \cong h^3/(3\eta_{bulk})$. Adopting instead a small, finite h_t only slightly alters the calculated values of η_{eff}, mostly in the limited region corresponding to $T \approx 380$ K and $h \approx 11$ nm, where $M_b(T)$ and $M_t(T)$ have similar orders of magnitude. Although we have derived the model by assuming the films to be bilayers in which individual layers have uniform properties, the result (Eq. 6), involving only the mobilities of individual layers, can be completely independent of the layer structure. In particular, Eq. 6 embraces systems with a gradient layer structure, which has been suggested recently (*9*, *24*).

In Eq. 5, the coupling term is not symmetric with respect to η_b and η_t. By exchanging the properties of the two layers, the model cannot fit well to the data at all. This can be traced to the fact that when the bulklike layer is riding on top of the mobile layer, the coupling term would become nonnegligible, whereby M_b cannot be approximated by $h^3/(3\eta_{bulk})$. This confirms the importance of the free surface in bringing about the reduction of the thin film T_g or enhancement in the glass transition dynamics, in disagreement with the percolation theory (*16*) and the possibility that the mobile layer may come from the polymer-substrate interface, as implied by simulation results (*15*). Our measurements are also incompatible with the models requiring the thickness of the surface mobile layer to diverge critically with temperature, as those discussed above. The fact that M_{tot} remains thickness independent among the $h < \sim 11$ nm films down to $h = 2.3$ nm (Fig. 3A, solid symbols) indicates that the surface mobile layer does not extend more than 2.3 nm from the free surface, because otherwise M_{tot} ($\approx M_t$ there) should decrease with decreasing h as the surface mobile layer gets trimmed down. It can, however, be thinner if a third, dynamically dead layer (*25*) exists next to the substrate, for example. The coefficient, 165 ± 7 Pa·s·m^{-3} displayed in Eq. 3, is reliant on the total amount of material contributing to the Arrhenius transport and thus dictated by the effective surface layer thickness h_t. Constancy of its value, as demonstrated by the good fit of Eq. 3 to the data (Fig. 3A, solid symbols), implies that there is at most a weak dependence of h_t on T and h. This finding is in good accord with the result of Kawana *et al.* (*25*), who measured the thickness variation of the thermal expansion coefficient of PS supported by silicon and found that their data was consistent with a surface mobile layer with a constant thickness. We further note that the fluorescence-label experiment of (*9*) has found that the surface mobile layer extends no more than 33% into the film at $T = T_{g,bulk} - 5$ K, contrary to expectation if it had undergone critical thickening (*7*, *13*). Nevertheless, critical thickening of a mobile layer at a water-surfactant-PS interface, differing from that studied here, is supported by a recent experiment (*26*). From our analysis, the surface mobile layer is able to dominate the flow in the $h < 9$ nm films at temperatures below ~385 K (Fig. 3A) because its viscosity at $T = 385$ K is at most 1/40 that of the bulklike inner layer, and the difference heightens rapidly with decreasing temperature. On the other hand, the thermal expansivity of the surface mobile layer was estimated to be only about 4 times that of the bulklike inner layer and does not change with temperature (*25*). Given the large discrepancies that can exist between different properties, the T_g of PS films obtained by different techniques can be different, which may explain some previous conflicting results (*27*).

It is remarkable that the Arrhenius dependence of $M_t(T)^{-1}$ is robust and persists from 306 to 400 K and over 7 orders of magnitude (Fig. 3A). Typically, Arrhenius temperature dependence is a signature of local dynamics. Our finding suggests that the molecules close to the free surface, with reduced coordination, are free of cooperative couplings, contrary to those in the bulk. Moreover, this cooperativity-free behavior continues down to 306 K, or 31 K below $T_{g,bulk}$. The temperature dependence we found of the surface-layer mobility (Eq. 3) is consistent with those measured by lateral force microscopy (*10*) and surface nanohole recovery (*11*). The activation energy we obtained, 185 kJ/mol, agrees within 20% with the values of 230 (*10*) and 150 kJ/mol (*11*) revealed in those experiments, although we caution that the nano-hole recovery time constant of (*11*) became T-independent below 303 K, outside the temperature range examined here. Although the surface dynamics discussed here do not necessarily have any direct counterpart in the bulk due to different constraints that may pertain at the free surface, we note that our activation energy roughly coincides with that of ~199 kJ/mol found in bulk PS below $T_{g,bulk}$ (*28*) and is of similar magnitude to that for the β relaxation (~140 kJ/mol), which has been attributed to dynamics confined to a very limited extent in the polymer chain (*29*).

We have shown that a surface mobile layer, exhibiting Arrhenius dynamics, with a thickness of less than 2.3 nm, is responsible for the reduction in the effective viscosity and, thereby, the T_g of unentangled, short-chain polystyrene-supported films. The thickness dependence of the T_K of the films found by viscosity measurement is in remarkable agreement with that of the T_g found by thermal expansivity measurement. Our result unfolds a mechanism by which the surface mobile layer can modify the overall dynamics of the films and does not require the surface layer thickness to be adjustable, thereby providing a more stringent test for the model. The other existing models, which either assume the surface mobile layer to be nonessential or to thicken critically with decreasing temperature, cannot explain our data.

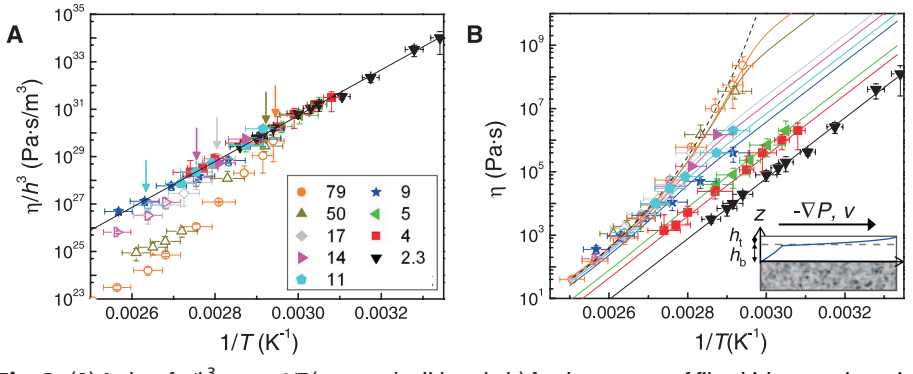

Fig. 3. (**A**) A plot of η/h^3 versus 1/T (open and solid symbols) for the same set of film thicknesses shown in Fig. 2A. The solid symbols label the data that collapse into the straight line shown by the solid line corresponding to Eq. 3. The open symbols label the rest of the data. The arrows indicate the temperatures at which the data of different thicknesses begin to depart from the solid line. (**B**) A plot of η versus 1/T (symbols). The same scheme used in Fig. 3A for the symbols applies here. The solid lines are generated from Eq. 6. (Inset) Schematic illustrating a simple two-layer model with homogeneous layer properties as discussed in the text. The blue curve represents the velocity profile for the fluid flow produced in the film by a uniform pressure gradient, ∇P, predicted by Eq. 4.

References and Notes

1. C. A. Angell, K. L. Ngai, G. B. McKenna, P. F. McMillan, S. W. Martin, *J. Appl. Phys.* **88**, 3113 (2000).
2. M. Alcoutlabi, G. B. McKenna, *J. Phys. Condens. Matter* **17**, R461 (2005).
3. J. Baschnagel, F. Varnik, *J. Phys. Condens. Matter* **17**, R851 (2005).
4. J. A. Forrest, K. Dalnoki-Veress, *Adv. Colloid Interface Sci.* **94**, 167 (2001).
5. C. B. Roth, J. R. Dutcher, *J. Electroanal. Chem.* **584**, 13 (2005).
6. O. K. C. Tsui, in *Polymer Thin Films*, O. K. C. Tsui, T. P. Russell, Eds., Series in Soft Condensed Matter (World Scientific, Singapore, 2008), pp. 267–294.
7. J. L. Keddie, R. A. L. Jones, R. A. Cory, *Europhys. Lett.* **27**, 59 (1994).
8. J. A. Forrest, K. Dalnoki-Veress, J. R. Stevens, J. R. Dutcher, *Phys. Rev. Lett.* **77**, 2002 (1996).
9. C. J. Ellison, J. M. Torkelson, *Nat. Mater.* **2**, 695 (2003).
10. K. Tanaka, A. Takahara, T. Kajiyama, *Macromolecules* **33**, 7588 (2000).
11. Z. Fakhraai, J. A. Forrest, *Science* **319**, 600 (2008).
12. S. Herminghaus, K. Jacobs, R. Seemann, *Eur. Phys. J. E* **5**, 531 (2001).
13. S. Herminghaus, *Eur. Phys. J. E* **8**, 237, discussion 245 (2002).

14. O. K. C. Tsui, H. F. Zhang, *Macromolecules* **34**, 9139 (2001).
15. F. Varnik, J. Baschnagel, K. Binder, *Phys. Rev. E Stat. Nonlin. Soft Matter Phys.* **65**, 021507 (2002).
16. D. Long, F. Lequeux, *Eur. Phys. J. E* **4**, 371 (2001).
17. Z. Yang *et al.*, *Appl. Phys. Lett.* **94**, 251906 (2009).
18. O. K. C. Tsui, Y. J. Wang, F. K. Lee, C.-H. Lam, Z. Yang, *Macromolecules* **41**, 1465 (2008).
19. Materials and methods are available as supporting material on *Science* Online.
20. J.-C. Majeste, J.-P. Montfort, A. Allal, G. Marin, *Rheol. Acta* **37**, 486 (1998).
21. Y. J. Wang, O. K. C. Tsui, *J. Non-Cryst. Solids* **352**, 4977 (2006).
22. J. W. Cahn, *J. Chem. Phys.* **42**, 93 (1965).
23. A. Vrij, J. T. G. Overbeek, *J. Am. Chem. Soc.* **90**, 3074 (1968).
24. S. Peter, H. Meyer, J. Baschnagel, R. Seemann, *J. Phys. Condens. Matter* **19**, 205119 (2007).
25. S. Kawana, R. A. L. Jones, *Phys. Rev. E Stat. Nonlin. Soft Matter Phys.* **63**, 021501 (2001).
26. S. Herminghaus, R. Seemann, K. Landfester, *Phys. Rev. Lett.* **93**, 017801 (2004).
27. J. S. Sharp, J. A. Forrest, *Phys. Rev. E Stat. Nonlin. Soft Matter Phys.* **67**, 031805 (2003).
28. A. Dhinojwala, G. K. Wong, J. M. Torkelson, *J. Chem. Phys.* **100**, 6046 (1994).
29. R. F. Boyer, S. G. Turley, Eds., *Molecular Basis of Transitions and Relaxations* (Gordon and Breach Science Publishers, New York, 1978), p. 33.

30. We thank C. A. Angell for useful discussions and G. B. McKenna for critical reading of this paper. Support from NSF (DMR-0706096 and DMR-0908651) is gratefully acknowledged.

Supporting Online Material

www.sciencemag.org/cgi/content/full/328/5986/1676/DC1
Materials and Methods
Figs. S1 and S2
References

9 November 2009; accepted 18 May 2010
10.1126/science.1184394

The Palladium-Catalyzed Trifluoromethylation of Aryl Chlorides

Eun Jin Cho, Todd D. Senecal, Tom Kinzel, Yong Zhang, Donald A. Watson,* Stephen L. Buchwald†

The trifluoromethyl group can dramatically influence the properties of organic molecules, thereby increasing their applicability as pharmaceuticals, agrochemicals, or building blocks for organic materials. Despite the importance of this substituent, no general method exists for its installment onto functionalized aromatic substrates. Current methods either require the use of harsh reaction conditions or suffer from a limited substrate scope. Here we report the palladium-catalyzed trifluoromethylation of aryl chlorides under mild conditions, allowing the transformation of a wide range of substrates, including heterocycles, in excellent yields. The process tolerates functional groups such as esters, amides, ethers, acetals, nitriles, and tertiary amines and, therefore, should be applicable to late-stage modifications of advanced intermediates. We have also prepared all the putative intermediates in the catalytic cycle and demonstrated their viability in the process.

The introduction of the strongly electron-withdrawing trifluoromethyl group into organic molecules can substantially alter their properties (such as lipophilicity, metabolic stability, and bioavailability) that affect the use of these molecules as pharmaceuticals and agrochemicals (*1*–*3*). Additionally, trifluoromethylated organic compounds find applications as materials such as liquid crystals (*2*). Despite the importance of this substituent, no general catalytic method exists for the introduction of the CF_3 group onto functionalized aromatic intermediates (*4*).

Structurally simple benzotrifluorides are accessible by radical chlorination of toluene derivatives and subsequent chlorine-fluorine exchange under harsh conditions (*5*). The replacement of an aromatic halide by a CF_3 group via copper-mediated coupling proceeds under milder reaction conditions but is mainly limited to aryl iodides (*6*–*16*). A catalytic version of this process was recently reported, but only aryl iodides with electron-withdrawing substituents and some heterocycles are good substrates (*17*).

A palladium-catalyzed trifluoromethylation of aryl halides (Fig. 1) has the potential to overcome these limitations: The use of a trifluoromethyl source as a transmetalating agent obviates the need for harsh reaction conditions that are required to replace individual substituents on benzylic carbon atoms with fluorine. Additionally, because many known ligands promote oxidative addition, even into unactivated aryl chlorides at low temperatures, a wide substrate scope is possible.

Mainly due to the high activation barrier for reductive elimination, the development of such a process has so far been unsuccessful. Several complexes (**4**) with bidentate ligands yield either no (*18*, *19*) or only trace amounts (*20*) of the benzotrifluoride products **5**, even after prolonged heating at 130°C. The chelating biphosphine ligands 1,2-Bis(diphenylphosphino)ethane (dppe) and 1,3-Bis(diphenylphosphino)propane (dppp) promote the reductive elimination of **4**, only at 145°C, to give $PhCF_3$ in 10 to 60% yield after 64 hours (*19*). On the other hand, the feasibility of fast Ar-CF_3 bond formation from a Pd(II) complex under mild conditions was demonstrated by Grushin and Marshall through quantitative conversion of the complex [XantphosPd(Ph)(CF_3)] to $PhCF_3$ upon heating to 80°C within 3 hours (*21*). However, the replacement of the Xantphos ligand in **3** with trifluoromethyl ions competes with transmetalation to **4**, and consequently, no catalytic system with this system was reported (*21*, *22*).

Complexes **4** are typically prepared from complexes **3**, where X = Br or I, by treatment with $TMSCF_3$ (TMS, trimethylsilyl) and a fluoride source such as CsF, thereby using the formation of a silicon-fluorine bond as driving force (*18*–*20*). The challenge of using trifluoromethylsilanes in the presence of fluoride originates in the fluoride-initiated self-decomposition of R_3SiCF_3 to give R_3SiF and difluorocarbene (*23*). In a catalytic setting, where elevated temperatures are presumably required to promote reductive elimination from **4**

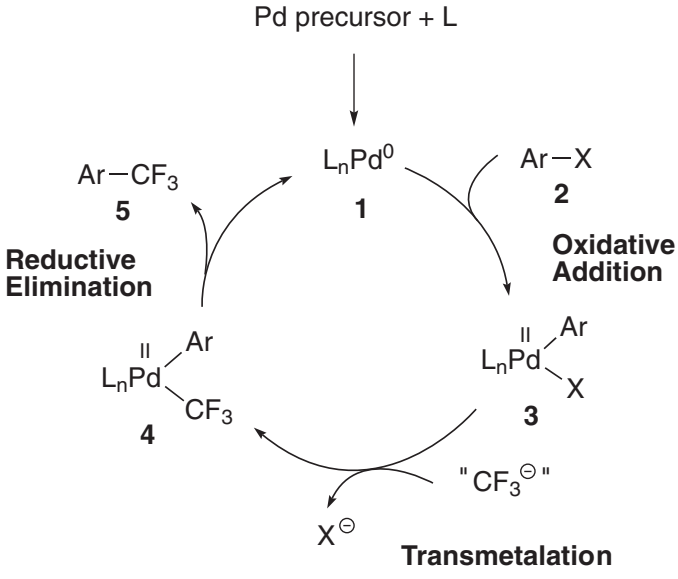

Fig. 1. Generalized catalytic cycle for aryl trifluoromethylation (L = ligand; Ar = aryl; X = Cl, Br, I, triflate).

Department of Chemistry, Massachusetts Institute of Technology (MIT), Cambridge, MA 02139, USA.

*Present address: Department of Chemistry and Biochemistry, University of Delaware, Newark, DE 19716, USA.
†To whom correspondence should be addressed. E-mail: sbuchwal@mit.edu

to **5**, transmetalation must be substantially faster than this process.

The oxidation of Pd(II)-CF_3 complexes with a F^+ reagent provides Pd(IV) complexes that readily reductively eliminate benzotrifluorides (*20*). The catalytic trifluoromethylation of arenes via C-H activation, oxidation of the Pd(II) intermediate with an electrophilic CF_3^+ source, and final reductive elimination have recently been reported, but are limited to substrates with specific directing groups (*24*).

We report the development of a palladium-catalyzed procedure to transform aryl chlorides into their trifluoromethylated analogs using $TESCF_3$ (TES, triethylsilyl) and KF. High functional-group tolerance under relatively mild conditions is exhibited, and a wide range of substrates, including heteroaryl ones, can be efficiently converted to the desired products. Mechanistic studies suggest that the reaction proceeds via a classical Pd(0)-Pd(II) catalytic cycle, as shown in Fig. 1.

Ligand **6** (BrettPhos) (Fig. 2A) has successfully been employed in challenging amination and fluorination cross-coupling reactions (*25*, *26*). We prepared the oxidative-addition complex **8** and examined numerous trifluoromethyl sources to identify conditions under which both transmetalation and reductive elimination would proceed (table S1) (*27*). Although most reagents failed to produce a product, the mixture of $TESCF_3$ and CsF in tetrahydrofuran (THF) at 60°C provided **9** in a promising yield of 28% (Fig. 2B). This result confirms that **6** does indeed promote reductive elimination to form Ar-CF_3 bonds and provides a starting point for the development of a catalytic procedure.

With 3 mole percent (mol %) $[(allyl)PdCl]_2$ and 12 mol % of ligand **6**, benzotrifluoride **9** was formed in 7% yield from aryl chloride **10** with $TESCF_3$ and CsF at 110°C. We next investigated several combinations of $TMSCF_3$ or $TESCF_3$ with simple fluoride salts and found that the highest yield was obtained using $TESCF_3$ with KF, demonstrating that the catalytic formation of **9** from **10** is possible with these transmetalating agents (Fig. 2C). Full conversion of **10** was achieved by switching the solvent to dioxane and performing the reaction at 120°C, providing **9** in 80% yield.

We studied the performance of other ligands under these conditions and found that **6** was the best ligand for this transformation (table S2). Most other monodentate biaryl phosphine ligands gave lower, but still observable, amounts between 5 and 20% of product **9**. No reaction occurred, however, when Xantphos was used.

The palladium-catalyzed process expands the scope to aryl chlorides and exhibits compatibility with a wide range of functional groups (Fig. 3). Both electron-poor and electron-rich aryl chlorides are suitable substrates and provide the trifluoromethylated products in good yields. More importantly, heteroaromatic substrates such as indoles, carbazoles, quinolines, and benzofuranes can be efficiently transformed into their trifluoromethylated analogs. When using ligand **6**, we found that

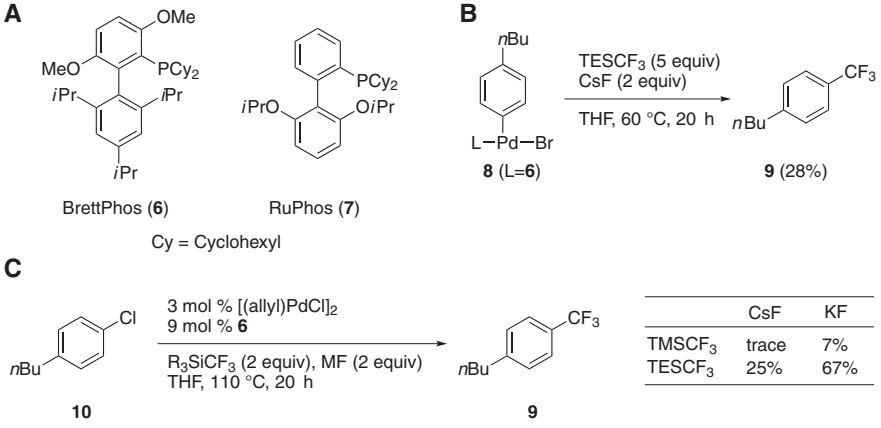

Fig. 2. (**A**) Ligands used in this study. Me, methyl; *i*Pr, isopropyl. (**B**) Best result from a reagent screen to convert complex **8** into benzotrifluoride **9**. *n*Bu, straight-chain butyl. (**C**) Identification of an optimal combination of trifluoromethyl source and activator for the catalytic conversion of **10** to **9**. R, methyl or ethyl.

Fig. 3. Scope of the palladium-catalyzed trifluoromethylation of aryl and heteroaryl chlorides. Isolated yields are based on an average of at least two runs. Minor amounts (2 to 5%) of reduced starting material (Ar-H) were usually observed. In a typical experiment, a solution of the palladium source and ligand **6** or **7** in dioxane was added to spray-dried KF and the aryl chloride. After addition of $TESCF_3$, the reaction was stirred at 120 to 140°C for 6 to 20 hours. Because KF is hygroscopic, all reactions were set up in a nitrogen-filled glovebox to prevent the hydrolysis of $TESCF_3$ in the course of the reaction. Et, ethyl; Hex, hexyl; Ph, phenyl.

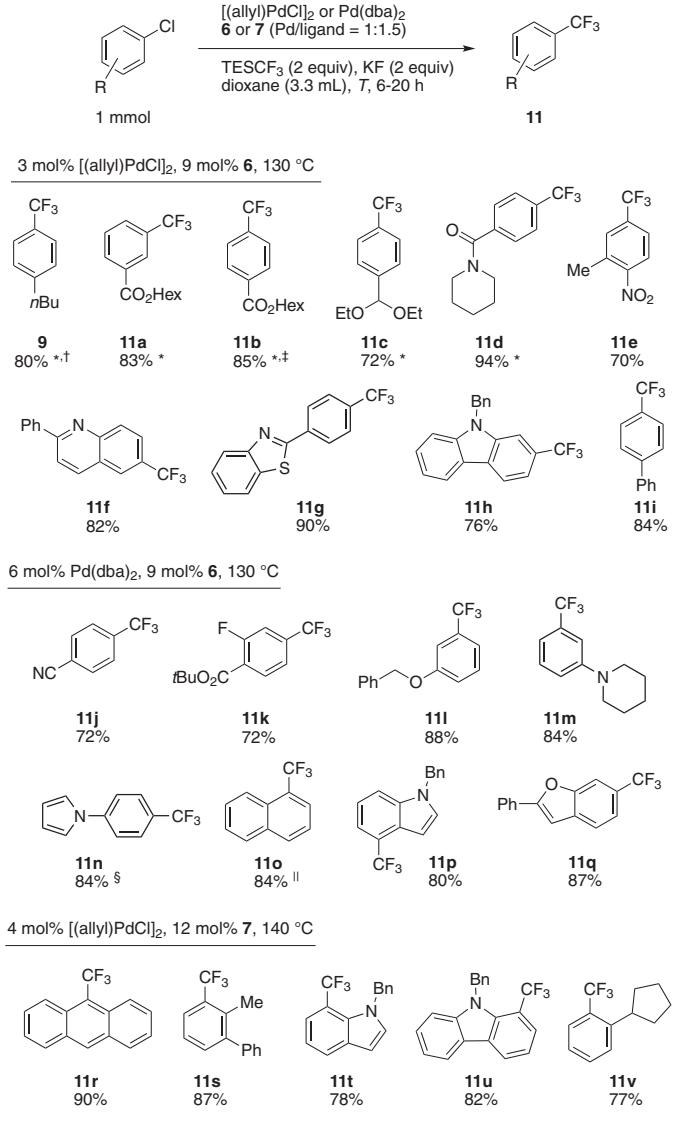

* 120 °C; † the compound could not be separated from the reduced Ar-H product. The given yield was estimated by gas chromatography; ‡ 2 mol% $[(allyl)PdCl]_2$, 6 mol% **6**; § 8 mol% $Pd(dba)_2$, 12 mol% **6**; || 12 mol% **6**

ortho-substituted substrates gave the corresponding products in low yields only. Switching to the less bulky ligand RuPhos (**7**) (Fig. 2A) (*28*) provided the desired ortho-substituted products **11r-v** in excellent yields. Scale-up proved to be straightforward; products **11j** and **11b** were prepared on 2- and 5-mmol scales, respectively, in the same yields as those reported for the 1-mmol–scale reactions.

Esters, acetals, amides, nitriles, ethers, dialkylamines, and a number of heteroaromatic substituents are tolerated. However, substrates bearing aldehydes or ketones are not suitable. Furthermore, substrates cannot contain unprotected OH or NH groups, presumably because of protonation of the CF_3 anion to form fluoroform, reaction at the silicon center of $TESCF_3$, and/or competing coordination to the palladium center.

To gain insight into the reaction mechanism, we prepared the presumptive Pd-CF_3 intermediates **13** and studied their reductive elimination to yield benzotrifluoride products. Treatment of complexes **12** with $TESCF_3$/CsF at room temperature in THF allowed the isolation of [**6**•Pd(Ar)(CF_3)] complexes **13** (Fig. 4A). The compounds exhibit a characteristic quartet in the ^{31}P–nuclear magnetic resonance (NMR) spectrum and a doublet in the ^{19}F-NMR spectrum with a coupling constant of ~45 Hz. The Pd atom in the crystal structures of **13a** (fig. S1) and **13b** (Fig. 4B) is coordinated by the upper-ring methoxy group of the ligand **6** and not by the ipso carbon atom of the lower aromatic ring.

We studied the reductive elimination of complexes **13** in dioxane at 80°C via ^{19}F-NMR and found first-order decay to give benzotrifluorides **14** in nearly quantitative yield. The rate constants for both the decomposition of **13a** and **13b** are almost identical (Fig. 4A and fig. S2 and S4). This surprising result is paralleled by density functional theory calculations that predict an activation energy of ~22 kcal mol^{-1} for both complexes (*29*, *30*). In comparison to the ground states, the calculated Pd-CF_3 distance in the transition states is substantially elongated, whereas the distance between the Pd atom and the aryl ring remains essentially unchanged, suggesting that the main contribution to the activation energy is the breaking of the strong Pd-CF_3 bond. Because the strength of this bond is only minimally influenced by the substituent on the aryl ring, similar rate constants are observed.

When complex **13a** was heated in the presence of excess methyl 4-chlorobenzoate, the oxidative-addition complex **12a** was formed in addition to product **14a**, thus closing the catalytic cycle. The yield and rate of benzotrifluoride formation were identical in the presence or absence of aryl chloride (fig. S3), which implies that reductive elimination affords a Pd(0) species that then undergoes oxidative addition to form **12a**. Therefore, we believe that these reactions proceed via a classical Pd(0)/Pd(II) catalytic cycle, as proposed in Fig. 1.

In preliminary experiments, we have demonstrated that this process is applicable, in somewhat lower yields, to aryl bromides and aryl triflates. We are currently seeking to develop a better understanding of the overall reaction mechanism, as well as to render this process more generally useful and practical. We hope to accomplish this by broadening its substrate scope, lowering the quantity of catalyst necessary, developing milder reaction conditions, and using less expensive and more environmentally friendly trifluoromethylating agents.

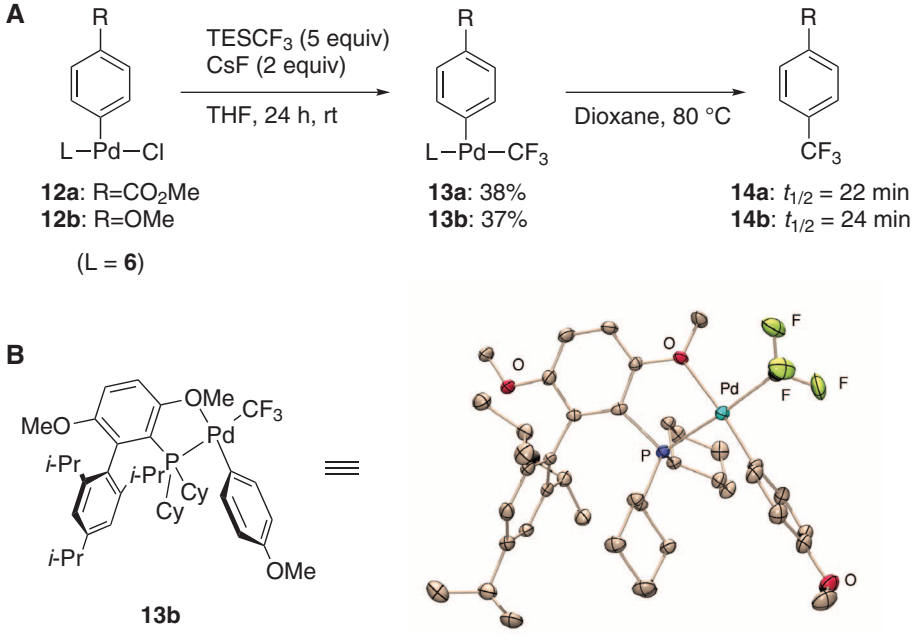

Fig. 4. (**A**) Formation of and reductive elimination from [**6**•Pd(Ar)(CF_3)] complexes. $t_{1/2}$ are the half-lives of the first-order reductive elimination kinetics. (**B**) X-ray structure of complex **13b**. ORTEP (*31*) drawing at 50% probability; hydrogen atoms are omitted for clarity.

References and Notes

1. D. Cartwright, in *Organofluorine Chemistry*, R. E. Banks, B. E. Smart, J. C. Tatlow, Eds. (Plenum, New York, 1994), pp. 237–262.
2. P. Kirsch, *Modern Fluoroorganic Chemistry* (Wiley-VCH, Weinheim, Germany, 2004).
3. K. Müller, C. Faeh, F. Diederich, *Science* **317**, 1881 (2007).
4. A. M. Thayer, *Chem. Eng. News* **84**, 15 (2006).
5. F. Swarts, *Bull. Soc. Chim. Belg.* **24**, 309 (1892).
6. V. C. R. Mcloughlin, J. Thrower, *Tetrahedron* **25**, 5921 (1969).
7. Y. Kobayashi, I. Kumadaki, *Tetrahedron Lett.* **10**, 4095 (1969).
8. N. V. Kondratenko, E. P. Vechirko, L. M. Yagupolskii, *Synthesis* **1980**, 932 (1980).
9. K. Matsui, E. Tobita, M. Ando, K. Kondo, *Chem. Lett.* **10**, 1719 (1981).
10. D. M. Wiemers, D. J. Burton, *J. Am. Chem. Soc.* **108**, 832 (1986).
11. G. E. Carr, R. D. Chambers, T. F. Holmes, D. G. Parker, *Perkin Trans. 1* **1988**, 921 (1988).
12. J. H. Clark, M. A. Mcclinton, R. J. Blade, *Chem. Commun.* **1988**, 638 (1988).
13. Q. Y. Chen, S. W. Wu, *Chem. Commun.* **1989**, 705 (1989).
14. H. Urata, T. Fuchikami, *Tetrahedron Lett.* **32**, 91 (1991).
15. F. Cottet, M. Schlosser, *Eur. J. Org. Chem.* **2002**, 327 (2002).
16. G. G. Dubinina, H. Furutachi, D. A. Vicic, *J. Am. Chem. Soc.* **130**, 8600 (2008).
17. M. Oishi, H. Kondo, H. Amii, *Chem. Commun. (Cambridge)* **2009**, 1909 (2009).
18. D. A. Culkin, J. F. Hartwig, *Organometallics* **23**, 3398 (2004).
19. V. V. Grushin, W. J. Marshall, *J. Am. Chem. Soc.* **128**, 4632 (2006).
20. N. D. Ball, J. W. Kampf, M. S. Sanford, *J. Am. Chem. Soc.* **132**, 2878 (2010).
21. V. V. Grushin, W. J. Marshall, *J. Am. Chem. Soc.* **128**, 12644 (2006).
22. D. Naumann *et al.*, *Z. Anorg. Allg. Chem.* **630**, 746 (2004).
23. W. Tyrra *et al.*, *Chemistry* **11**, 6514 (2005).
24. X. Wang, L. Truesdale, J. Q. Yu, *J. Am. Chem. Soc.* **132**, 3648 (2010).
25. B. P. Fors, D. A. Watson, M. R. Biscoe, S. L. Buchwald, *J. Am. Chem. Soc.* **130**, 13552 (2008).
26. D. A. Watson *et al.*, *Science* **325**, 1661 (2009); published online 13 August 2009 (10.1126/science.1178239).
27. Supporting material is available on *Science* Online.
28. J. E. Milne, S. L. Buchwald, *J. Am. Chem. Soc.* **126**, 13028 (2004).
29. M. J. Frisch *et al.*, Gaussian 03, Revision E.01 (Gaussian, Inc., Wallingford CT, 2004).
30. The employed level of theory is B3LYP/6-311++G(2d,p)/LanL2Dz//B3LYP/6-31G(d)/LanL2Dz.
31. ORTEP, www.ornl.gov/sci/ortep/ortep.html.

32. We thank the NIH for financial support of this project (grant GM46059) and Merck, Nippon Chemical, Boehringer Ingelheim, and BASF for gifts of chemicals and additional funds. T.K. thanks the Alexander von Humboldt Foundation for a Feodor Lynen postdoctoral fellowship. The Varian NMR instrument that we used was supported by the NSF (grants CHE 9808061 and DBI 9729592). We also thank P. Müller (MIT Chemistry Department, X-Ray Diffraction Facility) for obtaining the crystal structures of **13a** and **13b**. Cambridge Crystallographic Data Centre (CCDC) 771779 and 771780 contain the supplementary crystallographic data for this paper. These data can be obtained free of charge from the CCDC via www.ccdc.cam.ac.uk/data_request/cif.

Supporting Online Material

www.sciencemag.org/cgi/content/full/328/5986/1679/DC1
SOM Text
Figs. S1 to S5
Tables S1 to S3
References

6 April 2010; accepted 12 May 2010
10.1126/science.1190524

Detection of Hydrated Silicates in Crustal Outcrops in the Northern Plains of Mars

J. Carter,[1]* F. Poulet,[1] J.-P. Bibring,[1] S. Murchie[2]

The composition of the ancient martian crust is a key ingredient in deciphering the environment and evolution of early Mars. We present an analysis of the composition of large craters in the martian northern plains based on data from spaceborne imaging spectrometers. Nine of the craters have excavated assemblages of phyllosilicates from ancient, Noachian crust buried beneath the plains' cover. The phyllosilicates are indistinguishable from those exposed in widespread locations in the southern highlands, demonstrating that liquid water once altered both hemispheres of Mars.

Data acquired by the OMEGA (Observatoire pour la Minéralogie, l'Eau, les Glaces, et l'Activité) (*1*) and CRISM (Compact Reconnaissance Imaging Spectrometer for Mars) (*2*) instruments on board Mars Express and Mars Reconnaissance Orbiter, respectively, have confirmed that the surface of the ancient, Noachian-aged southern highlands is mostly unaltered, preserving old crustal materials (*3*–*5*), and revealed thousands of small outcrops of various hydrated silicates, mostly phyllosilicates (*6*–*8*). These altered minerals record an early era during which Mars likely harbored environmental conditions that sustained surface and subsurface liquid water. By contrast, in the younger northern lowlands that cover one-third of the planet, a hundreds-of-meters-to-few-kilometers-thick cover, interpreted to be volcanic and detrital sediments partly reworked by glacial processes, buries preexisting crust thought to be analogous to that in the southern highlands (*9*, *10*). Contrary to the highlands, the surface has a large dust cover index (*11*) and displays only weak and localized signatures of olivine and pyroxene, with no hydrated silicates (*4*, *12*–*14*). The structure and composition of the underlying crust are nearly unknown in spite of attempts to constrain them by surface altimetry and subsurface radar sounding (*15*, *16*).

An efficient way to access the crust buried beneath the northern plains is to study material ejected by impactors large enough to create craters tens of kilometers in diameter and penetrate to several kilometers in depth (*17*), below the Hesperian cover: Although violent, the cratering process partly preserves the composition of the ejected material. Previous studies of craters within the northern plains have included a thorough survey of their morphology (*10*, *18*) and of their spectral signatures, revealing that olivine is ubiquitous in craters larger than tens of km (*13*, *19*, *20*). After tentative detections of phyllosilicates in a few northern plains craters by OMEGA (fig. S1) (*21*), we used surface reflectance data from CRISM to investigate the composition of northern plains craters, focusing on central peaks, rims, and ejecta. CRISM acquires spectra of the surface covering 0.4 to 3.9 μm at a spatial sampling of 18 m per pixel, spectrally sampled at 6.5 nm (*2*).

We analyzed all craters greater than 30 km for which CRISM data were available and dozens of craters with diameters ranging from 4 to 30 km. We excluded from our survey observations of sites covered by seasonal ice. The remaining 160 high-resolution CRISM images cover 91 craters. Nine of them exhibit spectral signatures of hydrated minerals: Lyot, Kunowsky, Stokes, Santa Fe, Bamberg, and four unnamed craters. All nine craters are found in relatively young [$<2.5 \times 10^9$ years ago (Ga)] plains (Fig. 1), range in diameter from 20 to 60 km (except for the 230-km Lyot crater), and have well-exposed inner crater walls and rims. Preservation state varies greatly from one crater to another: Some are well preserved (e.g., Stokes, Santa Fe, and Bamberg), but overall northern plains craters have been heavily mantled and resurfaced by volcanic, glacial, periglacial, and sedimentary processes (*9*, *10*, *18*, *22*–*24*).

We built spectral parameter maps representing strengths of specific metal-OH vibration bands that allow discriminating between various hydrated minerals, which all exhibit a 1.9-μm feature (Fig. 2). A band near 2.2 μm indicated the presence of Al-rich phyllosilicates, whereas Fe-rich and Mg-rich (Fe/Mg-rich) phyllosilicates were identified on the basis of absorption bands from 2.28 to 2.35 μm (*6*, *25*). Chlorites and prehnite both exhibited bands between 2.2 and 2.4 μm, with prehnite uniquely identified by sharp bands

[1]Institut d'Astrophysique Spatiale (IAS), CNRS/Université Paris XI, 91405 Orsay, France. [2]Applied Physics Laboratory (APL), Laurel, MD 20723, USA.

*To whom correspondence should be addressed. E-mail: John.carter@ias.u-psud.fr

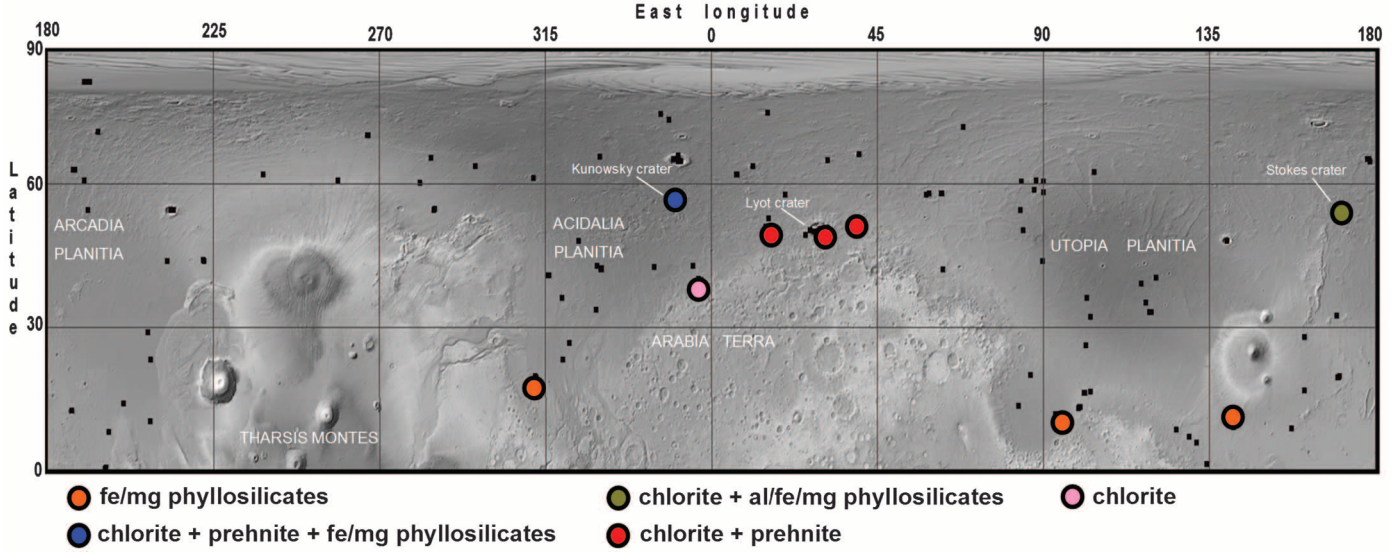

Fig. 1. Locations of nine exposures of hydrated silicate in northern plains craters, shown on a Mars Orbiter Laser Altimeter shaded relief map. Black squares indicate sites investigated with CRISM that did not yield detections.

at 2.35 and 1.48 μm. We also built maps of mafic mineral bands (resulting from olivine and pyroxene) based on absorptions in the 1- to 2.5-μm wavelength range (*26*).

By using these spectral criteria, we detected a variety of hydrated minerals. Signatures consistent with Fe/Mg phyllosilicates and chlorites were found in six out of nine sites, whereas Al-rich phyllosilicates were only found at Stokes crater (Fig. 2). At least four sites had signatures consistent with prehnite, and three sites may have contained a chlorite-prehnite assemblage, identifiable by their band shapes around 2.35 μm and the presence of two distinct shallow bands at 1.4 and 1.48 μm. Three lower-latitude craters had spectral signatures in their central mound consistent, at an 18-m-per-pixel scale, with either olivine partly altered into Fe/Mg-rich clay or subpixel mixtures of olivine and clay. In addition to hydrated minerals, all of the large craters had strong olivine signatures both in their bedrock and in dark dunes on the crater floors, in close proximity to the hydrated mineral deposits. Smaller pyroxene-bearing outcrops were also identified in the central peaks in a few craters.

All nine craters with hydrated minerals are located equatorward of 60°N (Fig. 1); six are close to the highlands units, and the remaining three are at distances > 1000 km. The hydrated minerals occur in the craters' central peaks with the exception of the Lyot crater, for which the relevant signatures were observed in inner and outer rim materials. There is no consistent geological trend regarding association with preservation state: Some occurrences were in degraded outcrops or knobs, whereas others were associated with mobile material. A given hydrated mineral specie may be found in different settings within a crater, suggesting erosion and aeolian transport.

Stokes, a 60-km crater located in northern Arcadia Planitia, exemplifies the diversity in hydrated mineral composition and morphological setting (Fig. 3). It is a complex crater with a highly fractured central uplift. Its major features include knobs, scarps, km-scale outcrops, and evidence for aeolian erosion and sedimentation. No periglacial mantling processes are evident at the scale of High-Resolution Imaging Science Experiment (HiRISE) images (<50 cm per pixel).

We detected numerous hydrated silicate signatures at various locations within Stokes. The spectral signatures agree well with those of two different aluminum phyllosilicates, montmorillonite and kaolinite, as well as with chlorites and mixed-layered Fe/Mg phyllosilicates/chlorites. The most spatially extensive hydrated mineral signature is consistent with the aluminum smectite montmorillonite, which occurs in small-scale, light-toned outcrops along a 2-km-long scarp. There is strong evidence for erosion and downhill transport of the altered outcropping material (Fig. 3C). We identified dozens of occurrences of Al phyllosilicate consistent with kaolinite, typically <100 m in size. These were correlated with rough material in outcrops or knobs, with some evidence of limited erosion and transport. The iron-magnesium phyllosilicate-bearing unit was also found in outcropping material, usually in close proximity to the Al-rich units (Fig. 3D). Olivine and pyroxene signatures were correlated with light-toned outcrops in the central structure (Fig. 3B) that appear randomly fractured. Olivine is the most common mineral detected, and pyroxene was seen in a few outcrops; both were more common than hydrated mineral-bearing outcrops. Hydrated mineral outcrops are more fractured and less well preserved than the olivine outcrops. A few olivine outcrops displayed a 2.3-μm band consistent with altered olivine or a subpixel spatial mixture of olivine and phyllosilicate.

Kunowsky crater (Fig. 4) exhibited signatures of Fe/Mg-rich phyllosilicates and what we interpret as a chlorite-prehnite assemblage. At the 6-m-per-pixel scale of CTX (Context Camera, also on Mars Renaissance Orbiter) images (Fig. 4B), there is evidence for aeolian and/or slope-driven displacement of the chlorite/prehnite-bearing material, emanating from a mound east of the central uplift. At the scale of HiRISE images (Fig. 4C), Fe/Mg-rich phyllosilicates appear broadly correlated with hundreds-of-meters-scale outcrops or mounds. The 230-km-diameter Lyot crater, formed during the Early Amazonian period, is the largest and deepest northern plains crater, with a partly preserved rim and ejecta (fig. S2). Although fluvial valley systems within Lyot crater were formed during Middle or Late Amazonian (*27*), we detected a chlorite-prehnite unit on the outer rim, indicating formation distinct from valley formation (fig. S2B).

Four scenarios could account for the formation of hydrated minerals in northern plains craters. First, parent minerals, likely mafic, were altered in situ by aqueous surface processes after having been exhumed by impact. The presence of the low-grade metamorphic mineral prehnite, which forms under specific conditions of <3 kbar, 200° to 350°C (*28*), argues against formation by this process. Moreover, no morphological evidence at the regional or crater scale points toward the existence of transient or standing bodies of liquid water on the surface. Second, phyllosilicate-bearing material was transported by wind from highlands and deposited since the time of crater formation. The correlation of phyllosilicate signatures with outcrops or rocky units and the absence of such signatures in crater floor dunes and elsewhere in the northern plains are strong evidences against this scenario. Third, hydrated minerals

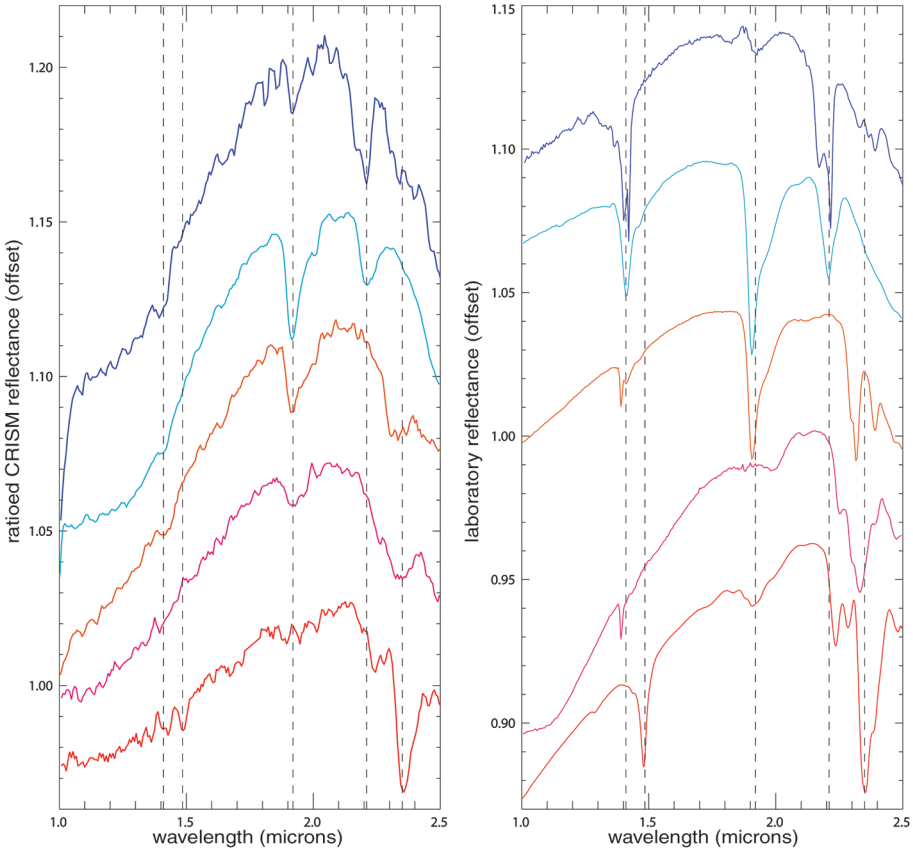

Fig. 2. CRISM hydrated silicate spectral signatures in northern plains craters (**left**). Candidate laboratory matches (**right**) are from the RELAB spectral database and (*35*). From top to bottom the colors are as follows: kaolinite, blue; montmorillonite, cyan; Fe/Mg saponite, orange; chlorite, purple; and prehnite, red. CRISM spectra are spatial averages of tens to hundreds of pixels.

formed by impact-driven hydrothermal alteration. Modeling shows that martian impact craters tens of km in size could have provided suitable pressure and temperature for phyllosilicate formation (*29*–*31*). Alteration would be strongest in the immediate vicinity of the central uplift and could have lasted 10^6 years. Recent calculations predict a variety of alteration minerals, for example, serpentine, chlorite, and the clay minerals nontronite and kaolinite (*31*). Some of these minerals are indeed identified; however, the mineral assemblage expected to be most abundant near the central uplift, a serpentine-hematite-talc assemblage, is not observed. The alteration minerals predicted in impact-induced hydrothermal systems vary in composition with the temperature, pressure, and water-to-rock ratio within the crater: One would therefore expect spatial gradients of abundances translating their stability. On the contrary, we observed unaltered olivine and phyllosilicates closely juxtaposed, randomly within the crater floors. The presence of prehnite is also difficult to explain by an impact process. Lastly, if impact hydrothermalism was responsible for the formation of phyllosilicates, one would expect their presence in craters across a variety of units, but they were detected only when the impact penetrated the spectrally featureless Hesperian layer and exposed underlying Noachian rock with clear mafic mineral signatures.

The fourth scenario, supported by our observations, is that hydrated silicates in the northern plains craters formed by aqueous alteration

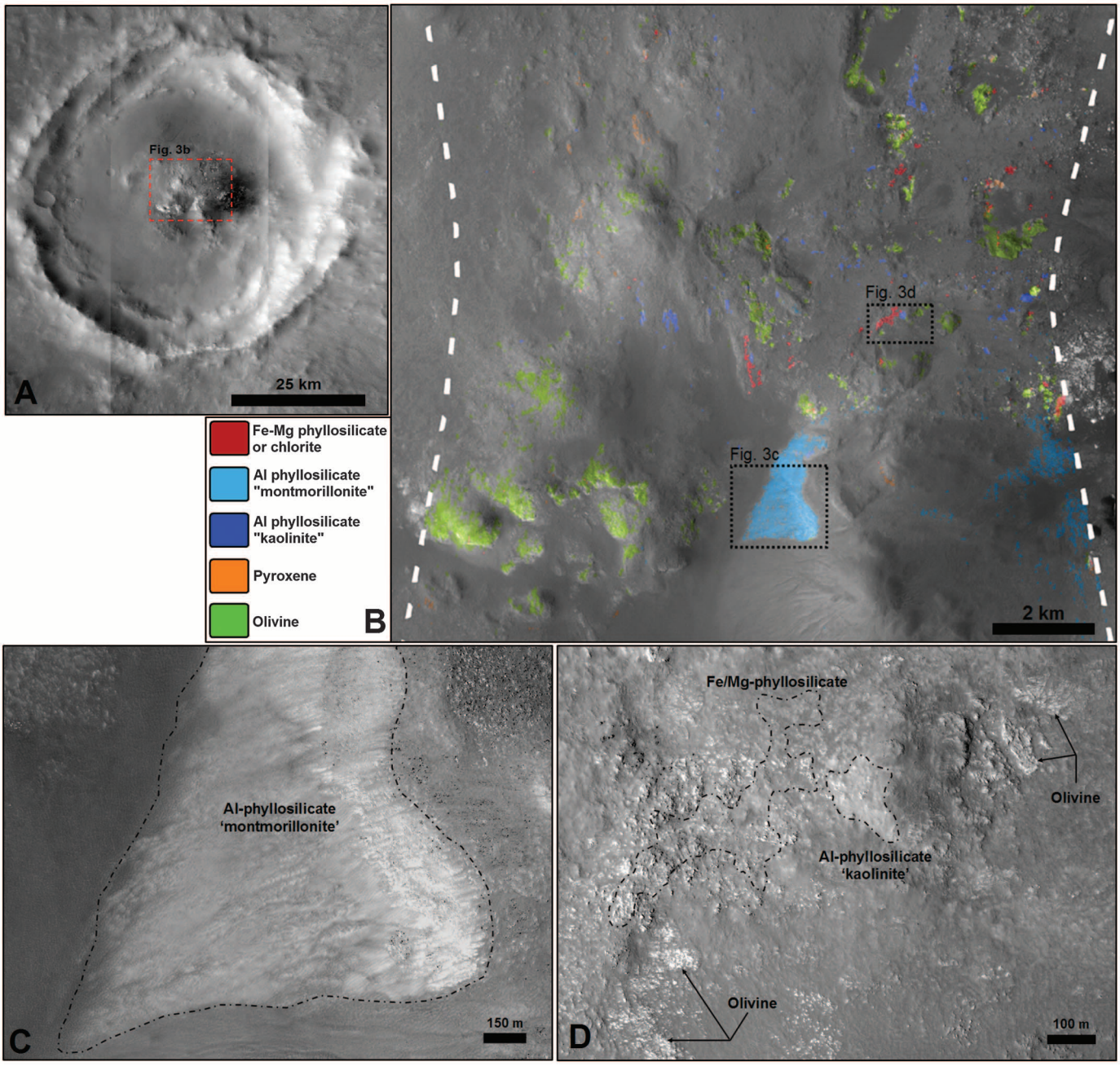

Fig. 3. (**A**) CTX–High-Resolution Stereo Camera (HRSC) mosaic of Stokes crater, centered at 171.35°E, 55.56°N. (**B**) CTX close-up (image P20_008686_2356). CRISM mineral maps from observation FRT0000ADA4 are overlain in color. The white dashed lines indicate the boundaries of the CRISM observation. (**C**) HiRISE close-up (image PSP_009332_2360) of the Al-phyllosilicate "montmorillonite"-bearing unit. The sources of the material are the bright outcrops near the scarp summit (right), whereas the light-toned unit (left) is material transported down-slope. (**D**) HiRISE close-up (image PSP_009332_2360) showing outcrops of olivine, Fe/Mg-, and Al-phyllosilicates in close spatial association.

before emplacement of the Hesperian cover and then were excavated by impacts that penetrated the cover. On the basis of the estimated crater excavation depth (*17*), the craters in which hydrated minerals are detected are large enough to have reached the crust; the impacts have excavated material buried hundreds of meters to a km below surface, consistent with our observations of altered minerals both in central uplifts and rims and ejecta. The composition of the hydrated minerals also favors a formation predating the craters. Prehnite forms at high temperatures only attainable within the crust or hydrothermally within the central uplift of large (>30 km) craters (*29*, *30*); it was detected in the central peak of a smaller crater as well as in the rim of Lyot crater, implicating formation at depth in the crust. More generally, the mineral assemblages found in these northern craters (such as smectites and chlorites) are very similar to those detected in craters in the southern highlands by using OMEGA and CRISM data (*6*, *7*, *32*, *33*). The geological contexts of highland detections point to formation by sustained aqueous alteration, commonly at elevated temperatures and possibly partly in the subsurface. Impact gardening, in particular during the likely late heavy bombardment, might have triggered some additional alteration of the mineral assemblies, but predominantly it might have mechanically mixed phyllosilicates and unaltered rock. In a similar way, craters that excavated hydrated minerals from beneath the northern plains may have induced some modifications of the mineral composition; however, the primary alteration took place within the crust, before excavation. The apparently random spatial distribution of unaltered olivine/pyroxene and phyllosilicate outcrops within the crater central structures is also consistent with the excavation of a differentiated and altered crust. Olivine is readily altered under aqueous conditions, which would be expected in an impact-generated hydrothermal environment.

Thus, the phyllosilicates detected in larger craters within the northern plains most likely record alteration processes that affected the northern crust before its being covered by kilometers-thick lava deposits. The similarities between their composition and those of the hydrated minerals in the southern highlands craters are an important indication that the martian crust was altered on a global scale during the Noachian period. This supports existence of an early environment conducive to the formation of life, with widespread liquid water, characterizing the phyllosian era (*34*).

This detection constrains the timing of ancient martian environments, in particular through the formation of the north-south hemispheric dichotomy; the heavy bombardment; and resurfacing of the northern lowlands by volcanism and sedimentary and volatile material. If the dichotomy formed by a giant impact, most of the record of preexisting shallow, low-temperature alteration would have been obliterated. Instead, craters

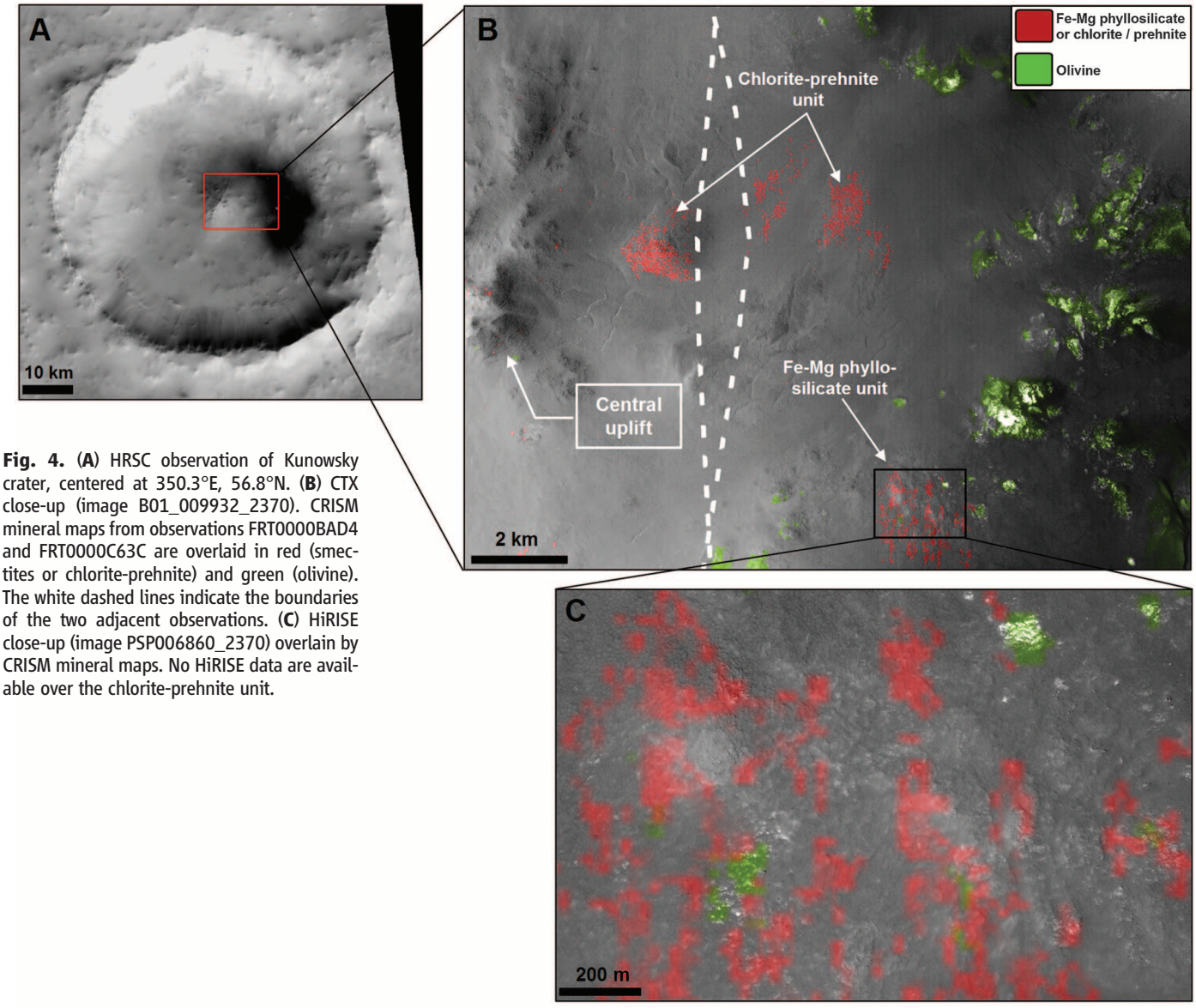

Fig. 4. (**A**) HRSC observation of Kunowsky crater, centered at 350.3°E, 56.8°N. (**B**) CTX close-up (image B01_009932_2370). CRISM mineral maps from observations FRT0000BAD4 and FRT0000C63C are overlaid in red (smectites or chlorite-prehnite) and green (olivine). The white dashed lines indicate the boundaries of the two adjacent observations. (**C**) HiRISE close-up (image PSP006860_2370) overlain by CRISM mineral maps. No HiRISE data are available over the chlorite-prehnite unit.

thousands of kilometers interior to the northern plains retain hydrated silicates. A likely sequence is thus as follows: The bulk of the aqueous alteration of the crust happened after the dichotomy formed but before the onset of volcanic activity that built the Tharsis plateau and contributed to the infilling of the northern plains. The phyllosian environment affected the entire planet during a highly restricted period of time.

References

1. J.-P. Bibring *et al.*, *Eur. Space Agency Spec. Pub.* **1240**, 37 (2004).
2. S. Murchie *et al.*, *J. Geophys. Res.* **114**, E00D07 (2009).
3. J. L. Bandfield, *J. Geophys. Res.* **107**, 5042 (2002).
4. J.-P. Bibring *et al.*, *Science* **307**, 1576 (2005); published online 17 February 2005 (10.1126/science.1108806).
5. P. R. Christensen *et al.*, *Nature* **436**, 504 (2005).
6. F. Poulet *et al.*, *Nature* **438**, 623 (2005).
7. J. F. Mustard *et al.*, *Nature* **454**, 305 (2008).
8. J. Carter *et al.*, *Proc. Lunar Planet. Sci. Conf.* **40**, abstr. 2028 (2009).
9. V. R. Baker *et al.*, *Nature* **352**, 589 (1991).
10. K. L. Tanaka *et al.*, *J. Geophys. Res.* **108**, (E4), 8043 (2003).
11. S. W. Ruff *et al.*, *Icarus* **168**, 131 (2004).
12. M. B. Wyatt, H. Y. McSween Jr., *Nature* **417**, 263 (2002).
13. M.R. Salvatore *et al.*, *Proc. Lunar Planet. Sci. Conf.* **40**, abstr. 2050 (2009).
14. J. F. Mustard *et al.*, *Science* **307**, 1594 (2005); published online 17 February 2005 (10.1126/science.1109098).
15. M. T. Zuber *et al.*, *Science* **287**, 1788 (2000).
16. G. Picardi *et al.*, *Science* **310**, 1925 (2005); published online 30 November 2005 (10.1126/science.1122165).
17. D. Baratoux *et al.*, *J. Geophys. Res.* **112**, E08S05 (2007).
18. M. A. Kreslavsky, J. W. Head, *Meteorit. Planet. Sci.* **41**, 1633 (2006).
19. D. Rogers, P. R. Christensen, *J. Geophys. Res.* **108**, 5030 (2003).
20. K. R. Stockstill-Cahill, F. S. Anderson, V. E. Hamilton, *J. Geophys. Res.* **113**, E07008 (2008).
21. B. Gondet *et al.*, in *Seventh International Conference on Mars*, Lunar and Planetary Institute, Pasadena, CA, 9 to 13 July 2007, abstr. 3185.
22. M. A. Kreslavsky, J. W. Head, *J. Geophys. Res.* **107**, 5121 (2002).
23. M. A. Kreslavsky, J. W. Head, *Geophys. Res. Lett.* **29**, 1719 (2002).
24. J. W. Head, M. A. Kreslavsky, S. Pratt., *J. Geophys. Res.* **107**, 10.1029/2000JE001445 (2002).
25. J. L. Bishop, M. D. Lane, M. D. Dyar, A. J. Brown, *Clay Miner.* **43**, 35 (2008).
26. S. M. Pelkey *et al.*, *J. Geophys. Res.* **112**, E08S14 (2007).
27. J. L. Dickson, C. I. Fassett, J. W. Head, *Geophys. Res. Lett.* **36**, L08201 (2009).
28. M. Frey, D. Robinson, *Low-Grade Metamorphism* (Blackwell, Oxford, 1999).
29. O. Abramov, D. A. Kring, *J. Geophys. Res.* **110**, (E12), E12S09 (2005).
30. J. A. Rathbun, S. W. Squyres, *Icarus* **157**, 362 (2002).
31. S. P. Schwenzer, D. A. Kring, *Geology* **37**, 1091 (2009).
32. B. L. Ehlmann *et al.*, *J. Geophys. Res.* **114**, E00D08 (2009).
33. S. L. Murchie *et al.*, *J. Geophys. Res.* **114**, E00D06 (2009).
34. J.-P. Bibring *et al.*, *Science* **312**, 400 (2006).
35. R. N. Clark *et al.*, U.S. Geological Survey (USGS) Digital Spectral Library splib06a, USGS Digital Data Series 231 (USGS, Denver, CO, 2007).

Supporting Online Material

www.sciencemag.org/cgi/content/full/328/5986/1682/DC1
Figs. S1 and S2

2 March 2010; accepted 20 May 2010
10.1126/science.1189013

Hydrogen Isotopes Preclude Marine Hydrate CH_4 Emissions at the Onset of Dansgaard-Oeschger Events

Michael Bock,[1,2]* Jochen Schmitt,[1,2] Lars Möller,[2] Renato Spahni,[1] Thomas Blunier,[3] Hubertus Fischer[1,2]

The causes of past changes in the global methane cycle and especially the role of marine methane hydrate (clathrate) destabilization events are a matter of debate. Here we present evidence from the North Greenland Ice Core Project ice core based on the hydrogen isotopic composition of methane [$\delta D(CH_4)$] that clathrates did not cause atmospheric methane concentration to rise at the onset of Dansgaard-Oeschger (DO) events 7 and 8. Box modeling supports boreal wetland emissions as the most likely explanation for the interstadial increase. Moreover, our data show that $\delta D(CH_4)$ dropped 500 years before the onset of DO 8, with CH_4 concentration rising only slightly. This can be explained by an early climate response of boreal wetlands, which carry the strongly depleted isotopic signature of high-latitude precipitation at that time.

Rapid stadial-interstadial climate changes during Marine Isotope Stage 3 (MIS3), as recorded in Greenland ice (*1*), had a strong impact around the globe (*2*–*5*). Some of the stadials were accompanied by large discharges of icebergs from the Laurentide ice sheet, known as Heinrich events (*4*). Atmospheric methane concentrations in ice cores show abrupt increases in concert with Dansgaard-Oeschger (DO) warmings (*5*, *6*), although the causes of these methane jumps are not yet unambiguously understood. Preindustrial methane sources include wetlands, thermokarst lakes, ruminants, termites, biomass burning, ultraviolet radiation–induced release by plants, and clathrates (*7*–*11*). Wetlands, the major natural source of atmospheric methane, may be able to respond rapidly enough to changes in temperature and the hydrological cycle to account for the CH_4 increases (*5*, *7*, *12*, *13*). Another hypothesis suggests that the observed rises were due to emissions of marine clathrates stored at the continental margins, which may have been destabilized by a warming of intermediate waters (*14*–*16*). Clathrate destabilization events were indeed found in selected marine sediments (*14*, *17*), although their contribution to the atmospheric budget has been questioned (*5*, *13*, *18*). A change in the CH_4 sink, and thus lifetime, may also have contributed to the observed CH_4 concentration changes.

Methanogenic pathways determine both the carbon and hydrogen isotopic signatures (*8*) of the emitted CH_4, which in turn can be used to better constrain the global methane budget (*9*). Source isotopic compositions may vary as a result of changes in methane precursor material, diffusion and oxidation processes that depend on water table depth in wetlands, or temperature changes in the aerobic zone of tundra soils (*19*). Moreover, the hydrogen isotopic composition of methane [$\delta D(CH_4)$] produced in terrestrial ecosystems is a function of the isotopic signature of precipitation (*8*). The hydrogen isotopic signature of precipitation changed globally because of the temporal variation in the isotopic composition of the ocean, which is a function of the size of polar ice sheets. Schrag *et al.* report δD values of the Last Glacial Maximum (LGM) ocean to be 6.5 to 9 per mil (‰) more enriched than those of today's ocean (*20*). Assuming a maximum sea-level rise of 30 m during DO 8 (*21*), this translates into a hydrogen isotopic shift of the well-mixed ocean of about 2‰. Superimposed on this global change, a stronger Rayleigh distillation effect in meteoric water is expected in high latitudes for cold climate conditions, due to the stronger pole-to-equator temperature gradient. For instance, water isotopes in modeled precipitation suggest that δD_{water} values were 15 to 30‰ lower in northern latitudes during the LGM, whereas values may have been 0 to 8‰ higher in the tropics (*22*).

Rapid changes in the low-latitude hydrological cycle are recorded in marine sediments (*23*), speleothems (*3*, *24*), and leaf waxes in lake

[1]Climate and Environmental Physics, Physics Institute and Oeschger Centre for Climate Change Research, University of Bern, Sidlerstrasse 5, 3012 Bern, Switzerland. [2]Alfred Wegener Institute for Polar and Marine Research, Am alten Hafen 26, 27568 Bremerhaven, Germany. [3]Centre for Ice and Climate, Niels Bohr Institute, University of Copenhagen, Juliane Maries Vej 30, DK-2100 Copenhagen Ø, Denmark.

*To whom correspondence should be addressed. E-mail: bock@climate.unibe.ch

sediments (*25*). These records show latitudinal swings in the Intertropical Convergence Zone (ITCZ), which may have had a strong impact on the local hydrological cycle. In general, little change in δD_{water} is expected close to the ITCZ, where atmospheric water is rapidly recycled. On a global scale, ITCZ swings should therefore lead to a latitudinal relocation of tropical wetlands, but we expect only a secondary effect on the methane hydrogen isotopic signature recorded in ice cores. Changes in the extent of tropical wetlands, which affect the source strength, are difficult to constrain because changes in land area, precipitation patterns, terrain slope, and water-retaining soil layers have to be considered.

Finally, the reaction of CH_4 with the OH radical is the major sink for methane (*9*). The change in kinetic fractionation due to stadial-interstadial temperature changes is limited to less than 3‰ (*18*). We also assume that the relative contributions of the OH, stratospheric, and soil sinks have not substantially changed over time and, therefore, that sink processes have only minor effects on our $\delta D(CH_4)$ record. In summary, we interpret the observed variations in our $\delta D(CH_4)$ time series to be mainly changes in the source mix, with secondary effects of changes in the isotopic composition of precipitation, especially in high latitudes.

Because the hydrogen isotopic composition of methane emitted by marine clathrates (~−190‰) is much heavier than that of the predominant wetland sources (−300 to −400‰) (*18*, *26*), $\delta D(CH_4)$ measurements are well suited to assessing the contribution of marine clathrates to the atmospheric CH_4 budget (*14*). The first $\delta D(CH_4)$ data from an ice core suggested that methane clathrates were stable during the rapid Bølling-Allerød and Younger Dryas–Preboreal warmings (*18*). Furthermore, a complete $\delta^{13}CH_4$ record over the last glacial-interglacial transition (*13*), together with the interhemispheric CH_4 gradient (IHG) (*5*, *27*), showed that boreal wetland CH_4 emissions were essentially shut down during cold stages, and that the atmospheric lifetime of methane was substantially reduced (*13*).

Here we present a high-resolution atmospheric $\delta D(CH_4)$ record (Fig. 1) from the NGRIP ice core spanning DO events 7 and 8, i.e., 33.7 to 41.0 ky B.P. (thousand years before present, where present is defined as 1950 CE). We analyzed 61 samples in randomized order with high precision (±3.4‰), using a technique described previously (*26*, *28*). Over DO 7 and 8, the mean nominal time resolution was 88 years. Reconstructed atmospheric values for $\delta D(CH_4)$ ranged from −77.6 to −98.5‰. In general, we observed higher $\delta D(CH_4)$ for stadial (about −80‰) than interstadial (<−90‰) conditions. This depleted isotopic composition during interstadials precludes a dominant influence of isotopic-enriched clathrate emissions. There are also notable features superimposed that highlight differences between the two investigated DO cycles. In particular, we find a pronounced, 16‰ drop in $\delta D(CH_4)$ that precedes the fast CH_4 increase into DO 8 by ~500 years, in agreement with the few previously published data points from the Greenland Ice Sheet Project 2 (GISP2) ice core (*18*). The drop occurs simultaneously with a slight increase in NGRIP temperatures (*6*) and Greenland ice core CH_4 concentrations [~40 parts per billion by volume (ppbv)] late in the stadial (Fig. 1), at a time when ice rafting debris counts had relaxed from peak Heinrich event conditions (*4*). We propose a slow restart of the Atlantic Meridional Overturning Circulation (AMOC) 500 years before the rapid DO warming in the north. As expected from the bipolar seesaw concept, this would lead to a change in the Southern Ocean warming rate. Although the synchronization error of bipolar ice core records is on the order of 400 years for this interval (*2*) and does not allow a firm conclusion on the exact timing, a change in the warming rate is observed in Antarctic ice cores before the CH_4 increase (*2*). Later during interstadial 8, $\delta D(CH_4)$ rises to stadial levels with two excursions of about +10‰ that occurred at 36.7 and 37.4 ky B.P., i.e., when CH_4 is near its interstadial level and $\delta^{18}O_{ice}$ in the NGRIP ice core is slowly decreasing.

The IHG is small during stadials and large during DO 7 and at the beginning of DO 8, but again reduced at the end of interstadial 8 (*2*). Accordingly, we used the combined information from the IHG and CH_4 isotopes (*26*) to quantify source contributions for three time slices ["stadial," "early-interstadial," and "late-interstadial" (table S1)] using a model approach described previously (*13*). A simple four-box model of the atmosphere was run with prescribed values for CH_4 source strengths, lifetime, and source isotopic compositions in a Monte Carlo approach to constrain our CH_4 budget (*13*, *26*).

An initial estimate constrained only by the ice core records (table S1 and fig. S4) revealed significantly reduced atmospheric lifetimes for both climatic stages compared to the present, with even lower lifetimes during the stadial (4.3 years) compared to both interstadial (4.8 years) runs. For our final best-guess estimate (*26*) (table S2 and fig. S5), we limited our model to lifetimes longer than 5 years (*13*), in line with a three-dimensional chemistry model (*29*). This approach showed a strong reduction of boreal wetland sources during the stadial and an increased contribution in both interstadial scenarios. Moreover, a substantial interstadial increase in marine clathrate emissions can be excluded by our modeled CH_4 budget for both interstadial scenarios. According to our model, the high-latitude wetland emissions strengthened by a factor of 6 (from ~5 to ~32 Tg CH_4 $year^{-1}$) from stadial to early-interstadial conditions, whereas tropical wetland emissions strengthened only moderately for the long interstadial 8 (from ~84 to ~118 Tg CH_4

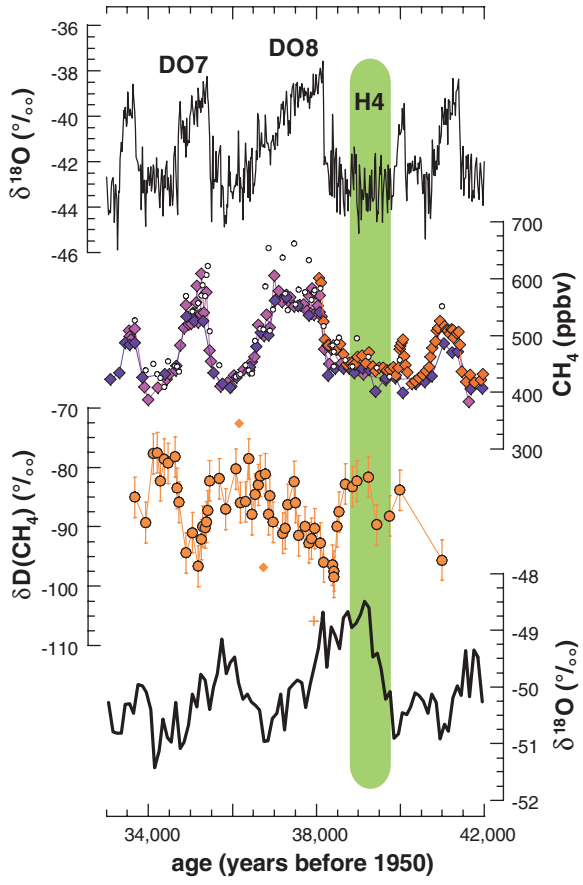

Fig. 1. Stadial and interstadial changes in temperature proxies, CH_4 and $\delta D(CH_4)$. Top and bottom panels show the temperature proxy $\delta^{18}O_{ice}$ from NGRIP (*1*) and the European Project for Ice Coring in Antarctica ice core from Dronning Maud Land (EDML) (*2*), respectively. The second panel shows CH_4 records from GRIP (Greenland Ice Core Project) (purple diamonds), NGRIP (orange diamonds) [(*2*) and this study (open circles), but the latter with much lower precision due to a higher error in determining the total air content)], and EDML (blue diamonds) (*2*). $\delta D(CH_4)$ values in the third panel are from the NGRIP ice core (orange circles) (this study) with a precision of 3.4‰. All data sets are given on the NGRIP GICC05 age scale after CH_4 synchronization. The green bar indicates the Heinrich 4 event (H4). Two $\delta D(CH_4)$ samples (orange diamonds) were excluded from the data set due to technical problems, and one sample (orange cross) was rejected as the gas enclosure process in ice precludes a jump of this size within less than 1 m [for further details, see (*26*)].

year^{-1}). Biomass-burning emissions showed slightly higher values during the interstadial time slices (~55 to 60 versus ~45 Tg CH_4 year^{-1} in the stadial), and marine hydrate emissions were rather constant at ~25 Tg CH_4 year^{-1}. Recent work has shown that other geologic CH_4 emissions may also play a greater role than previously assumed (*30*). Incorporating a geologic source in our model with $\delta D(CH_4)$ in the same range as clathrates and $\delta^{13}CH_4$ between wetlands and biomass burning (*8*) would reduce emission estimates from both biomass burning and clathrates.

To assess the drop in $\delta D(CH_4)$ observed before the onset of DO 8, we ran our model in a transient mode (Fig. 2, left panels). We could not reproduce the strong drop in $\delta D(CH_4)$ along with the small CH_4 concentration rise by strengthening a single source only (*26*). We ran the model with the stadial best-guess setting and forced it with 3.2 times higher boreal emissions (19 Tg CH_4 year^{-1}) and 10% higher tropical wetland emissions to explain both the $\delta D(CH_4)$ and IHG changes. Moreover, we also had to lower the hydrogen isotopic signatures of the boreal source by 30‰ and the tropical source by 5‰ to achieve the drop in $\delta D(CH_4)$ without violating the IHG constraint. Such a lowering of the boreal wetland $\delta D(CH_4)$ seems to be justified in view of the strongly depleted δD signature of high-latitude precipitation and snow melt during cold stadial conditions (*26*). An alternative explanation for this massive isotopic effect may be an increase in net to gross CH_4 production in wetlands (*18*), with net emissions increasing slightly. Global vegetation modeling including CH_4 emissions and isotopes may clarify this issue in the future.

In a second transient model run, we assessed the possibility of marine clathrates contributing to the two positive excursions lasting ~300 years with an amplitude of ~10‰ in $\delta D(CH_4)$ during interstadial 8 (Fig. 1), where evidence for local clathrate destabilization events had been found in marine sediments (*17*). To constrain $\delta D(CH_4)$, we ran the model with the late-interstadial best-guess setting, superimposed with a clathrate CH_4 injection of 20 Tg CH_4 year^{-1} for 250 years, as estimated by (*17*) (Fig. 2, right panels). Such a scenario can explain the observed increase in δD (CH_4), but would require a concurrent increase in CH_4 concentration by ~42 ppbv (Fig. 2). Although this is not supported by currently available CH_4 concentration data, it cannot be entirely ruled out, owing to their insufficient precision and temporal resolution (*2*).

Explanations that alter $\delta D(CH_4)$ but keep the total methane flux constant are more attractive. A synchronous reduction in wetland methane emissions when clathrates are strengthening would be coincidental, as no causal connection between the two exists. However, biomass burning might be opposite in phase with wetland CH_4 emission changes (*31*), thus replacing a depleted wetland with an enriched biomass-burning source. Again, changes in the net to gross CH_4 production from wetlands would shift atmospheric $\delta D(CH_4)$ to heavier values when gross production increases while the net flux stays constant (*18*). Analogously, this could explain the slow rise in $\delta D(CH_4)$ during DO 8 in parallel to an increasingly colder and drier climate. Alternatively, short-term changes in δD in high-latitude precipitation could contribute to the positive excursions without affecting boreal emission strength. NGRIP and EDML $\delta^{18}O_{ice}$ show temperature variations in the course of the interstadial; however, uncertainties in the ice age–gas age difference do not allow us to unambiguously synchronize temperature and CH_4 variations.

Even though the methane cycle is still underdetermined, our measurements show that marine hydrate destabilization did not occur at the end of stadials, and if it occurred at all, then only intermittently in the course of interstadials, when the surface warming had propagated to intermediate depths in the ocean. In contrast, our isotopic budget is consistent with the idea that wetlands were the main drivers of short- and longer-term CH_4 concentration variations in the past. In addition to changes in the source mix, our hydrogen isotopic signature of atmospheric methane appears to be affected by changes in δD of precipitation in high latitudes. In our $\delta D(CH_4)$ data, we find clear evidence for a climate response in boreal wetland regions that precedes the rapid warming into DO 8. This has implications for the timing of the trigger for the DO 8 warming and suggests that the AMOC is already slowly recovering in the preceding stadial.

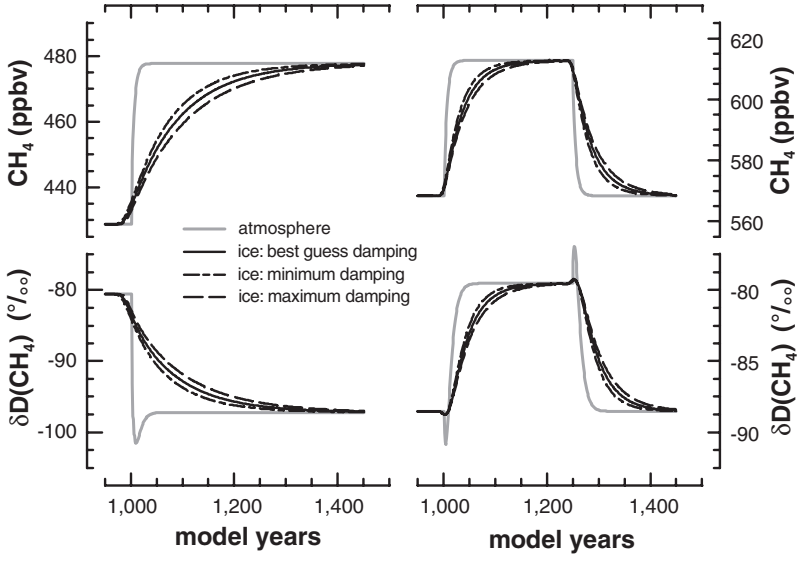

Fig. 2. Transient model response to rapid emission changes. Transient model runs were used to assess the timing and amplitude of simultaneous concentration changes along with observed δD (CH_4) variations. Concentrations (top panels) and $\delta D(CH_4)$ (bottom panels) for the "early boreal wetland" simulation (left panels) and the "clathrate destabilization event" (right panels). We assume a sudden increase in CH_4 emissions. The corresponding atmospheric peak (gray line) was filtered using ice core gas age distributions (black lines) calculated with a diffusion model (*26*) to account for the low-pass filtering effect of the bubble enclosure process (fig. S1). Overshooting of the atmospheric $\delta D(CH_4)$ signal is due to an imbalance in the source and sink composition. We made use of three different age distributions to assess model uncertainties. The stadial gas enclosure characteristic (stronger damping) and the interstadial gas enclosure characteristic (weaker damping) are preferred for the boreal wetland and clathrate simulations, respectively. For the clathrate destabilization, in total 5000 Tg CH_4 with $\delta^{13}CH_4 = -60‰$ and $\delta D(CH_4) = -190‰$ were added in 250 years.

References and Notes

1. North Greenland Ice Core Project members, *Nature* **431**, 147 (2004).
2. EPICA Community Members, *Nature* **444**, 195 (2006).
3. S. J. Burns, D. Fleitmann, A. Matter, J. Kramers, A. A. Al-Subbary, *Science* **301**, 1365 (2003).
4. L. de Abreu, N. J. Shackleton, J. Schönfeld, M. Hall, M. Chapman, *Mar. Geol.* **196**, 1 (2003).
5. E. J. Brook, S. Harder, J. Severinghaus, E. J. Steig, C. M. Sucher, *Global Biogeochem. Cycles* **14**, 559 (2000).
6. C. Huber *et al.*, *Earth Planet. Sci. Lett.* **243**, 504 (2006).
7. G. M. MacDonald *et al.*, *Science* **314**, 285 (2006).
8. M. J. Whiticar, in *Atmospheric Methane: Sources, Sinks, and Role in Global Change*, M. A. K. Khalil, Ed. (Springer, Berlin, 1993), pp. 138–167.
9. P. Quay *et al.*, *Global Biogeochem. Cycles* **13**, 445 (1999).
10. F. Keppler, J. T. G. Hamilton, M. Brass, T. Röckmann, *Nature* **439**, 187 (2006).
11. K. M. Walter, M. E. Edwards, G. Grosse, S. A. Zimov, F. S. Chapin III, *Science* **318**, 633 (2007).
12. J. Chappellaz *et al.*, *Nature* **366**, 443 (1993).
13. H. Fischer *et al.*, *Nature* **452**, 864 (2008).
14. J. P. Kennett, K. G. Cannariato, I. L. Hendy, R. J. Behl, *Methane Hydrates in Quaternary Climate Change: The Clathrate Gun Hypothesis*, B. Jean-Luis, Ed. (AGU Special Publication, Vol. 54, 2003).

15. "Clathrates" hereafter refers to those in intermediate depth, whereas shallow hydrates in (submerged) permafrost are considered to be part of the boreal terrestrial source.
16. E. G. Nisbet, J. Chappellaz, *Science* **324**, 477 (2009).
17. T. de Garidel-Thoron, L. Beaufort, F. Bassinot, P. Henry, *Proc. Natl. Acad. Sci. U.S.A.* **101**, 9187 (2004).
18. T. Sowers, *Science* **311**, 838 (2006).
19. I. Levin, in *Carbon Cycling in the Glacial Ocean: Constraints on the Ocean's Role in Global Change*, R. Zahn et al., Eds. (NATO ASI Series I17, Springer, Berlin, 1994), pp. 1–6.
20. D. P. Schrag *et al.*, *Quat. Sci. Rev.* **21**, 331 (2002).
21. M. Siddall *et al.*, *Nature* **423**, 853 (2003).
22. J. Jouzel, G. Hoffmann, R. D. Koster, V. Masson, *Quat. Sci. Rev.* **19**, 363 (2000).
23. L. C. Peterson, G. H. Haug, K. A. Hughen, U. Röhl, *Science* **290**, 1947 (2000).
24. X. Wang *et al.*, *Nature* **432**, 740 (2004).
25. J. E. Tierney *et al.*, *Science* **322**, 252 (2008).
26. Materials and methods are available as supporting material on *Science* Online.
27. A. Dällenbach *et al.*, *Geophys. Res. Lett.* **27**, 1005 (2000).
28. M. Bock *et al.*, *Rapid Commun. Mass Spectrom.* **24**, 621 (2010).
29. J. Lelieveld, P. J. Crutzen, F. J. Dentener, *Tellus B Chem. Phys. Meterol.* **50**, 128 (1998).
30. G. Etiope, A. V. Milkov, *Environ. Geol. (Berl.)* **46**, 997 (2004).
31. P. Bergamaschi *et al.*, *J. Geophys. Res.* **114**, D22301 (2009).
32. We thank I. Levin for providing a reference air tank along with calibrated isotope values. We thank T. Sowers and two anonymous reviewers for carefully reviewing the manuscript. Financial support for this study was provided in part by the German Secretary of Education and Research program GEOTECHNOLOGIEN, by Deutsche Forschungsgemeinschaft (DFG project MEPHISTO), Schweizerischer Nationalfonds (SNF project *prime*METHANE), and the European Research Council advanced grant MATRICs. This work is a contribution to the North-GRIP ice core project, which is directed and organized by the Department of Geophysics at the Niels Bohr Institute for Astronomy, Physics and Geophysics, University of Copenhagen. It is supported by funding agencies in Denmark (SNF), Belgium (FNRS-CFB), France (IFRTP and INSU/CNRS), Germany (AWI), Iceland (RannIs), Japan (MEXT), Sweden (SPRS), Switzerland (SNF), and the United States (NSF).

Supporting Online Material

www.sciencemag.org/cgi/content/full/328/5986/1686/DC1
Materials and Methods
Figs. S1 to S5
Tables S1 to S3
References and Notes

28 January 2010; accepted 19 May 2010
10.1126/science.1187651

ATP-Binding Cassette Transporters and HDL Suppress Hematopoietic Stem Cell Proliferation

Laurent Yvan-Charvet,[1]*† Tamara Pagler,[1]* Emmanuel L. Gautier,[2] Serine Avagyan,[2] Read L. Siry,[1] Seongah Han,[1] Carrie L. Welch,[1] Nan Wang,[1] Gwendalyn J. Randolph,[2] Hans W. Snoeck,[2] Alan R. Tall[1]

Elevated leukocyte cell numbers (leukocytosis), and monocytes in particular, promote atherosclerosis; however, how they become increased is poorly understood. Mice deficient in the adenosine triphosphate–binding cassette (ABC) transporters ABCA1 and ABCG1, which promote cholesterol efflux from macrophages and suppress atherosclerosis in hypercholesterolemic mice, displayed leukocytosis, a transplantable myeloproliferative disorder, and a dramatic expansion of the stem and progenitor cell population containing $Lin^{-}Sca\text{-}1^{+}Kit^{+}$ (LSK) in the bone marrow. Transplantation of *Abca1*$^{-/-}$ *Abcg1*$^{-/-}$ bone marrow into apolipoprotein A-1 transgenic mice with elevated levels of high-density lipoprotein (HDL) suppressed the LSK population, reduced leukocytosis, reversed the myeloproliferative disorder, and accelerated atherosclerosis. The findings indicate that ABCA1, ABCG1, and HDL inhibit the proliferation of hematopoietic stem and multipotential progenitor cells and connect expansion of these populations with leukocytosis and accelerated atherosclerosis.

Leukocytosis and monocytosis are risk factors for coronary heart disease (CHD) and probably have a causal relationship to this disorder (*1*). In contrast, plasma high-density lipoprotein (HDL) levels are inversely correlated with the incidence of CHD (*2*); however, this observation has not been linked to leukocytosis. The athero-protective effect of HDL is mediated in part by promotion of cholesterol efflux from macrophage foam cells in atherosclerotic lesions (*3*–*5*). Two adenosine triphosphate–binding cassette (ABC) transporters, ABCA1 and ABCG1, play a key role in promoting cholesterol efflux from macrophages to lipid-poor apolipoprotein A-1 (apoA-1) and HDL, respectively. Deletion of *Abca1* and *Abcg1* in mice led to additive defects in macrophage cholesterol efflux and reverse cholesterol transport (*6*, *7*) and accelerated atherosclerosis in a susceptible hypercholesterolemic background (*6*). *Abca1*$^{-/-}$ *Abcg1*$^{-/-}$ mice also showed marked leukocytosis and infiltration of various organs with macrophage foam cells (*6*, *8*–*10*). This led us to hypothesize that these changes might arise, from either an inflammatory response mediated by excessive signaling of Toll-like receptors (TLRs) (*10*) or an excessive proliferation of bone marrow (BM) myeloid cells.

Six-week-old, chow-fed *Abca1*$^{-/-}$ *Abcg1*$^{-/-}$ mice developed increased myeloid cells ($Gr\text{-}1^{high}$ $CD11b^{high}$), monocytosis, and neutrophilia in blood and BM (fig. S1, A and B) (*11*). Blood counts indicated monocytosis, neutrophilia, and eosinophilia (fig. S1C) but normal T and B cell numbers (fig. S1C) and normal hematocrit and platelet counts. Consuming a high-fat diet further increased the peripheral leukocyte and monocyte counts with a balanced increase in "inflammatory" Ly-$6C^{high}$ and "patrolling" Ly-$6C^{low}$ monocyte subsets in *Abca1*$^{-/-}$ *Abcg1*$^{-/-}$ mice, but not in wild-type (WT) mice (figs. S1C and S2). Besides leukocytosis, 12-week-old *Abca1*$^{-/-}$ *Abcg1*$^{-/-}$ mice fed a chow diet developed hepato-splenomegaly and hypertrophy of intestinal Peyer's patches with a cellular infiltrate of macrophage foam cells (*6*, *9*) and neutrophils (fig. S3).

To determine if leukocytosis in *Abca1*$^{-/-}$ *Abcg1*$^{-/-}$ mice might represent an inflammatory response, we bred *Abca1*$^{-/-}$ *Abcg1*$^{-/-}$ to *MyD88*$^{-/-}$ mice, which lack the adapter molecule MyD88 necessary for signaling downstream of some TLRs. These animals showed only slight reductions in leukocyte and neutrophil counts compared with *Abca1*$^{-/-}$ *Abcg1*$^{-/-}$ mice, although spleen weight was similar (fig. S4, A and B). Furthermore, treatment of *Abca1*$^{-/-}$ *Abcg1*$^{-/-}$ mice with broad spectrum antibiotics to suppress potential TLR-dependent responses to the endogenous intestinal flora (*12*) did not reverse leukocytosis or splenomegaly in *Abca1*$^{-/-}$ *Abcg1*$^{-/-}$ mice (fig. S4, C and D). These findings were inconsistent with the hypothesis that leukocytosis represented a TLR/MyD88-dependent inflammatory response.

The phenotype of the *Abca1*$^{-/-}$ *Abcg1*$^{-/-}$ mice suggested a myeloproliferative disorder, and both ABCA1 and ABCG1 are highly expressed in hematopoietic stem and multipotential progenitor cells (HSPCs) (*13*, *14*). Thus, we quantified BM HSPCs and other myeloid populations in chow-fed animals (Fig. 1) (*15*). Remarkably, the $Lin^{-}Sca^{+}cKit^{+}$ (LSK) population representing HSPCs showed a fivefold increase in both frequency and number in *Abca1*$^{-/-}$ *Abcg1*$^{-/-}$ BM (Fig. 1A and fig. S5, A to D). Although the common lymphoid progenitor (CLP) population was unchanged, the granulocyte-monocyte progenitor (GMP) and the common myeloid progenitor (CMP) numbers were increased up to 100% in *Abca1*$^{-/-}$ *Abcg1*$^{-/-}$ BM compared with WT BM (Fig. 1A and fig. S5, E and F). Analysis of different populations within the LSK cells showed

[1]Division of Molecular Medicine, Department of Medicine, Columbia University, New York, NY 10032, USA. [2]Department of Gene and Cell Medicine, Mount Sinai School of Medicine, New York, NY 10029, USA.

*These authors contributed equally to this work.
†To whom correspondence should be addressed. E-mail: ly2159@columbia.edu

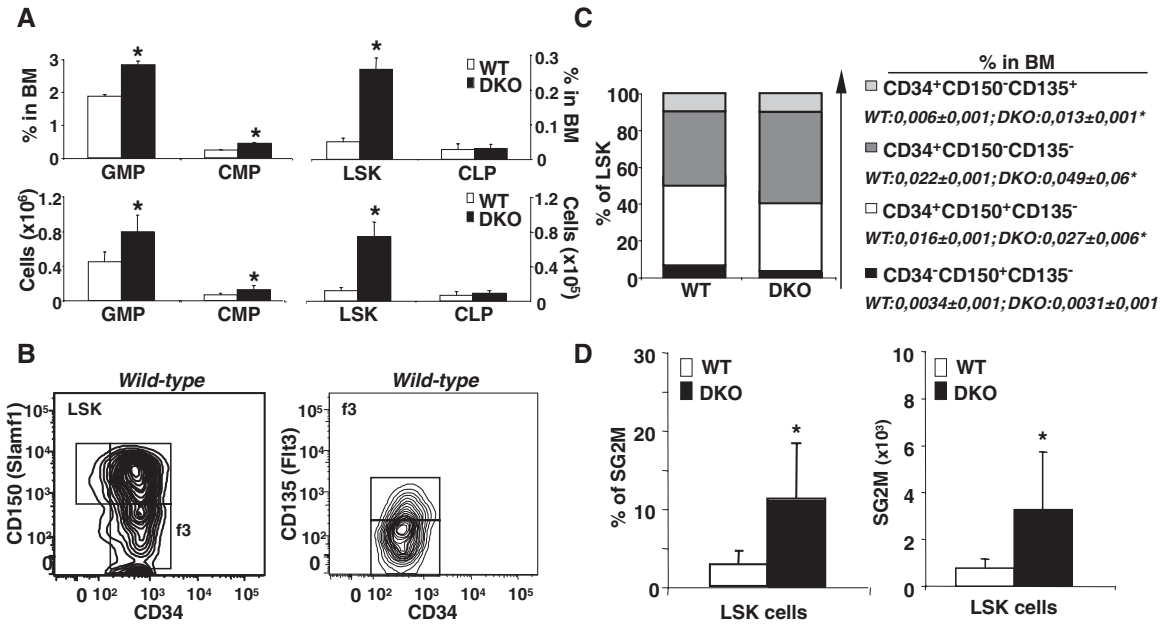

Fig. 1. Increased expansion and cycling activity of nontransplanted *Abca1*$^{-/-}$ *Abcg1*$^{-/-}$ HSCs. (**A**) Quantification of LSK, CMP, GMP, and CLP compartments expressed as percentage of total BM or absolute numbers. DKO, double knockout. (**B**) Using flow cytometric analysis, LSK populations were subdivided into four populations based on differential expression of CD34 and CD150, and CD135 (Flt3) represents gated CD34^{+} CD150^{-} LSK cells. (**C**) Quantification of LSK subpopulations from the most quiescent (long-term HSCs) to the most cycling LSK subset (short-term HSCs and multipotential progenitors) (CD34^{-} CD150^{+} CD135^{-} > CD34^{+} CD150^{+} CD135^{-} > CD34^{+} CD150^{-} CD135^{-} > CD34^{+} CD150^{-} CD135^{+}) expressed as percentage of LSK population or whole BM. (**D**) Percentage and absolute number of LSK cells in S/G2M phase as determined by Hoechst staining and flow cytometric analysis. Data are means ± SEM (error bars) and are representatives of at least one experiment performed with five animals per group. *P < 0.05.

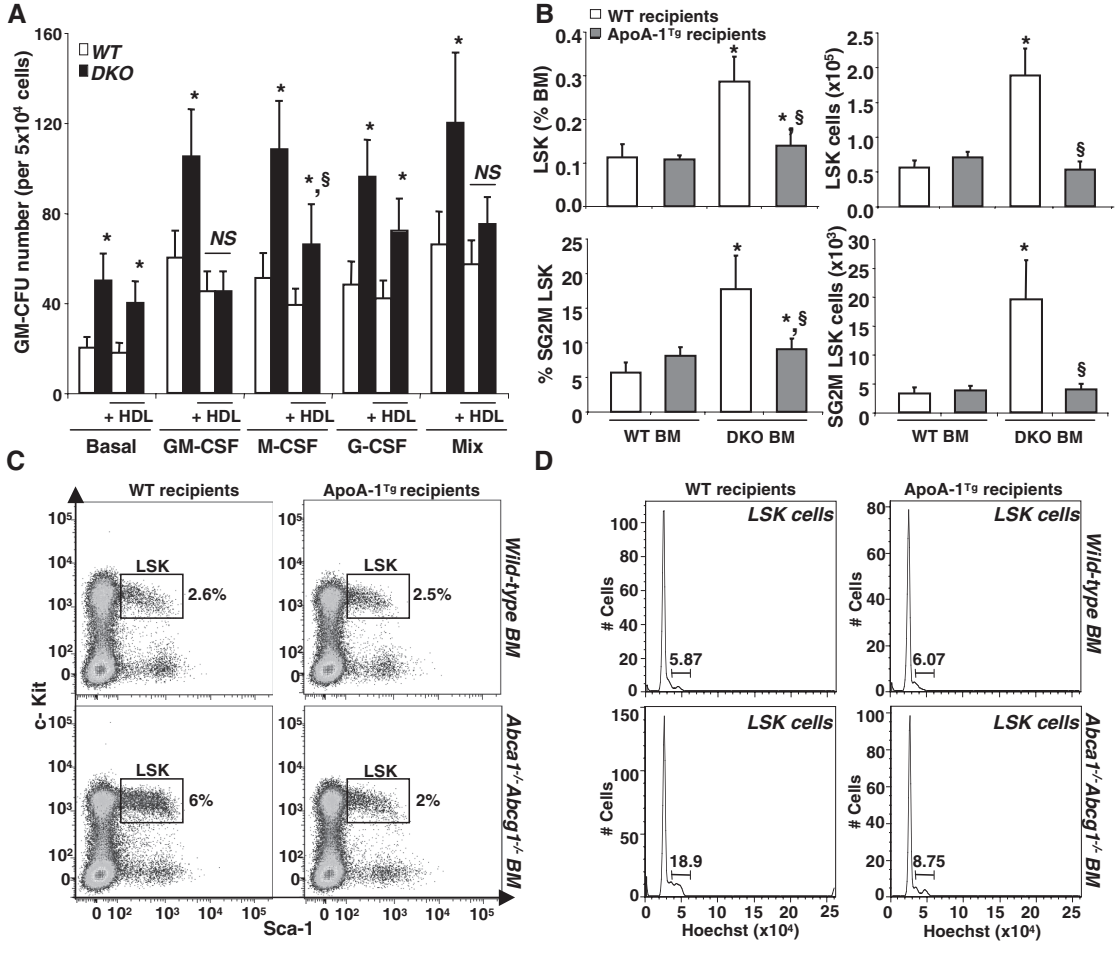

Fig. 2. HDL prevents HSCs from entry into the cell cycle. (**A**) Colony-forming assay using control and *Abca1*$^{-/-}$ *Abcg1*$^{-/-}$ BM was performed in presence or absence of 50 μg/mL HDL cholesterol. GM-CFU numbers induced by indicated growth factors alone or in combination (Mix) were determined from methylcellulose dishes after 10 days in culture. Results are ± SEM (error bars) of four mice per experimental group. (**B**) Quantification and (**C**) representative dot plots of LSK in chow-fed WT and apoA-I transgenic recipient mice transplanted with control or *Abca1*$^{-/-}$ *Abcg1*$^{-/-}$ BM. (**D**) Comparison of the cell cycle of LSK cells by flow cytometric analysis of Hoechst staining. Data are means ± SEM of five to six animals per group. *P < 0.05 genotype effect; §P < 0.05 treatment effect.

that $CD34^+CD150^-CD135^-$ multipotential progenitors were increased as a percentage of the LSK population (Fig. 1, B and C). However, because the overall LSK population was increased fivefold (Fig. 1A), all $CD34^+$ cells were expanded as a percentage of total BM cells (Fig. 1C), including short-term hematopoietic stem cells (HSCs) ($CD34^+CD150^+CD135^-$) and both populations of $CD34^+$ multipotential progenitors (*15*, *16*). However, $CD34^-CD150^+CD135^-$ long-term HSCs were not increased. The expansion of myeloid progenitors and LSK cells in double-knockout BM reflected an increase in cell cycling. In *Abca1*$^{-/-}$ *Abcg1*$^{-/-}$ mice, there was a threefold increase in the SG2M fraction in total BM cells (fig. S5G) and a fivefold increase in the SG2M fraction in LSK cells compared with controls (Fig. 1D and fig. S5H). Colony-forming assays also confirmed an approximately twofold increase in the number and size of granulocyte/macrophage colony-forming units (GM-CFUs) for all of the growth factors tested in *Abca1*$^{-/-}$ *Abcg1*$^{-/-}$ compared with WT cultures (Fig. 2, A and B, and fig. S6A).

To test whether this phenotype was caused by cell autonomous effects of ABCA1 and ABCG1 within the hematopoietic system or an effect of the microenvironment, we mixed BM cells from CD45.1 WT mice with CD45.2 *Abca1*$^{-/-}$ *Abcg1*$^{-/-}$ BM in vitro. CD45.1 WT BM cell proliferation was not affected by the presence of CD45.2 *Abca1*$^{-/-}$ *Abcg1*$^{-/-}$ cells, confirming a cell autonomous effect (fig. S6B). The competitive advantage of *Abca1*$^{-/-}$ *Abcg1*$^{-/-}$ cells was also shown in a BM transplantation experiment with similar mixed donor-cell populations (fig. S7).

We next investigated the relation of BM myeloid proliferation to HDL-mediated cholesterol efflux. HDL markedly reduced the number and size of GM-CFUs from *Abca1*$^{-/-}$ *Abcg1*$^{-/-}$ mice and also reduced the size of the GM-CFUs from WT mice (Fig. 2A and fig. S6A). Consistent with these findings, HDL also decreased the proliferation rates of interleukin-3 (IL-3) and granulocyte macrophage colony-stimulating factor (GM-CSF)–treated WT and *Abca1*$^{-/-}$ *Abcg1*$^{-/-}$ BM cells in a dose-dependent fashion, but *Abca1*$^{-/-}$ *Abcg1*$^{-/-}$ cells showed smaller responses to HDL, in terms of both proliferation and cholesterol efflux (fig. S8, A and B). Whereas lipid-poor apoA-1 had no effect on proliferation of

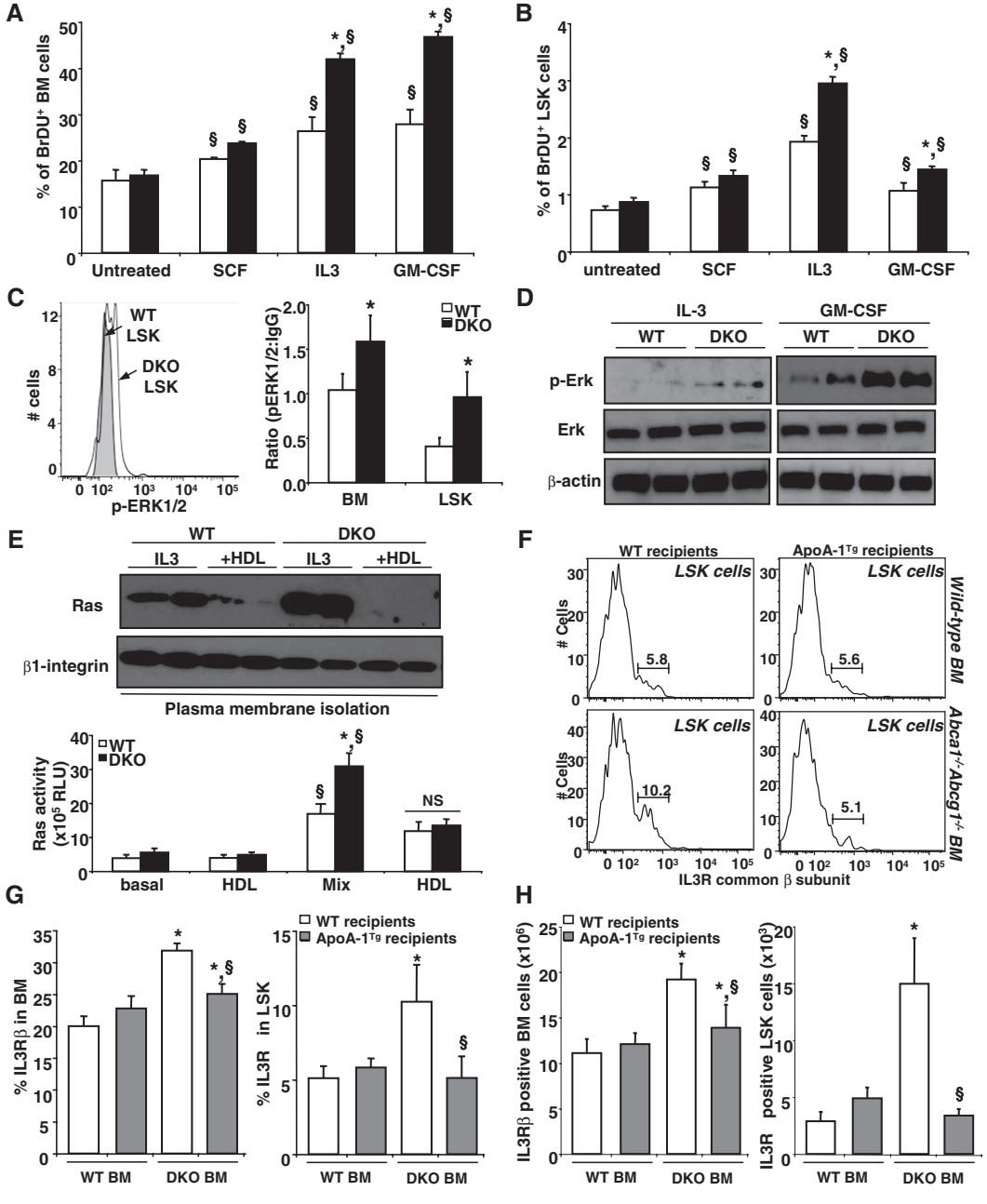

Fig. 3. HDL protects myeloid cells from activation of IL-3–receptor β canonical pathway. (**A**) WT and *Abca1*$^{-/-}$ *Abcg1*$^{-/-}$ BM cells and (**B**) LSK cells were grown for 72 hours in liquid culture in the presence of indicated growth factors and were analyzed for BrdU incorporation by flow cytometry. (**C**) Representative histogram and bar graph showing the expression of phoshpERK1/2 by flow cytometry in freshly isolated BM and LSK cells from WT mice transplanted with control or *Abca1*$^{-/-}$ *Abcg1*$^{-/-}$ BM. (**D**) Western blot analysis shows phospho-ERK, total ERK, and β-actin expression in WT and *Abca1*$^{-/-}$ *Abcg1*$^{-/-}$ BM cells treated with indicated growth factors in duplicate samples. (**E**) Duplicate samples of BM cells treated with indicated growth factors and 50 μg/mL HDL cholesterol were subjected to plasma membrane fractionation and analyzed for Ras and β1-integrin expression or used to quantify Ras activity. (**F**) Representative histograms showing the expression of the IL-3–receptor β in LSK cells from WT and apoA-I transgenic recipient mice transplanted with control or *Abca1*$^{-/-}$ *Abcg1*$^{-/-}$ BM. (**G**) Percentage and (**H**) absolute number of BM and LSK cells expressing the IL-3Rβ are depicted from the above-mentioned mice. Results are means ± SEM (error bars) of five to six mice per group. *P < 0.05 genotype effect; §P < 0.05 treatment effect.

Abca1$^{-/-}$ *Abcg1*$^{-/-}$ cells, mouse plasma HDL showed a similar suppression of proliferation, and this was greater for apoA-1 transgenic plasma HDL compared with control HDL (fig. S8C). These results suggest that HDL suppresses the proliferation of myeloid progenitor cells by promoting cholesterol efflux. This effect is still observed in *Abca1*$^{-/-}$ *Abcg1*$^{-/-}$ BM, possibly reflecting the ability of HDL to promote cholesterol efflux by alternative pathways such as passive or diffusional cholesterol efflux (*17*). Single-knockout deficiency revealed only a slight increase in proliferation for *Abca1*$^{-/-}$ cultures and no effect for *Abcg1*$^{-/-}$ cultures (fig. S8D), consistent with the synergistic role of these transporters in mediating cellular cholesterol efflux (*6*). Although liver X receptor (LXR) transcription factors induce expression of both *Abca1* and *Abcg1,* and LXR knockout mice have increased lymphocyte proliferation (*18*), we did not observe any increase in T or B cells in blood (fig. S1C), spleen, or lymph nodes in *Abca1*$^{-/-}$ *Abcg1*$^{-/-}$ mice. Expansion of myeloid populations was not reported in LXRα/β$^{-/-}$ mice (*18*), possibly due to their relatively high levels of basal *Abca1* and *Abcg1* expression (*19*). Treatment of BM myeloid cells with an LXR activator (TO901317), however, resulted in increased cholesterol efflux and decreased growth factor–stimulated proliferation in WT (but not *Abca1*$^{-/-}$ Abcg1$^{-/-}$) cells (fig. S9, A and B). This indicates that activation of LXR induced *Abca1* and *Abcg1*, promoting cholesterol efflux and suppressing proliferation. Conversely, stimulation of WT BM myeloid cell proliferation with IL-3 or GM-CSF markedly reduced the expression of these transporters (fig. S9, C and D).

ApoA-1 transgenic mice have increased apoA-1 and HDL levels and are resistant to atherosclerosis (*20*, *21*). To examine whether HDL could suppress myeloproliferation in vivo, we transplanted BM from WT and *Abca1*$^{-/-}$ *Abcg1*$^{-/-}$ mice into chow-fed normo-cholesterolemic WT or apoA-1 transgenic recipients. We observed a dramatic decrease in the frequency, numbers, and cycling activity of the LSK population and a reversal of the splenomegaly in apoA-1 transgenic recipients of *Abca1*$^{-/-}$ *Abcg1*$^{-/-}$ BM, but not in WT recipients (Fig. 2, B to D, and fig. S9E). The increased proliferation of *Abca1*$^{-/-}$ *Abcg1*$^{-/-}$ LSK cells was associated with increased cholera toxin subunit B (CTx-B) staining of the cell surface of *Abca1*$^{-/-}$ *Abcg1*$^{-/-}$ compared with WT LSK cells (fig. S9F), suggesting increased formation of cholesterol-rich lipid rafts (*22*, *23*). This staining was decreased in LSK cells isolated from apoA-1 transgenic mice transplanted with WT or *Abca1*$^{-/-}$ *Abcg1*$^{-/-}$ BM (fig. S9F). In vitro treatment of *Abca1*$^{-/-}$ *Abcg1*$^{-/-}$ LSK cells with cyclodextrin, which mediates cholesterol efflux

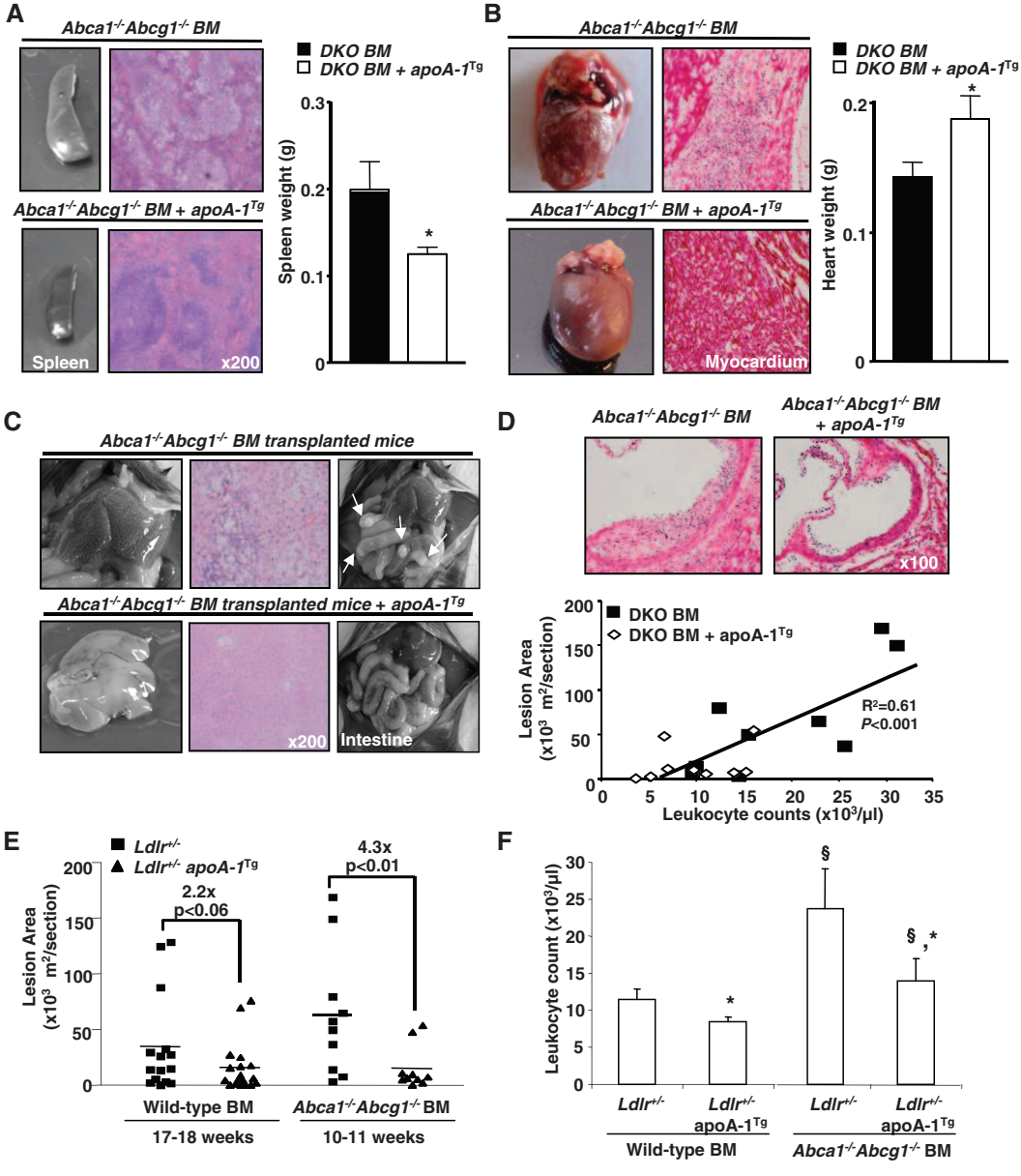

Fig. 4. HDL rescue the myeloproliferative disorder and accelerated atherosclerosis of *Abca1*$^{-/-}$ *Abcg1*$^{-/-}$ BM transplanted mice. (**A**) Representative spleen, (**B**) heart, (**C**) liver, Peyer's patches, and hematoxylin and eosin (H&E) staining of paraffin-embedded sections from high cholesterol–fed *Ldlr*$^{+/-}$ and *Ldlr*$^{+/-}$ apoA-1 transgenic recipient mice transplanted with *Abca1*$^{-/-}$ *Abcg1*$^{-/-}$ BM. (**D**) Representative H&E staining of the proximal aortas showing atherosclerotic lesions and correlation between mean lesion areas and leukocyte counts. (**E**) Lesion areas (individual and mean) were determined by morphometric analysis of H&E-stained sections. BM transplanted mice were fed a high-cholesterol diet for different time periods to approximately match lesion areas for mice not expressing apoA-1 transgene. (**F**) Leukocyte counts from WT and *Abca1*$^{-/-}$ *Abcg1*$^{-/-}$ transplanted recipients. Results are means ± SEM (error bars) of six to nine mice per group. *$P < 0.05$ apoA-I transgene effect; §$P < 0.05$ BM transplant effect.

and reduces lipid raft formation, also led to markedly decreased CTx-B staining (fig. S9G).

To identify the underlying mechanisms responsible for the myeloproliferative phenotype, we cultured BM cells in the presence of different growth factors known to induce the proliferation of HSCs. Although stem cell factor (SCF or kit-ligand) increased the percentage of bromodeoxyuridine (BrdU, used to measure proliferating cells)–positive cells in BM or LSK cells, there was no significant difference in response between the genotypes (Fig. 3, A and B). In contrast, both IL-3 and GM-CSF significantly increased the percentage of BrdU-positive cells in *Abca1*$^{-/-}$ *Abcg1*$^{-/-}$ BM and LSK cells. Consistent with these findings, increased activation of phospho–extracellular signal–regulated kinase (ERK) in response to IL-3 and GM-CSF treatments was observed in both *Abca1*$^{-/-}$ *Abcg1*$^{-/-}$ BM and LSK cells in vivo (Fig. 3C) and in response to IL-3 and GM-CSF in cell culture (Fig. 3D). Increased phospho-ERK was associated with increased Ras protein in the plasma membrane of *Abca1*$^{-/-}$ *Abcg1*$^{-/-}$ BM myeloid cells and increased Ras guanosine triphosphatase activity; these changes were reversed by HDL treatment (Fig. 3E). Treatment with cyclodextrin or with a farnesyl transferase inhibitor known to prevent the anchorage of Ras in the plasma membrane also caused a marked reduction in proliferation of WT and *Abca1*$^{-/-}$ *Abcg1*$^{-/-}$ BM cells (fig. S10, A and B). The IL-3 and GM-CSF receptors share a common β subunit (*24*, *25*). The number of cells expressing the IL-3 receptor β subunit at the cell surface was increased twofold in *Abca1*$^{-/-}$ *Abcg1*$^{-/-}$ BM cells and fivefold in *Abca1*$^{-/-}$ *Abcg1*$^{-/-}$ LSK cells; this was reversed in the presence of the apoA-1 transgene (Fig. 3, F to H). Other potential mechanisms to explain increased numbers of *Abca1*$^{-/-}$ *Abcg1*$^{-/-}$ BM myeloid cells were also investigated, such as decreased apoptosis, oxidative stress, or increased TLR- or wnt-dependent signaling. Although the small decrease in numbers of apoptotic cells observed in the basal state might also contribute to the increased number of myeloid cells (fig. S10C), neither lack of Myd88 or antioxidant treatment was able to reduce the enhanced proliferation rates of *Abca1*$^{-/-}$ *Abcg1*$^{-/-}$ BM myeloid cells (fig. S10, D to F). mRNA expression analysis of GM-CSF colony-forming cells also did not reveal up-regulation of the canonical wnt signaling target genes Axin1 and Axin2 or changes in the key transcriptional factors C/EBPα and ε known to regulate both the proliferation and differentiation of myeloid progenitors in contrast to increased phospho-Erk target gene expression such as c-jun and cyclin D1 (fig. S11). Consistent with the proposed mechanism, we also found an increase in PU.1, a key transcription factor that promotes development of myeloid lineages, including monocytes and neutrophil lineages (*26*). Together, these data suggest that increased membrane cholesterol content secondary to ABC transporter deficiency results in increased cell-surface expression of the common β subunit of the IL-3/GM-CSF receptor that, in turn, leads to increased downstream Ras/Erk signaling and increased proliferative responses to IL-3 and GM-CSF.

To investigate whether the apoA-1 transgene could suppress the myeloproliferative phenotype and accelerated atherosclerosis of hypercholesterolemic *Abca1*$^{-/-}$ Abcg1$^{-/-}$ mice, we also transplanted BM from WT and *Abca1*$^{-/-}$ *Abcg1*$^{-/-}$ mice into high cholesterol–fed, atherosclerosis-susceptible *Ldlr*$^{+/-}$ mice with or without the human apoA-1 transgene. HDL cholesterol and human apoA-I levels were similar in the two groups of mice (fig. S12, A and B). Remarkably, the myeloid cell infiltration of different organs in *Abca1*$^{-/-}$ *Abcg1*$^{-/-}$ BM recipients was almost completely suppressed by expression of the human apoA-1 transgene (Fig. 4, A to C). There was marked reduction of splenomegaly with normalization of the hypercellularity (Fig. 4A). The livers that had a nutmeg appearance became normal, and the hypertrophied Peyer's patches (Fig. 4C) disappeared. The small, pale hearts infiltrated with neutrophils and foam cells were replaced with normal-sized hearts without cellular infiltration (Fig. 4B). The apoA-I transgene also dramatically suppressed the accelerated atherosclerosis in atherogenic diet–fed *Ldlr*$^{+/-}$ mice receiving *Abca1*$^{-/-}$ *Abcg1*$^{-/-}$ BM (Fig. 4, D and E). In *Abca1*$^{-/-}$ *Abcg1*$^{-/-}$ BM recipients, the extent of atherosclerosis was correlated with the degree of leukocytosis (Fig. 4D), and leukocytosis was suppressed by the apoA-1 transgene (Fig. 4F). A serum inflammatory marker, apoSAA, was also suppressed by the apoA-1 transgene in *Abca1*$^{-/-}$ *Abcg1*$^{-/-}$ mice, but there was no correlation between levels of apoSAA and the extent of atherosclerosis (fig. S12, C and D).

Collectively, our results suggest that proliferation of HSPCs is normally regulated by cholesterol efflux mechanisms involving LXRs, ABCA1, ABCG1, and HDL. Our studies also suggest a previously unsuspected role of HSPC proliferation in the leukocytosis of atherosclerosis and reveal that HDL can exert an anti-atherogenic effect by suppressing this proliferation. Hypercholesterolemia and high-fat feeding in different species results in leukocytosis and monocytosis (*27*–*30*) and increased entry of monocytes into atherosclerotic lesions (*28*–*30*). Although monocytosis is insufficient to induce atherosclerosis, lesion burden is directly proportional to monocyte counts in the blood (*31*). Our studies indicate a link between expansion of HSPCs, leukocytosis, and accelerated atherosclerosis in *Abca1*$^{-/-}$ *Abcg1*$^{-/-}$ mice. The apoA-1 transgene significantly reduced leukocytosis in hypercholesterolemic *Ldlr*$^{+/-}$ mice receiving WT BM (Fig. 4F), suggesting a general role for HDL in the suppression of HSPC proliferation in hypercholesterolemic animal models. Although increasing HDL levels may reduce atherosclerosis by several different mechanisms, our findings suggest that the suppression of BM myeloid proliferation, leukocytosis, and monocytosis might represent a previously unidentified anti-atherogenic effect of HDL acting at an earlier stage in the leukocyte life cycle than subsequent anti-inflammatory or antioxidant effects occurring in the vessel wall (*3*–*5*). This property might also find an application in the treatment of myeloproliferative disorders.

References and Notes

1. B. S. Coller, *Arterioscler. Thromb. Vasc. Biol.* **25**, 658 (2005).
2. D. J. Gordon, B. M. Rifkind, *N. Engl. J. Med.* **321**, 1311 (1989).
3. P. J. Barter, R. Puranik, K. A. Rye, *Curr. Cardiol. Rep.* **9**, 493 (2007).
4. A. R. Tall, L. Yvan-Charvet, N. Terasaka, T. Pagler, N. Wang, *Cell Metab.* **7**, 365 (2008).
5. D. Duffy, D. J. Rader, *Nat. Rev. Cardiol.* **6**, 455 (2009).
6. L. Yvan-Charvet *et al.*, *J. Clin. Invest.* **117**, 3900 (2007).
7. X. Wang *et al.*, *J. Clin. Invest.* **117**, 2216 (2007).
8. R. Out *et al.*, *Arterioscler. Thromb. Vasc. Biol.* **28**, 258 (2008).
9. R. Out *et al.*, *Circ. Res.* **102**, 113 (2008).
10. L. Yvan-Charvet *et al.*, *Circulation* **118**, 1837 (2008).
11. Materials and methods are available as supporting material on *Science* Online.
12. E. E. Turer *et al.*, *J. Exp. Med.* **205**, 451 (2008).
13. S. D. Peeters *et al.*, *Exp. Hematol.* **34**, 622 (2006).
14. E. P. de Grouw *et al.*, *Leukemia* **20**, 750 (2006).
15. I. L. Weissman, J. A. Shizuru, *Blood* **112**, 3543 (2008).
16. A. Wilson *et al.*, *Cell* **135**, 1118 (2008).
17. M. P. Adorni *et al.*, *J. Lipid Res.* **48**, 2453 (2007).
18. S. J. Bensinger *et al.*, *Cell* **134**, 97 (2008).
19. B. L. Wagner *et al.*, *Mol. Cell. Biol.* **23**, 5780 (2003).
20. E. M. Rubin, R. M. Krauss, E. A. Spangler, J. G. Verstuyft, S. M. Clift, *Nature* **353**, 265 (1991).
21. A. S. Plump, C. J. Scott, J. L. Breslow, *Proc. Natl. Acad. Sci. U.S.A.* **91**, 9607 (1994).
22. C. Dietrich, Z. N. Volovyk, M. Levi, N. L. Thompson, K. Jacobson, *Proc. Natl. Acad. Sci. U.S.A.* **98**, 10642 (2001).
23. B. J. Nichols, *Curr. Biol.* **13**, 686 (2003).
24. F. Chang *et al.*, *Leukemia* **17**, 1263 (2003).
25. U. Testa *et al.*, *Leukemia* **18**, 219 (2004).
26. F. Geissmann *et al.*, *Science* **327**, 656 (2010).
27. L. E. Averill, R. C. Meagher, R. G. Gerrity, *Am. J. Pathol.* **135**, 369 (1989).
28. F. K. Swirski *et al.*, *Proc. Natl. Acad. Sci. U.S.A.* **103**, 10340 (2006).
29. F. K. Swirski *et al.*, *J. Clin. Invest.* **117**, 195 (2007).
30. F. Tacke *et al.*, *J. Clin. Invest.* **117**, 185 (2007).
31. C. Combadière *et al.*, *Circulation* **117**, 1649 (2008).

32. This work is supported by a Program Project grant from the NIH to A.R.T. (HL54591) and a grant from the American Heart Association to L.Y.-C. (SDG2160053), by the FWF Austrian Science Fund (T.P.), and by NIH grants R01A1061741 (E.L.G. and G.J.R.) and R01AG016327 (H.W.S.). A.R.T. serves on scientific advisory boards for Merck and Arisaph Pharmaceuticals and provides paid consulting services to Roche, Merck, Arisaph Pharmaceuticals, and CSL Limited related to the development of drugs that would increase HDL levels.

Supporting Online Material

www.sciencemag.org/cgi/content/full/science.1189731/DC1
Materials and Methods
Figs. S1 to S12

17 March 2010; accepted 28 April 2010
Published online 20 May 2010;
10.1126/science.1189731
Include this information when citing this paper.

A Novel miRNA Processing Pathway Independent of Dicer Requires Argonaute2 Catalytic Activity

Daniel Cifuentes,[1] Huiling Xue,[1] David W. Taylor,[2] Heather Patnode,[1] Yuichiro Mishima,[1,3] Sihem Cheloufi,[4,5] Enbo Ma,[6] Shrikant Mane,[7] Gregory J. Hannon,[4] Nathan D. Lawson,[8] Scot A. Wolfe,[8,9] Antonio J. Giraldez[1,10]*

Dicer is a central enzyme in microRNA (miRNA) processing. We identified a Dicer-independent miRNA biogenesis pathway that uses Argonaute2 (Ago2) slicer catalytic activity. In contrast to other miRNAs, miR-451 levels were refractory to *dicer* loss of function but were reduced in MZ*ago2* (maternal-zygotic) mutants. We found that pre-miR-451 processing requires Ago2 catalytic activity in vivo. MZ*ago2* mutants showed delayed erythropoiesis that could be rescued by wild-type Ago2 or miR-451-duplex but not by catalytically dead Ago2. Changing the secondary structure of Dicer-dependent miRNAs to mimic that of pre-miR-451 restored miRNA function and rescued developmental defects in MZ*dicer* mutants, indicating that the pre-miRNA secondary structure determines the processing pathway in vivo. We propose that Ago2-mediated cleavage of pre-miRNAs, followed by uridylation and trimming, generates functional miRNAs independently of Dicer.

MicroRNAs (miRNAs) are ~22-nucleotide (nt) small RNAs that regulate deadenylation, translation, and decay of their target mRNAs (*1*, *2*). In animals, most miRNAs are processed from a primary transcript (termed pri-miRNA) by two ribonuclease III (RNase III) enzymes, Drosha and Dicer. Recent studies have identified several miRNA classes that bypass Drosha-mediated processing, namely miRtrons, tRNAZ, and small nucleolar RNA (snoRNA) (*2*–*6*). In contrast to Drosha, Dicer has been viewed as a central processing enzyme in the maturation of small RNAs (*2*). But are there functional miRNAs that bypass Dicer? To identify pathways that might process miRNAs in a Dicer-independent manner, we sequenced small RNAs (19 to 36 nt) in wild-type and maternal-zygotic *dicer* mutants (MZ*dicer*) (*7*). We analyzed 48-hour-old embryos in two wild-type replicates and two *dicer* mutant alleles (*8*), *dicer*^{hu715} and *dicer*^{hu896} (fig. S1). Of the ~2 million reads per sample, 69 to 82% mapped to known 5′- or 3′-derived miRNAs in the wild type, whereas 4 to 9% mapped to miRNAs in the MZ*dicer* mutants

[1]Department of Genetics, Yale University School of Medicine, New Haven, CT 06510, USA. [2]Department of Molecular Biophysics and Biochemistry, Yale University School of Medicine, New Haven, CT 06510, USA. [3]Department of Biology, Graduate School of Science, Kobe University, 1-1 Rokkodaicho Nadaku, Kobe 657-8501, Japan. [4]Howard Hughes Medical Institute, Watson School of Biological Sciences, Cold Spring Harbor Laboratory, Cold Spring Harbor, NY 11724, USA. [5]Program in Genetics, Stony Brook University, Stony Brook, NY 11794, USA. [6]Department of Molecular and Cell Biology, University of California, Berkeley, CA 94720, USA. [7]Yale Center for Genome Analysis, Yale West Campus, Orange, CT 06477, USA. [8]Program in Gene Function and Expression, University of Massachusetts Medical School, Worcester, MA 01605, USA. [9]Department of Biochemistry and Molecular Pharmacology, University of Massachusetts Medical School, Worcester, MA 01605, USA. [10]Yale Stem Cell Center, Yale University School of Medicine, New Haven, CT 06520, USA.

*To whom correspondence should be addressed. E-mail: antonio.giraldez@yale.edu

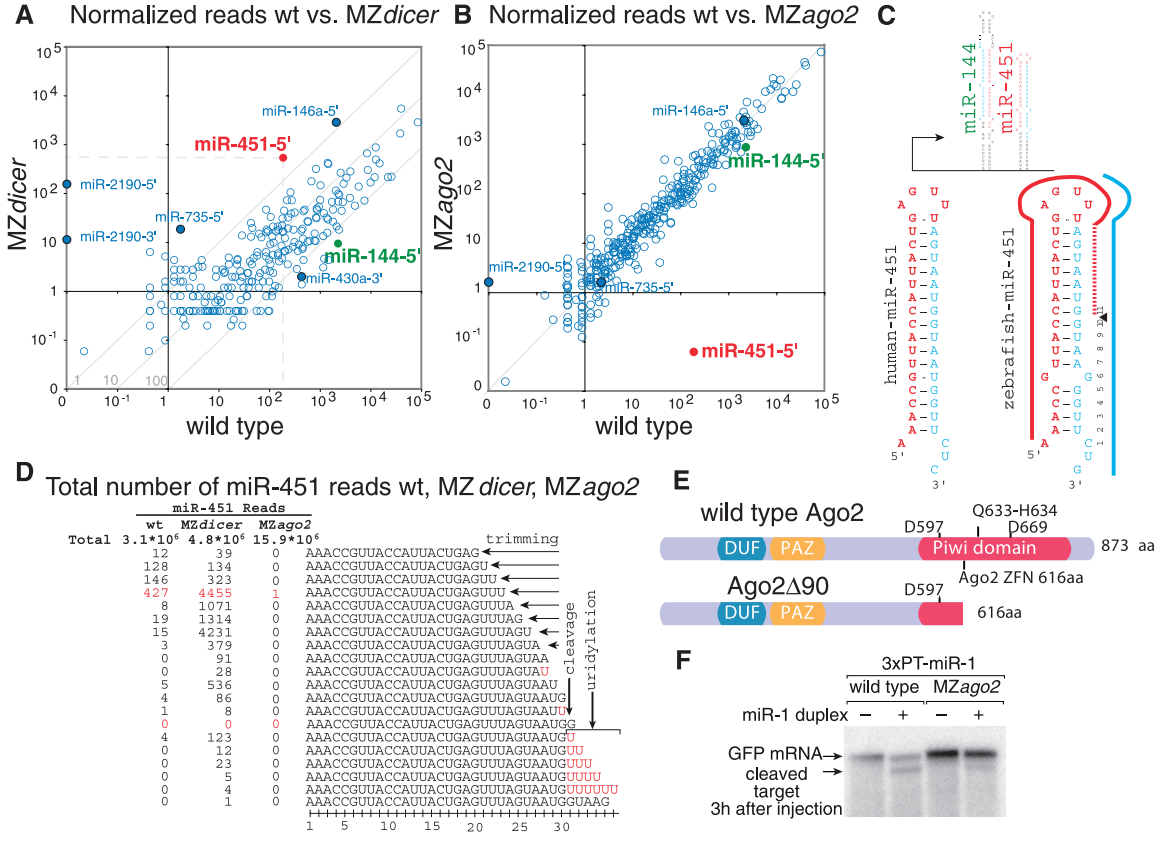

Fig. 1. MicroRNA analysis in wild type (wt) and in MZ*dicer* and MZ*ago2* mutants. (**A** and **B**) Normalized reads from wild type versus MZ*dicer* (A) or MZ*ago2* (B) libraries for all annotated zebrafish miRNAs. Some miRNAs are shown as a reference for enhanced and reduced miRNAs (solid circles); miR-144-5′ (green) and miR-451-5′ (red) are expressed in the same pri-miRNA. (**C**) Scheme of miR-144/miR-451 genomic loci and predicted secondary structure of both human and zebrafish pre-miR-451 (mature miRNA in red). (**D**) Total number of reads that match miR-451 in wild type, MZ*dicer*, and MZ*ago2*. Nontemplated uridines are shown in red. (**E**) Domain organization of Ago2. The 90-nt deletion (Δ90) results in a predicted truncated protein lacking two of three catalytic residues. Amino acid positions are based on the mammalian Ago2. (**F**) Northern blot of embryos to detect slicer cleavage of an injected GFP target mRNA with three complementary targets to miR-1 (3xPT-miR-1) in the presence (+) or absence (–) of miR-1 (*7*). Slicer activity is indicated by the higher-mobility product (fig. S1) (*18*).

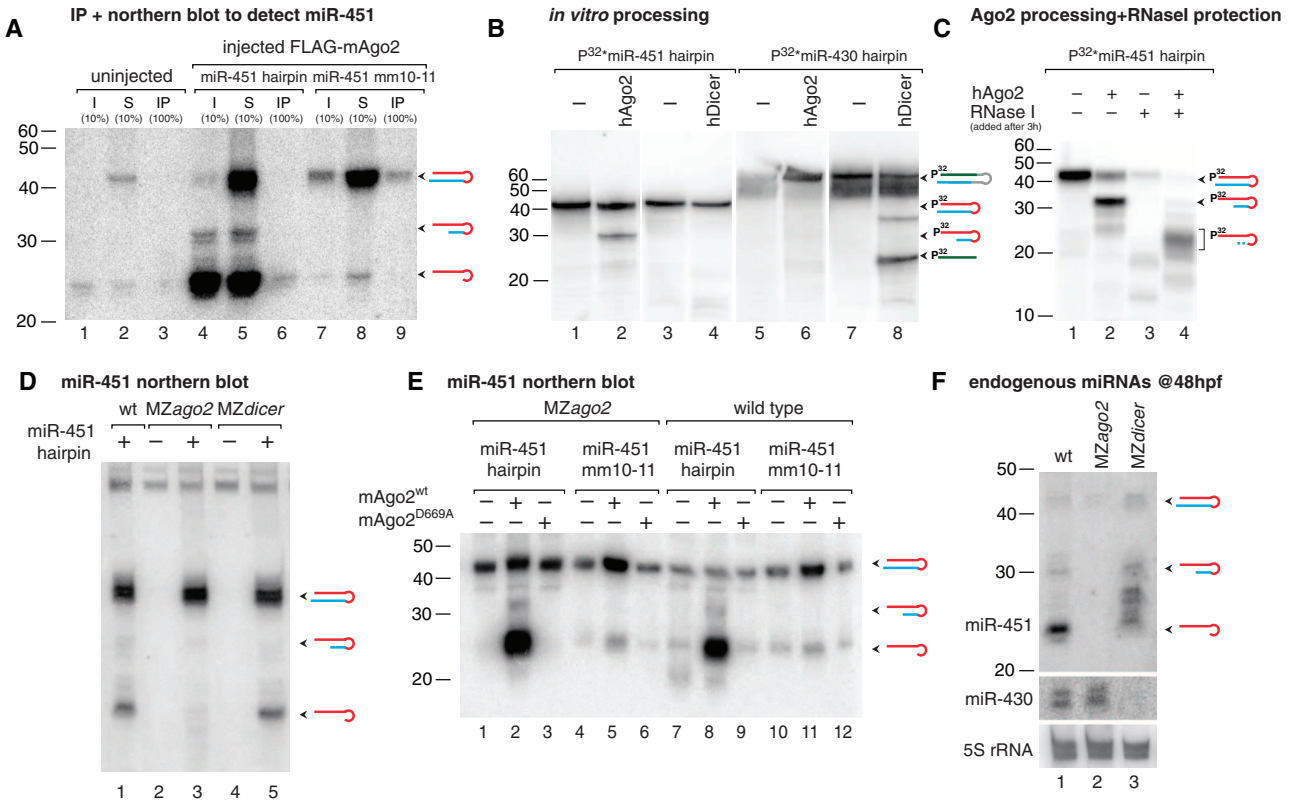

Fig. 2. Ago2 binds and processes pre-miR-451. (**A**) Immunoprecipitation of FLAG-mAgo2 in wild-type and mutant embryos injected with pre-miR-451 followed by Northern blot analysis to detect bound miR-451. Input (I), supernatant (S), and immunoprecipitate (IP) are indicated. (**B** and **C**) In vitro cleavage assay using hAgo2 or hDicer protein and 5′-radiolabeled pre-miR-430 or pre-miR-451. (C) Ago2 processing reactions were treated with (+) or without (–) RNase I to assay protection of the processed hairpin by Ago2. (**D** to **F**) Northern blot analyses to detect mature miR-451 after injection with pre-miR-451 (+) [(D) and (E)] or endogenous miR-451 and miR-430 (F). Injection of wild-type mAgo2 but not a catalytically dead mAgo2^{D669A} rescues pre-miR-451 processing in vivo (E). The processing of miR-451$^{mm10-11}$ is strongly reduced. Endogenous pre-miR-451 at 48 hpf is processed in wild type and MZ*dicer* but not in MZ*ago2* mutants. Diagrams for predicted hairpins, cleavage intermediates, mature miR-451 (red), miR-430 (green), and miRNA* (blue) are shown. P^{32}* indicates that injected hairpins were radiolabeled (*18*).

Fig. 3. MZ*ago2* mutants show reduced erythropoiesis. (**A**) Expression of hemoglobin (brown) visualized by the oxidation of *o*-dianisidine (o-das) at 48 hpf in the ducts of Cuvier. Hemoglobinized cells accumulate in wild type but are reduced in MZ*ago2* mutants [group II (mild) and group III (severe) reduction of o-das–positive cells]. (**B**) Percentage of embryos with hemoglobinized cells in MZ*ago2* mutants (n = 61) compared to wild-type embryos (n = 200), showing strongly reduced (group III; light gray) and partially reduced (group II; gray) numbers of o-das (+) cells (χ^2 test, $P < 0.001$). (**C**) Whole-mount in situ hybridization of *ago2* expression at 24 hpf. (**D**) May-Grünwald/Giemsa stain of erythrocytes from wild-type, MZ*ago2* mutants, and MZ*ago2* injected at one-cell stage with various RNAs as shown (+). Erythrocytes are representative of the mean for each group. (**E**) Scatterplot of the nuclear cytoplasmic ratio (N:C) for each genotype in (D) as a readout of erythrocyte maturation (*17*). Distributions of the N:C ratios in wild-type compared to MZ*ago2* differed significantly (Wilcoxon rank-sum test after Bonferroni correction, $P < 10^{-15}$). Erythrocyte maturation is rescued by miR-451-duplex (MZ*ago2* and MZ*ago2*+miR-451, $P < 10^{-15}$) and wild-type mAgo2 (MZ*ago2* and MZ*ago2*+mAgo2, $P < 10^{-15}$) but not catalytically dead mAgo2^{D669A} (MZ*ago2* and MZ*ago2*+mAgo2^{D669A}, $P > 0.1$).

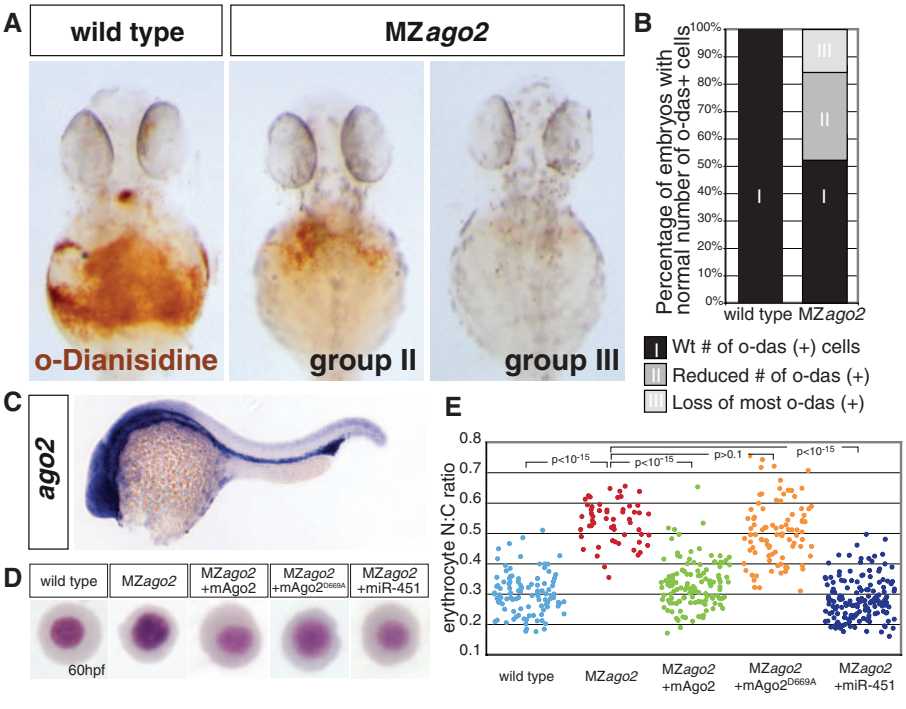

(fig. S2). Several miRNAs appeared refractory to *dicer* loss of function, notably miR-451-5′, miR-2190-5′, miR-2190-3′, and miR-735-5′ (Fig. 1A and figs. S3 and S4). On the basis of read frequency, reproducibility, and evolutionary conservation, we focused subsequent analysis on miR-451. miR-451 differs from other "canonical" miRNAs for several reasons: (i) It is encoded in a conserved 42-nt hairpin (fig. S5) with a 17-nt stem, whereas Dicer requires a >19-nt stem for efficient processing (*9*); (ii) miR-451 has a defined 5′ end but a variable 3′ end that extends over the loop region and ranges between 20 and 30 nt (Fig. 1, C and D); and (iii) reads stopped at nucleotide 30, and longer reads carried one to five nontemplated uridines, with nucleotide 31 mostly being a nontemplated U (Fig. 1D). The final templated base pairs with nucleotide 10 of the mature miRNA (Fig. 1C and fig. S1), a site where slicer activity cleaves the passenger strand in siRNAs (*10*–*12*). These observations lead us to hypothesize that Ago2 slicer activity could participate in miRNA maturation (fig. S1).

To determine whether Ago2 participates in miRNA maturation, we generated a deletion in the Piwi domain of the *ago2* gene (*ago2*$^{\Delta 90}$) with the use of zinc finger nucleases (*13*–*15*) (Fig. 1E and fig. S1). Because argonaute genes are maternally expressed (fig. S6), we generated maternal-zygotic *ago2* mutants (MZ*ago2*). Indeed, slicer cleavage of an mRNA with perfectly complementary targets to miR-1 was severely reduced in MZ*ago2* but not Z*ago2* relative to wild-type embryos (Fig. 1F and fig. S1).

To investigate the role of Ago2 in miRNA processing, we sequenced small RNAs (19 to 36 nt) from 48-hour-old MZ*ago2* mutant embryos. Comparing the normalized read frequency for each 5′- and 3′-mature miRNA between wild-type and MZ*ago2* mutants revealed a reduction in the number of reads that mapped to miR-451 (Fig. 1, B and D). In contrast, other miRNAs remained largely unchanged. miR-451 and miR-144 are coexpressed from a common primary transcript in the erythroid lineage (*16*, *17*) (Fig. 1C). Whereas miR-451 accumulated in the absence of Dicer (factor of ~3 increase), miR-144 reads were reduced by a factor of >200 in MZ*dicer* mutants (*18*) (Fig. 1A). Conversely, *ago2* loss of function did not affect the read frequency of miR-144 (Fig. 1B) but did reduce miR-451 levels by a factor of >8000. Taken together, these results indicate that Ago2 regulates miR-451 levels posttranscriptionally by affecting either its processing or stability.

Recent studies suggest that Ago2 binds pre-miRNAs and miRNA:miRNA* duplexes (*19*–*22*), where miRNA* denotes the complementary strand. Ago2 interacted with radiolabeled synthetic pre-miR-451 in vitro (fig. S7). Coexpression of Flag-mouse-Ago2 (mAgo2) with pre-miR-451 or a mutant pre-miR-451$^{mm10\text{-}11}$ (with two mismatches in the predicted slicer cleavage site) followed by Ago2 immunoprecipitation showed that Ago2 bound to both mature miR-451 and pre-miR-451$^{mm10\text{-}11}$ (Fig. 2A). Incubation of human Ago2 (hAgo2) with pre-miR-451 but not pre-miR-430 resulted in a sharp 30-nt band corresponding with the predicted slicer

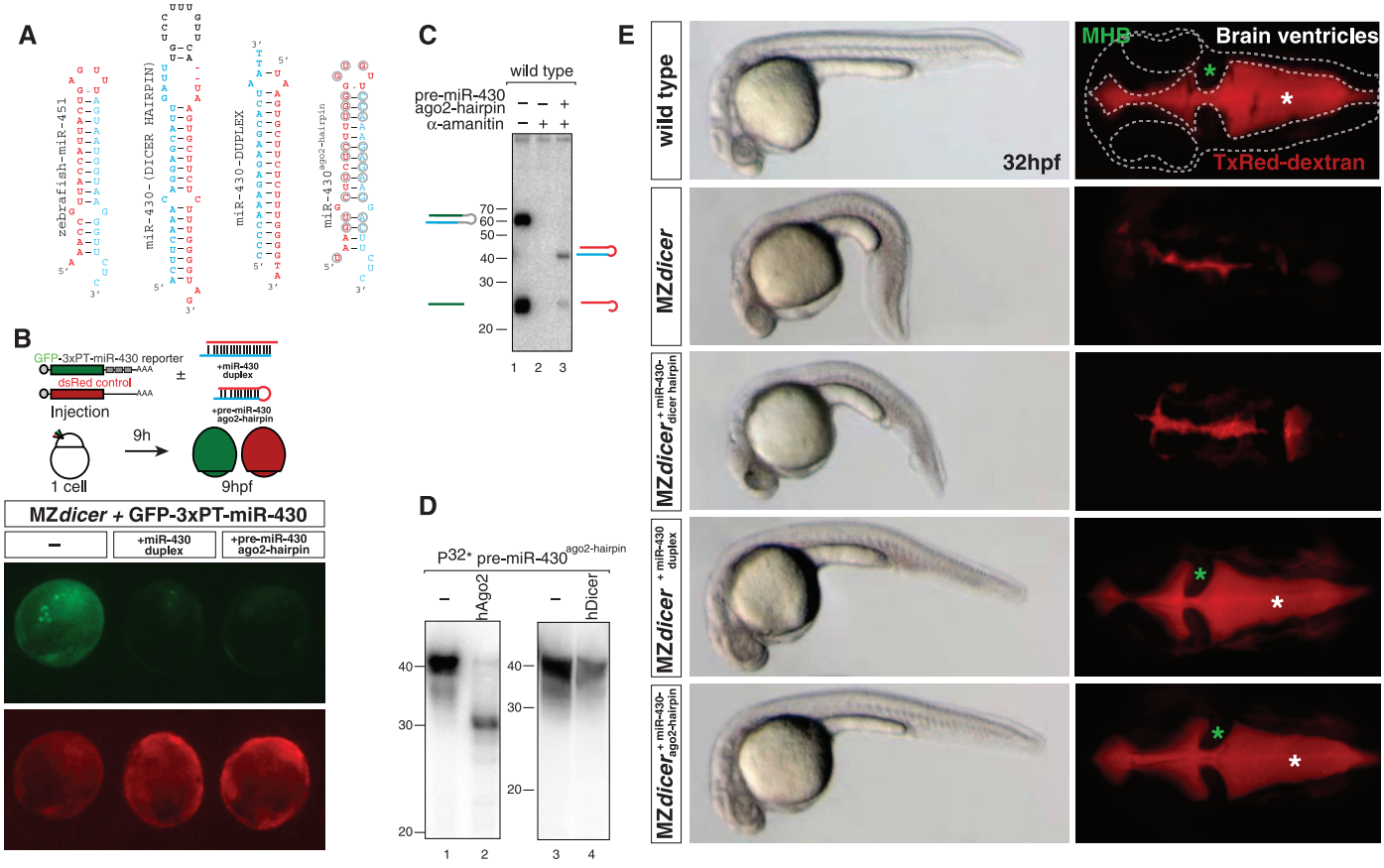

Fig. 4. A Dicer-independent miRNA. (**A**) Zebrafish pre-miRNAs and duplexes as indicated. pre-miR-430$^{ago2\text{-}hairpin}$ is a miR-430c hairpin that has been mutated and shortened to form a 42-nt hairpin mimicking pre-miR-451 (ago2-hairpin). (**B**) GFP-reporter mRNA (green) was co-injected at the one-cell stage with control dsRed mRNA (red). The GFP reporter contains three complementary target sites to miR-430 in its 3′-untranslated region. (**C**) Northern blot to detect miR-430 in wild-type embryos injected with hairpins as indicated. α-Amanitin was co-injected to inhibit transcription of endogenous pri-miR-430. (**D**) Northern blot to detect 5′-radiolabeled pre-miR-430$^{ago2\text{-}hairpin}$ after in vitro processing by recombinant hAgo2 and hDicer. (**E**) In vivo assay to rescue miR-430 function in MZ*dicer* mutants. Bright-field and fluorescent images of the dorsal view of the brain after injection of TxRed dextran in the ventricles (right) in 32-hpf embryos. Brain outline (dashed line), mid-hindbrain boundary (green asterisk), and ventricles (red, white asterisk) are shown. Morphogenesis defects are rescued by injection of a Dicer-independent pre-miR-430$^{ago2\text{-}hairpin}$ or a miR-430-duplex but not a Dicer-dependent pre-miR-430.

cleavage product of miR-451 (Fig. 2B). Conversely, recombinant Dicer bound both pre-miRNAs (fig. S7) but could only process pre-miR-430 (Fig. 2B). To investigate whether Ago2 processes miR-451, we injected pre-miRNAs into one-cell-stage embryos. Synthetic and endogenous pre-miR-451 hairpins were processed into ~30-nt intermediates and a ~22- to 26-nt mature miR-451 in wild-type and MZ*dicer* mutant but not in MZ*ago2* mutant embryos (Fig. 2, D and F). In contrast, a canonical mature miR-430 was processed in both wild-type and MZ*ago2* mutant embryos but not in MZ*dicer* (Fig. 2F). On the basis of the sequencing results, we hypothesized that Ago2-processed hairpin might undergo nucleolytic trimming at the 3′ end (Fig. 1D). We observed that Ago2 protected the ~30-nt slicer-cleaved intermediate from RNase I in vitro, resulting in a ~20- to 26-nt 3′-end trimmed product (Fig. 2C), similar to the mature miRNAs observed in vivo (Fig. 2, D to F). Ago2 slicer activity depends on its catalytic triad (DDH) and the pairing between the guide and the target mRNA (*23*–*25*). Expressing wild-type but not catalytically dead (D669A) mAgo2 in MZ*ago2* mutants rescued pre-miR-451 processing in vivo (Fig. 2E). Furthermore, a hairpin with mismatches that disrupt pairing in the predicted slicer cleavage was bound by Ago2 (fig. S7) but was inefficiently processed into mature miR-451 (Fig. 2E). These results indicate that Ago2 binds and cleaves pre-miR-451 in a process that requires the slicer catalytic activity and is independent of Dicer.

MZ*ago2* mutant embryos displayed normal morphogenesis during gastrulation, brain development, and heart development (fig. S8). Ago2 is maternally expressed, and later in development it acquires tissue-specific expression in the brain and intermediate cell mass (ICM) (Fig. 3C and fig. S6). The ICM corresponds to the hematopoietic precursors and overlaps with the expression domain of miR-451 (*16*), which plays an important role in erythrocyte maturation in zebrafish (*16*, *17*). Consistent with the Ago2-dependent processing of miR-451, MZ*ago2* but not MZ*dicer* mutants showed a reduction in the number of hemoglobinized erythrocytes (Fig. 3, A and B, and fig. S8). In zebrafish, erythrocyte maturation can be monitored by changes in erythrocyte morphology and reduced nuclear/cytoplasmic (N:C) ratio (*17*, *26*, *27*). Erythrocyte maturation was delayed in MZ*ago2* mutants, as manifested by a significant increase in N:C ratio at 60 hours post-fertilization (hpf) ($P < 10^{-15}$) (Fig. 3, D and E). Providing back wild-type mAgo2 or mature miR-451-duplex but not catalytically dead mAgo2^{D669A} rescued erythrocyte maturation in MZ*ago2* mutants (Fig. 3, D and E). Thus, Ago2 catalytic function plays an important role during erythrocyte maturation.

Whereas miR-451 is a 42-nt miRNA hairpin, canonical vertebrate miRNAs are ~60 nt, and unlike most miRNAs, mature miR-451 extends into the loop of the hairpin where it overlaps with the miRNA* (Fig. 4A and fig. S5). We hypothesized that selection of the processing pathway may be determined by structural differences or by specific sequence motifs. To distinguish between these two scenarios, we modified the sequence of pre-miR-451 to encode a Dicer-dependent miRNA (miR-430c or miR-1) mimicking pre-miR-451 structure and length (pre-miRNA$^{ago2\text{-}hairpin}$) (Fig. 4A and fig. S10). miR-430c is a member of a zygotically expressed miRNA family that regulates maternal mRNA clearance, gastrulation, and brain morphogenesis (*7*, *28*). These processes are disrupted in MZ*dicer* mutants but can be rescued by injection of a Dicer-independent miR-430-duplex (*7*, *28*). Three lines of evidence indicate that pre-miR-430$^{ago2\text{-}hairpin}$ is processed and functional independently of Dicer: (i) Synthetic pre-miRNA$^{ago2\text{-}hairpin}$ was processed into a ~23-nt mature miRNA in vivo (Fig. 4C and fig. S10) and processed by recombinant hAgo2 but not hDicer in vitro (Fig. 4D); (ii) injection of miR-430c$^{ago2\text{-}hairpin}$ into MZ*dicer* embryos repressed translation of a green fluorescent protein miR-430 reporter (GFP-miR-430) relative to a dsRed control (Fig. 4B); and (iii) injection of pre-miR-430c$^{ago2\text{-}hairpin}$ into MZ*dicer* mutants rescued the gastrulation and brain morphogenesis defects similarly to a miR-430-duplex (Fig. 4E). In contrast, equimolar levels of the annotated Dicer-dependent pre-miR-430 did not rescue the MZ*dicer* phenotype (Fig. 4E). A second engineered miRNA (miR-1$^{ago2\text{-}hairpin}$) was also processed independently of Dicer and down-regulated a GFP-miR-1 reporter in vivo (fig. S10). These results support a model in which the secondary structure of the hairpin determines whether a pre-miRNA is processed by Ago2 to form a physiologically functional Dicer-independent miRNA.

Our study defines a Dicer-independent pathway for miRNA processing that is dependent on Ago2 catalytic activity. We propose a model whereby Ago2 binds the pre-miRNA and cleaves the paired miRNA* passenger strand 10 nucleotides away from the 5′ end of the Ago2-bound miRNA guide strand (*18*). On the basis of our small RNA sequencing, this intermediate would undergo polyuridylation and nuclease-mediated removal of uridines and templated nucleotides not protected by Ago2 to generate the mature miRNA (fig. S11). Previous studies have shown that the terminal uridylyl transferase (TUT4) is recruited by lin-28 to uridylate pre-let7 (*29*), which blocks miRNA maturation and accelerates its degradation. Although we cannot exclude the possibility that miR-451–uridylated intermediates are targeted for complete degradation, our model favors a scenario where uridylated Ago2-cleaved pre-miRNAs are trimmed by a cellular nuclease to generate mature miRNA sequences protected by Ago2.

Ago2 has been reported to cleave siRNAs and pre-miRNAs (*21*). Ago2-cleaved precursors (ac-pre-miRNAs) can serve as Dicer substrates, but their physiological functions remain unclear (*21*). Here, we show that Ago2 cleavage is necessary for the generation of a functional miRNA (Figs. 1, 2, and 4). The identification of a miRNA-processing pathway that bypasses Dicer function might have wide implications for the processing of canonical miRNAs. Our study provides a biological context in which Ago2 slicer activity is needed to process a blood-specific miRNA, miR-451 (*30*). Although it is likely that Ago2 has additional roles in the cell by cleaving perfectly complementary targets (*1*), the strong conservation of the sequence and secondary structure of miR-451 across vertebrates suggests that constraints are in place to maintain this Ago2-mediated miRNA processing pathway through evolution (*18*).

References and Notes

1. D. P. Bartel, *Cell* **136**, 215 (2009).
2. R. W. Carthew, E. J. Sontheimer, *Cell* **136**, 642 (2009).
3. J. E. Babiarz, J. G. Ruby, Y. Wang, D. P. Bartel, R. Blelloch, *Genes Dev.* **22**, 2773 (2008).
4. E. Berezikov, W. J. Chung, J. Willis, E. Cuppen, E. C. Lai, *Mol. Cell* **28**, 328 (2007).
5. K. Okamura, J. W. Hagen, H. Duan, D. M. Tyler, E. C. Lai, *Cell* **130**, 89 (2007).
6. J. G. Ruby, C. H. Jan, D. P. Bartel, *Nature* **448**, 83 (2007).
7. A. J. Giraldez *et al.*, *Science* **308**, 833 (2005).
8. E. Wienholds, M. J. Koudijs, F. J. van Eeden, E. Cuppen, R. H. Plasterk, *Nat. Genet.* **35**, 217 (2003).
9. D. Siolas *et al.*, *Nat. Biotechnol.* **23**, 227 (2004).
10. C. Matranga, Y. Tomari, C. Shin, D. P. Bartel, P. D. Zamore, *Cell* **123**, 607 (2005).
11. J. Martinez, A. Patkaniowska, H. Urlaub, R. Lührmann, T. Tuschl, *Cell* **110**, 563 (2002).
12. B. Czech *et al.*, *Mol. Cell* **36**, 445 (2009).
13. Y. Doyon *et al.*, *Nat. Biotechnol.* **26**, 702 (2008).
14. M. L. Maeder *et al.*, *Mol. Cell* **31**, 294 (2008).
15. X. Meng, M. B. Noyes, L. J. Zhu, N. D. Lawson, S. A. Wolfe, *Nat. Biotechnol.* **26**, 695 (2008).
16. L. C. Dore *et al.*, *Proc. Natl. Acad. Sci. U.S.A.* **105**, 3333 (2008).
17. L. Pase *et al.*, *Blood* **113**, 1794 (2009).
18. See supporting material on *Science* Online.
19. S. M. Hammond, S. Boettcher, A. A. Caudy, R. Kobayashi, G. J. Hannon, *Science* **293**, 1146 (2001).
20. B. Wang *et al.*, *Nat. Struct. Mol. Biol.* **16**, 1259 (2009).
21. S. Diederichs, D. A. Haber, *Cell* **131**, 1097 (2007).
22. G. S. Tan *et al.*, *Nucleic Acids Res.* **37**, 7533 (2009).
23. J. Liu *et al.*, *Science* **305**, 1437 (2004).
24. J. J. Song, S. K. Smith, G. J. Hannon, L. Joshua-Tor, *Science* **305**, 1434 (2004).
25. N. H. Tolia, L. Joshua-Tor, *Nat. Chem. Biol.* **3**, 36 (2007).
26. B. M. Weinstein *et al.*, *Development* **123**, 303 (1996).
27. F. Qian *et al.*, *PLoS Biol.* **5**, e132 (2007).
28. A. J. Giraldez *et al.*, *Science* **312**, 75 (2006).
29. Z. S. Kai, A. E. Pasquinelli, *Nat. Struct. Mol. Biol.* **17**, 5 (2010).
30. S. Cheloufi, C. O. Dos Santos, M. M. W. Chong, G. J. Hannon, *Nature* 10.1038/nature09092 (2010).

31. We thank J. Doudna, D. O'Carroll, L. Zon, S. Lacadie, G. Lieschke, D. Krausse, and S. Halene for reagents and protocols; A. Enright, C. Abreu-Goodger, and J. Brennecke for initial small RNA analysis; and B. Schachter, C. Takacs, V. Greco, and D. Cazalla for discussions and manuscript editing. Supported by Fundación Ramón Areces (D.C.), a Human Frontier Science Program fellowship (H.X.), NIH grants R01GM081602-03/03S1 (A.J.G.) and R01HL093766 (N.D.L. and S.A.W.), the Yale

Scholar program, and the Pew Scholars Program in the Biomedical Sciences (A.J.G.). Contributions: D.C. and A.J.G. designed and performed experiments; H.X. performed computational analysis; D.C. and D.W.T. performed in vitro assays; H.P. performed in situ hybridizations; Y.M., G.J.H., and S.C. helped with initial small RNA library sequencing and discussion; E.M. provided recombinant Ago2; S.M. provided small RNA sequencing; S.A.W. and N.L. designed the zinc finger nucleases; and A.J.G. wrote the manuscript. Sequencing data are deposited in Gene Expression Omnibus (accession number GSE21503).

Supporting Online Material
www.sciencemag.org/cgi/content/full/science.1190809/DC1
Materials and Methods
Figs. S1 to S11
References

12 April 2010; accepted 27 April 2010
Published online 6 May 2010;
10.1126/science.1190809
Include this information when citing this paper.

Control of Membrane Protein Topology by a Single C-Terminal Residue

Susanna Seppälä,[1] Joanna S. Slusky,[1] Pilar Lloris-Garcerá,[1] Mikaela Rapp,[1]* Gunnar von Heijne[1,2]†

The mechanism by which multispanning helix-bundle membrane proteins are inserted into their target membrane remains unclear. In both prokaryotic and eukaryotic cells, membrane proteins are inserted cotranslationally into the lipid bilayer. Positively charged residues flanking the transmembrane helices are important topological determinants, but it is not known whether they act strictly locally, affecting only the nearest transmembrane helices, or can act globally, affecting the topology of the entire protein. Here we found that the topology of an *Escherichia coli* inner membrane protein with four or five transmembrane helices could be controlled by a single positively charged residue placed in different locations throughout the protein, including the very C terminus. This observation points to an unanticipated plasticity in membrane protein insertion mechanisms.

Integral α-helical membrane proteins carry out a wide range of central biological functions. They have two conspicuous structural features: hydrophobic transmembrane α helices and a strong bias in the distribution of positively charged arginine (Arg) and lysine (Lys) residues between cytoplasmic and extracytoplasmic loops, with up to three times the frequency of Arg and Lys found in the cytoplasmic loops (*1*). Positively charged residues exert local control over the orientation of transmembrane helices in their immediate neighborhood (*2*, *3*), but whether they can also affect the global topology of a protein is unknown. Multispanning membrane proteins insert into their target membrane cotranslationally; therefore, positively charged residues in a more C-terminal region of the protein might be expected not to be able to influence the orientation of distant N-terminal transmembrane helices. How-

[1]Center for Biomembrane Research, Department of Biochemistry and Biophysics, Stockholm University, SE-106 91 Stockholm, Sweden. [2]Science for Life Laboratory, Stockholm University, Box 1031, SE-171 21 Solna, Sweden.

*Present address: Department of Medical Biochemistry and Biophysics, Karolinska Institutet, SE-171 77 Stockholm, Sweden. †To whom correspondence should be addressed. E-mail: gunnar@dbb.su.se

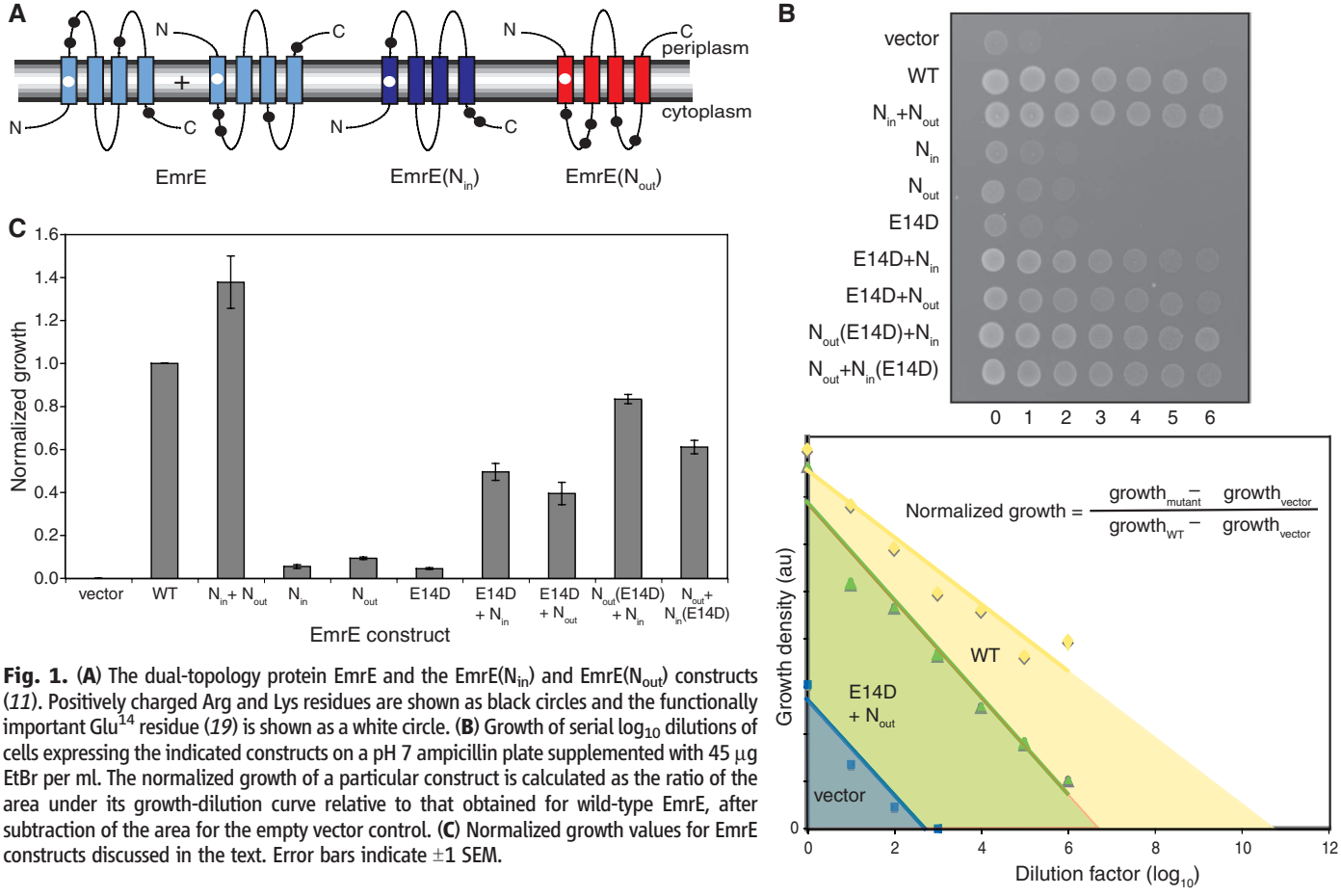

Fig. 1. (**A**) The dual-topology protein EmrE and the EmrE(N_{in}) and EmrE(N_{out}) constructs (*11*). Positively charged Arg and Lys residues are shown as black circles and the functionally important Glu^{14} residue (*19*) is shown as a white circle. (**B**) Growth of serial $\log_{10}$ dilutions of cells expressing the indicated constructs on a pH 7 ampicillin plate supplemented with 45 μg EtBr per ml. The normalized growth of a particular construct is calculated as the ratio of the area under its growth-dilution curve relative to that obtained for wild-type EmrE, after subtraction of the area for the empty vector control. (**C**) Normalized growth values for EmrE constructs discussed in the text. Error bars indicate ±1 SEM.

ever, charged residues can affect the orientation of a protein domain, and individual transmembrane helices do not always insert into the membrane in a strict N- to C-terminal order or can reorient during the insertion process (*4*–*7*), which suggests a certain flexibility in the way multispanning membrane proteins are handled by the insertion machinery.

We asked to what extent global control of membrane protein topology by positively charged residues is possible, and so we looked for a multispanning protein that is poised near the threshold between an N_{in} topology with the N terminus facing the cytoplasm and an oppositely oriented N_{out} topology. EmrE is an *Escherichia coli* inner membrane protein with four transmembrane helices (TMHs) that meets this criterion. It belongs to the Small Multidrug-Resistance family of transporters and imparts resistance to toxic compounds like ethidium bromide (EtBr) and acriflavin (*8*). The active form of EmrE is a homodimer, and structural (*9*, *10*), biochemical (*11*–*13*), and phylogenetic (*14*) data support a so-called dual topology for EmrE, i.e., the monomers have a mixed membrane orientation (Fig. 1A). In the available two- and three-dimensional crystal structures (*9*, *10*), two oppositely oriented monomers form an antiparallel homodimer, although other models have been proposed (*13*).

The homodimeric, dual-topology EmrE protein can be engineered into a functional heterodimer composed of two oppositely oriented monomers, EmrE(N_{in}) and EmrE(N_{out}), by suitable placement of positively charged residues in the two EmrE versions (*11*) (Fig. 1A). Moreover, the conserved glutamic acid residue Glu^{14} in TMH1 can be changed to aspartic acid (E14D mutation) in one, but not both, monomers while retaining a functional heterodimer, although the change imparts a lower toxin-resistance level (*11*). Thus, it is possible to determine the orientation of any EmrE mutant by coexpressing the mutant protein, including the E14D mutation, with either EmrE(N_{in}) or EmrE(N_{out}). Any homodimers formed by the mutant protein itself will be inactive because they carry the E14D mutation in both monomers, and coexpression of the mutant protein with either EmrE(N_{in}) or EmrE(N_{out}) will result in active protein only when an antiparallel heterodimer is formed. Quantitative activity assays can be carried out either in liquid culture (*11*) or on toxin-containing plates (*15*) (Fig. 1B). *E. coli* cells expressing EmrE(E14D), EmrE(N_{in}), or EmrE(N_{out}) by themselves were at best marginally resistant to EtBr (Fig. 1C). Coexpression of EmrE(N_{in}) with EmrE(N_{out}) made cells resistant to EtBr. Coexpression of EmrE(E14D) with either EmrE(N_{in}) or EmrE(N_{out}) also imparted resistance, as expected if EmrE(E14D) had a dual topology and could form active heterodimers with either EmrE(N_{in}) or EmrE(N_{out}).

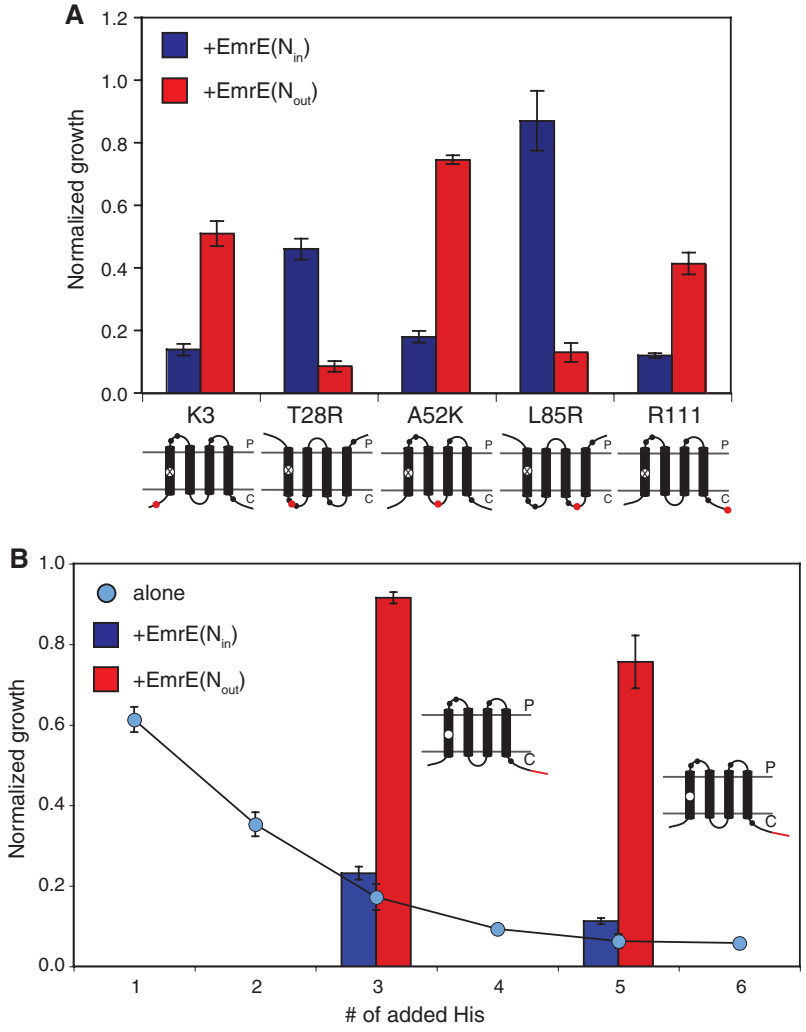

Fig. 2. (**A**) Topological effects of a single positively charged residue placed in the indicated positions in EmrE(E14D). Normalized growth values during coexpression with EmrE(N_{in}) (blue bars) and EmrE(N_{out}) (red bars). The predominating topology is shown for each construct as a miniature cartoon where black circles indicate positively charged (Arg or Lys) residues in EmrE(E14D), the crossed white circle indicates Asp^{14}, and the red circle indicates the position of the added positively charged residue. C, cytoplasm; P, periplasm. (**B**) Topological effects of adding C-terminal His tails to EmrE (Glu^{14} is retained in these constructs). Blue circles show the normalized growth values for the indicated EmrE construct expressed by itself. Blue and red bars indicate coexpression with EmrE(N_{in}) and EmrE(N_{out}), respectively. Error bars indicate ±1 SEM.

Using the coexpression assay, we determined the topology for a series of EmrE(E14D) mutants with one extra positively charged Arg or Lys residue placed in the N-terminal tail, in one of the loops between the TMHs, or at the C terminus. The orientation of each mutant faithfully followed the positive-inside rule, i.e., the added positively charged residue always promoted the topology where this residue was in the cytoplasm (Fig. 2A), even for the most C-terminal mutation, where an Arg was added as the last residue in the protein. To confirm these results, we made a construct totally devoid of positively charged residues and then added back Arg or Lys residues, one at a time. The E14D mutant of the construct lacking Arg and Lys residues imparted EtBr resistance only when coexpressed with EmrE(N_{out}) (fig. S1), which indicated that it had adopted the N_{in} orientation. As expected, adding one Arg or Lys residue to the N-terminal tail, to the loop between TMH2 and TMH3, or to the C-terminal tail did not change the N_{in} orientation. Positively charged residues added to the TMH1-TMH2 or TMH3-TMH4 loops progressively changed the orientation to N_{out}. However, compared with the single-charge effects observed for EmrE(E14D), higher numbers of Arg or Lys were required to reach full inversion of the topology, presumably because, in this case, the starting topology was N_{in} rather than dual.

That the topological effect of a positively charged residue was equally strong regardless of where in the protein it was placed prompted us also to study the effect of His residues. Histidine carries only a partial positive charge at the pH prevailing in the *E. coli* cytoplasm (*16*), and if charge is the controlling factor, its effect on topology should be weaker but qualitatively similar to that of Arg. Indeed, EmrE constructs with three or more His added at the C terminus were inactive when expressed alone but yielded a highly active

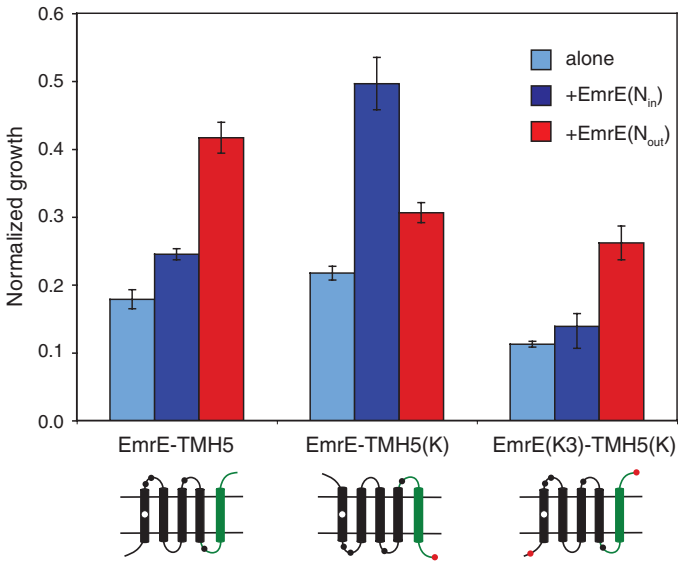

Fig. 3. Topological effects of adding Lys residues to the N- and C-termini of the EmrE-TMH5 construct (Glu[14] is retained in these constructs). TMH5 (green in the miniature cartoons) is a GGPG. . .GPGG-flanked 19-residue-long segment composed of four Leu and 15 Ala. Normalized growth values during coexpression with EmrE(N_{in}) (blue bars) and EmrE(N_{out}) (red bars) are shown. Error bars indicate ±1 SEM.

protein when coexpressed with EmrE(N_{out}) (Fig. 2B). This appeared to be a result of the charge and not the length of the C-terminal tail, because the addition of up to six Gly had little effect on the dual topology of EmrE (fig. S2).

Finally, to examine whether a C-terminal positively charged residue could influence the global topology when moved even farther from the N terminus, we extended EmrE by adding a fifth TMH, composed only of alanines and leucines, to the C terminus. Given its composition, this TMH was not expected to interact in any specific way with TMHs 1 to 4. EmrE-TMH5 had an N_{in} topology, as it was inactive when expressed alone but imparted EtBr resistance—albeit at a lower level than wild-type EmrE—when coexpressed with EmrE(N_{out}) (Fig. 3). However, adding a C-terminal Lys to EmrE-TMH5 resulted in a protein [EmrE-TM5(K)] that imparted EtBr resistance only when coexpressed with EmrE(N_{in}). Thus, the C-terminal Lys can reverse the orientation of as many as five upstream TMHs. Finally, the N_{in} topology was regained when the C-terminal Lys was complemented with an N-terminal Lys [EmrE(K3)-TMH5(K)].

In summary, the membrane orientation of the 4-TMH, dual-topology protein EmrE and a 5-TMH version of the same protein could be shifted both to N_{in} and to N_{out} by adding a single positively charged residue in various locations throughout the protein. In all cases, the shift in orientation was as predicted by the positive-inside rule. A C-terminal Arg or Lys was as effective in this regard as were positively charged residues placed in other locations closer to the N terminus. Apparently, the protein remains "topologically uncommitted" until the last residue has been synthesized. These and other observations of a related kind (*17*) raise important questions regarding the mechanism of membrane protein insertion and assembly. Specifically, how much protein can the translocon pore accommodate? Are translocon-associated proteins, such as YidC (*18*), involved in chaperoning membrane proteins to their final topology? Is postinsertion conversion between different topologies, so far seen only under conditions of extreme alterations in membrane lipid composition (*17*), possible also in wild-type cells?

References and Notes

1. G. von Heijne, *EMBO J.* **5**, 3021 (1986).
2. G. von Heijne, *Nature* **341**, 456 (1989).
3. G. Gafvelin, G. von Heijne, *Cell* **77**, 401 (1994).
4. M. Monné, G. Gafvelin, R. Nilsson, G. von Heijne, *Eur. J. Biochem.* **263**, 264 (1999).
5. G. von Heijne, *Nat. Rev. Mol. Cell Biol.* **7**, 909 (2006).
6. W. R. Skach, *Nat. Struct. Mol. Biol.* **16**, 606 (2009).
7. M. Bogdanov, J. Xie, P. Heacock, W. Dowhan, *J. Cell Biol.* **182**, 925 (2008).
8. S. Schuldiner, *Biochim. Biophys. Acta* **1794**, 748 (2009).
9. I. Ubarretxena-Belandia, J. M. Baldwin, S. Schuldiner, C. G. Tate, *EMBO J.* **22**, 6175 (2003).
10. Y. J. Chen *et al.*, *Proc. Natl. Acad. Sci. U.S.A.* **104**, 18999 (2007).
11. M. Rapp, S. Seppälä, E. Granseth, G. von Heijne, *Science* **315**, 1282 (2007).
12. T. Nara *et al.*, *J. Biochem.* **142**, 621 (2007).
13. I. Nasie, S. Steiner-Mordoch, A. Gold, S. Schuldiner, *J. Biol. Chem.* **285**, 15234 (2010).
14. M. Rapp, E. Granseth, S. Seppälä, G. von Heijne, *Nat. Struct. Mol. Biol.* **13**, 112 (2006).
15. Materials and methods are available as supporting material on *Science* Online.
16. E. Padan, D. Zilberstein, S. Schuldiner, *Biochim. Biophys. Acta* **650**, 151 (1981).
17. W. Dowhan, M. Bogdanov, *Annu. Rev. Biochem.* **78**, 515 (2009).
18. K. Xie, R. E. Dalbey, *Nat. Rev. Microbiol.* **6**, 234 (2008).
19. H. Yerushalmi, S. S. Mordoch, S. Schuldiner, *J. Biol. Chem.* **276**, 12744 (2001).

20. We thank Ann-Louise Johansson for technical assistance. This work was supported by grants to G.v.H. from the European Research Council (ERC-2008-AdG 232648), the Swedish Cancer Foundation, the Swedish Research Council, and the Swedish Foundation for Strategic Research, to J.S.S. from the International Human Frontier Science Program Organization, and to P.L.G. from the European Communities (TranSys PITN-2008-215524).

Supporting Online Material

www.sciencemag.org/cgi/content/full/science.1188950/DC1
Materials and Methods
Figs. S1 and S2
References

1 March 2010; accepted 4 May 2010
Published online 27 May 2010;
10.1126/science.1188950
Include this information when citing this paper.

A Generalization of Hamilton's Rule for the Evolution of Microbial Cooperation

jeff smith,*† J. David Van Dyken, Peter C. Zee

Hamilton's rule states that cooperation will evolve if the fitness cost to actors is less than the benefit to recipients multiplied by their genetic relatedness. This rule makes many simplifying assumptions, however, and does not accurately describe social evolution in organisms such as microbes where selection is both strong and nonadditive. We derived a generalization of Hamilton's rule and measured its parameters in *Myxococcus xanthus* bacteria. Nonadditivity made cooperative sporulation remarkably resistant to exploitation by cheater strains. Selection was driven by higher-order moments of population structure, not relatedness. These results provide an empirically testable cooperation principle applicable to both microbes and multicellular organisms and show how nonlinear interactions among cells insulate bacteria against cheaters.

Social evolution has illuminated many different areas of biology, from altruistic behavior in insects to sex ratios, selfish genetic elements, and multicellularity (*1*, *2*). The central puzzle in this field is how cooperation—increasing the fitness of other individuals—persists when cheaters can benefit without paying the cost of cooperating. The most prominent explanation for the evolution of cooperation is kin selection, in which benefits preferentially

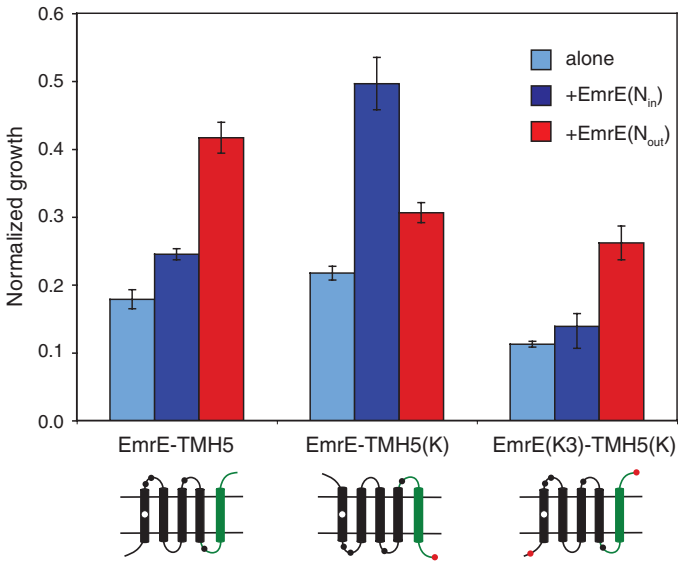

Fig. 3. Topological effects of adding Lys residues to the N- and C-termini of the EmrE-TMH5 construct (Glu[14] is retained in these constructs). TMH5 (green in the miniature cartoons) is a GGPG. . .GPGG-flanked 19-residue-long segment composed of four Leu and 15 Ala. Normalized growth values during coexpression with EmrE(N_{in}) (blue bars) and EmrE(N_{out}) (red bars) are shown. Error bars indicate ±1 SEM.

protein when coexpressed with EmrE(N_{out}) (Fig. 2B). This appeared to be a result of the charge and not the length of the C-terminal tail, because the addition of up to six Gly had little effect on the dual topology of EmrE (fig. S2).

Finally, to examine whether a C-terminal positively charged residue could influence the global topology when moved even farther from the N terminus, we extended EmrE by adding a fifth TMH, composed only of alanines and leucines, to the C terminus. Given its composition, this TMH was not expected to interact in any specific way with TMHs 1 to 4. EmrE-TMH5 had an N_{in} topology, as it was inactive when expressed alone but imparted EtBr resistance—albeit at a lower level than wild-type EmrE—when coexpressed with EmrE(N_{out}) (Fig. 3). However, adding a C-terminal Lys to EmrE-TMH5 resulted in a protein [EmrE-TM5(K)] that imparted EtBr resistance only when coexpressed with EmrE(N_{in}). Thus, the C-terminal Lys can reverse the orientation of as many as five upstream TMHs. Finally, the N_{in} topology was regained when the C-terminal Lys was complemented with an N-terminal Lys [EmrE(K3)-TMH5(K)].

In summary, the membrane orientation of the 4-TMH, dual-topology protein EmrE and a 5-TMH version of the same protein could be shifted both to N_{in} and to N_{out} by adding a single positively charged residue in various locations throughout the protein. In all cases, the shift in orientation was as predicted by the positive-inside rule. A C-terminal Arg or Lys was as effective in this regard as were positively charged residues placed in other locations closer to the N terminus. Apparently, the protein remains "topologically uncommitted" until the last residue has been synthesized. These and other observations of a related kind (*17*) raise important questions regarding the mechanism of membrane protein insertion and assembly. Specifically, how much protein can the translocon pore accommodate? Are translocon-associated proteins, such as YidC (*18*), involved in chaperoning membrane proteins to their final topology? Is postinsertion conversion between different topologies, so far seen only under conditions of extreme alterations in membrane lipid composition (*17*), possible also in wild-type cells?

References and Notes

1. G. von Heijne, *EMBO J.* **5**, 3021 (1986).
2. G. von Heijne, *Nature* **341**, 456 (1989).
3. G. Gafvelin, G. von Heijne, *Cell* **77**, 401 (1994).
4. M. Monné, G. Gafvelin, R. Nilsson, G. von Heijne, *Eur. J. Biochem.* **263**, 264 (1999).
5. G. von Heijne, *Nat. Rev. Mol. Cell Biol.* **7**, 909 (2006).
6. W. R. Skach, *Nat. Struct. Mol. Biol.* **16**, 606 (2009).
7. M. Bogdanov, J. Xie, P. Heacock, W. Dowhan, *J. Cell Biol.* **182**, 925 (2008).
8. S. Schuldiner, *Biochim. Biophys. Acta* **1794**, 748 (2009).
9. I. Ubarretxena-Belandia, J. M. Baldwin, S. Schuldiner, C. G. Tate, *EMBO J.* **22**, 6175 (2003).
10. Y. J. Chen *et al.*, *Proc. Natl. Acad. Sci. U.S.A.* **104**, 18999 (2007).
11. M. Rapp, S. Seppälä, E. Granseth, G. von Heijne, *Science* **315**, 1282 (2007).
12. T. Nara *et al.*, *J. Biochem.* **142**, 621 (2007).
13. I. Nasie, S. Steiner-Mordoch, A. Gold, S. Schuldiner, *J. Biol. Chem.* **285**, 15234 (2010).
14. M. Rapp, E. Granseth, S. Seppälä, G. von Heijne, *Nat. Struct. Mol. Biol.* **13**, 112 (2006).
15. Materials and methods are available as supporting material on *Science* Online.
16. E. Padan, D. Zilberstein, S. Schuldiner, *Biochim. Biophys. Acta* **650**, 151 (1981).
17. W. Dowhan, M. Bogdanov, *Annu. Rev. Biochem.* **78**, 515 (2009).
18. K. Xie, R. E. Dalbey, *Nat. Rev. Microbiol.* **6**, 234 (2008).
19. H. Yerushalmi, S. S. Mordoch, S. Schuldiner, *J. Biol. Chem.* **276**, 12744 (2001).

20. We thank Ann-Louise Johansson for technical assistance. This work was supported by grants to G.v.H. from the European Research Council (ERC-2008-AdG 232648), the Swedish Cancer Foundation, the Swedish Research Council, and the Swedish Foundation for Strategic Research, to J.S.S. from the International Human Frontier Science Program Organization, and to P.L.G. from the European Communities (TranSys PITN-2008-215524).

Supporting Online Material

www.sciencemag.org/cgi/content/full/science.1188950/DC1
Materials and Methods
Figs. S1 and S2
References

1 March 2010; accepted 4 May 2010
Published online 27 May 2010;
10.1126/science.1188950
Include this information when citing this paper.

A Generalization of Hamilton's Rule for the Evolution of Microbial Cooperation

jeff smith,*† J. David Van Dyken, Peter C. Zee

Hamilton's rule states that cooperation will evolve if the fitness cost to actors is less than the benefit to recipients multiplied by their genetic relatedness. This rule makes many simplifying assumptions, however, and does not accurately describe social evolution in organisms such as microbes where selection is both strong and nonadditive. We derived a generalization of Hamilton's rule and measured its parameters in *Myxococcus xanthus* bacteria. Nonadditivity made cooperative sporulation remarkably resistant to exploitation by cheater strains. Selection was driven by higher-order moments of population structure, not relatedness. These results provide an empirically testable cooperation principle applicable to both microbes and multicellular organisms and show how nonlinear interactions among cells insulate bacteria against cheaters.

Social evolution has illuminated many different areas of biology, from altruistic behavior in insects to sex ratios, selfish genetic elements, and multicellularity (*1*, *2*). The central puzzle in this field is how cooperation—increasing the fitness of other individuals—persists when cheaters can benefit without paying the cost of cooperating. The most prominent explanation for the evolution of cooperation is kin selection, in which benefits preferentially

go to individuals who share cooperation alleles (*3*, *4*). The centerpiece of kin selection theory is Hamilton's rule (*3*, *5*, *6*). It states that cooperation will evolve if $rb - c > 0$, where b is the benefit of cooperation; c is the cost of cooperation; and r is the genetic relatedness of actors to recipients (Fig. 1A). Kin selection relatedness is a statistical regression coefficient describing the similarity of actors and recipients at relevant cooperation loci and is not necessarily equal to whole-genome similarity (*5*–*7*).

Hamilton's rule is an elegant evolutionary principle, but it encounters problems when selection is strong and fitness effects are nonadditive (*5*, *8*). Nonadditivity occurs whenever fitness is a nonlinear function of social environment (Fig. 1B) or when different genotypes have different slopes (Fig. 1C). Under these circumstances, b and c are functions of r (*9*). This confounds fitness effects with population structure, obscures the biological causes of selection, and limits the usefulness of Hamilton's rule as an interpretive tool (fig. S1). It also makes it difficult to test kin selection with Hamilton's rule, because costs and benefits cannot be extrapolated to other population structures. Social evolution needs theory that makes testable predictions for specific systems (*10*, *11*).

These problems are especially pronounced for cooperation among microbes. Microbial traits as diverse as quorum sensing, biofilms, development, metabolism, mutualism, and virulence are social and vulnerable to cheating (*11*–*18*). Many systems show strong frequency-dependent selection, one form of nonadditivity (*12*, *14*, *16*–*18*). So far, social evolution theory has mostly been a qualitative, heuristic guide to interpretation. Models are seldom compared with data, and attempts to measure Hamilton's rule are rare [but see (*19*, *20*)]. Even though microbes have been singled out as important tests of social evolution theory (*11*), it is still unclear how much relatedness is required to prevent cheaters from spreading, whether relatedness in natural populations is sufficient, and whether kin selection acts differently in microbes and in animals.

To bridge the gap between theory and data, we derived a generalization of Hamilton's rule that does not assume additivity or weak selection and whose parameters are empirically measurable (*21*). We found that cooperators increase in frequency if

$$\mathbf{r} \cdot \mathbf{b} - c + \mathbf{m} \cdot \mathbf{d} > 0 \qquad (1)$$

Distributions can be described by their moments: parameters that measure their shape and location. The relatedness vector $\mathbf{r} = \{r_1, r_2, ...\}$ measures how the distributions of social environments encountered by cooperators and noncooperators differ in each of these moments (fig. S2). r_1 is equivalent to r in Hamilton's rule (*5*). The other terms are higher-order relatedness coefficients (*22*, *23*). Any smooth function can be expanded into a Taylor polynomial series whose coefficients measure its linear, quadratic, and higher-order components. The benefit vector $\mathbf{b}$ describes noncooperator fitness as a function of social environment (red lines in Fig. 1) in terms of its Taylor coefficients. c is the cost of cooperation when all neighbors are noncooperators. $\mathbf{m} \cdot \mathbf{d}$ is nonzero when benefits depend on recipient genotype (Fig. 1C). $\mathbf{m}$ is the moments vector for cooperators. $\mathbf{d}$ is the difference between the Taylor series of cooperators and noncooperators. Unlike Hamilton's rule, Eq. (1) disentangles fitness effects from population structure and is valid for arbitrarily complex forms of social selection. When fitness effects are additive, Eq. (1) reduces to $rb - c > 0$.

Department of Biology, Indiana University, Bloomington, IN 47405, USA.

*Present address: Department of Ecology and Evolutionary Biology, Rice University, Houston, TX 77005, USA.
†To whom correspondence should be addressed. E-mail: smith74@indiana.edu

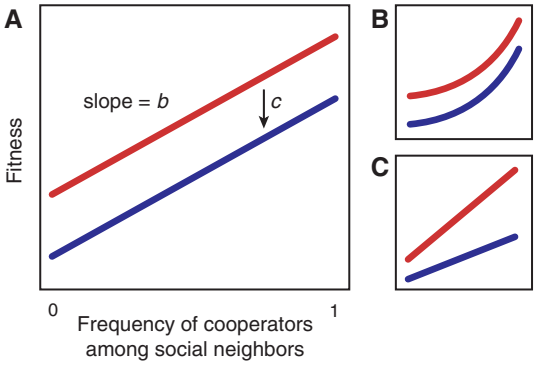

Fig. 1. Measuring the costs and benefits of cooperation in microbes. Blue, cooperator fitness; red, noncooperator fitness. (**A**) In Hamilton's rule, b is the slope of fitness against the frequency of cooperators among social neighbors; c is the fitness difference between cooperators and noncooperators for a given social environment. Fitness effects are nonadditive when benefits are (**B**) nonlinear or (**C**) depend on recipient genotype.

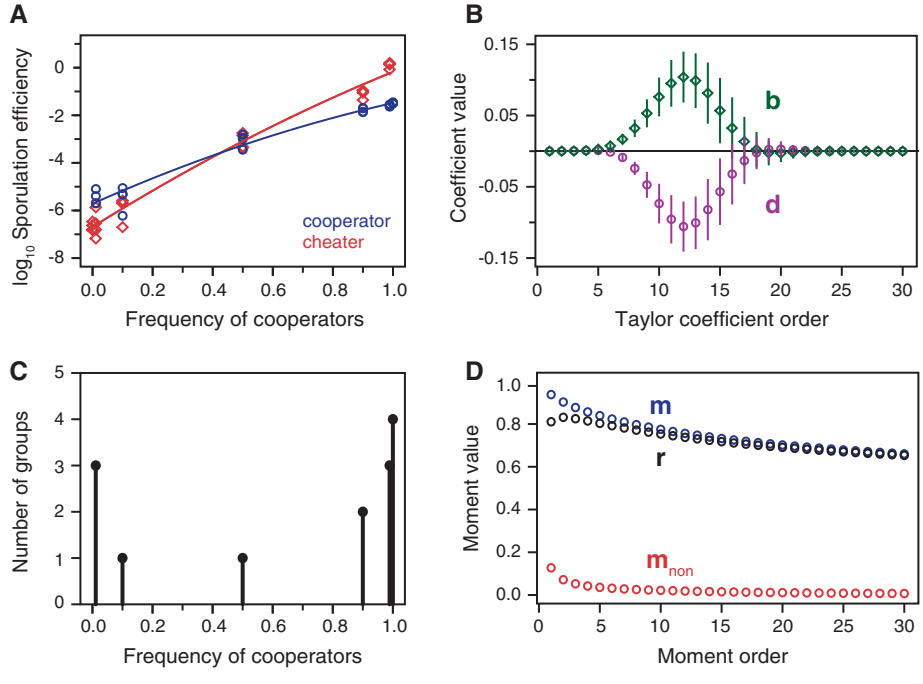

Fig. 2. Parameters of the generalized Hamilton's rule measured in an experimental population of sporulating *Myxococcus* bacteria. (**A**) Absolute fitness of a cooperator strain (blue circles) and a cheater strain (red diamonds) as a function of their frequency within groups. Data points are independent experimental replicates; lines, regression model fit to data. (**B**) Fitness terms in Eq. (1), calculated from the data shown in (A). Green diamonds, benefit vector **b**; purple circles, genotype-dependence vector **d**. Points show best-fit model (±SD from bootstrapped data). (**C**) Initial distribution of cooperators among groups for a specific experimental population. (**D**) Social structure terms in Eq. (1) were calculated for the population shown in (C). Blue, cooperator moments **m**; red, noncooperator moments $\mathbf{m}_{non}$; black, relatedness vector **r**.

We applied our generalized rule to data from experimental populations of *Myxococcus xanthus* bacteria. When starved of amino acids, *M. xanthus* cells aggregate and form fruiting bodies in which a small fraction of cells become stress-resistant spores; the rest die (*24*). Some cheater strains sporulate superefficiently among cooperators but do poorly on their own (*14*). We mixed a cooperator strain and a cheater strain at different frequencies, let them develop, and measured their abundance among surviving spores. Fitness effects were strongly nonadditive (Fig. 2A). Cooperators increased the fitness of both genotypes [$F_{(1,43)} = 1872.92$, $P < 0.0001$; $n = 48$], but the effect was strongly nonlinear [slightly less than exponential; $F_{(1,43)} = 15.69$, $P < 0.001$]. Cheaters benefited more than cooperators [$F_{(1,43)} = 81.87$, $P < 0.0001$]. Cooperators were more fit than cheaters at low frequencies [$F_{(1,43)} = 51.54$, $P < 0.0001$] but less fit at high frequencies. Cooperating was therefore altruistic when locally common but mutually beneficial when rare (*25*).

We calculated **b** and **d** in Eq. (1) from the Taylor series of the fitted statistical model and found that their linear, additive components were very small (Fig. 2B). The largest terms were order 10 to 15. This is caused by the steepness of the curves in Fig. 2A and means that fitness was disproportionately determined by groups with high frequencies of cooperators. The genotype of individual neighbors mattered less than the genotype of several neighbors collectively. Under such circumstances, the most important components of population structure are the corresponding higher-order moments—not first-order relatedness. c was -1.73 ± 0.02 (SEM) $\times 10^{-6}$. A negative cost indicated that cooperation provided a direct fitness benefit when most neighbors were noncooperators. This was a minor component of fitness, however. Large negative values of **d** indicated that cheaters mainly gain advantage by benefiting from cooperative groups more than cooperators do.

We calculated **r** and **m** for an experimental population where most groups contained both genotypes, but with a strong skew toward one or the other (Fig. 2C). The components of these vectors varied less than those of **b** and **d** (Fig. 2D). Kin selection relatedness was $r_1 \approx 0.8$. Putting it all together, the predicted inclusive fitness effect of cooperation was $\mathbf{r} \bullet \mathbf{b} - c + \mathbf{m} \bullet \mathbf{d} = 0.014$ spores per cell [95% confidence interval (CI) 0.004 to 0.021], which did not significantly differ from the observed value of 0.0135. A positive inclusive fitness effect indicated that, in this population, kin selection favored cooperation.

To better understand kin selection in this system, we calculated the inclusive fitness effect for populations with different global cooperator frequencies and rates of migration between groups. We found that cooperative development in *M. xanthus* is markedly resilient to cheating. In the conventional island model of population structure (*26*), cheaters could invade populations of cooperators only if migration was high enough that $r_1 < 0.6$ (Fig. 3A). Considering the large fitness advantage cheaters often had within groups, this is a remarkably low relatedness threshold. Reexamining Fig. 3A gives an intuitive explanation for this result. Compared with cooperators in all-cooperator groups, cheaters had a net advantage only in groups with >70% cooperators. Population structure limits the abundance of groups in this narrow range of frequencies (fig. S2). The specific form nonadditivity takes is crucial. Increasing returns from cooperation limit the ability of cheaters to invade, whereas decreasing returns make it easier (fig. S3). When population structure was very low, direct fitness benefits allowed cooperators to escape being displaced by cheaters. Instead, both genotypes coexisted in a balanced polymorphism (Fig. 3A). Population structure reduced the equilibrium frequency of cheaters and their effect on population mean fitness ("cheater load") (Fig. 3B). Selection was frequency dependent because the higher-order components of population structure that dominate selection were also frequency dependent (fig. S4). Hamilton's rule, however, misleadingly placed the cause of frequency dependence in its fitness terms b and c instead of its population structure term r (fig. S4).

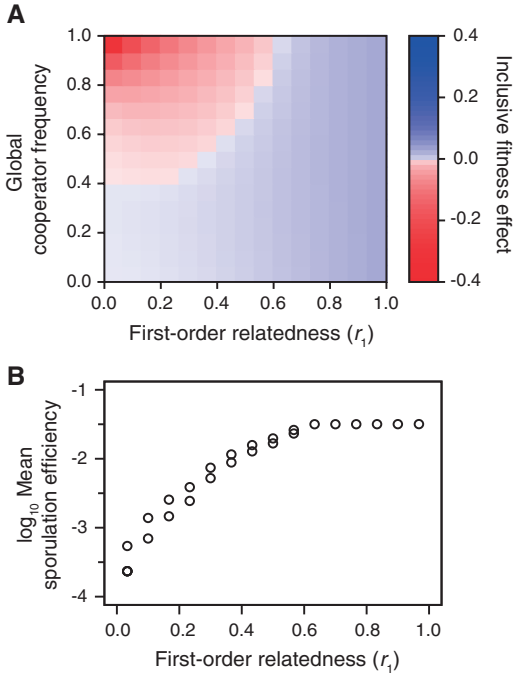

Fig. 3. *M. xanthus* development is resilient to cheating. (**A**) Conditions under which kin selection favors cooperation. Blue signifies conditions in which cooperators have higher mean fitness than cheaters; red, cheaters have higher mean fitness. In an island model of population structure, cheaters invade only when migration between groups is large enough that first-order relatedness is <0.6. When cheaters can invade, they reach an equilibrium frequency where cooperators remain at least 40% of the population. We report population structure in terms of first-order relatedness instead of migration rate to aid comparison with other systems. (**B**) Cheater load. Points show population mean fitness near the selective equilibrium for a given level of population structure.

Our generalization of Hamilton's rule provides a kin selection principle that is valid for systems with strong nonadditive fitness effects. It shows why higher-order moments of population structure appear in models of social evolution (*23*, *27*), shows when they are important, and provides a general method for handling them. Because Eq. (1) refers only to fitness and genotype frequencies, it is independent of many system-specific details and can be applied to cooperation at all levels of biological organization—not just microbes. It also lets social evolution theory be more than a heuristic guide to interpretation. Because all the terms in Eq. (1) are empirically measurable, it is both a quantitative analytical tool and a testable hypothesis. The inclusive fitness effect ($\mathbf{r} \bullet \mathbf{b} - c + \mathbf{m} \bullet \mathbf{d}$) is a quantitative measure of selection that one can use to compare different hypothetical mechanisms for the evolution of cooperation. One could, for example, evaluate the relative importance of population structure and infectious transfer of cooperation genes (*28*) by comparing the amount of allele frequency change due to kin selection or gene transfer. The inclusive fitness effect also shows when "Trojan horse" strategies for controlling microbial infections with human-introduced cheaters (*29*) are likely to be successful.

Strong nonadditivity plays an important role in microbial cooperation. It causes these systems to deviate from the traditional scheme where social interactions are classified as altruistic, mutually beneficial, selfish, or spiteful (*24*, *25*). Frequency-dependent selection within groups can create situations where cooperation is altruistic at some frequencies but mutually beneficial at others (Fig. 2A). With nonadditivity, the r in Hamilton's rule can also be a relatively unimportant component of population structure. In our *M. xanthus* system, selection is primarily determined by higher-order terms that measure the abundance of groups with high frequencies of cooperators. Finally, strong population structure is not always needed to prevent the spread of strong cheaters. The cheater strain we examined has a hundred-fold fitness advantage within groups when it is rare, and it massively reduces

group fitness when it is common. Nevertheless, increasing-returns nonadditivity allows cooperation to evolve at levels of population structure comparable to that seen among social insect colonies (*30*). Cheaters have a rare advantage in several systems (*12*, *16*–*18*) and may be a common property of microbial cooperation.

References and Notes

1. J. Maynard Smith, E. Szathmary, *The Major Transitions in Evolution* (Oxford Univ. Press, New York, 1995).
2. L. Keller, Ed., *Levels of Selection in Evolution* (Princeton Univ. Press, Princeton, NJ, 1999).
3. W. D. Hamilton, *J. Theor. Biol.* **7**, 1 (1964).
4. A. S. Griffin, S. A. West, *Trends Ecol. Evol.* **17**, 15 (2002).
5. D. C. Queller, *Evolution* **46**, 376 (1992).
6. P. D. Taylor, S. A. Frank, *J. Theor. Biol.* **180**, 27 (1996).
7. A. Grafen, *Oxf. Surv. Evol. Biol.* **2**, 28 (1985).
8. T. Wenseleers, *J. Evol. Biol.* **19**, 1419, discussion 1426 (2006).
9. A. Gardner, S. A. West, N. H. Barton, *Am. Nat.* **169**, 207 (2007).
10. O. Leimar, P. Hammerstein, *J. Evol. Biol.* **19**, 1403, discussion 1426 (2006).
11. S. A. West, S. P. Diggle, A. Buckling, A. Gardner, A. S. Griffin, *Annu. Rev. Ecol. Evol. Syst.* **38**, 53 (2007).
12. P. E. Turner, L. Chao, *Nature* **398**, 441 (1999).
13. J. E. Strassmann, Y. Zhu, D. C. Queller, *Nature* **408**, 965 (2000).
14. G. J. Velicer, L. Kroos, R. E. Lenski, *Nature* **404**, 598 (2000).
15. P. B. Rainey, K. Rainey, *Nature* **425**, 72 (2003).
16. R. C. MacLean, I. Gudelj, *Nature* **441**, 498 (2006).
17. S. P. Diggle, A. S. Griffin, G. S. Campbell, S. A. West, *Nature* **450**, 411 (2007).
18. A. Ross-Gillespie, A. Gardner, S. A. West, A. S. Griffin, *Am. Nat.* **170**, 331 (2007).
19. O. M. Gilbert, K. R. Foster, N. J. Mehdiabadi, J. E. Strassmann, D. C. Queller, *Proc. Natl. Acad. Sci. U.S.A.* **104**, 8913 (2007).
20. R. Kümmerli, P. van den Berg, A. S. Griffin, S. A. West, A. Gardner, *J. Evol. Biol.* **23**, 699 (2010).
21. Materials and methods are available as supporting material on *Science* Online.
22. Moments of allele frequency distributions can also be expressed in terms of probabilities of identity by descent (IBD). For example, the second and third moments are proportional to the probabilities that two or three (respectively) randomly sampled alleles within a group are IBD (23).
23. M. C. Whitlock, *Genetics* **160**, 1191 (2002).
24. G. J. Velicer, M. Vos, *Annu. Rev. Microbiol.* **63**, 599 (2009).
25. S. A. West, A. S. Griffin, A. Gardner, S. P. Diggle, *Nat. Rev. Microbiol.* **4**, 597 (2006).
26. S. Wright, *Genetics* **16**, 97 (1931).
27. P. Godfrey-Smith, B. Kerr, *Am. Nat.* **174**, 906 (2009).
28. J. Smith, *Proc. Biol. Sci.* **268**, 61 (2001).
29. S. P. Brown, S. A. West, S. P. Diggle, A. S. Griffin, *Philos. Trans. R. Soc. London B Biol. Sci.* **364**, 3157 (2009).
30. R. H. Crozier, P. Pamillo, *Evolution of Social Insect Colonies* (Oxford Univ. Press, Oxford, 1996).

31. We thank G. Velicer for funding and laboratory support through NIH grant GM07690 and S. Alizon, W. Castle, D. Queller, and W. Ratcliff for discussion and comments on the manuscript. J.D.V.D. was supported by NIH grant R01GM084238 to M.J. Wade. P.C.Z. was supported by the Genetics, Cellular and Molecular Sciences Training Grant (T32GM007757). All authors conceived the project, discussed the results, and commented on the paper. j.s. and D.V.D. designed the theoretical approach. j.s. did the math, designed and performed the experiments, and wrote the paper. j.s. and P.C.Z. analyzed the data.

Supporting Online Material

www.sciencemag.org/cgi/content/full/328/5986/1700/DC1
Materials and Methods
Figs. S1 to S4
References

16 March 2010; accepted 18 May 2010
10.1126/science.1189675

c-di-AMP Secreted by Intracellular *Listeria monocytogenes* Activates a Host Type I Interferon Response

Joshua J. Woodward,[1] Anthony T. Iavarone,[2] Daniel A. Portnoy[1,3]*

Intracellular bacterial pathogens, such as *Listeria monocytogenes*, are detected in the cytosol of host immune cells. Induction of this host response is often dependent on microbial secretion systems and, in *L. monocytogenes*, is dependent on multidrug efflux pumps (MDRs). Using *L. monocytogenes* mutants that overexpressed MDRs, we identified cyclic diadenosine monophosphate (c-di-AMP) as a secreted molecule able to trigger the cytosolic host response. Overexpression of the di-adenylate cyclase, *dacA* (*lmo2120*), resulted in elevated levels of the host response during infection. c-di-AMP thus represents a putative bacterial secondary signaling molecule that triggers a cytosolic pathway of innate immunity and is predicted to be present in a wide variety of bacteria and archea.

The mammalian innate immune system is composed of receptors that collectively serve as a pathogen sensor to monitor the extracellular, vacuolar, and cytosolic cellular compartments (*1*). Recognition of microbes within these distinct compartments leads to cellular responses that are commensurate with the microbial threat. Although both pathogenic and nonpathogenic microbes interact with extracellular and vacuolar compartments, infectious disease agents often mediate their pathogenesis by directly entering the cytosol or through delivery of virulence factors into the host cell cytosolic compartment. Thus, the innate immune system may distinguish between pathogenic and nonpathogenic microbes by monitoring the cytosol (*2*, *3*).

Several distinct pathways of innate immunity are present in the host cell cytosol. One, termed the cytosolic surveillance pathway (CSP), detects bacterial, viral, and protozoan pathogens, leading to the activation of interferon regulatory factor 3 (IRF3) and nuclear factor kappa–light-chain-enhancer of activated B cells (NF-κB), resulting in the induction of interferon-β (IFN-β) and co-regulated genes (*4*). Some ligands that activate this pathway are known, for example, viral and bacterial nucleic acids (*5*). However, the ligands and host receptors that lead to IFN-β production after exposure to nonviral microbes—including *L. monocytogenes*, *M. tuberculosis*, *F. tularensis*, *L. pneumophila*, *B. abortis*, and *T. cruzi*—remain unknown (*4*–*9*).

Expression of *L. monocytogenes* multidrug efflux pumps (MDRs) of the major facilitator superfamily controls the capacity of cytosolic bacteria to induce host expression of IFN-β (*10*). Ectopic expression of multiple MDRs enhances IFN-β production, while one, MdrM, controls the majority of the response to wild-type bacteria (*10*). Given that MDRs transport small molecules (<1000 daltons), we hypothesized that *L. monocytogenes* secretes a bioactive small molecule that is recognized within the host cell cytosol. To identify the bioactive ligand(s) secreted by *L. monocytogenes* MDRs, we performed solid phase extraction (SPE) of the culture supernatant from an MdrM overexpressing *L. monocytogenes* strain (*marR*-, DP-L5445) that exhibits an IFN-β hyperactivating phenotype (*11*). Delivery of the fraction to the macrophage cytosol using reversible digitonin permeabilization (*12*) resulted in a dose-dependent increase in type-I IFN (Fig. 1A). Addition of this fraction in the absence of digitonin resulted in no IFN production, consistent with cytosolic detection of the active ligand.

In *L. monocytogenes* strains that exhibit variable levels of MDR expression, IFN-β production correlates with increases in transporter levels (*10*). Supernatants from four *L. monocytogenes* strains—*mdrM*-, WT, *marR*-, and *tetR*::*Tn917*, each with increasing levels of MDR expression—were tested for activity. Comparable to infection assays, MDR expression correlated with IFN-inducing activity of the culture supernatants (Fig. 1B). The *tetR*::*Tn917* strain exhibited high-

[1]Department of Molecular and Cellular Biology, University of California, Berkeley, CA 94720, USA. [2]QB3/Chemistry Mass Spectrometry Facility, University of California, Berkeley, CA 94720, USA. [3]School of Public Health, University of California, Berkeley, CA 94720, USA.

*To whom correspondence should be addressed. E-mail: portnoy@berkeley.edu

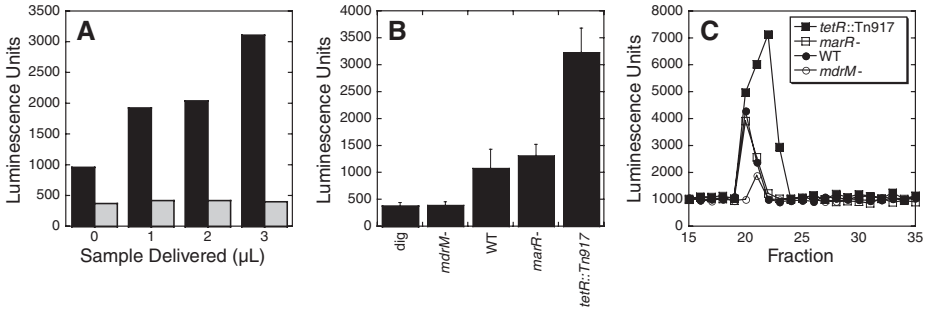

Fig. 1. Characterization and isolation of *L. monocytogenes* secreted IFN-β stimulatory ligand. (**A**) IFN-β production by BMDMs in response to solid phase extracts (SPE) of *marR-* *L. monocytogenes* supernatants in the presence (black bars) and absence (gray bars) of digitonin. IFN-β activity was measured using interferon-stimulated response element (ISRE) L929 cells that generate luciferase in response to type-I IFN stimulation. Data are mean of biological replicates (N = 2). (**B**) IFN-β activity by BMDMs in response to solid-phase extracts of sterile filtered culture supernatants from *mdrM-*, wild-type (WT), *marR-*, and *tetR*::*Tn*917 strains of *L. monocytogenes*. Negative control consists of digitonin permeabilizing solution alone (dig). Data are mean ± SD (N = 2). Data representative of two independent experiments. (**C**) IFN-β stimulatory activity of culture supernatants fractionated using reversed-phase HPLC. Activity measured as in (A). Data are the mean activity of biological replicates (N = 2).

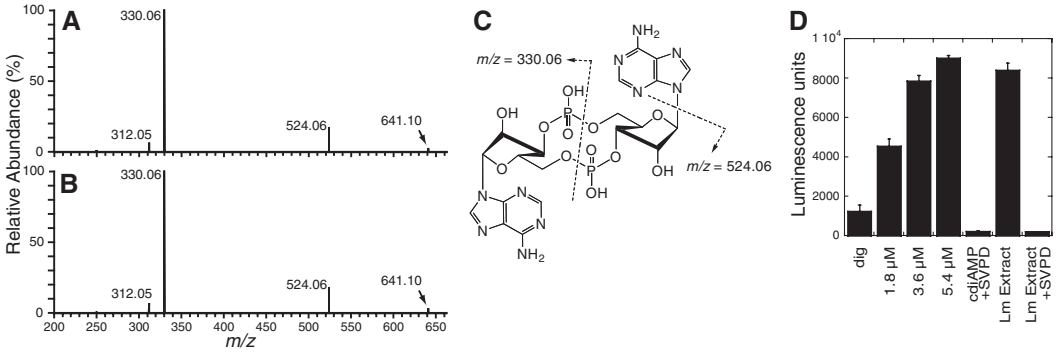

Fig. 2. Cyclic di-AMP is an IFN-β activating ligand. (**A**) Tandem mass spectrum resulting from collisionally activated dissociation of the singly charged positive ion at m/z = 659.11 formed from an active fraction of *Listeria monocytogenes*. (**B**) Tandem mass spectrum of commercially obtained sample of c-di-AMP (BioLog Life Sciences Institute, Denmark). Fragmentation pathways of c-di-AMP are shown in (**C**). The fragment ions at m/z = 641.10 and 312.05 correspond to neutral losses of 18 daltons from the precursor ion (m/z = 659.11) and from the fragment ion at m/z = 330.06, respectively, and are consistent with neutral loss of water molecules from these respective ions. (**D**) Commercial c-di-AMP standard was added to BMDMs in increasing amount. IFN-β production by BMDMs was detected using the type I IFN reporter cell line (ISRE L929). Commercial c-di-AMP standard and the active *L. monocytogenes* fraction were treated with snake venom phosphodiesterase (SVPD). Data are mean of biological replicates ± SD (N = 2).

er activity than any other strain, whereas the *mdrM-* strain lacked detectable activity above background.

Fractionation of the active samples obtained from each MDR strain was performed using reversed-phase high-performance liquid chromatography (RP-HPLC). The active component of each supernatant eluted as a single peak from the column with similar retention time (Fig. 1C), consistent with each containing the same active ligand. Furthermore, the magnitude of the active peak correlated with MDR expression. The sample with the highest activity exhibited a significant absorbance at 260 nm (fig. S1A). Incubation with anion but not cation exchange resin removed the active molecule from solution (fig. S1B), and treatment of the active sample was resistant to DNAse (fig. S1C). These observations were consistent with a non-DNA nucleic acid as the active component.

To identify the IFN-β–inducing metabolite contained in the fractions, samples were analyzed by high-resolution mass spectrometry. A single ion (m/z = 659.11, z = 1) was identified as exclusively present in the active fractions and absent in the inactive samples (fig. S2A). The parent ion mass was consistent with cyclic di-adenosine monophosphate (c-di-AMP) (fig. S2B). Collision-induced dissociation was performed to further characterize the identified ion (Fig. 2A). Quantification of c-di-AMP in each sample showed that mdrM-, WT, and *marR-* strains had 23%, 34%, and 35% as much c-di-AMP in the culture supernatants relative to *tetR*::*Tn*917 (53 nM). Thus, IFN-β–inducing activity of *L. monocytogenes* supernatants correlates linearly with c-di-AMP concentration (fig. S3).

Next, we tested the ability of commercially available c-di-AMP to induce IFN-β in macrophages. c-di-AMP exhibited a dose-dependent response when delivered to the cytosol of murine bone marrow–derived macrophages (BMDMs) (Fig. 2D). Treatment of the purified active fraction and the commercial standard with snake venom phosphodiesterase (SVPD) abolished the activity of each sample. The host pathway responsible for cytosolic detection of *L. monocytogenes* is dependent on IRF3 and independent of MyD88/Trif and mitochondrial antiviral signaling protein (MAVS) (*10*). Detection of c-di-AMP is MyD88/Trif and MAVS independent but requires IRF3 (fig. S4). Thus, c-di-AMP requires a parallel host-signaling pathway to activate the CSP, consistent with c-di-AMP as the relevant ligand of *L. monocytogenes*.

Here, we report that the intracellular pathogen *L. monocytogenes* generates c-di-AMP, which induces the host cytosolic surveillance pathway. Di-adenylate cyclase (DAC) activity has been assigned to a domain of unknown function (previously DUF147) within the protein DisA of *B. subtilis* (*13*), and c-di-AMP is thought to act as a secondary signaling molecule that regulates bacterial sporulation (*14*). Bioinformatic analysis identified the widespread presence of the DAC domain in bacteria and archeae, including pathogenic *Staphylococci*, *Streptococci*, *Mycobacteria*, *Chlamydia*, and *Mycoplasma* spp. (*15*).

In *L. monocytogenes*, a single gene, *lmo2120*, contains a predicted DAC domain. This gene is present in an operon with the downstream gene *lmo2119*, a gene of unknown function (Fig. 3A). Attempts to delete the gene *lmo2120* using standard techniques were unsuccessful. Genetic screens identified genes containing DAC domains in *Streptococci* and two species of *Mycoplasma* as essential (*16*–*18*), supporting a similar indispensable role in *L. monocytogenes*. However, overexpression of *lmo2120* did not affect bacterial growth but led to increased CSP activation during macrophage infection (Fig. 3, B and C), consistent with DAC activity encoded by the *lmo2120* gene, which we have named here *dacA*.

MDRs are generally recognized to function in conferring resistance to small toxic molecules

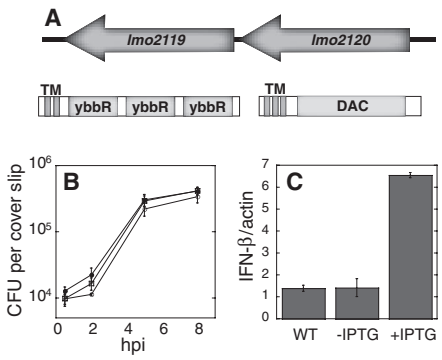

Fig. 3. The di-adenylate cyclase gene *dacA* (*lmo2120*) alters CSP activation during infection. (**A**) Predicted operon of genes *lmo2120*, renamed here *dacA*, and *lmo2119*. The gene product of *lmo2119* contains three ybbR domains of unknown function. The gene product of *lmo2120* contains a single di-adenylate cyclase (DAC) domain. Transmembrane-spanning segments (TM) predicted using Topcons (http://topcons.cbr.su.se/index.php). (**B**) Intracellular growth curves of WT *L. monocytogenes* (closed circles) and *L. monocytogenes* with an integration vector (pLIV2) containing isopropyl-β-D-thiogalactopyranoside (IPTG)–inducible *dacA* in the absence (open circles) and presence (open squares) of IPTG (1 mM) in BMDMs. Data are mean ± SD (N = 3). (**C**) Quantitative real-time reverse transcription polymerase chain reaction analysis of IFN-β induction by each strain in BMDMs. Data are mean ± SD (N = 2). Data representative of two independent experiments.

such as antibiotics by active efflux, preventing accumulation of lethal concentrations within the cell. A number of instances have described transport of small molecules that are not toxic (*19*–*21*), leading to the hypothesis that these transporters have evolved to transport specific natural substrates as well (*22*). Our observations suggested that these proteins play a broader biological role beyond general drug resistance, perhaps involved in bacterial signaling. Moreover, bacterial signaling nucleotides are generally considered to act within the cell. Here, we provided evidence that c-di-AMP is exported from the cell and thus may be involved in extracellular signaling by *L. monocytogenes*.

The ability of the host to discriminate between pathogen and nonpathogen is often mediated by the compartmentalized detection of microbial ligands. For instance, *L. monocytogenes* mutants that cannot escape the primary vacuole are avirulent and do not activate IRF3-dependent inflammation, whereas those that are virulent enter the cytosol, leading to type I interferon production. The results of this study showed that host cells detect and respond to cytosolic c-di-AMP, recapitulating the effects of cytosolic infection. These observations are consistent with reports in which host responses to bacterial peptidoglycan, c-di-GMP, and flagellin are dependent on cytosolic delivery (*23*–*27*). The conserved and critical role of bacterial cyclic di-nucleotides fulfills the criteria of ligands that alert the immune system to the presence of live pathogenic bacteria that engage the host cytosol.

References and Notes

1. K. J. Ishii, S. Koyama, A. Nakagawa, C. Coban, S. Akira, *Cell Host Microbe* **3**, 352 (2008).
2. R. E. Vance, R. R. Isberg, D. A. Portnoy, *Cell Host Microbe* **6**, 10 (2009).
3. M. Lamkanfi, V. M. Dixit, *Immunol. Rev.* **227**, 95 (2009).
4. M. O'Riordan, C. H. Yi, R. Gonzales, K. D. Lee, D. A. Portnoy, *Proc. Natl. Acad. Sci. U.S.A.* **99**, 13861 (2002).
5. D. B. Stetson, R. Medzhitov, *Immunity* **24**, 93 (2006).
6. T. Henry, A. Brotcke, D. S. Weiss, L. J. Thompson, D. M. Monack, *J. Exp. Med.* **204**, 987 (2007).
7. C. M. Roux *et al.*, *Cell. Microbiol.* **9**, 1851 (2007).
8. S. A. Stanley, J. E. Johndrow, P. Manzanillo, J. S. Cox, *J. Immunol.* **178**, 3143 (2007).
9. S. Vaena de Avalos, I. J. Blader, M. Fisher, J. C. Boothroyd, B. A. Burleigh, *J. Biol. Chem.* **277**, 639 (2002).
10. G. T. Crimmins *et al.*, *Proc. Natl. Acad. Sci. U.S.A.* **105**, 10191 (2008).
11. Materials and methods are available as supporting material on *Science* Online.
12. S. E. Girardin *et al.*, *Science* **300**, 1584 (2003).
13. G. Witte, S. Hartung, K. Büttner, K. P. Hopfner, *Mol. Cell* **30**, 167 (2008).
14. M. Bejerano-Sagie *et al.*, *Cell* **125**, 679 (2006).
15. U. Römling, *Sci. Signal.* **1**, pe39 (2008).
16. C. T. French *et al.*, *Mol. Microbiol.* **69**, 67 (2008).
17. J. H. Song *et al.*, *Mol. Cells* **19**, 365 (2005).
18. J. I. Glass *et al.*, *Proc. Natl. Acad. Sci. U.S.A.* **103**, 425 (2006).
19. D. P. Woolridge *et al.*, *J. Biol. Chem.* **272**, 8864 (1997).
20. A. van Helvoort *et al.*, *Cell* **87**, 507 (1996).
21. S. Yang, C. R. Lopez, E. L. Zechiedrich, *Proc. Natl. Acad. Sci. U.S.A.* **103**, 2386 (2006).
22. A. A. Neyfakh, *Trends Microbiol.* **5**, 309 (1997).
23. J. Viala *et al.*, *Nat. Immunol.* **5**, 1166 (2004).
24. Y. H. Sun, H. G. Rolán, R. M. Tsolis, *J. Biol. Chem.* **282**, 33897 (2007).
25. A. B. Molofsky *et al.*, *J. Exp. Med.* **203**, 1093 (2006).
26. T. Ren, D. S. Zamboni, C. R. Roy, W. F. Dietrich, R. E. Vance, *PLoS Pathog.* **2**, e18 (2006).
27. S. M. McWhirter *et al.*, *J. Exp. Med.* **206**, 1899 (2009).

28. We would like to thank K. Monroe and R. Vance for MAVS$^{-/-}$ BMDMs and Portnoy laboratory members J. D. Sauer and C. Rae for BMDMs. This work was supported by NIH grant P01 AI063302 (D.A.P.) and NIH training grant T32 CA 009179 (J.J.W.). D. A. Portnoy has a consulting relationship with and a financial interest in Aduro BioTech, which stands to benefit from commercialization of the results of this research. A patent covering the use of *Listeria monocytogenes* strains that express enhanced or diminished levels of c-di-AMP for use as vaccine vectors has been applied for.

Supporting Online Material

www.sciencemag.org/cgi/content/full/science.1189801/DC1
Materials and Methods
Figs. S1 to S4
References

18 March 2010; accepted 4 May 2010
Published online 27 May 2010;
10.1126/science.1189801
Include this information when citing this paper.

Reversible Microbial Colonization of Germ-Free Mice Reveals the Dynamics of IgA Immune Responses

Siegfried Hapfelmeier,[1,2]* Melissa A. E. Lawson,[2] Emma Slack,[1,2] Jorum K. Kirundi,[1,2] Maaike Stoel,[2] Mathias Heikenwalder,[3] Julia Cahenzli,[2] Yuliya Velykoredko,[2] Maria L. Balmer,[1] Kathrin Endt,[4] Markus B. Geuking,[2] Roy Curtiss 3rd,[5] Kathy D. McCoy,[2] Andrew J. Macpherson[1,2]*

The lower intestine of adult mammals is densely colonized with nonpathogenic (commensal) microbes. Gut bacteria induce protective immune responses, which ensure host-microbial mutualism. The continuous presence of commensal intestinal bacteria has made it difficult to study mucosal immune dynamics. Here, we report a reversible germ-free colonization system in mice that is independent of diet or antibiotic manipulation. A slow (more than 14 days) onset of a long-lived (half-life over 16 weeks), highly specific anticommensal immunoglobulin A (IgA) response in germ-free mice was observed. Ongoing commensal exposure in colonized mice rapidly abrogated this response. Sequential doses lacked a classical prime-boost effect seen in systemic vaccination, but specific IgA induction occurred as a stepwise response to current bacterial exposure, such that the antibody repertoire matched the existing commensal content.

Immunoglobulin (Ig) A is the dominant antibody produced in mammals, mostly secreted across mucous membranes, especially in the intestine. Intestinal dendritic cells (DCs) sample small numbers of commensal bacteria at the mucosal surface and induce IgA-producing B cells through T cell–dependent and –independent mechanisms (*1*–*3*). It has long been known that the IgA responses in the intestine are strongly induced by colonization of germ-free animals with commensal bacteria. The kinetics and longevity of these responses are unknown, however, because it has not been possible to uncouple IgA induction from constant bacterial exposure.

We developed a reversible in vivo germ-free colonization system by studying the persistence of auxotrophic *E. coli* K-12 mutants with a requirement for essential nutrients that could not be satisfied by any mammalian host metabolites (fig. S1A). Initial experiments in which germ-free mice were gavaged with an *asd* deletion mutant deficient in meso-diaminopimelic acid (*m*-DAP) biosynthesis (*4*) resulted in persistent intestinal colonization of some of the mice with high numbers of this strain, which could be recovered from feces and cecal contents and grown without *m*-DAP supplementation. The recovered bacteria displayed gross changes in colony morphology (fig. S1B). We reasoned that, under the strong selective pressure in the intestine, compensatory mutants became selected that were able to modify their peptidoglycan crosslink structure of the cell wall. To prevent this, we introduced two further auxotrophic deletions (*alr*, alanine racemase-1, and *dadX*, alanine racemase-2) to abrogate biosynthesis of the D isomer of alanine (D-Ala), which is required in the peptidoglycan crosslink but is not a mammalian host metabolite (fig. S1, A and C). This triple mutant (strain HA107) showed initial intestinal colonization identical to the wild-type parental strain, JM83, but the numbers of fecal live bacteria decreased 12 to 48 hours after gavage (Fig. 1, A and B). Even after six successive doses of 10^{10} colony-forming units (CFU) of HA107, the mice all became germ-free again by 72 hours after the last dose (Fig. 1C), which demonstrated the tight control of this reversible germ-free colonization system.

We investigated whether *E. coli* HA107, which cannot divide and persist in vivo, could induce mucosal immune responses of a magnitude similar to irreversible microbial colonization. We observed an equivalent increase in numbers of intestinal IgA plasma cells throughout the intestine in germ-free mice 4 weeks after either six treatments with 10^{10} live *E. coli* HA107 or colonization with an altered Schaedler flora (ASF) (Fig. 1, D to F, and fig. S2). We concluded that reversible germ-free colonization where animals have returned to germ-free status induces IgA immune responses that are similar to those seen with irreversible colonization. Commensal bacterial stimulation can therefore be uncoupled from the mucosal immune response in vivo.

Our reversible colonization system has a number of advantages as a way to study specific IgA induction. First, the dose of bacteria was defined, and immune induction had a finite duration. Secondly, live bacteria were used in the system. Thirdly, the problems of microbiota complexity or possible bacterial overgrowth and systemic penetration during monocolonization (*5*) were avoided.

We investigated the specificity of the IgA response induced by *E. coli* HA107 as com-

[1]DKF (Maurice Müller Laboratories), MEM, Universitätsklinik für Viszerale Chirurgie und Medizin (UVCM), University of Bern, 3013 Bern, Switzerland. [2]Farncombe Family Digestive Health Research Institute, McMaster University, Hamilton, ON L8N 3Z5, Canada. [3]Department of Pathology, University Hospital Zurich, 8091 Zurich, Switzerland. [4]Institute of Microbiology, Federal Institute of Technology, 8093 Zurich, Switzerland. [5]Center for Infectious Diseases and Vaccinology, The Biodesign Institute, Arizona State University, Tempe, AZ 85287, USA.

*To whom correspondence should be addressed. E-mail: andrew.macpherson@insel.ch (A.J.M.); hapfelmeier@gmail.com (S.H.)

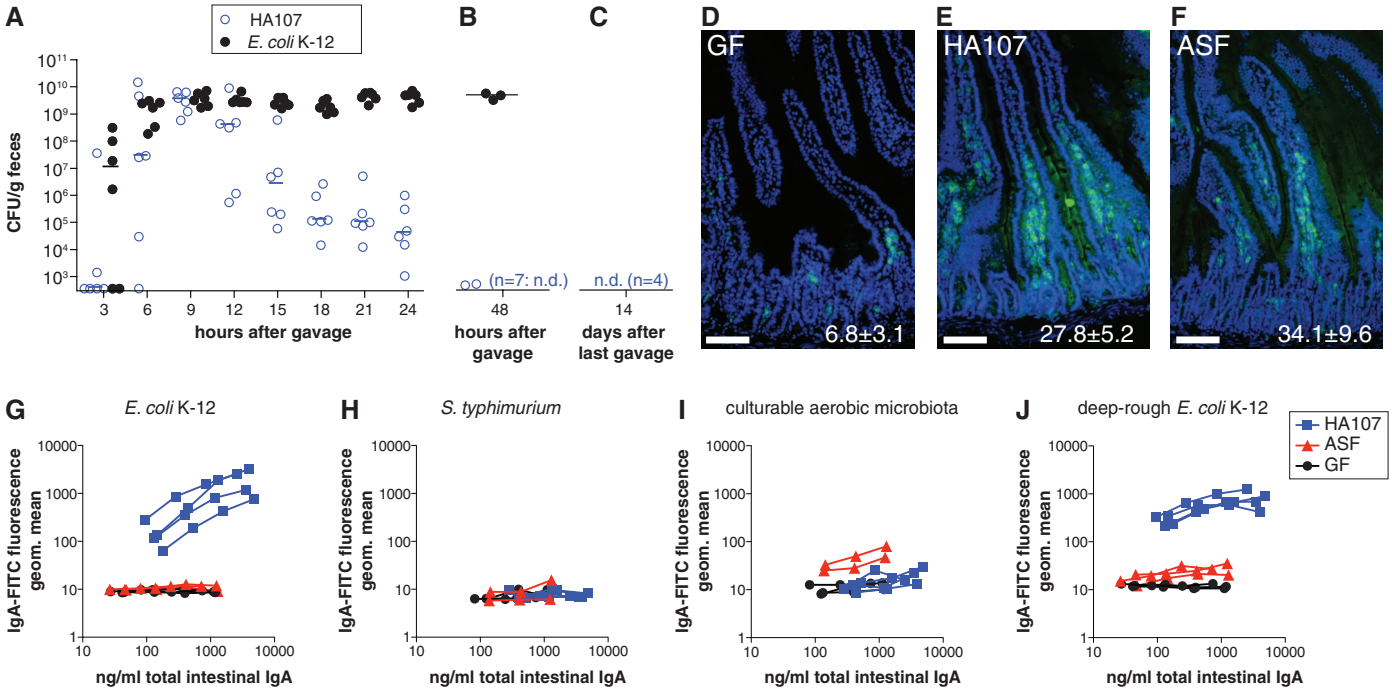

Fig. 1. Reversible *E. coli* HA107 colonization induces specific mucosal IgA. (**A**) Germ-free Swiss-Webster mice were analyzed for fecal shedding of live *E. coli* by bacterial plating and enrichment culture in *m*-DAP– and D-Ala–supplemented media of fecal material at indicated times after gavage of 10^{10} CFU of HA107 (n = 6) or wild-type parent strain JM83 (*E. coli* K-12, n = 6). Data points represent individual mice from one experiment. Bars indicate medians. (**B**) Germ-free SwissWebster mice treated as in (A) with HA107 (n = 9) or *E. coli* K-12 (n = 3) and analyzed after 48 hours. Data from one of two independent experiments are shown. (**C**) Germ-free Swiss-Webster mice were gavaged six times over 14 days with doses of 10^{10} CFU of HA107, and after a further 14 days their germ-free status was confirmed by bacterial culture from feces and intestinal contents and culture-independent bacterial staining (*7*). n.d., not detected by enrichment culture from cecal or fecal material (<10^1 CFU). Data from n = 4 mice from one of seven independent experiments are shown. (**D** to **F**) Germ-free Swiss-Webster mice were gavaged six times over 2 weeks [10^{10} CFU of HA107 per dose, (E), n = 4] or colonized with a sentinel colonized mouse containing an *E. coli*-free ASF [(F), n = 3)] and compared to age-matched germ-free controls [(D), GF, n = 3)]. Sections of duodenum were stained with a fluorescein isothiocyanate (FITC)–mouse–IgA antibody (green) and 4′,6′-diamidino-2-phenylindole (DAPI) (blue) as a nuclear counterstain. Insets indicate numbers of IgA plasma cells per intestinal villus (mean ± SD). (**G** to **J**) Live bacterial flow cytometric analysis of IgA-bacterial binding using IgA-containing intestinal washes from the mice depicted in (D) to (F) (see fig. S3 for technical details). Blue squares, HA107-gavaged mice; red triangles, ASF sentinel colonized mice; and black circles, germ-free control mice (GF). Images and curves in (D) to (J) represent individual mice from one of seven independent experiments.

pared with wild-type *E. coli* or a restricted ASF microbiota by using flow cytometry staining of whole bacteria (*6*, *7*) (fig. S3). There was a clear specific mucosal IgA response to *E. coli* HA107 in germ-free mice that had previously been treated with this organism (Fig. 1G) but not to *Salmonella typhimurium*, to which they had never been exposed (Fig. 1H). This response was similar to that seen in persistently wild-type *E. coli*–mono-associated mice (fig. S4). In contrast, germ-free mice colonized with an *E. coli*–free ASF microbiota (*8*) had equivalent amounts of total IgA induction (Fig. 1I) but no specific *E. coli* binding (Fig. 1G). Lipopolysaccharide (LPS) O-antigen and core polysaccharides can mask bacterial surface proteins and thereby define bacterial antibody binding to a large degree (*9*). Bacterial preabsorption analysis of HA107-induced IgA showed that the LPS core antigen of *E. coli* K-12 was not a dominant IgA epitope but could partially shield other surface epitopes that became accessible on a "deep-rough" *E. coli* Δ*rfaC* mutant that expresses a truncated core antigen (fig. S5). Because shielding was only partial, flow cytometry of deep-rough *E. coli* gave very similar results to those of wild-type *E. coli* K-12 (Fig. 1J). This indicates induction of a highly specific IgA response to live bacterial antigen, rather than expansion of a natural polyclonal or oligoclonal response by stochastic class switch recombination of random natural specificities.

We were able to address the dose of live bacteria required for IgA induction because our reversible system used live but nonreplicating bacteria. We found that in germ-free mice there was no measurable IgA response if we gavaged mice with doses below 10^9 HA107 CFU (Fig. 2, A and B). Bacteria killed by heat treatment (Fig. 2C) or peracidic acid fixation (Fig. 2, D to F) were ineffective at inducing the response. Sim-

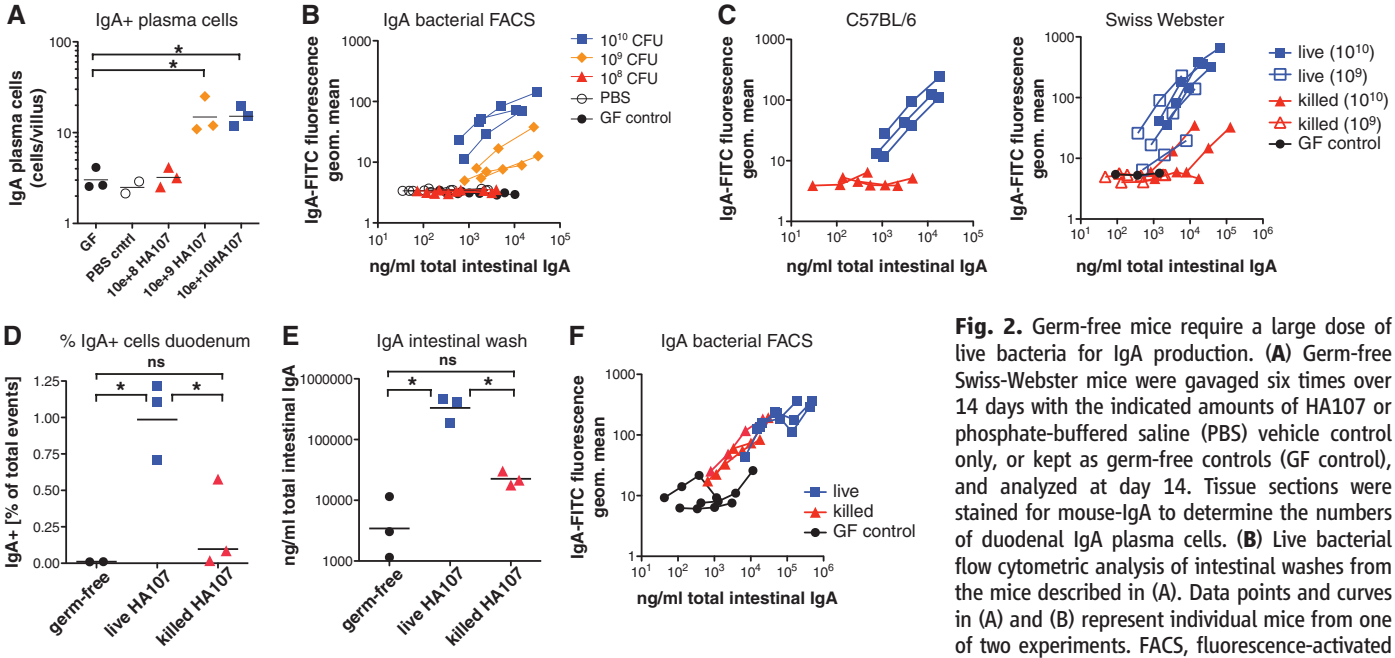

Fig. 2. Germ-free mice require a large dose of live bacteria for IgA production. (**A**) Germ-free Swiss-Webster mice were gavaged six times over 14 days with the indicated amounts of HA107 or phosphate-buffered saline (PBS) vehicle control only, or kept as germ-free controls (GF control), and analyzed at day 14. Tissue sections were stained for mouse-IgA to determine the numbers of duodenal IgA plasma cells. (**B**) Live bacterial flow cytometric analysis of intestinal washes from the mice described in (A). Data points and curves in (A) and (B) represent individual mice from one of two experiments. FACS, fluorescence-activated cell sorting. (**C**) Doses of 10^9 or 10^{10} CFU of either live or heat-killed (15-min autoclaving) HA107 were gavaged into germ-free C57BL/6 and Swiss-Webster mice (six times over 2 weeks) and analyzed by live bacterial flow cytometry on day 14. Black circles, germ-free control kept in the same isolator. Curves represent individual mice from one experiment. (**D** to **F**) Doses of 10^{10} CFU of live or peracidic acid–killed HA107 were gavaged into germ-free Swiss-Webster mice (six times over 2 weeks) and analyzed by flow cytometric analysis of duodenal leukocytes (D), IgA-specific enzyme-linked immunosorbent assay (ELISA) (E), and live bacterial flow cytometry (F) on day 14. Germ-free controls are depicted as black circles. Data points and curves represent individual mice from one experiment. Horizontal bars indicate means; *P < 0.05; one-way analysis of variance (ANOVA); ns, nonsignificant.

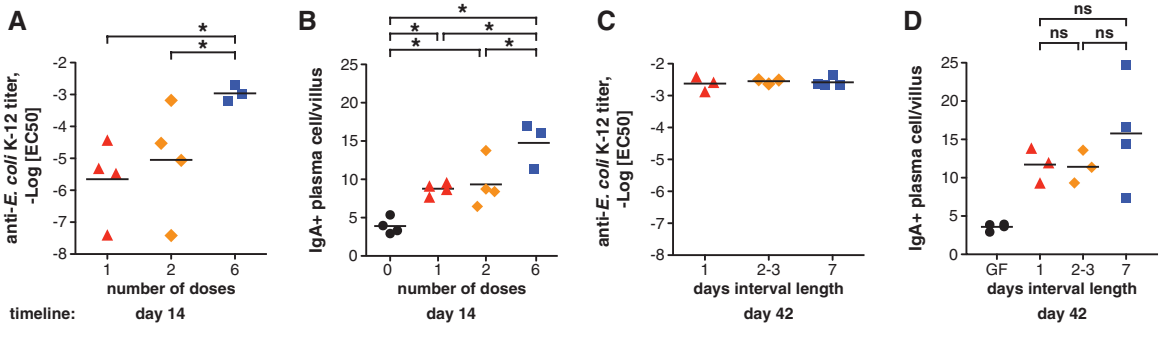

Fig. 3. Additive induction of intestinal IgA in proportion to bacterial exposure. Germ-free C57BL/6 mice were (**A** and **B**) given one, two, or six doses of 10^{10} CFU HA107 over the course of 1 week and analyzed at day 14. (**C** and **D**) In parallel, three groups of mice were given six doses in intervals of 1, 2 to 3, or 7 days apart and analyzed on day 42. Intestinal washes were analyzed by IgA-specific ELISA and live bacterial flow cytometry. –LogEC50 (where EC50 indicates median effective concentration) values of IgA–*E. coli* binding were calculated as described in (*7*) [(A) and (B)], and numbers of duodenal IgA plasma cells were determined from 7-μm frozen sections stained for mouse IgA [(C) and (D)]. Bars indicate means; *P < 0.05 (one-way ANOVA); ns, nonsignificant. Data points represent individual mice from one of two experiments.

ilar high bacterial thresholds for mucosal IgA induction were observed previously in conventional mice treated with live wild-type bacteria (*1*). Early translocation of live bacteria to the mesenteric lymph nodes (MLNs) in germ-free C57BL/6 mice is similar to that in germ-free $J_H^{-/-}$ mice (table S1), suggesting that preformed "natural" IgA, which does not bind commensal bacteria (Fig. 1, G, I, and J), does not contribute to this threshold. This strongly suggests that the high threshold for IgA induction is not attributable to competition with endogenous bacteria or their breakdown molecules. Assuming that the intestinal barrier during repeated transient colonization is representative of colonized animals, the high threshold is an intrinsic property of the mucosal bacterial sampling system, which appears to sample only a tiny fraction of the live bacteria present (*1*), in order to mount a protective mucosal immune response without the risk of mucosal or systemic infection.

Immune memory conferring lifelong immunity to infections such as measles can be mediated by neutralizing antibody against systemic pathogens (*10*). Persistence of the immune response and larger, more rapid subsequent responses are a key part of the success of many vaccines and responses to pathogens in vivo (*11*). Primary systemic immune responses normally result in low IgM antibody titers and the establishment of a memory cell population, which generates a rapid increase in antibody-producing cells and high-affinity antibody production upon subsequent challenge. This synergistic effect of repeated immunizations normally increases with the interval length between sequential doses (*12*). Furthermore, memory serum antibody responses may also benefit from nonspecific stimulation, such as commensal bacterial products (*13*), but it is unclear whether this could apply to specific responses in the mucosal immune system.

The persistent nature of intestinal bacterial colonization has made it previously impossible to study immunological memory in the context of intestinal anti-microbiota IgA production. Reversible bacterial colonization, however, allowed us to immunize orally with defined pulses of live bacteria and measure the effects of single and sequential immunizations and, later, persistence or loss of the response. The IgA response increased in an additive fashion with the number of bacterial doses (one, two, or six doses of 10^{10} CFU, spread over 7 days and measured after 14 days; Fig. 3, A and B; fig. S6, A and B), but six repetitive bacterial doses of 10^{10} CFU generated equivalent IgA responses independent of the dose interval length (24 hours, 2 to 3 days, or 7 days; Fig. 3, C and D; fig. S6, C and D). Even in the extreme case where a dose of 3×10^{10} HA107 was given within 24 hours or spread out as three equally spaced sequential doses of 1×10^{10} CFU over 2 weeks (a 7-day interval), the secretory IgA and the response to deep-rough bacterial surface antigens were equivalent (fig. S7, A, C, and E), although there was a small increase in the plasma cell number and the response to wild-type *E. coli* K-12 (fig. S7, B, D, and F). We therefore conclude that the commensal-specific IgA response does not show synergistic but mainly additive effects of sequential immunizations regardless of dose interval, in contrast to the paradigm of systemic immune memory.

The integration of specific bacterial numbers over time into bacterial-specific IgA titers could serve to adjust the intestinal IgA repertoire to gradually changing microbiota composition. The persistence of specific antibody titers can also be used to assess immunological memory. We therefore determined IgA persistence after reversible HA107 colonization. The longevity of microbiota-induced intestinal IgA plasma cells of conventional mice had been determined previously with an average half-life of 5 days and a maximum lifetime of 6 to 8 weeks (*14*), although this contrasts with measurements of a very long life span of some plasma cells (≥1 year) in the bone marrow (*15*, *16*). We found no measurable decrease in the specific IgA responses in HA107-treated mice 16 weeks after exposure (Fig. 4, A and B, and fig. S8A), despite the frequencies of MLN and Peyer's patch GL-7^+ germinal center B cells returning to germ-free levels within 2 to 6 weeks (fig. S9). Short-lived induction of germinal centers and persistent intestinal IgA plasma cells would be consistent with very long plasma cell half-lives as previously measured in the bone marrow, and, although there is no evidence of live bacterial long-term persistence in lymphoid organs (fig. S10) and IgA heavy chain sequences show N-nucleotide insertion but very limited hypermutation (table S2), there may still be low amounts of ongoing B cell activation through commensal antigen retention in immune complexes or by follicular or conventional DCs. Preexisting or induced CD4 T cells may also contribute to IgA induction dynamics (*17*). Our data, however, suggested that, once the IgA response was induced in mice that have returned to germ-free status, the specific repertoire is effectively altered only by restimulation with new bacterial species.

To test whether there is attrition of specific IgA production in the lamina propria of animals colonized with a commensal bacterial flora, we gavaged ASF mice with HA107. This resulted in a similar HA107 response to that seen in germ-free animals after 2 weeks, but the response was attenuated within <17 weeks of discontinuing the intestinal HA107 immunization (Fig. 4C and fig. S8B). Similar attrition of the specific IgA response induced by HA107 in germ-free mice was seen when they were subsequently treated with commensal species *Enterococcus faecalis*, *Enterobacter cloacae*, and *Staphylococcus xylo-*

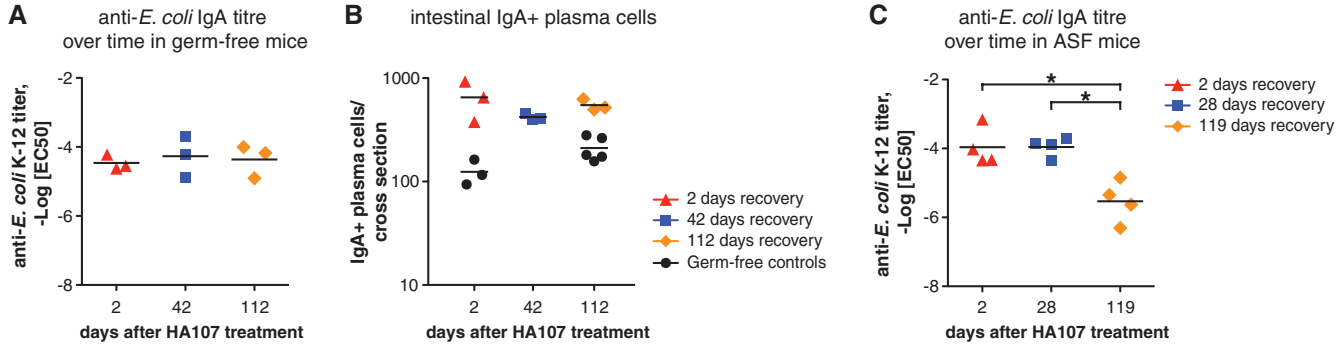

Fig. 4. Commensal-induced specific IgA is long-lived in germ-free mice but rapidly lost in the face of ongoing IgA induction in microbiota-colonized mice. (**A**) Germ-free Swiss-Webster mice were gavaged six times over 2 weeks with 10^{10} CFU of HA107 and kept germ-free for up to 112 days after discontinuation of HA107 treatment. Intestinal washes taken at the indicated time points were analyzed by IgA-specific ELISA and live bacterial flow cytometry, and –LogEC50 values of IgA–*E. coli* binding were calculated. (**B**) Tissue sections from the experimental mice described in (A) were stained for mouse IgA to determine the numbers of IgA plasma cells in HA107-treated and germ-free control mice. (**C**) Colonized mice containing an *E. coli*–free ASF microbiota were treated as described in (A), kept under barrier conditions for up to 119 days after discontinuation of HA107 treatment, and analyzed as above at the indicated time points. Bars indicate means; *$P < 0.05$; one-way ANOVA. Data points in (A) and (B), respectively, and in (C) represent individual mice from one of two independent experiments.

sus (fig. S11). This suggests that in colonized animals persistence of a specific IgA response is limited by restimulation with other commensal bacterial species, allowing the mucosal immune system to adapt its IgA to commensals that are currently present in the intestine.

By using this system to allow transient colonization of germ-free mice in the absence of any other manipulation, we described that (i) induction of high-titer IgA can be uncoupled from permanent intestinal bacterial colonization, (ii) an intrinsic threshold exists between 10^8 and 10^9 bacteria below which the intestinal IgA system does not respond, (iii) the intestinal IgA system lacks classical immune memory characteristics, and (iv) the intestinal IgA repertoire is characterized by constant attrition and thus represents the dominant species currently present in the intestine. This deviates substantially from classical systemic immune memory paradigms and affects mucosal vaccine design and harnessing the effects of probiotic bacteria. Teleologically, intestinal IgA and serum IgG systems can be seen as complementary systems, with the intestinal IgA system continuously adapting to and protecting from the current microbiota and the systemic IgG system being capable of rapid and highly specific responses to previously encountered invasive pathogens.

References and Notes

1. A. J. Macpherson, T. Uhr, *Science* **303**, 1662 (2004).
2. A. J. Macpherson *et al.*, *Science* **288**, 2222 (2000).
3. D. A. Peterson, N. P. McNulty, J. L. Guruge, J. I. Gordon, *Cell Host Microbe* **2**, 328 (2007).
4. K. Nakayama, S. M. Kelly, R. Curtiss, *Nat. Biotechnol.* **6**, 693 (1988).
5. K. E. Shroff, K. Meslin, J. J. Cebra, *Infect. Immun.* **63**, 3904 (1995).
6. E. Slack *et al.*, *Science* **325**, 617 (2009).
7. Materials and methods are available as supporting material on *Science* Online.
8. B. Stecher *et al.*, *PLoS Pathog.* **6**, e1000711 (2010).
9. A. T. Bentley, P. E. Klebba, *J. Bacteriol.* **170**, 1063 (1988).
10. R. M. Zinkernagel, H. Hengartner, *Immunol. Rev.* **211**, 310 (2006).
11. D. F. Tough, *Trends Immunol.* **24**, 404 (2003).
12. A. I. Fecsik, W. T. Butler, A. H. Coons, *J. Exp. Med.* **120**, 1041 (1964).
13. N. L. Bernasconi, E. Traggiai, A. Lanzavecchia, *Science* **298**, 2199 (2002).
14. C. A. Mattioli, T. B. Tomasi Jr., *J. Exp. Med.* **138**, 452 (1973).
15. R. A. Manz, A. Thiel, A. Radbruch, *Nature* **388**, 133 (1997).
16. M. K. Slifka, R. Antia, J. K. Whitmire, R. Ahmed, *Immunity* **8**, 363 (1998).
17. Y. Cong, T. Feng, K. Fujihashi, T. R. Schoeb, C. O. Elson, *Proc. Natl. Acad. Sci. U.S.A.* **106**, 19256 (2009).

18. We thank D. Zhang, H. Roberts, J. Notarangelo, S. Armstrong, S. Competente, M. Provenza, J. Bodewes, and R. McArthur for their technical support and B. Stecher, W.-D. Hardt, A. J. Müller, N. A. Bos, C. Mueller, R. M. Zinkernagel, A. G. Rolink, A. Lanzavecchia, and C. Reis e Sousa for their helpful comments and editing the manuscript. Grant support: Swiss National Science Foundation (310030_124732), Canadian Institutes of Health Research, Crohn's and Colitis Foundation of Canada, Genome Canada, Farncombe Foundation, Canadian Association of Gastroenterology. This research was also supported with funding from the Canada Research Chairs program to K.D.M. and A.J.M. M.H. is a fellow of the Prof. Dr. Max Cloëtta foundation and was supported by grants of the Oncosuisse Foundation (OCS 02113-08-2007). S.H. was supported in part by a German Science Foundation fellowship, and the clean mouse facility Bern was supported by the Genaxen Foundation. The authors have no conflicts of interests to declare.

Supporting Online Material

www.sciencemag.org/cgi/content/full/328/5986/1705/DC1
Materials and Methods
Figs. S1 to S11
Tables S1 and S2
References

17 February 2010; accepted 14 May 2010
10.1126/science.1188454

Transition to Addiction Is Associated with a Persistent Impairment in Synaptic Plasticity

Fernando Kasanetz,[1,2]* Véronique Deroche-Gamonet,[1,2]* Nadège Berson,[1,2] Eric Balado,[1,2] Mathieu Lafourcade,[1,2] Olivier Manzoni,[1,2]†‡ Pier Vincenzo Piazza[1,2]†‡

Chronic exposure to drugs of abuse induces countless modifications in brain physiology. However, the neurobiological adaptations specifically associated with the transition to addiction are unknown. Cocaine self-administration rapidly suppresses long-term depression (LTD), an important form of synaptic plasticity in the nucleus accumbens. Using a rat model of addiction, we found that animals that progressively develop the behavioral hallmarks of addiction have permanently impaired LTD, whereas LTD is progressively recovered in nonaddicted rats maintaining a controlled drug intake. By making drug seeking consistently resistant to modulation by environmental contingencies and consequently more and more inflexible, a persistently impaired LTD could mediate the transition to addiction.

The transition to addiction defines the shift from a controlled drug use to a compulsive drug taking that culminates in loss of control over drug consumption (*1*, *2*). This pathological behavior is observed in a restricted number of drug users after a prolonged period of drug intake (*2*, *3*).

To uncover the biological basis of transition to addiction, substantial resources have been devoted to the study of the neurobiological effects of drugs of abuse. These investigations have identified a large number of drug-induced modifications in brain physiology (*4*–*10*) and morphology (*11*, *12*). Despite these advances, which drug-induced alterations specifically underlie the transition to addiction in vulnerable individuals are currently unknown (*13*).

A few years ago it was discovered that addiction exists and can be studied in animals (*14*–*16*). Similar to humans, after a prolonged period of drug intake, a restricted number of rodents develop addiction-like behaviors (Addict rats), although the largest percentage maintains a controlled drug intake (Non-Addict rats). Because Addict and Non-Addict rats did not differ in the amount of drug taken (*14*), comparing these two groups of animals allows one to identify the biological changes specifically associated with the transition to addiction in vulnerable individuals.

Using this approach, we evaluated the role of synaptic plasticity in the transition to addiction. Activity-dependent long-term depression (LTD) and long-term potentiation (LTP) of synaptic transmission are the two principal forms of synaptic plasticity that permit strengthening (LTP) or weakening (LTD) of synapses in an interplay that allows the refinement of neuronal circuits necessary to adapt behavior to an ever-changing environment (*17*). Drugs of abuse modify LTP and LTD (*5*, *10*, *18*–*20*) in different areas (*21*) of the mesocorticolimbic system, one of the major substrates of drugs of abuse (*6*, *19*, *22*, *23*). Drug-induced alterations in LTP and LTD have been proposed to be important factors leading to compulsive drug intake that they would facilitate by rendering drug taking impermeable to changes (*5*, *24*). However, whether changes in synaptic plasticity occur specifically in individuals developing addiction or are nonspecific adaptations common to all the individuals exposed to drugs is currently unknown (*13*).

In the first experiment, rats were trained for cocaine intravenous self-administration (SA), the

[1]INSERM U862, NeuroCentre Magendie, 147 Rue Léo Saignat, 33077, Bordeaux Cedex, France. [2]Université de Bordeaux, 147 Rue Léo Saignat, 33077, Bordeaux Cedex, France.

*These authors contributed equally to this work.
†These authors contributed equally to this work.
‡To whom correspondence should be addressed. E-mail: olivier.manzoni@inserm.fr (O.M.); pier-vincenzo.piazza@inserm.fr (P.V.P.)

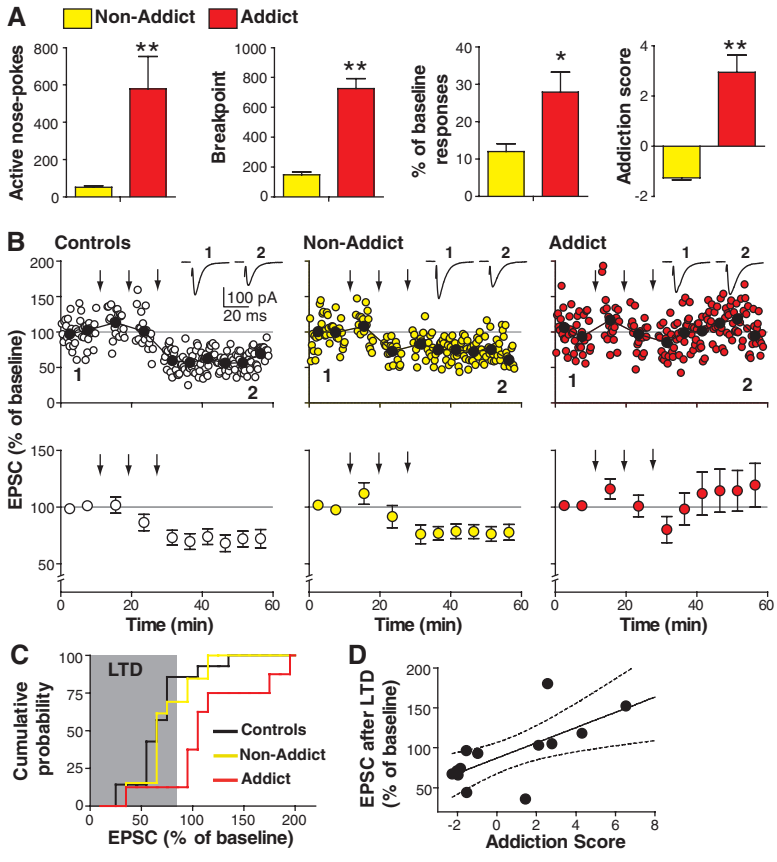

Fig. 1. NMDAR-dependent LTD was disrupted in Addict animals. (**A**) Differences between Addict (n = 8) and Non-Addict rats (n = 8) in (from left to right) persistence in responding when the drug is not available [$F(1,26) = 9.14$, $P < 0.01$]; motivation for cocaine measured by the breakpoint in a progressive ratio schedule [$F(1,26) = 70.36$, $P < 0.00001$]; responding despite negative consequences measured when cocaine infusions were associated with electric footshocks [$F(1,26) = 6.15$, $P < 0.05$]; and addiction score [$F(1,26) = 42.84$, $P < 0.0001$]. (**B**) Individual experiments (top) with representative excitatory postsynaptic current (EPSC) traces and averaged data (bottom) showing that LTD was induced in controls (71.7 ± 7.1% of baseline, $n = 14$, $W = 69$, $P < 0.01$) and Non-Addict animals (77.8 ± 6.9%, $n = 13$, $W = 66$, $P < 0.005$) but not in Addicts (118.9 ± 17.9%, $n = 8$, $W = -9$, $P = 0.4$). Controls were left undisturbed in the home cage for the duration of the experiments. Arrows indicate pairing stimulations; horizontal lines denote baseline levels. (**C**) Cumulative probability distribution of normalized EPSCs after LTD induction. Gray area represents LTD window. (**D**) Positive correlation (r) between the normalized EPSC after LTD and the addiction score ($r = 0.675$, $P < 0.01$). *$P < 0.05$, **$P < 0.01$ compared to Non-Addict.

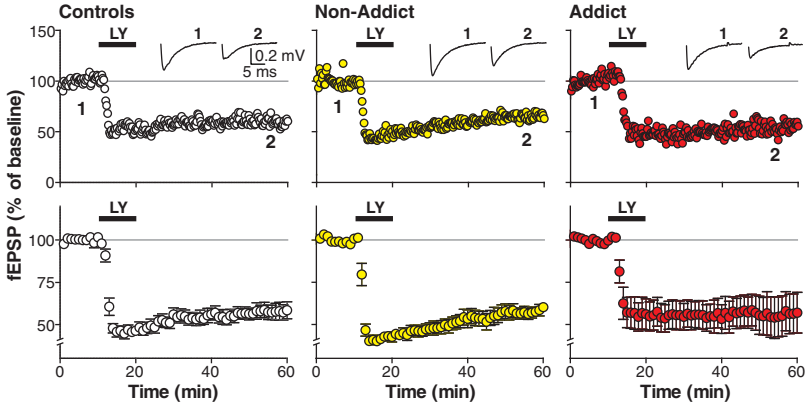

Fig. 2. Presynaptic mGluR2/3-mediated LTD in the NAC was intact after prolonged cocaine SA. Individual experiments (top) with representative field excitatory postsynaptic potential (fEPSP) traces and averaged data (bottom) showing that mGluR2/3-mediated LTD was induced in controls (54.9 ± 3.7% of baseline, $n = 6$, $W = 21$, $P < 0.05$), Non-Addicts (53.8 ± 4.6%, $n = 7$, $W = 28$, $P < 0.05$), and Addicts (55.8 ± 9.1%, $n = 6$, $W = 21$, $P < 0.05$). Horizontal thin lines: baseline levels; LY: 10-min administration of the mGluR2/3 agonist (LY 379268, 100 nM).

most used procedure to evaluate voluntary drug intake in animals (*25*). As previously described (*14*), between 40 and 50 days of SA, we measured behaviors that are similar to the hallmarks of substance dependence in the reference diagnostic manual DSM-IV (*1*, *26*): (i) The subject has difficulty stopping drug use and/or limiting drug intake. We measured cocaine seeking during a period in which the drug was signaled as not available. (ii) The subject has an extremely high motivation to take the drug, with activities focused on its procurement and consumption. We used a progressive ratio schedule in which the number of responses (ratio) to obtain one drug infusion progressively increases within the session, and we measured the breakpoint, the last ratio completed, which is considered a reliable index of the motivation for the drug (*16*). (iii) Drug use is continued despite negative consequences. We measured the persistence of the animal in seeking cocaine when it was signaled that its delivery would be associated with a punishment.

In agreement with what was previously shown (*14*, *27*), after 50 days of SA, ~20% of the rats were positive for the three addiction-like behaviors (Addict group), whereas a large proportion of the animals (40%) were positive for none (Non-Addict group) (Fig. 1A) (*26*).

Addict and Non-Addict animals were compared for glutamate-dependent LTD in the nucleus accumbens core (NAC), which is an important substrate of drug seeking (*4*, *22*). This comparison was made between 50 and 72 days of SA with NAC slices that were obtained 24 hours after the last SA session. In the NAC, basic parameters of synaptic transmission, such as the amplitude and the frequency of spontaneous excitatory postsynaptic currents (EPSCs) as well as short-term synaptic plasticity, were not modified by prolonged cocaine SA (fig. S1). In contrast, *N*-methyl-D-aspartate receptor (NMDAR)–dependent LTD (fig. S2), induced in medium spiny neurons with a pairing protocol (*26*), was suppressed in Addict rats, although it was normal in Non-Addict and control animals (Fig. 1, B and C). Strengthening this result, we also found a positive correlation between the normalized EPSC after LTD induction, an

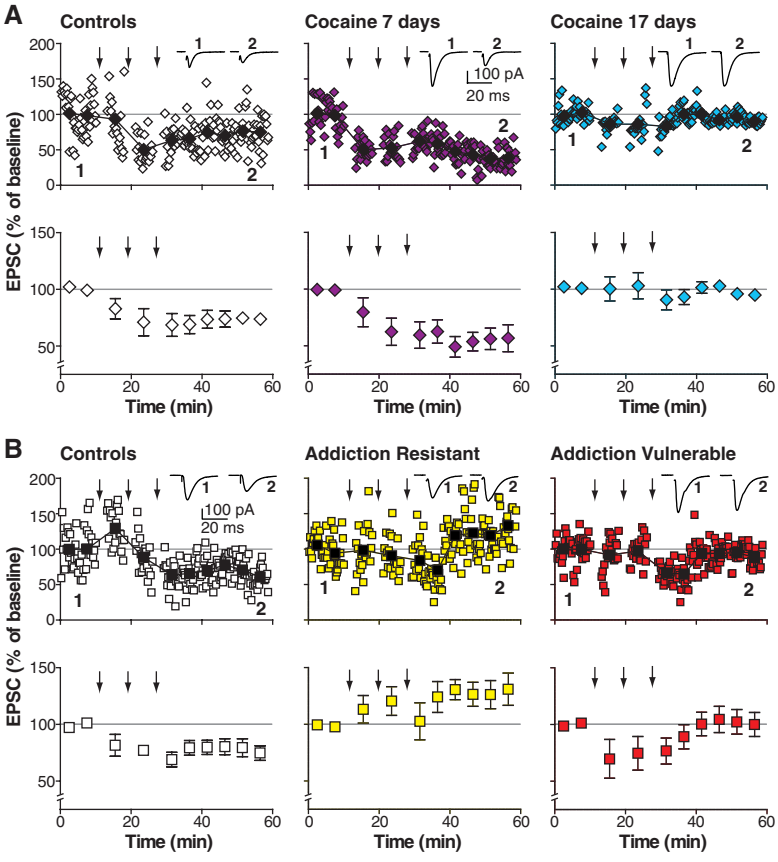

Fig. 3. NMDAR-dependent LTD was impaired during early stages of cocaine self-administration (SA). (**A**) LTD in the nucleus accumbens in animals self-administering cocaine for 7 or 17 days. LTD induction (in percent of baseline) was normal in controls (73.3 ± 3.5%, $n = 8$, $W = 36$, $P < 0.01$) and in Cocaine 7 days (56.7 ± 7.8%, $n = 7$, $W = 21$, $P < 0.05$) groups, but was absent in Cocaine 17 days animals (96.7 ± 1.5%, $n = 6$, $W = 18$, $P = 0.07$). Rats tested for saline SA for either 7 ($n = 4$) or 17 ($n = 4$) sessions were used for the control group. (**B**) After 17 days of cocaine SA, LTD was observed in controls (77.2 ± 7.2% of baseline, $n = 11$, $W = 50$, $P < 0.05$), but was absent in both Addiction Resistant (134.4 ± 10.6%, $n = 7$, $W = -24$, $P > 0.05$) and Addiction Vulnerable animals (106.8 ± 12.1%, $n = 6$, $W = -3$, $P > 0.84$). Rats of matching age and purchase, left undisturbed in the animal house, were used as controls. For both (A) and (B), individual experiments (top) with representative EPSC traces and averaged data (bottom) are shown. Arrows: pairing stimulations; horizontal lines: baseline levels.

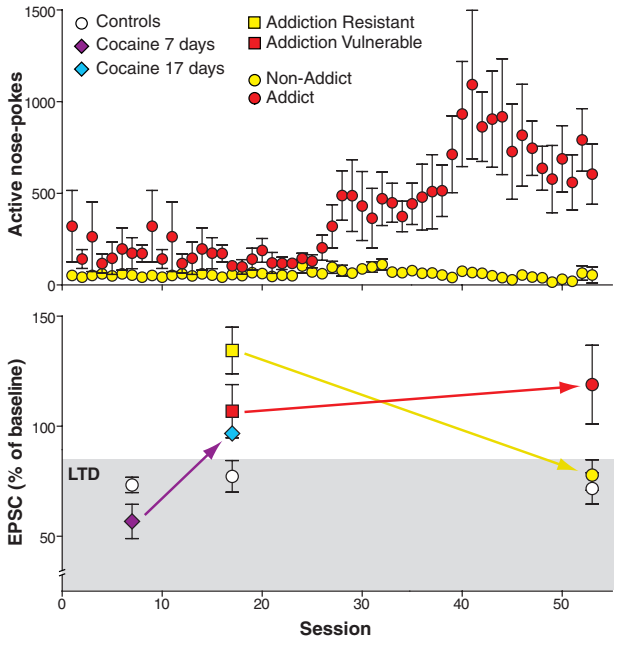

Fig. 4. Persistent impairment in NMDAR-dependent LTD is associated with transition to cocaine addiction. (**Top**) Transition to addiction as shown by the evolution over sessions of the persistence in responding during the nondrug periods in Addict and Non-Addict animals. (**Bottom**) Changes in NMDAR-dependent LTD in the NAC as a function of cocaine exposure and vulnerability to addiction.

inverse measure of LTD, and the animals' addiction scores (Fig. 1D).

To evaluate if there was a general impairment of synaptic plasticity in Addict animals, we also measured the LTD mediated by mGluR2/3 receptors (*28*). In contrast to what was observed with NMDAR-LTD, no difference between groups was found for mGluR2/3-mediated LTD (Fig. 2).

We then studied, in our SA conditions, the evolution along time of NMDAR-LTD. One week of cocaine SA had no effect on NMDAR-LTD (Fig. 3A). However, confirming previous published observations (*29*, *30*), NMDAR-LTD was completely abolished in rats that had self-administered cocaine for 17 days (Fig. 3A). A caveat of our and published experiments is that, after 17 days of SA, NMDAR-LTD was measured in rats that were not characterized for their vulnerability to addiction. Because in a general population only 20% of the rats belong to the Addict group, it is likely that very few future Addicts have been tested after 17 days of SA and that most of the modifications described concern Non-Addicts. To overcome this potential bias, we developed a method that allows Addict rats to be identified as early as after 17 days of SA (*26*) (fig. S3). We then compared animals that will (Addiction Vulnerable) or will not (Addiction Resistant) develop addiction after 17 days of SA. We found that NMDAR-LTD was suppressed in both groups of animals (Figs. 3B and 4).

Taken together, the results of the three experiments (Fig. 4) show that during the acquisition phase of SA (the first week), synaptic plasticity in the nucleus accumbens is not impaired by cocaine, supporting a role for NMDAR-LTD in the NAC in learning new reward-response associations. During the next stage (between 2 and 3 weeks of SA), once the learning has been consolidated, LTD is suppressed in all subjects. However, subsequently (between 8 and 10 weeks), a normal NMDAR-LTD is progressively recovered in animals that maintain a controlled drug intake, whereas it is persistently lost in animals undergoing the transition to addiction (Fig. 4). Because 2 weeks of SA are not sufficient for addiction-like behaviors to fully develop (Fig. 4 and fig. S4), these observations suggest that it is not a transitory loss in NMDAR-

LTD, but rather its persistent impairment, that is associated with the transition to addiction.

This persistent impairment in LTD could explain the loss of control on drug intake observed in Addict rats. LTD in the NAC is considered important in rescaling synapses that were enhanced during acquisition of motor responses and cue-reward associations (*31*, *32*), allowing those synapses to encode future associations and restore flexibility to neuronal circuits. The persistent inability to rescale synapses in Addict animals may render drug-seeking behavior consistently resistant to modulation by environmental contingencies, finally resulting in loss of control over drug intake. Thus, the major behavioral difference between Addict and Non-Addict animals, similar to that in humans (*1*), is their capacity to adjust their drug intake as a function of environmental contingencies. Non-Addicts can stop seeking drugs if they know that the drug is not available, if it requires an excessively high workload, or if taking the drug acquires negative consequences. Addicts have lost this ability and continue to seek drugs independently of environmental conditions.

Our results also provide unanticipated insight into the type of homeostatic alterations that characterize Addicts. We expected, as largely assumed in the field, to discover a specific pathological adaptation—a particular phenotype—characterizing synaptic plasticity in Addicts. In contrast, the transition to addiction was associated, at least in the NAC, with a form of anaplasticity, i.e., the incapacity of Addicts to counteract initial drug-induced impairments.

The anaplasticity of Addict rats is relevant to revising conceptualizations of the transition to addiction, currently seen as the progressive development of specific brain adaptations that lead to loss of control over drug intake. Our data suggest that instead, the transition to addiction could be mediated by the incapacity to engage the active processes that allow control of drug intake. After a prolonged exposure to drugs, all the subjects are probably at the point of losing control over drug-intake behavior, as shown by the loss of LTD in all rats. This probably corresponds to the situation when an individual engaged in sustained drug use experiences the sensation that "it is becoming too much" and that "a line is being crossed." Fortunately, for most individuals, the brain adapts to recover a normal plasticity and allows learning to control drug intake. In contrast, the anaplasticity that characterizes addicts makes them enter a downward spiral in which drug-associated stimuli, which can no longer be overridden by other associations, gain more and more power in controlling behavior, finally leading to the compulsive drug intake that characterizes addiction.

Our results suggest that the failure of an individual to counteract the impairment in NMDAR-LTD induced by chronic cocaine intake, which results in a persistent deficit in synaptic plasticity, contributes to the transition to addiction. A clear understanding of the molecular substrates that mediate this lack of adaptation in Addicts could unravel new targets for the development of efficient therapies for drug abuse.

References and Notes

1. A. P. Association, *American Psychiatric Press* (Washington, DC, 2000).
2. C. P. O'Brien, *Science* **278**, 66 (1997).
3. L. A. Warner, R. C. Kessler, M. Hughes, J. C. Anthony, C. B. Nelson, *Arch. Gen. Psychiatry* **52**, 219 (1995).
4. P. W. Kalivas, *Nat. Rev. Neurosci.* **10**, 561 (2009).
5. J. A. Kauer, R. C. Malenka, *Nat. Rev. Neurosci.* **8**, 844 (2007).
6. G. F. Koob, M. Le Moal, *Nat. Neurosci.* **8**, 1442 (2005).
7. S. E. Hyman, R. C. Malenka, E. J. Nestler, *Annu. Rev. Neurosci.* **29**, 565 (2006).
8. E. J. Nestler, *Philos. Trans. R. Soc. Lond. B Biol. Sci.* **363**, 3245 (2008).
9. Y. Shaham, B. T. Hope, *Nat. Neurosci.* **8**, 1437 (2005).
10. M. E. Wolf, X. Sun, S. Mangiavacchi, S. Z. Chao, *Neuropharmacology* **47** (suppl. 1), 61 (2004).
11. T. E. Robinson, B. Kolb, *Neuropharmacology* **47** (suppl. 1), 33 (2004).
12. I. Maze *et al.*, *Science* **327**, 213 (2010).
13. P. W. Kalivas, *Nat. Neurosci.* **8**, 1440 (2005).
14. V. Deroche-Gamonet, D. Belin, P. V. Piazza, *Science* **305**, 1014 (2004).
15. L. J. Vanderschuren, B. J. Everitt, *Science* **305**, 1017 (2004).
16. C. Sanchis-Segura, R. Spanagel, *Addict. Biol.* **11**, 2 (2006).
17. R. C. Malenka, M. F. Bear, *Neuron* **44**, 5 (2004).
18. C. Bellone, C. Lüscher, *Nat. Neurosci.* **9**, 636 (2006).
19. P. W. Kalivas, N. Volkow, J. Seamans, *Neuron* **45**, 647 (2005).
20. K. L. Conrad *et al.*, *Nature* **454**, 118 (2008).
21. M. Mameli *et al.*, *Nat. Neurosci.* **12**, 1036 (2009).
22. B. J. Everitt *et al.*, *Philos. Trans. R. Soc. Lond. B Biol. Sci.* **363**, 3125 (2008).
23. M. J. Thomas, P. W. Kalivas, Y. Shaham, *Br. J. Pharmacol.* **154**, 327 (2008).
24. B. T. Chen *et al.*, *Neuron* **59**, 288 (2008).
25. L. V. Panlilio, S. R. Goldberg, *Addiction* **102**, 1863 (2007).
26. Materials and methods and supporting data are available on *Science* Online.
27. D. Belin, E. Balado, P. V. Piazza, V. Deroche-Gamonet, *Biol. Psychiatry* **65**, 863 (2009).
28. D. Robbe, G. Alonso, S. Chaumont, J. Bockaert, O. J. Manzoni, *J. Neurosci.* **22**, 4346 (2002).
29. M. Martin, B. T. Chen, F. W. Hopf, M. S. Bowers, A. Bonci, *Nat. Neurosci.* **9**, 868 (2006).
30. K. Moussawi *et al.*, *Nat. Neurosci.* **12**, 182 (2009).
31. G. D. Stuber *et al.*, *Science* **321**, 1690 (2008).
32. H. H. Yin *et al.*, *Nat. Neurosci.* **12**, 333 (2009).

33. Supported by ANR (2005), EU-STREPPheCOMP (FP6), MILDT/INCa/Inserm (2008) grants to P.V.P., O.M., and V.D.-G. The authors report no conflict of interest.

Supporting Online Material

www.sciencemag.org/cgi/content/full/328/5986/1709/DC1
Materials and Methods
Figs. S1 to S4
References

2 February 2010; accepted 13 May 2010
10.1126/science.1187801

Incidental Haptic Sensations Influence Social Judgments and Decisions

Joshua M. Ackerman,[1] Christopher C. Nocera,[2] John A. Bargh[3]

Touch is both the first sense to develop and a critical means of information acquisition and environmental manipulation. Physical touch experiences may create an ontological scaffold for the development of intrapersonal and interpersonal conceptual and metaphorical knowledge, as well as a springboard for the application of this knowledge. In six experiments, holding heavy or light clipboards, solving rough or smooth puzzles, and touching hard or soft objects nonconsciously influenced impressions and decisions formed about unrelated people and situations. Among other effects, heavy objects made job candidates appear more important, rough objects made social interactions appear more difficult, and hard objects increased rigidity in negotiations. Basic tactile sensations are thus shown to influence higher social cognitive processing in dimension-specific and metaphor-specific ways.

The hand is one of the most important adaptations in our evolutionary history. From infancy, humans use their hands for two primary functions: to acquire information and to manipulate their environments. These sensory and effector capabilities facilitate learning, communication, the development of social bonds, and a host of other fundamental processes. Yet, despite the fact that tactile sensations are critical to both our intrapersonal and interpersonal lives, touch remains perhaps the most underappreciated sense in behavioral research (*1*).

Hands are purposive devices—they typically are used on objects (active touch) rather than objects being used on them (passive touch) (*2*). Active touch in particular allows for the integration of exploratory and information-processing abilities, as when sensory and motor systems exert influence over each other. That is, tactile sensations can suggest the use of specific muscle movements, whereas physically manipulating objects can enhance sensory sensitivity, improving information acquisition and making subsequent

[1]Sloan School of Management, Massachusetts Institute of Technology, 77 Massachusetts Avenue, E62, Cambridge, MA 02142, USA. [2]Department of Psychology, Harvard University, 33 Kirkland Street, Cambridge, MA 02138, USA. [3]Department of Psychology, Yale University, Post Office Box 208205, New Haven, CT 06520, USA.

perceptual and cognitive judgments more accurate (*3*). For instance, shoppers more readily understand and form confident impressions about products with which they physically interact (*4*). Perhaps less intuitively, this remains true even when tactile cues are nondiagnostic for the actual qualities of the item, as when packaging influences conceptions about products (for example, water seems to taste better from a firm bottle than from a flimsy bottle) (*5*). Findings such as this packaging-to-product transfer suggest that haptically acquired information exerts a rather broad influence over cognition, in ways of which we are probably often unaware. We tested how three dimensions of haptic experience—weight, texture, and hardness—can nonconsciously influence judgments and decisions about unrelated events, situations, and objects.

Why might our sense of touch direct our impressions about untouched or even untouchable things? One possibility is that sensorimotor experiences in early life form a scaffold for the development of conceptual knowledge (*6*, *7*). This conceptual knowledge can subsequently be applied to new experiences. Physical-to-mental scaffolding is, in fact, reflected in the use of shared linguistic descriptors, such as metaphors (*8*–*10*). For example, grasping motions and feelings of warmth elicited by interpersonal touch may form the foundation for beliefs about holding and caring, as expressed in the aphorism, "the world is in our hands." Such metaphors provide insight into the existence of particular scaffolded connections. This "scaffolded mind" perspective (*11*) describes the ontological process by which touch experiences might ground touch-related conceptual knowledge.

How would this work in the moment? Given that established associative links between sensorimotor events and scaffolded concepts do not evaporate over time, touching objects may simultaneously cue the processing of physical sensation and touch-related conceptual processing. Accordingly, feeling the rough bark of an oak tree sensitizes us to rough textures and may also make accessible concepts relevant to metaphorical roughness. Research on embodied cognition is consistent with this position. From this perspective, mental action is grounded in a physical substrate, and thus sensory and motor processing constitute necessary components of cognition (*12*). Our understanding of the world is not an abstract proposition but fundamentally depends on our multisensory experiences with it. Relevant experiences include movements (*13*), emotional events (*14*), and the processing of spatial and temperature dimensions (*15*, *16*). For example, time is understood not by abstract instruction or watching the clock, but by its relation to our experiences with movement through physical space (or spacetime) (*13*). Scaffolding, and the related principle of "neural reuse" (*17*), describe the process by which higher-order cognition emerges from bodily experience: Physical actions and sensations are used to acquire an initial comprehension of more abstract concepts and, as such, become automatically tied to their activation.

In the current paper, we propose that experiences with specific object-related tactile qualities elicit a "haptic mindset," such that touching objects triggers the application of associated concepts (and only associated concepts, not more general feelings or unrelated preferences), even to unrelated people and situations. We report six studies demonstrating how weight, texture, and hardness nonconsciously influence both the acquisition and management of information (social impression formation) and the manipulation of environments (decision-making). We experimentally introduce the connections between these tactile dimensions and conceptual knowledge using common touch-related metaphors.

The experience of weight, exemplified by heaviness and lightness, is metaphorically associated with concepts of seriousness and importance (*18*). This is exemplified in the idioms "thinking about weighty matters" and "gravity of the situation." In our first study, testing influences of weight on impression formation, we had 54 passersby evaluate a job candidate by reviewing resumes on either light (340.2 g) or heavy (2041.2 g) clipboards (*19*). Participants using heavy clipboards rated the candidate as better overall (Table 1) [$F(1, 52) = 4.08$, $P = 0.049$] and specifically as displaying more serious interest in the position [$F(1, 52) = 4.40$, $P = 0.041$] (*19*). However, the candidate was not rated as more likely to "get along" with co-workers ($F < 1$), suggesting that the weight cue affected impressions of the candidate's performance and seriousness, consistent with a "heavy" metaphor, but not the metaphorically irrelevant trait of social likeability. Further, participants using the heavy clipboard rated their own accuracy on the task as more important [mean (M) = 5.35, SD = 1.57] than did participants using the light clipboard ($M = 4.36$, SD = 1.68), $F(1, 52) = 4.96$, $P = 0.030$, but they did not self-report devoting more effort to the task ($F < 1$), suggesting that impressions were not due to a self-perception effect (people perceiving their own increased effort as indicative of participation in an especially important study).

Our second study investigated how metaphorical associations with weight affect decision-making. Again, 43 passersby were given either light (453.6 g) or heavy (1559.2 g) clipboards, this time featuring a "social action survey" asking whether particular public issues should receive more or less government funding. Issues included several that are considered socially important and serious (such as air pollution standards) and several that are considered idiosyncratic and less widely important (such as public bathroom regulation). Here, a main effect of clipboard condition, $F(1, 38) = 5.46$, $P = 0.025$, was qualified by an interaction with participant gender, $F(1, 38) = 4.59$, $P = 0.039$. Men allocated more money to social issues in the heavy condition ($M = 4.00$, SD = 0.72) than in the light condition ($M = 2.50$, SD = 2.12; simple contrast, $P = 0.003$). In contrast, women chose to fund social issues at close to the maximum amount in both heavy ($M = 4.00$, SD = 0.58) and light ($M = 4.02$, SD = 0.73) conditions. No effects emerged for the idiosyncratic composite ($F < 1$). These studies suggest that haptic experiences with weight exert conceptually specific influences on both impressions and decisions but do not produce more general positivity or mood influences.

The next two studies examined sensations involving texture, specifically roughness and smoothness, which is metaphorically associated with the concepts of difficulty and harshness. This is exemplified in the idioms "having a rough day" and "coarse language." In study three, 64 passersby read a passage describing an ambiguously valenced social interaction and formed impressions about the nature of this interaction (*20*). Two sets of impressions were collected, one set involving social coordination quality (whether the interaction was adversarial or friendly, competitive or cooperative, a discussion or an argument, and consisted of people on the same side or on opposite sides) and one involving relationship familiarity (closeness of relationship and business or casual interaction style). Before reading, participants completed a five-piece puzzle, either a version with pieces covered in rough sandpaper (rough condition) or a version with the pieces uncovered (smooth condition). Results indicated that participants who completed the rough puzzle rated the interaction as less coordinated (more difficult and harsh) than did

Table 1. Influence of haptic experiences on social impressions. Higher numbers indicate stronger evaluations, with standard deviations in parentheses. For ratings of job candidates on heavy or light clipboards (scale = 1 to 7), $F(1, 52) = 4.08$, $P = 0.049$. For perceived social coordination after rough or smooth puzzles (scale = 1 to 9), $F(1, 62) = 5.15$, $P = 0.027$. For perceptions of employee rigidity (scale = 1 to 7), $F(1, 47) = 4.52$, $P = 0.039$.

Experiment 1: Job candidate suitability		Experiment 3: Perceived social coordination		Experiment 5: Employee rigidness/strictness	
Heavy prime ($n = 26$)	Light prime ($n = 28$)	Rough prime ($n = 33$)	Smooth prime ($n = 31$)	Hard prime ($n = 25$)	Soft prime ($n = 24$)
5.80	5.38	4.74	5.47	5.15	4.44
(0.76)	(0.79)	(1.13)	(1.41)	(1.27)	(1.02)

participants who completed the smooth puzzle (Table 1), $F(1, 62) = 5.15$, $P = 0.027$, but no effect was found for relationship familiarity ($F < 1$). Thus, roughness specifically changed evaluations of social coordination, consistent with a "rough" metaphor, but did not make the interaction seem more generally impersonal.

Would these rough impressions change the decisions people make in social situations? In study four, 42 participants first completed the smooth or rough puzzle and then played an Ultimatum game (*21*). Participants each received 10 tickets for a $50 lottery and chose to give 0 to 10 of the tickets to an anonymous (bogus) participant. If participant 2 accepted the offer, the split became official, but if participant 2 rejected the offer, all tickets were forfeited. Thus, in this bargaining situation, the power was in participant 2's hands. Afterward, participants completed a social value orientation (SVO) scale identifying chronic interaction styles as "prosocial/cooperator," "individualist," "competitor," or "unclassified" (*22*, *23*). Analyses revealed that participants who completed the rough puzzle offered more lottery tickets ($M = 4.22$, SD = 1.35) than participants who completed the smooth puzzle ($M = 3.32$, SD = 1.42), $F(1, 40) = 4.45$, $P = 0.041$. SVO classifications suggest that this was not because rough-puzzle participants were simply more cooperative. Of participants classified prosocial/cooperative, 70.6% actually completed the smooth puzzle, whereas of those classified individualistic, 75.0% completed the rough puzzle, $B = -1.97$, Wald statistic = 7.09, $P = 0.008$. Following from the results of the previous study in which texture changed impressions about social coordination, here roughness appeared to promote compensatory bargaining behavior (giving more tickets so that the offer is not rejected) in a situation perceived as uncoordinated. The rough priming experience did not merely produce more negative behavior overall.

Our last two studies tested haptic experiences with hardness, which is metaphorically associated with the concepts of stability, rigidity, and strictness. This is exemplified in the idioms "she is my rock" and "hard-hearted." In study five, 49 passersby were asked to watch a magic act and guess the secret. As in many magic acts, participants first examined and verified that there was nothing unusual about the object to be used in the trick—either a soft piece of blanket or a hard block of wood. The act was then postponed (forever) while participants completed an impression formation task as in study three. Here the two target individuals in the ambiguous interaction were described as a boss and an employee. Participants evaluated the employee's personality on trait terms relating to positivity (for example, kind) and rigid/strictness (for example, unyielding). Consistent with metaphorical associations of hardness, participants who felt the hard block judged the employee to be more rigid/strict than participants who felt the soft blanket (Table 1), $F(1, 47) = 4.52$, $P = 0.039$, but they did not judge the employee more positively overall ($F < 1$).

Study six moved beyond active touch manipulations to investigate whether passive touch experiences can similarly drive embodied cognitive processing. Instead of having participants touch objects with their hands, we primed participants by the seat of their pants (*24*). Eighty-six participants sat in either a hard wooden chair or a soft cushioned chair while completing both an impression formation task (similar to study five) and a negotiation task. This latter decision-making task had participants imagine shopping for a new car (sticker price $16,500) and subsequently place two offers on the car (the second assuming that the dealer rejected the first offer). Comparable to study five, participants who sat in hard chairs judged the employee to be both more stable, $F(1, 84) = 4.90$, $P = 0.030$, and less emotional, $F(1, 84) = 5.03$, $P = 0.028$, but not more positive overall ($F < 1$) than did participants who sat in soft chairs. On the negotiation task, no differences in offer prices emerged ($P > 0.14$). We next calculated the change in offer prices from first to second offer, on the presumption that activating the concepts of stability and rigidity should reduce people's decision malleability or willingness to change their offers. Among participants who made a second offer, hard chairs indeed produced less change in offer price ($M = \$896.5$, SD = $529.6) than did soft chairs ($M = \$1243.6$, SD = $775.9), $F(1, 66) = 4.30$, $P = 0.042$. Controlling for whether people reported wanting to buy a car in the next year strengthened this effect, $F(1, 65) = 6.95$, $P = 0.010$. Thus, hardness produces perceptions of strictness, rigidity, and stability, reducing change from one's initial decisions, even when the touch experience is passive in nature. These findings highlight the metaphorical specificity of haptic priming effects: Instead of changing the overall valence of evaluations, hard objects made others seem both more negative (strict and rigid) and more positive (stable), with corresponding effects on decision-making.

These six experiments showed that physical interactions with three fundamental dimensions of touch influence our impressions and decisions, even when the people and events those impressions and decisions concern are entirely unrelated to what is being touched. Each dimension was associated with cognitions reflected in common metaphors: Heaviness produced impressions of importance and seriousness, as well as a preference for funding solutions to important problems; roughness led to impressions of decreased coordination and increased donations as a compensatory response; hardness made others appear more strict and stable but less emotional, and also decreased negotiation flexibility. Across studies, these findings emphasize the power of that unique adaptation, the hand, to manipulate the mind as well as the environment. Our last study also suggested that a haptic mindset can be triggered even when touch occurs in other areas of the body, as might be expected given that many tactile experiences are not limited to the hands.

Theoretically, this research suggests interesting implications for human life history processes. Touch is the first sense to develop ontogenetically (*25*) and thus may be the most relevant for scaffolding later conceptual knowledge. Consider that contemporary interpretations of the classic "Big Five" personality traits posit two higher-order factors with the (tactile metaphor–relevant) labels "stability" and "plasticity" (*26*). Such factors are associated with different hormonal substrates (serotonergic and dopaminergic systems, respectively), and it would be interesting to consider the influence (if any) of varieties of touch experience on these systems' activation. With respect to embodiment more generally, evidence suggests that instances of physical or mental action (such as moving an arm or reading a word) are accompanied by reduced cortical activity in relevant brain regions (*27*), which is indicative of neural pathways being (nonconsciously) cued for further processing of similar actions (*28*). We might expect that neural cueing for particular dimensions of touch experience map onto those that register the associated metaphorical concepts identified here.

Although we have focused on interpersonal perceptions, we expect that self-perceptions are similarly affected by what we touch, which is consistent with the dual nature of priming effects (*28*, *29*). Of course, practical implications abound as well. First impressions are liable to be influenced by one's tactile environment, and control over that environment may be especially important for negotiators, pollsters, job seekers, sensory marketers, and others who are interested in interpersonal evaluation processes. Perhaps the use of such "tactile tactics" will represent the next advance in social influence and communication.

References and Notes

1. A. Gallace, C. Spence, *Neurosci. Neurobehav. Rev.* **34**, 246 (2010).
2. J. J. Gibson, *Psychol. Rev.* **69**, 477 (1962).
3. S. J. Lederman, R. L. Klatzky, *Cogn. Psychol.* **19**, 342 (1987).
4. J. Peck, T. L. Childers, *J. Consum. Res.* **30**, 430 (2003).
5. A. Krishna, M. Morrin, *J. Consum. Res.* **34**, 807 (2008).
6. L. W. Barsalou, *Lang. Cogn. Process.* **18**, 513 (2003).
7. J. M. Mandler, *Psychol. Rev.* **99**, 587 (1992).
8. H. H. Clark, *Using Language* (Cambridge Univ. Press, Cambridge, 1996).
9. Z. Kövecses, *Metaphor in Culture: Universality and Variation* (Cambridge Univ. Press, New York, 2005).
10. G. Lakoff, M. Johnson, *Metaphors We Live By* (Univ. of Chicago Press, Chicago, 1980).
11. L. E. Williams, J. Y. Huang, J. A. Bargh, *Eur. J. Soc. Psychol.* **39**, 1257 (2009).
12. P. M. Niedenthal, L. W. Barsalou, P. Winkielman, S. Krauth-Gruber, F. Ric, *Pers. Soc. Psychol. Rev.* **9**, 184 (2005).
13. L. Boroditsky, M. Ramscar, *Psychol. Sci.* **13**, 185 (2002).
14. P. M. Niedenthal, *Science* **316**, 1002 (2007).
15. B. P. Meier, M. D. Robinson, *Psychol. Sci.* **15**, 243 (2004).

16. L. E. Williams, J. A. Bargh, *Science* **322**, 606 (2008).
17. M. L. Anderson, *Philos. Psychol.* **20**, 143 (2007).
18. We conducted these two studies before the publication of Jostmann *et al*. (*30*), which also explored embodied weight experiences, although using different outcomes.
19. Materials, methods, and additional results are available as supporting material on *Science* Online.
20. A. C. Kay, S. C. Wheeler, J. A. Bargh, L. Ross, *Organ. Behav. Hum. Decis. Process.* **95**, 83 (2004).
21. W. Güth, R. Schmittberger, B. Schwarze, *J. Econ. Behav. Org.* **3**, 367 (1982).
22. D. M. Messick, C. G. McClintock, *J. Exp. Soc. Psychol.* **4**, 1 (1968).
23. P. A. M. Van Lange, *J. Pers. Soc. Psychol.* **77**, 337 (1999).
24. S. D. Goldinger, W. A. Hansen, *Psychol. Sci.* **16**, 525 (2005).
25. A. Gallace, C. Spence, *Conscious. Cogn.* **17**, 370 (2008).
26. C. G. DeYoung, J. B. Peterson, D. M. Higgins, *Pers. Individ. Dif.* **33**, 533 (2002).
27. D. L. Schacter, G. S. Wig, W. D. Stevens, *Curr. Opin. Neurobiol.* **17**, 171 (2007).
28. D. M. Wegner, J. A. Bargh, in *Handbook of Social Psychology,* D. Gilbert, S. Fiske, G. Lindzey, Eds. (McGraw-Hill, Boston, MA, 1998), vol. 1, pp. 446–496.
29. C. R. Mortensen, D. V. Becker, J. M. Ackerman, S. L. Neuberg, D. T. Kenrick, *Psychol. Sci.* **21**, 440 (2010).
30. N. B. Jostmann, D. Lakens, T. W. Schubert, *Psychol. Sci.* **20**, 1169 (2009).
31. This research was supported by the Sloan School of Management and by National Institute of Mental Health grant MH60767 to J.B. We thank L. Williams, E. Morsella, the Yale ACME lab, and many research assistants for their feedback and aid.

Supporting Online Material

www.sciencemag.org/cgi/content/full/328/5986/1712/DC1
Materials and Methods
Additional Results
References

23 March 2010; accepted 17 May 2010
10.1126/science.1189993

NEW PRODUCTS

LIQUID HANDLING WORKSTATION

The Nimbus iProbe compact liquid handling workstation features up to four independent channels that can be configured with any combination of 1-ml or 5-ml pipetting heads. The new instrument provides flexible pipetting choices to and from microplates or tubes in volumes from 1 µl to 5,000 µl. It performs a wide range of liquid handling steps such as tube-to-tube, tube-to-plate, and plate-to-plate transfers, including pipetting from nonstandard labware. The flexibility offered by independently spaced channels is particularly suitable for hit picking and sample preparation from tubes. The 5-ml capability enhances high-volume applications such as vacuum-based solid-phase extraction. The Nimbus iProbe includes an intuitive graphical interface that facilitates programming.

Hamilton Robotics

For info: 775-858-3000 | www.hamiltonrobotics.com

IMAGING SOFTWARE

The cellSens software for life science imaging applications is available in three different packages designed to meet various user requirements. The software's user-definable interface allows the imaging process to be personalized from start to finish, for complete control over the entire experiment. Each package integrates seamlessly with Microsoft Windows and other Office programs. The cellSens Entry program provides the ability to perform simple image acquisition and documentation for basic image capture. The cellSens Standard software enables more advanced image capture, including time-lapse TWAIN acquisition. It offers the ability to motorize processes such as objective and filter changes, focusing, and internal shutter control. The cellSens Dimension supports the control and processing requirements for microscope-based experimental systems, providing a broad range of advanced features as well as optional specialized modules.

Olympus

For info: +49-40-2-37-73-5406 | www.microscopy.olympus.eu

WORKFLOW MODULE

The QIAsymphony AS module extends the capabilities of the QIAsymphony SP sample purification system and simplifies routine work processes through easy-to-use, intuitive software. The new module provides fully automated setup of Qiagen assays and polymerase chain reaction (PCR) kits. It addresses the complexity of laboratory processes and logistics of PCR assay setup in a straightforward way while maintaining the high performance of Qiagen real-time and end-point PCR kits and PCR assays. Samples processed on the QIAsymphony SP can be automatically transferred to the QIAsymphony AS, which reduces manual handling steps and documentation requirements.

Qiagen

For info: 800-362-7737 | www.qiagen.com

BLUE FLUORESCENT PROTEIN

A monomeric blue fluorescent protein with high photostability and pH stability is available. For use in protein labeling and organelle labeling, the TagBFP's narrow fluorescence emission peak makes it suitable for multicolor imaging. TagBFP features bright blue fluorescence with excitation and emission maxima at 402 nm and 457 nm. It offers a relatively short maturation half-time at 37°C. TagBFP can be expressed and detected in a wide range of organisms. Mammalian cells transiently transfected with TagBFP expression vectors give bright fluorescence within 10 to 12 hours and show no cytotoxic effects or protein aggregation. The protein's performance in fusions has also been demonstrated in the β-actin and α-tubulin models.

Axxora

For info: 800-550-3033 | www.axxora.com

STAUDINGER CHEMISTRY REAGENTS

A new line of Staudinger Ligation Reagents for in vivo and in vitro labeling of biomolecules features Staudinger chemistry, which relies on an azide-phosphine conjugation that works well in live-cell labeling and mass spectrometry applications. It is particularly useful in the study of protein glycosylation. It features a high degree of chemoselectivity, which eliminates off-target ligations with other biomolecules. The Staudinger ligation reactions are performed in aqueous solutions at physiological pH without side reactions with buffers and detergents. Azido-labeled biomolecules can be incorporated into a protein metabolically and detected with a variety of phosphine probes, including Thermo Scientific DyLight Fluorescent Dye–based probes. These reagents offer an alternative that is nontoxic to biological systems because there is no biomolecule oxidation.

Thermo Fisher Scientific

For info: 815-968-0747 | www.thermofisher.com

Electronically submit your new product description or product literature information! Go to **www.sciencemag.org/products/newproducts.dtl** for more information.

Newly offered instrumentation, apparatus, and laboratory materials of interest to researchers in all disciplines in academic, industrial, and governmental organizations are featured in this space. Emphasis is given to purpose, chief characteristics, and availability of products and materials. Endorsement by *Science* or AAAS of any products or materials mentioned is not implied. Additional information may be obtained from the manufacturer or supplier.